The Interaction of Proteins with Membranes: Combined Computational and Neutron Studies



Laura John

Structural Bioinformatics and Computational Biochemistry Unit

Department of Biochemistry, Magdalen College

University of Oxford

A thesis submitted for the degree of

DPhil in Biochemistry

April 2023

To my parents
Andrea and Jürgen Knörr

The same thrill, the same awe and mystery, comes again and again when we look at any question deeply enough. With more knowledge comes a deeper, more wonderful mystery, luring one on to penetrate deeper still. Never concerned that the answer may prove disappointing, with pleasure and confidence we turn over each new stone to find unimagined strangeness leading on to more wonderful questions and mysteries - certainly a grand adventure!

Richard P. Feynman - What Do You Care What Other People Think?

Acknowledgements

First thanks go to my supervisors, Mark Sansom and Luke Clifton, for providing me this opportunity, for always being ready to help and for the interesting project which enabled me to work interdisciplinarily between computational and experimental biophysics. The enthusiastic supervision of both motivated and inspired me to stay curious, excited but also critical at the same time.
I feel very privileged to have been part of the SBCB research group. Particular thanks goes to Fiona, Robin and Owen for their help during my initial stages of learning and their advice whenever needed, Andreas for the great collaborations, as well as to Irfan and Michael for maintaining the working stations and clusters; and to everyone else - thank you for having made the office such a great place to work at. On the experimental side, big thanks go to Suzi for supplying me with all the protein samples. Huge thanks go also to my parents and Toby, who support me in any possible way. Thank you for being there for me, celebrating the highs and helping me through the lows. In addition, a special thanks goes to Toby for his professional advice and support, for proofreading my thesis and for many fruitful discussions. Finally, I want to thank Magdalen College, the Department of Biochemistry and my funding bodies BBSRC, Oxford Interdisciplinary Bioscience DTP and ISIS Neutron and Muon Source.

Laura John
April 2023, University of Oxford

Declaration of Authorship

This report, and the work of which it is a record, were carried out by myself unless otherwise acknowledged.

The QCM-D measurements described in *Chapter 2* were conducted and alaysed by Dr. Luke Clifton.
For *Chapter 4* experimental protein samples were provided by Dr. Susan Black.
The Grp1-PH supported lipid bilayer experiments in *Chapter 4* were conducted in collaboration with Dr. Luke Clifton and Tao Ni.
Keith A. Gillow, Sam Evans and John McManigle provided the LaTeX template this thesis is based on.

Laura John
Oxford, April 2023

Abstract

The Interaction of Proteins with Membranes: Combined Computational and Neutron Studies | The interaction between proteins and membranes is essential for cell signalling. Planar model membrane sample systems enable structural and functional investigations of protein/membrane interactions via a variety of experimental methods, like neutron reflectometry (NR), quartz crystal microbalance (QCM) and attenuated total reflection Fourier transform infrared spectroscopy (ATR-FTIR). The free floating membrane (FFM) sample system is a promising, novel planar model membrane system, in which a water layer prevents direct contact between the membrane and the adjacent substrate surface, consisting of a carboxylate terminated oligo (ethylene glycol) self assembling monolayer (OEG-SAM). Our molecular dynamics (MD) simulations of the FFM system showed that membrane dynamics like lipid diffusion are not affected by the substrate surface system above a water inter-layer extent of around 25 Å. Therefore, the FFM system provides better membrane mimicking characteristics compared to previous planar model membrane systems, in which the membrane is in close contact with the substrate surface. Furthermore, our NR and QCM measurements demonstrated how changes in the buffer solution cation concentrations within physiological ranges cause an, as yet, unseen range (> 200 Å) of reversible bilayer movements from the surface. MD simulations suggested that cations, especially Ca^{2+} ions decrease the electrostatic repulsion between the anionic membrane and OEG-SAM by modulating the OEG-SAM surface charge, while structured hydration layers above the OEG-SAM surface prevent contact between OEG-SAM and membrane. Changing the nature and concentration of cations allowed us to modulate the extent of electrostatic repulsion between OEG-SAM and membrane. Different pH values of the buffer solution showed bilayer movements from the surface within the same range as buffer cations did, supporting our findings that the OEG-SAM surface charge modulation is the main cause of the large reversible membrane movements. These results suggest that within a complex interplay of forces acting in the free floating bilayer sample system, electrostatic interactions can be manipulated to provide a direct means of controlling the membrane-to-surface distance. This "cation switchable" sample system offers a new opportunity to mimic the intracellular and extracellular environment using a planar membrane model system. Thus, our goal was to use this novel sample system to investigate the interaction between peripheral membrane proteins and their target membranes. The proteins of interest were the Kindlin-2 and the T-lymphoma invasion and metastasis 2 (TIAM2) proteins, involved in integrin activation and Rac1 GTPase activation, respectively. Both proteins contain a phosphatidylinositol lipid binding pleckstrin homology domain, responsible for membrane localization of the protein. The combination of NR and MD provided structural insights into the membrane binding orientation and position of the proteins. For instance, our computational and experimental results confirmed the previously suggested clustering of Kindlin-2 upon membrane binding. Together, this work provides an in-depth understanding of the processes within the FFM system in order to make it accessible to complex membrane interaction studies. The full understanding of acting forces within the system allowed us to apply the FFM system for protein/membrane interactions. Our investigations pave the way to further protein/membrane studies using the FFM system, as well as to an extension of the usage to integral membrane proteins and native membranes. Furthermore, our studies showed the powerful approach of combining NR with MD.

Contents

List of Abbreviations **ix**

1 Introduction **1**
1.1 Biological Role of Membrane/Protein Interactions . . . 1
1.1.1 Composition and Function of Biological Membranes . . . 1
1.1.2 Membrane Recruitment of PMPs by Phospholipids . . . 6
1.2 Studying Membrane/Protein Interactions . . . 16
1.2.1 Experimental Model Membrane Systems . . . 17
1.2.2 Experimental Methods . . . 24
1.2.3 Computational Methods . . . 37
1.2.4 Aim and Outline of this Thesis . . . 45

2 The Effect of Salt Buffer Condition on Free Floating Model Membranes **48**
2.1 Introduction . . . 48
2.2 Results . . . 51
2.2.1 NR Reveals Cation Induced Bilayer-to-SAM Distance Modulation . . . 51
2.2.2 Complementary Analysis on QCM-D Sensor Surfaces . . . 62
2.2.3 MD Simulations Reveal Differences in Ion Binding between OEG-SAM and FFM . . . 64
2.3 Discussion . . . 79
2.4 Materials and Methods . . . 81
2.4.1 Materials . . . 81
2.4.2 Neutron Reflectometry (NR) Measurements . . . 82
2.4.3 Quartz Crystal Microbalance with Dissipation Monitoring (QCM-D) Measurements . . . 86
2.4.4 Molecular Dynamics (MD) Simulations . . . 88

3 Influence of pH Condition and Substrate on Free Floating Model Membranes **98**
3.1 Introduction . . . 98
3.2 Results . . . 100
3.2.1 Influence of pH Condition on the FFM System . . . 100
3.2.2 Influence of OEG-SAM Substrate on Free Floating Membranes . . . 114
3.3 Discussion . . . 123
3.4 Materials and Methods . . . 126
3.4.1 Materials . . . 126
3.4.2 Neutron Reflectometry (NR) Measurements . . . 126
3.4.3 Molecular Dynamics (MD) Simulations . . . 127
3.4.4 Appendix . . . 132

4 Applying the FFM System to Study Peripheral Membrane Proteins 138
4.1 Introduction . . . 138
4.2 Results . . . 141
4.2.1 NR Experiments Reveal Crucial Conditions for Studying PMPs . . . 141
4.2.2 MD Simulations Provide Further Insights in Binding Conformations . . . 160
4.3 Discussion . . . 179
4.4 Methods . . . 184
4.4.1 Materials . . . 184
4.4.2 Protein Constructs . . . 185
4.4.3 ATR-FTIR Experiments . . . 188
4.4.4 Neutron Reflectometry Experiments . . . 189
4.4.5 MD Simulations . . . 194
4.5 Appendix . . . 198

5 Conclusion and Outlook 207

Bibliography 211

List of Abbreviations

AA . . . . . all atomistic

APM . . . . . area per molecule

ATR-FTIR . . . attenuated total reflection Fourier transform infrared spectroscopy

AuMW . . . . . gold matching water (mixture of 75% deuterium and 25% water)

BS . . . . . binding site

Ca^{2+} . . . . . calcium cation

$CaCl_2$ . . . . . calcium chloride

CC . . . . . coiled coil

CG . . . . . coarse grained

Chol . . . . . cholesterol

COM . . . . . center of mass

DGDG . . . . . digalactosyldiacylglycerol

D_2O . . . . . deuterium

DOPIP2 . . . . 1,2-dioleoyl-*sn*-glycero-3-phospho-(1'-myo-inositol-4',5'-bisphosphate)

DOPIP3 . . . . 1,2-dioleoyl-*sn*-glycero-3-phospho-(1'-myo-inositol-3',4',5'-trisphosphate)

ECC . . . . . electronic continuum correction

Ex . . . . . extra

FFM . . . . . free floating membrane

FWHM . . . . . full width at half maximum

Grp1 . . . . . general receptor for phosphoinositides 1

HEPES . . . . . 2-[4-(2-Hydroxyethyl)piperazin-1-yl]ethane-1-sulfonic acid

H_2O . . . . . water

IMP . . . . . integral membrane protein

IRE . . . . . internal reflection element

LB . . . . . Langmuir-Blodgett

LJ . . . . . Lennard-Jones

LS . . . . . Langmuir-Schaefer

MCMC . . . . . Markov chain Monte Carlo

MD . . . . . molecular dynamics

Na^+ . . . . . sodium cation

NaCl . . . . . sodium chloride

NMR . . . . . nuclear magnetic resonance

NR . . . . . neutron reflectometry

OEG . . . . . carboxylate terminated oligo(ethylene glycol) alkanthiol, HS-C_{11}-EG_3-OCH_2-COOH

PH . . . . . pleckstrin homology

PIP . . . . . phosphatidylinositol

PIP2 . . . . . phosphatidylinositol bisphosphate

PIP3 . . . . . phosphatidylinositol trisphosphate

PMP . . . . . peripheral membrane protein

POPC 1-palmitoyl-2-oleoyl-*sn*-glycero-3-phosphocholine

POPIP2 . . . . 1-palmitoyl-2-oleoyl-*sn*-glycero-3-phospho-(1'-myo-inositol-4',5'-bisphosphate)

POPIP3 . . . . 1-palmitoyl-2-oleoyl-*sn*-glycero-3-phospho-(1'-myo-inositol-3',4',5'-trisphosphate)

POPS 1-palmitoyl-2-oleoyl-*sn*-glycero-3-phospho-L-serine

PrMW . . . . . protein matching water (mixture of 42% deuterium and 58% water)

QCM-D . . . . quartz crystal microbalance with dissipation monitoring

RMSD . . . . . root-mean-square deviation

SAM . . . . . self-assembled monolayer

SAPIP3 . . . . . 1-stearoyl-2-arachidonoyl-*sn*-glycero-3-phospho-(1'-myo-inositol-3',4',5'-trisphosphate))

SASA . . . . . solvent accessible surface areas

Si . . . . . silicon

SiO_2 . . . . . silicon dioxide

SLB . . . . . supported lipid bilayer

nSLD . . . . . neutron scattering length density

SMW . . . . . silicon matched water (mixture of 38% deuterium and 62% water)

SUVs . . . . . small unilamellar vesicles

TIAM2 . . . . . T-lymphoma invasion and metastasis 2

vdW . . . . . van der Waals

VFP . . . . . volume fraction plot

1 Introduction

Contents

1.1 Biological Role of Membrane/Protein Interactions 1
1.1.1 Composition and Function of Biological Membranes 1
1.1.2 Membrane Recruitment of PMPs by Phospholipids 6
1.2 Studying Membrane/Protein Interactions 16
1.2.1 Experimental Model Membrane Systems 17
1.2.2 Experimental Methods 24
1.2.3 Computational Methods 37
1.2.4 Aim and Outline of this Thesis 45

1.1 Biological Role of Membrane/Protein Interactions

1.1.1 Composition and Function of Biological Membranes

In a macroscopic view biological membranes act as a selective barrier, surrounding cells and organelles and allowing only specific molecules to pass through. Therefore, membranes prevent free diffusion of molecules and ions, providing controlled conditions in cells and organelles. However, in a microscopic view the whole complexity of biological membranes is revealed. Biological membranes are lipid bilayers of varying lipid composition depending on the organism and the function of the membrane. In human cells the most abundant lipids are glycerophospholipids composing of a polar head group (e.g. choline for phosphatidylcholine (PC), ethanolamine for phosphatidylethanolamine (PE), serine for phosphatidylserine (PS) or inositol for phosphatidylinositol (PIP)) and two fatty acid tails (Figure 1.1,1.2).[1], [2] Among phospholipids PC is with 45-55% of total lipids the most abundant, followed

by PE (15-25%), PS (10-15%) and PIP (5-10%). The second most abundant class of lipids in human cells are sterols (cholesterol, 10-20%), followed by sphingolipids (sphingomyelin (SM), 5-10%), and glycolipids (glycosphingolipids, 2-5%).[3], [4] However, looking at different membranes individually, these concentrations vary quite significantly. For example, in the mammalian plasma membrane, cholesterol has a concentration of 40-50 mol%. The remaining 50-60 mol% are split in glycerophospholipids and sphingolipids with $\sim$30 mol% PC, $\sim$27 mol% PE, $\sim$26 mol% SM and $\sim$17 mol% anionic lipids including PS, PI, PA.[2], [5]

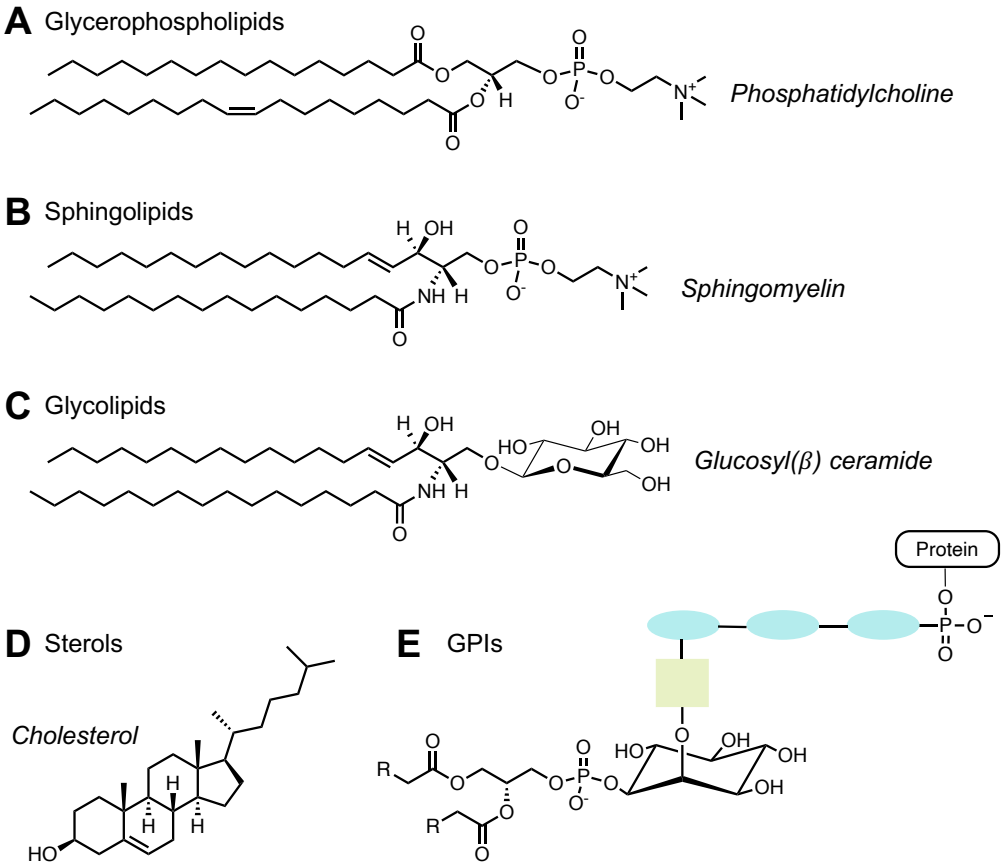


Figure 1.1 | Structural Overview of Most Abundant Lipid Species. Shown are examples for the most abundant lipid species in human and plant cell membranes: **A** Phosphatidylcholine represents the group of glycerophospholipids which have a characteristic glycerol group connecting two fatty acid tails with a polar head group, which is unique for each glycerophospholipid species (see Figure 1.2). **B** Sphingomyelin is shown as example for sphingolipids. In sphingolipids, the unsaturated amino alcohol sphingosine and a fatty acyl tail are linked by an amide bond (forming a ceramide). A polar, sphingolipid specific head group is bound to the terminating hydroxy group of the amino alcohol sphingosine. **C** Glucosyl(β) ceramide, a glycosphingolipid, was chosen as example for representing glycolipids. In glycolipids one or a chain of carbohydrate/s is attached to the glycerol group or the terminating hydroxy group of sphingosine via a glycosidic bond forming glycoglycerolipids or glycosphingolipid, respectively. **D** The structure of cholesterol, the most abundant sterol, is illustrated. **E** Schematic presentation of a GPI (glycosylphosphatidylinositol). GPIs anchor proteins to the membrane. Different sugars (indicated by differently shaped/colored building blocks) are bound to phosphatidylinositol, forming a sugar chain which links the protein with the lipid. Structures were produced with ChemDraw.

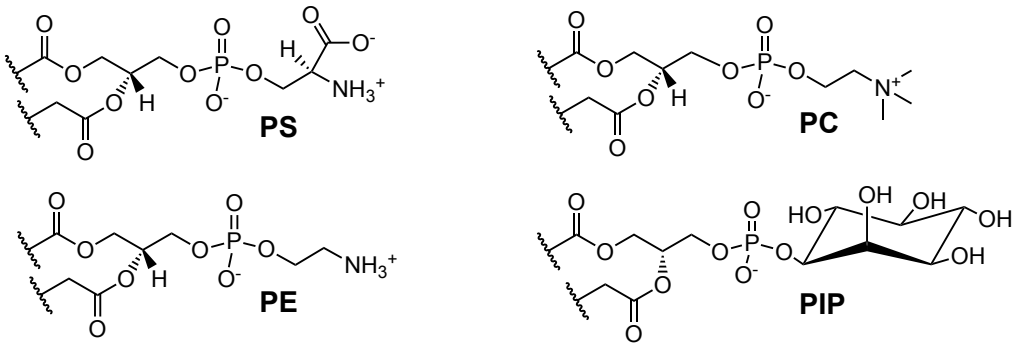


Figure 1.2 | Structural Overview of Glycerophospholipid Head Groups. Shown are molecular structures for the polar head groups of most abundant glycerophospholipids, namely choline for phosphatidylcholine (PC), ethanolamine for phosphatidylethanolamine (PE), serine for phosphatidylserine (PS) and inositol for phosphatidylinositol (PIP). Structures were produced with ChemDraw.

In plant plasma membranes glycerophospholipids are with PC and PE also the most abundant lipids, followed by sterols, glycosylphosphatidylinositols and sphingolipids (Figure 1.1).[6] However, the relative abundance and lipid composition always depends on the type and physiological state of the respective cell.[2], [7] The abundance of different lipid species depends even on the leaflet of the membrane due to the strong asymmetric nature of the plasma membrane. In the human cell membrane, for example, PC and SM are primarily found in the extracellular leaflet, while PE and PIP are mainly, and PS almost exclusively located in the cytosolic leaflet of the cell membrane.[8]–[10] In addition, the lateral arrangement of lipids within a membrane is also considered crucial. Within the membrane, microdomains can be formed which are enriched in cholesterol and sphingolipids. These so called lipid 'rafts' are thought to play an important role in cell signaling and trafficking, although their detailed physiological role remains often elusive.[11], [12]

Aside from the complexity of lipid composition and distribution, there is also a wide range of proteins embedded in specific biological membranes, so called integral membrane proteins (IMPs), as well as a wide range of proteins binding reversibly to the surface of specific biological membranes, so called peripheral membrane proteins (PMPs).

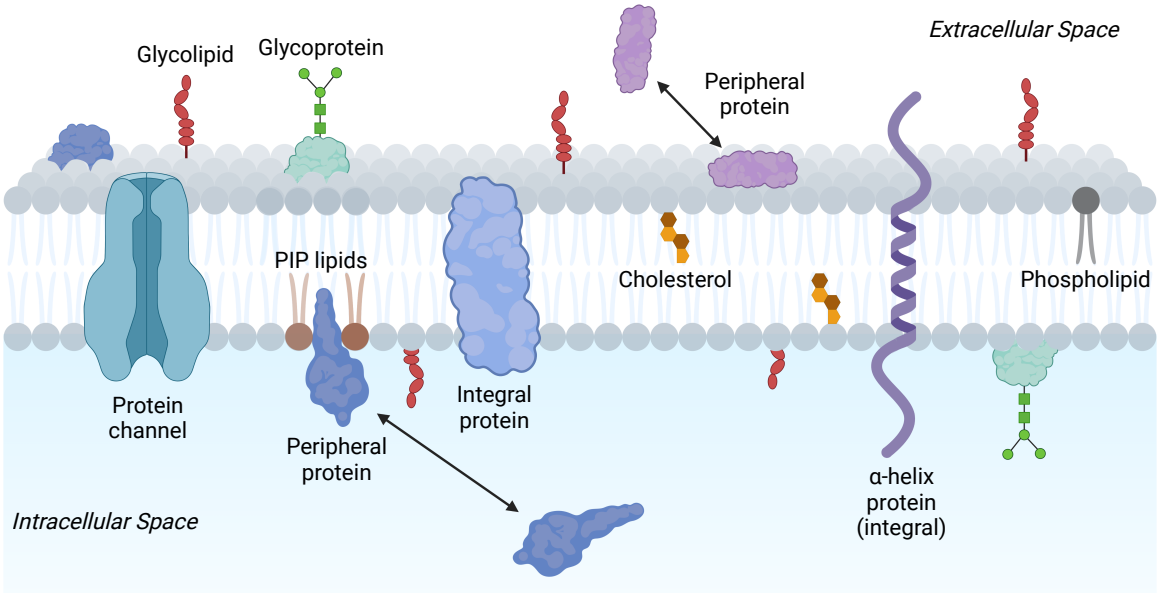


Figure 1.3 | Typical Cell Membrane Composition. Extracellular and intracellular leaflet contain different lipid species. Some lipids are primarily in one of the two leaflets, leading to an asymmetric lipid distribution. Carbohydrates are bound to some lipids and proteins, forming glycolipids and glycoproteins, respectively. While integral membrane proteins (IMP) are in permanent contact with the membrane, peripheral membrane proteins (PMPs) bind transiently to the membrane (indicated with arrows). PMPs have a soluble and a membrane bound state. Adapted from "Phospholipid Bilayer Membrane", by BioRender.com (2023). Retrieved from *https://app.biorender.com/biorender-templates*.

IMPs and PMPs are crucial for the function of the respective biological membrane. IMPs serve as ion channels, transporters, receptors, enzymes, cell adhesion molecules or energy transducers and are vital in a range of cellular processes, including cell signalling, cell adhesion, enzymatic activity, structural support and transport.[13], [14] PMPs are also involved in cell signaling, structural support, enzymatic activity, and transport.[15] Therefore, PMPs and IMPs are attractive as drug targets with membrane proteins constituting more than 60% of current drug targets.[16] But inversely, the membrane is also crucial for the function of the membrane proteins, forming a harmonized interplay between membrane and IMPs/PMPs. Hence, the interactions of different lipid species with an IMP can have a structural effect on the protein by e.g. tightly fixing the IMP and/or inducing oligomer formation of the IMP within the membrane.[17], [18] For example, cardiolipin binding is obligatory for functional dimer formation of the bacterial homologue of the eukaryotic biogenic transporters (LeuT4) and the beacterial Na^+/H^+ antiporter NhaA.[17] Also, nucleotide sugar transporters like the yeast GDP-mannose transporter,

Vrg4, require the presence of interfacial lipids to form higher order oligomers. Hereby, only short chain interfacial lipids allow the conformational change between inward and outward facing state necessary for the transport activity.[18] Another well known PMP controlling lipid interaction is the interplay between cholesterol and ion channels with various types of ion channels showing functional dependence on the level of cholesterol in the membrane.[19]–[21] One of the most popular examples are the inwardly rectifying K^+ channels (Kir channels).[22], [23] Recently, a computational study of Kir2.2 suggested a model how an increasing cholesterol concentration in the membrane decreases channel activity by occupying specific cholesterol binding sites, which stabilize the closed channel state.[24]

PMPs are often recruited to a specific cellular membrane by a specific lipid species for which they show high selectivity and affinity.[25] And some lipid interactions of membrane proteins can affect the function of the protein either through direct functional contributions [26]–[28] or allosteric modulation.[29]–[31] Therefore, the interactions between IMPs/PMPs and biological membranes are of fundamental importance. In our studies we were interested in the interactions between phospholipid membranes and PMPs, which have a pleckstrin homology (PH) domain driving the binding to the membrane.

1.1.2 Membrane Recruitment of PMPs by Phospholipids

PMPs contain one or more domains driving the binding to the membrane through electrostatic interactions with the polar head groups of the membrane lipids or with integral membrane proteins. They are interacting either on the cytosolic or extracellular leaflet of the membrane, which divides them into two broad groups. These two groups of PMPs differ in the type of lipids they interact with, as well as in their biological role. Thus, PMPs that interact with the cytosolic leaflet mostly interact with negatively charged lipids such as PS or PIPs,[32]–[34] while PMPs that interact with the external leaflet predominantly interact with glycosphingolipids, which are typically more abundant in the extracellular leaflet.[35], [36] The cytosolic group of PMPs generally plays a crucial role in the normal functioning of the cell, while the extracellular group comprises bacterial exotoxins that bind to the host membrane as part of their pathogenic mechanism. Upon membrane binding PMPs can have an effect on lipid

organization within the cell membrane. So, many PMPs have multiple lipid binding sites and induce clustering of their target lipid around the membrane bound protein.[37]–[39] In addition, PMPs can form protein-protein clusters on the membrane and therefore lead to lipid 'rafts' formation.[40], [41]

Although less abundant than PS, PIPs are probably the most important cytosolic lipid species, which recruit PMPs to the target membrane.[33], [34], [42] There are several different docking sites interacting with PIPs, including the FYVE, PX, ENTH, ANTH, FERM, PTB, GLUE, EHD, BAR, PDZ, KA1, C2 and PH domain.[33], [43] While each domain has its unique overall structure and lipid binding mechanism, most of them contain basic grooves, pockets or loop regions on the protein surface, which enable electrostatic interactions with the negatively charged lipid head groups of the PIP lipids. Furthermore, some of the PIP binding domains share structural features, as well as lipid binding motifs within the lipid binding sites. For example, the PH, PTB, PDZ and FERM domains contain seven β strands, with the first four and the last three β strands forming two almost perpendicular β sheets. These β sandwich structures are closed on one side by a C-terminal α-helix.[25] Several PH, PDZ and FERM domains show PIP binding in the pocket between the two β sheets. Flexible loops surrounding the PIP binding site at the open end of the β sandwich structure often determine via their amino acid composition and length the PIP binding specificity and affinity. For this, one of the most prominent examples is the loop between the first two β strands (β1-β2) with its basic sequence motif of "KX_n(K/R)XR", contained in many PH domains.[44] In contrast, PTB domains often have an additional α-helix located between the β1 and β2 strand, thereby blocking the binding pocket between the two β sheets. Here, PIP binding occurs mostly on the outer surface of this additional α-helix.[25] Also, across the different PIP binding domains, there are different modes of membrane targeting. Even within classes of PIP binding domains, there are different mechanisms. For example, the C2 domains can be divided into Ca^{2+} dependent and Ca^{2+} independent domains. In the case of Ca^{2+} dependent C2 domains membrane binding is mediated via Ca^{2+} ions, which bridge negatively charged patches on the protein surface with PIPs. Alternatively, for Ca^{2+} independent C2 domains direct, electrostatic interactions between negatively charged PIPs and positively charged patches on the protein surface enable membrane

binding. Both binding modes are often followed by hydrophobic loop and/or helix insertion into the membrane, thereby increasing the stability of the protein-membrane complex.[45], [46]

Due to various structural characteristics like, for example, the previously mentioned loops around a PIP binding site, the different protein domains favour different PIP species, which vary in number and position of phosphate groups in the inositol ring (Figure 1.4). The interconversion between different PIP species is often carried out by interacting PMPs via phosphorylation and dephosphorylation and is essential for a large number of cell signaling processes. Figure 1.4 shows the possibilities of interconversion between different PIPs conducted by kinases and phosphatases. One well-known example is the dephosphorylation of PI(3,4,5)P3 to PI(4,5)P2 conducted by the PMP called phosphatase and tension homologue (PTEN). PTEN consists of an N-terminal phosphatase (Ptase) domain, followed by a C2 domain. While the Ptase domain contains the active sites, the C2 is the membrane-anchoring domain targeting PI(3,4,5)P3. The dephosphorylation of PI(3,4,5)P3 is the initial step of a cell signalling cascade leading to apoptosis. Consequently, dysfunction of PTEN results in tumor development and numerous mutations in the *PTEN* gene have been associated with cancer.

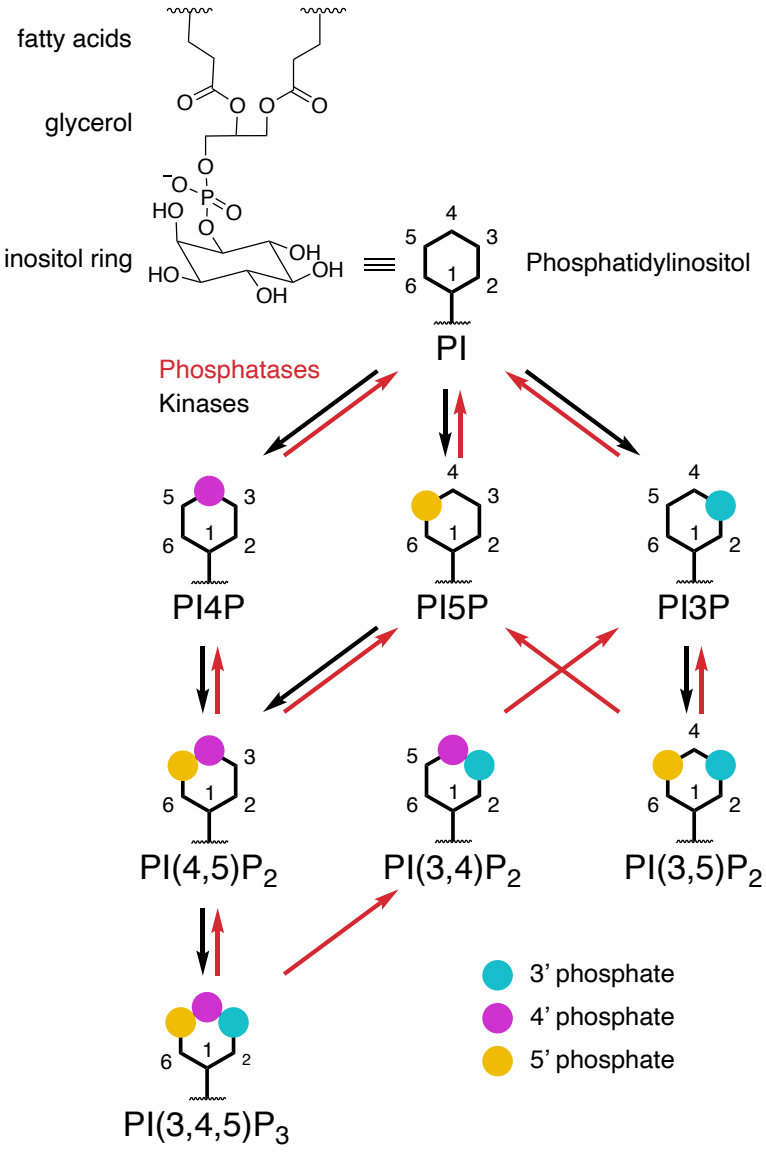


Figure 1.4 | Possible Interconversions between PIP Species. Shown are different PIP species and their interconversion by different kinases and phosphatases. The possible direction of conversions conducted by kinases and phosphatates is shown with black and red arrows, respectively. For simplicity the hydroxy groups attached to the inositol ring are not shown and the phosphate groups respresented as cyan (3'), magenta (4') and orange (5') balls. Adapted from [33].

One of the largest families of PIP binding domains is that of PH domains. More than 250 human proteins contain a pleckstrin homology (PH) domain, which show high sequence variability of up to 80%.[47]–[49] However, the three-dimensional structures are remarkably conserved across protein families.[45], [50] PH domains contain a seven-stranded antiparallel β-sheet core, one end of which is closed by a characteristic C-terminal α-helix (Figure 1.5).[49], [51]

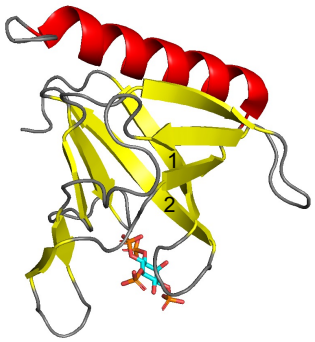


Figure 1.5 | Conserved PH Domain Structure. As an example the crystal structures of the Grp1 PH domain is shown in complex with inositol 1,3,4,5-tetrakisphosphate (I(1,3,4,5)P4, cyan), the head group of PI(3,4,5)P3 (1FGY).[52] The characteristic C-terminal α-helix is highlighted in red and the seven-stranded β-sheet core in yellow. The β-sheets between which the PIP binding site is located are labeled with 1 and 2.

Furthermore, due to conserved positioning of certain acidic and basic residues the structures of PH domains are commonly polarized.[53] Although the structure of many PH domains is well characterized, their lipid-binding properties are still a topic of debate in many cases. Thus, while a previous study suggested that most *Saccharomyces cerevisiae* PH domains have weak or no binding affinity for PIPs,[54] a more recent investigation of 67 human PH domain-containing proteins revealed that over half of these proteins showed significant binding affinity for PIPs.[48] In most PIP binding PH domains the dominant PIP binding site is located in the pocket between the two β sheets formed by positively charged residues in the loops connecting the $\beta1$ with the $\beta2$ strand and the $\beta3$ with the $\beta4$ strand (Figure 1.5).[49], [51] Hereby, the "KXn(K/R)XR" motif in the $\beta1/\beta2$ loop is conserved across many PH domains and enables contacts between the negatively charged phosphate groups of PIPs and the protein domain.[44], [55], [56] Thus, this binding site is often referred as canonical PIP binding site of PH domains. However, certain PH domains, e.g. found in β-spectrin and ArhGAP9, lack the PIP binding motif in the $\beta1/\beta2$ loop and have an alternative binding site located between the $\beta1/\beta2$ and the $\beta5/\beta6$ loops.[44], [57] This binding site is often referred as non-canonical binding site. Some PH domains, like ASAP1, show simultaneous PIP binding in the canonical and non-canonical PIP binding site and computational studies suggested even three simultaneously bound PIP molecules in case of Grp1 via a third, less well spatially defined interaction site.[58], [59] The specific residues involved in PIP binding contain often some positively charged amino acids, like Arginine and Lysine, but vary

between PH domain proteins.[49] Nevertheless, the overall conserved structure ensures the positioning of the PIP binding site in similar location and orientation for each kind of PH domain. In the following we focus on examples of proteins containing a PIP binding PH domain, which we used in our studies.

Grp1

The general receptor for phosphoinositides 1 (Grp1) protein (399 residues) is a GDP/GTP exchange factor and contains an N-terminal Sec7 domain enclosing residues 77 to 206 and a C-terminal PH domain enclosing residues 264 to 380 (see UniProt entry O08967, Figure 1.6). The Sec7 domain catalyzes the GDP/GTP exchange on ADP ribosylation factor protein (ARF) 1 and 5. Therefore, Grp1 is involved in actin rearrangement, endo- and exocytosis, membrane budding and trafficking.[60] The PH domain of Grp1 acts as membrane anchoring domain and binds to PIP(3,4,5)P3 with unusually high selectivity and affinity.[61]–[63] This enables spatial and temporal membrane docking of Grp1 in response to insulin-stimulated accumulation of PIP(3,4,5)P3.[60], [64] Insulin is known to activate PI3-kinase (phosphoinositide 3-kinase), which catalyzes the lipid phosphorylation of PI(4,5)P2 into PI(3,4,5)P3.[65] Therefore, insulin stimulates via different downstream signalling pathways glucose uptake, cytoskeletal rearrangement, cell adhesion, chemotaxis, secretion, cell growth, and apoptosis, as well as the regulation of early endosome structure.[64] Grp1 is involved in the insulin-stimulated signaling pathway of cytoskeletal rearrangement. Through its GDP/GTP exchange factor activity on ARF proteins, membrane bound Grp1 propagates the insulin stimulated signal to downstream signaling pathways leading to insulin induced actin rearrangement.[64] The PH domain of Grp1 (Grp1-PH) is a well-studied protein domain with several previous studies, computational[59], [66]–[70] and experimental[52], [55], [60], [71], providing insights in PIP binding sites, lipid or membrane binding affinities, membrane bound conformations, as well as detailed structural insights of the membrane binding process. Therefore, Grp1-PH is an ideal candidate for exploring the potential of, for example, newly developed experimental or computational techniques/methods for studying PMPs.

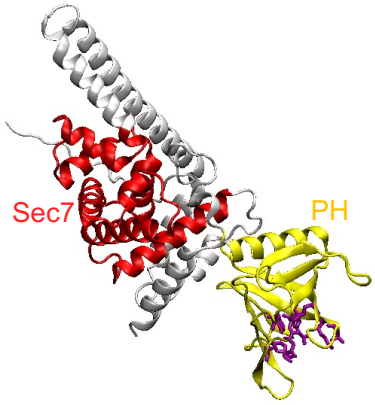


Figure 1.6 | Structure and Composition of Grp1. Shown is the predicted AlphaFold structure of the whole Grp1 protein (AF-O08967-F1). The N-terminal catalytic Sec7 domain is colored in red (residues 77-206) and the C-terminal membrane anchoring PH domain in yellow (residues 264-380). The previously via crystal structure analysis suggested PIP binding site in the PH domain is highlighted with the stick model in purple and includes mainly positively charged amino acids, namely K273, T280, K282, R284, Y295, R305, K343, N354, H355.[52], [55]

TIAM2

The T-lymphoma invasion and metastasis 2 (TIAM2) protein (1715 residues) contains an N-terminal PH domain (residues 504-625), followed by a coiled coil region (CC, residues 630-700) and an Extra domain (Ex, residues 707-741), often referred as PH-CC-Ex domain.[72] Additionally, TIAM2 contains a Ras-binding domain (RBD, residues 831-902), a PSD-95/DlgA/ZO-1 (PDZ, residues 911-997) domain, a Dbl homology domain (DH, residues 1120-1314) and a second, C-terminal PH domain (PHc, residues 1347-1478) (see UniProt entry Q6ZPF3, Figure 1.7). TIAM2 is a closely related homolog of TIAM1 with high sequence similarity,[73] both belonging to the same family of guanine nucleotide exchange factors that specifically activate Rac GTPases, mainly the small GTPase Rac1 (Rac1).[74], [75] The activity of Rac1 plays a critical role in regulating a variety of cellular processes, including actin cytoskeleton dynamics, cell adhesion, polarity and migration. Additionally, Rac1 has been shown to modulate transcription and gene regulation.[76], [77] TIAM2 seems to be particularly important in Rac1 activation related to dendritic growth in young neurons.[78], [79] TIAM1/2 activate Rac1 by catalysing the ejection of GTPase-bound GDP and the loading of GTP.[80] Hereby, the catalytic Dbl homology (DH) domain of TIAM1/2 interacts with the flexible switch

regions of Rac1, inducing significant conformational changes of the nucleotide-binding pocket and enabling the exchange of the nucleotide.[80] The directly adjacent N-terminal PH domain is thought to enhance the catalytic activity of the DH domain by positioning the active site in the DH domain towards the nucleotide-binding cleft of Rac1 while bound to TIAM1/2.[81]

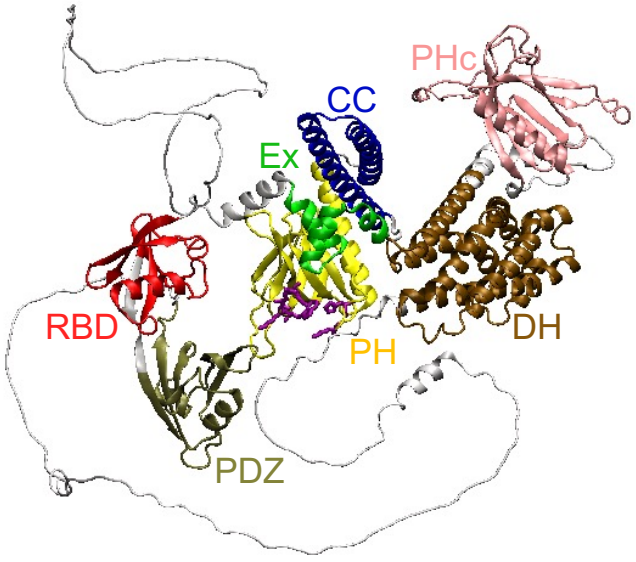


Figure 1.7 | Structure and Composition of TIAM2. Shown are the protein domains of the TIAM2 protein and their connecting loop regions in the predicted AlphaFold structure of TIAM2 (AF-Q6ZPF3-F1). The N-terminal PH domain is colored in yellow (residues 504-625) and the following CC region (residues 630-700) and Ex domain (residues 707-741) are highlighted in blue and green, respectively. The previously suggested PIP binding site in the N-terminal PH domain is highlighted with the stick model in purple and includes mainly positively charged amino acids, namely K514, R531, K532, W533, H579 and K581.[72] Further domains of TIAM2 are highlighted in red (RBD), tan (PDZ), brown (DH) and pink (C-terminal PH, cPH). The connecting loop regions between the protein domains are shown in light grey. These loop regions are mainly of unknown structure and therefore of high uncertainty concerning their conformation. Thus, for reasons of clarity, additional C- and N-terminal loop regions (residues 1-503 and 1479-1715) of unknown structure are not shown.

An essential step of Rac1 activation is the membrane binding of TIAM1/2. It has been shown that the N-terminal PH-CC-Ex region, containing an N-terminal PH domain (nPH), a coiled coil (CC) region and the Extra domain (Ex), is the membrane anchoring domain of TIAM1/2.[82] Interestingly, the PH domain alone is not able to bind to the membrane, suggesting that the CC-Ex domain increases the membrane affinity of TIAM1/2 by stabilizing the lipid binding site of the adjacent PH domain towards the substrate.[72] The substrate of the membrane interacting nPH domain of TIAM1/2 is PI(3,4,5)P3, PI(3,4)P2, as well as PI(4,5)P2.[57] In addition to its membrane anchoring role, the

PH-CC-Ex domain functions as a protein-protein interaction site, mediating interactions with different integral, as well as peripheral membrane proteins, e.g. PAR3, CD44, JIP2.[72], [83] The protein-protein interactions via the PH-CC-Ex domain are crucial for the location of TIAM1/2 to particular membrane subdomains and signalling complexes. Despite numerous investigations into TIAM2, which holds significant medical and biological relevance,[84] detailed insights in the membrane binding mechanism of TIAM2, including lipid binding sites, membrane bound conformations and contributions of different subdomains continue to elude us.

K2

The 680 residue long kindlin-2 protein belongs to the kindlin family, which is a group of cytoplasmic proteins with critical roles in cell adhesion and signalling, including three members: kindlin-1 (K1), kindlin-2 (K2) and kindlin-3 (K3). Like all kindlin proteins, K2 contains an N-terminal F0 domain, adjacent to a FERM domain (Four-point-one, ezrin, radixin, moesin), divided into three subdomains (F1, F2, F3), and a PH domain, which is inserted into the FERM domain, interrupting the F2 subdomain (Figure 1.8).[85]

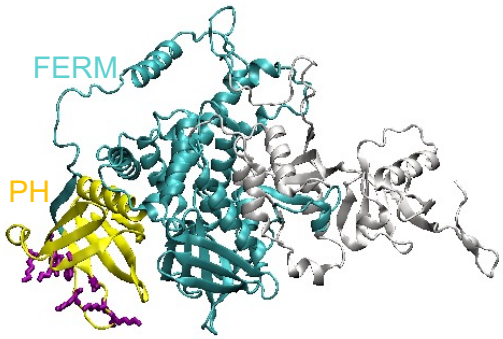


Figure 1.8 | Structure and Composition of K2. Shown is the predicted AlphaFold structure of the whole K2 protein AF-Q96AC1-F1). The FERM domain is colored in cyan (residues 189-661) and its inserted PH domain in yellow (residues 380-476). The previously via NMR structure analysis suggested PIP binding site in the PH domain is highlighted with the stick model in purple and includes mainly positively charged amino acids, namely K383, K385, K386, K390, K393, K408, H419, Y395.[86]

The K2-PH domain has been found to specifically bind to two PIPs, namely PI(4,5)P_2 and PI(3,4,5)P_3. Hereby, K2-PH shows a stronger affinity for PIP3 compared to PIP2, forming a weaker ligand for K2-PH.[86] A recent computational study showed that the difference between the K2-PH conformation

when bound to a PIP3 *versus* a PIP2 containing membrane is maximal for both PIPs being deprotonated at the phosphate group located at position 4' in the inositol ring (see Figure 1.4 for PIP structures).[87] These findings indicated an influence of the PIP protonation state on K2 binding selectivity and affinity. Membrane bound K2 binds to a specific binding region at the β cytoplasmic tail of integrins.[88] Integrins are transmembrane receptors, each composed of two subunits, α and β, that form a heterodimer (Figure 1.9). Each of the subunits consist of a large extracellular domain, a helical transmembrane domain and a C-terminal cytoplasmic tail. Integrins get activated by the binding of the proteins talin and K2 at the β cytoplasmic tail.[88]–[90] Once activated, integrins bind to the extracellular matrix via their extracellular domain. As talin interacts simultaneously with the β cytoplasmic tail of integrin and the actin cytoskeleton, activated integrins serve as a linker between cytoskeleton and the extracellular matrix.[90], [91] In addition to the integrin activation, there is evidence that K2 facilitates the clusering of activated integrin, thereby increasing multivalent ligand binding.[92] Furthermore, recent crystal structures of K2 revealed unexpected dimeric K2 structures, which provide a mechanistic and structural explanation of how K2 promotes integrin clustering.[93] However, further experimental and computational studies are needed to validate and fully understand the K2 and integrin clustering.

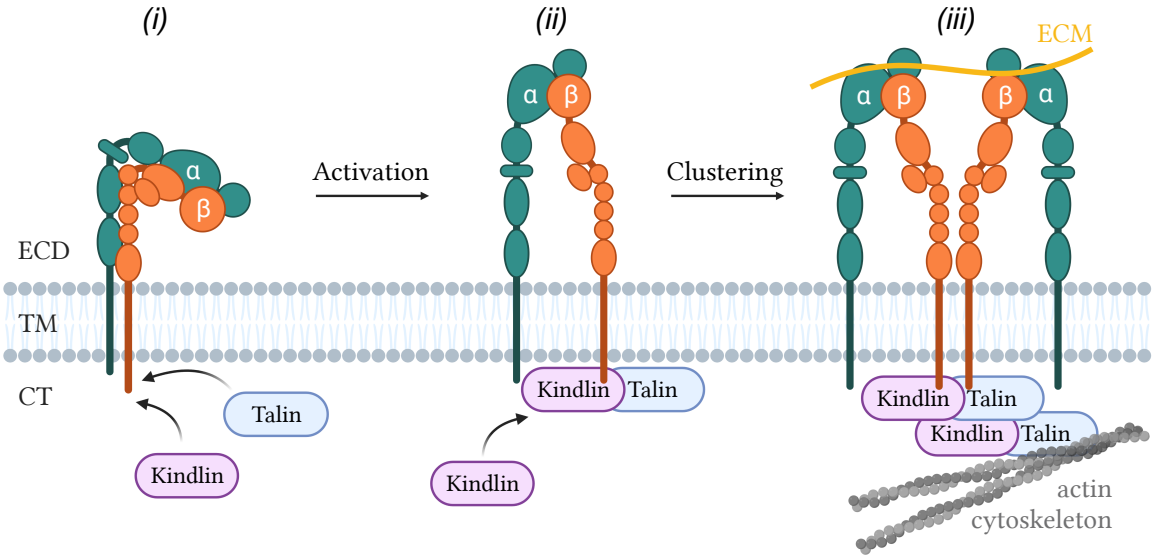


Figure 1.9 | Cytoplasmic K2 Interaction with Integrin Mediates Integrin Activation and Clustering. Illustrated are schematic representations of three different integrin conformations: (***i***) closed, inactive, (***ii***) open, active, (***iii***) active, clustered. Integrin consists of an extracellular domain (ECD), a trans membrane domain (TM) and a cytoplasmic tail (CT). The binding of talin and K2 to the CT of β integrin activates integrin, leading to the open conformation of the ECD (***ii***). Talin and K2 are also facilitating and stabilizing integrin clustering through dimerization. Talin interacts with the actin cycloskeleton, while the ECD associates with the extracellular martrix (ECM), forming a linkage between ECM and cytoskeleton (***iii***). Adapted from "Integrin Structure and Activation", by BioRender.com (2023). Retrieved from *https://app.biorender.com/biorender-templates*.

1.2 Studying Membrane/Protein Interactions

Computational methods like molecular dynamics (MD) simulations are a powerful tool to investigate membrane proteins and their lipid interactions. MD simulations provide atomistic resolution, as well as methods to calculate binding energies for the protein binding to a membrane or for single lipid binding to a membrane protein. However, for validation of computational results, biophysical experimental data are needed. To obtain these experimental biophysical data by experimental investigations of membrane/protein interactions, experimental model membrane systems which mimic the natural biophysical behaviour of membranes well, are essential.

1.2.1 Experimental Model Membrane Systems

Because of the complexity of biological membranes, several different model membrane systems have been developed, which replicate the essential lipid bilayer structure, while simplifying the system so that the function, organization and dynamics of individual components can be investigated.[94] The choice of the model membrane system depends on the research question being addressed, as well as on the analysis technique being used. Besides vesicles and nanodiscs, one of the most commonly used group of membrane model systems is the family of planar model membrane systems at the solid-liquid interface.[95] In the following we present the different types of planar model membrane systems along with their advantages and limitations.

Supported Lipid Bilayers

In the sample system of supported lipid bilayers (SLBs) a single lipid bilayer is deposited on the surface of a solid substrate. The most common substrate surfaces used in supported lipid bilayer sample systems are silicon, glass or mica. Gold and titanium oxide are also used as substrate surfaces, but are less common.[96], [97] In general, SLBs are produced by vesicle fusion or Langmuir-Blodgett (LB) and Langmuir-Schaefer (LS) deposition. For vesicle fusion, small unilamellar vesicles (SUVs) are used as their small size and high curvature promote faster movement and fusion upon surface binding.[97], [98] In the presence of a low concentration of Ca^{2+} (around 2 mM) the negatively charged surface of common silicon, glass or mica substrates attracts phospholipids, resulting in absorption of phospholipid vesicles. In the presence of negatively charged lipids within the SUVs, increased sodium chloride concentrations of 100-200 mM or the presence of a low concentration of calcium chloride (2-3 mM) is necessary for sufficient vesicle adsorption.[99], [100] A stochastic simulation approach predicted a flattening of surface absorbed vesicles caused by adhesion forces.[101] These stretched vesicles push their bilayers towards their neighbors and once in contact, they rupture and form a patch of supported bilayer, which itself has edges of strong vesicle attraction.

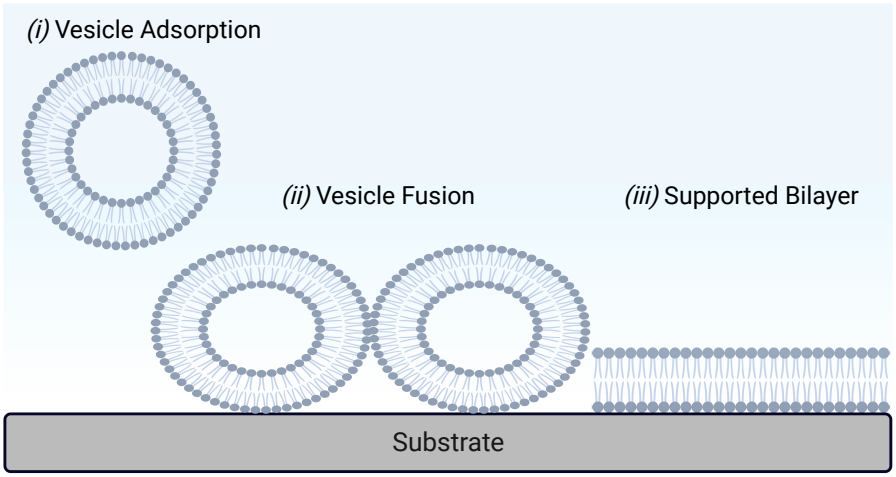


Figure 1.10 | SLB Deposition via Vesicle Fusion. Shown is a schematic representation of the process of forming an SLB via vesicle fusion, including the different phases involved, namely ***(i)*** vesicle adsorption to the substrate surface, ***(ii)*** vesicle fusion of the adsorbed, flattened vesicles, ***(iii)*** collapsed vesicles forming a supported lipid bilayer. This Figure was created with *BioRender.com*.

To help avoid unpredictable asymmetric lipid distribution across the membrane leaflets, the typical practice is to conduct the membrane deposition at temperatures exceeding the lipid melting temperate, at which lipids undergo a phase transition from solid-ordered (*So*; also called *gel*) to liquid-disordered (*Ld*; also called *fluid*) phase.[98], [102] Furthermore, it has been shown that a continuous flow of lipid solution through the sample cell during the vesicle adsorption process, as well as diluting the lipid solution within the sample cell promptly after sufficient vesicle adsorption prevents the formation of multi-lamellar stacks of lipid bilayers.[100], [102] The main advantage of the vesicle fusion method is the ease of generating supported lipid bilayer with high membrane coverage. However, the disadvantage of vesicle fusion is that there is less control over the leaflet asymmetry of the supported lipid bilayer. Fully controlled membrane leaflet asymmetry of supported lipid bilayers can only be achieved by the LB-LS deposition.[95]

LB-LS deposition can be used to deposit both symmetric and asymmetric SLBs. Hereby, the membrane leaflets are deposited sequentially onto the substrate surface, enabling a controlled lipid composition in each membrane leaflet.[103] Initially, a trough out of low-surface-energy material (e.g. Teflon) is filled with water or buffer solution (called the subphase) and the cleaned substrate immersed in the subphase. Then, lipids are spread on the air-liquid interface in the trough and compressed

to a lipid monolayer with high surface pressure (36 mN/m). Once the desired pressure level has been achieved, the substrate is vertically drawn out of the subphase (at a constant speed of around 2 mm/min). In parallel, lipids from the generated monolayer at the air-liquid interface are deposited onto the solid interface while keeping the monolayer surface pressure constant (Figure 1.11).[103] After completion of the LB deposition step, a second lipid monolayer is generated at the air-liquid interface and compressed to target surface pressure. In parallel to the lipid monolayer at the air-liquid interface, the lipid monolayer coated substrate is slowly lowered through the lipid monolayer at the air-liquid interface. Once the hydrophobic lipid tails of both lipid monolayers come in contact with each other, they form a fully assembled SLB (Figure 1.11).[95] The LB-LS deposition has been used to produce model membranes of high complexity, like asymmetric models of Gram negative bacterial outer membranes, as well as asymmetric models of fungal membranes.[104], [105]

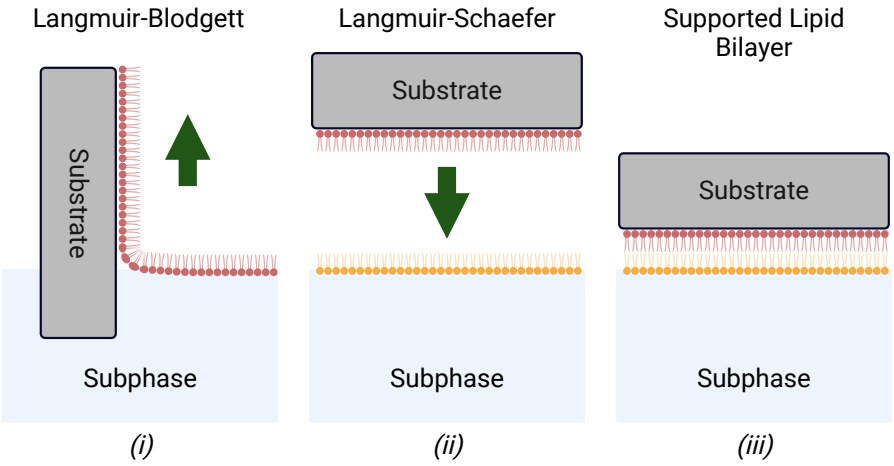


Figure 1.11 | SLB Deposition vie Langmuir-Blodgett (LB) and Langmuir-Schaefer (LS) Deposition. Shown is a schematic representation of the process of forming an SLB via LB-LS deposition, including the different phases involved, namely ***(i)*** LB deposition by drawing the substrate out of the subphase and through the lipid monolayer at the air-lipid interface, ***(ii)*** LS deposition by lowering down the monolayer coated substrate onto the monolayer at the air-lipid interface, ***(iii)*** completely formed SLB on the substrate. This Figure was created with *BioRender.com*.

The advantage of supported lipid bilayers is their reproducibility and stability. Additionally, their fixed and well defined structures make them an ideal model system for various surface-sensitive, biophysical techniques.[97] However, a significant disadvantage of supported lipid bilayers is the direct contact with the adjacent substrate. This close contact can influence the diffusion of lipids and of proteins

interacting with the membrane compared to natural membrane dynamics.[106] Furthermore, naturally occurring membrane fluctuations are hampered by the close contact between supported bilayer and substrate.[107] Therefore, more advanced planar model membrane systems have been developed, trying to overcome the issue of substrate influence on biophysical membrane behaviour.

Sophisticated Planar Model Membrane Systems

There are three main groups of planar model membrane systems currently in use: cushioned, tethered and free floating model membrane systems (Figure 1.12).

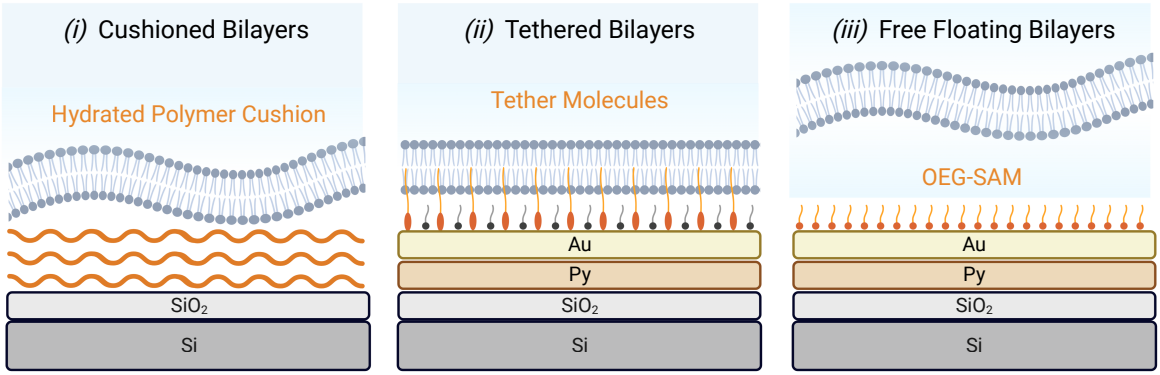


Figure 1.12 | Advanced Planar Model Membrane Systems. Shown are schematic representations of sophisticated planar model membrane systems: ***(i)*** Cushioned Lipid Bilayers with silicon (Si)/ silicon dioxide (SiO_2) substrate, as well as ***(ii)*** Tethered Lipid Bilayers and ***(iii)*** Free Floating Lipid Bilayers, both with silicon (Si)/ silicon dioxide (SiO_2)/ permalloy (Py)/ gold (Au) substrate. This Figure was created with *BioRender.com*.

In cushioned model membrane sample systems a polymer layer between substrate surface and membrane functions as a water containing interlayer, preventing the membrane to be in direct contact with the solid surface of the adjacent substrate (Figure 1.12, ***(i)***).[108] The polymer has to be hydrophilic and relatively chemically inert to prevent any interactions with membrane components.[109] Ideally, the polymer cushion mimics the cytoskeleton or extracellular matrix in elasticity and mechanical support for the bilayer.[110], [111] There is either no direct linkage to the substrate and the polymer layer attaches to the solid support just by adhesion or an intermediary binding molecule couples the polymer with the substrate surface (e.g. alkylthiols on gold coated substrates [112]).[109] The thickness of the spin coated [113] or via sequential dipping [114] deposited polymer layer is variable

and typically between a few nanometers and hundreds of microns.[95], [109] One of the most widely used polymers in cushioned bilayer systems is cellulose.[108], [109] Other commonly used membrane supports are polyacrylamide,[115] polylactic acid,[113] agarose,[116] polyelectrolytes.[114] After polymer cushion formation, the membrane is generally deposited via LB-LS (Figure 1.11) or vesicle fusion deposition (Figure 1.10). It has been shown that membrane components show less frictional coupling with the substrate in cushioned lipid bilayers compared to supported lipid bilayers, therefore providing more natural membrane dynamics.[117] However, the disadvantage is that the manufacturing procedure is much more labour-intensive and challenging compared to the production of simple supported lipid bilayers.[109]

In contrast to the non-membrane-linked polymer support in cushioned bilayers, in tethered bilayers so called tether molecules couple the substrate surface and the bilayer. Tether molecules are lipopolymers, which contain a surface binding hydrophilic polymer and a covalently bound lipophilic tail at the end, e.g. polyethylene glycol lipopolymers.[118]–[120] In most common tethered lipid bilayer systems, the tether molecules are terminated by a thiol group, so they self assemble onto a 100–1000 Å thick gold-film, covering a silicon or glass substrate.[119]–[121] Between the silicon/glass and the gold layer is a permalloy (alloy of $\sim$75% Ni : $\sim$25% Fe) or chromium layer as binding layer completing the multilayer substrate (Figure 1.12, ***(ii)***).[122], [123] The lipophilic tails of the gold bound tether molecules interact with the substrate facing membrane leaflet and thereby form a subset of this membrane leaflet.[124] The hydrophilic polymer section between surface and membrane interacting groups functions as spacer and ensures a water reservoir between substrate and membrane.[121] The length of this section and therefore the extent of the water reservoir is variable.[125] Also, the viscosity of the water containing spacer section can be adjusted by mixing the tether molecules with another shorter, gold binding molecule prior to the self assembling process and therefore decreasing the density of the tether molecules within the spacer section.[126] Additionally, diluting the tether molecules with another self assembling molecule, lacking the lipophilic membrane anchoring region, keeps the tether molecules down to a minor subgroup within the substrate facing membrane leaflet.[127] β-Mercaptoethanol is a popular example for such a filling molecule, the task of which it is to increase

the lateral space between the tether molecules.[124] The membrane can be assembled either by precipitating it from the solvent or through vesicle fusion.[128], [129] These tethered bilayers showed lipid diffusion which is close to that in natural biological membranes.[130] The additional ease of generating the lipopolymer layer and the membrane via self assembling processes have made tethered bilayers a popular planar membrane mimetic sample system.

The most recent and most advanced planar model membrane sample system is the free floating model membrane (FFM) system. Here, the membrane is no longer in contact with the substrate or substrate bound inter-layer (Figure 1.12, ***(iii)***). The membrane is either deposited onto an SLB or a self-assembled monolayer (SAM) composed of ω-thiolipids, in which the thiol group is at the ω-end of the palmitoyl chain.[131], [132] The deposition onto an SLB requires multiple LB-LS deposition steps, whereas for a specific SAM it has been shown recently that the fabrication of the floating membrane can be achieved via simple vesicle fusion.[132], [133] The SAM used was a carboxylate terminated oligo (ethylene glycol) alkanthiol self-assembled monolayer (OEG-SAM, see Figure 1.13 for molecular structure).[133]

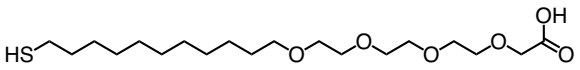


Figure 1.13 | Chemical Structure of OEG-SAM Molecule.

The simple fabrication makes the approach using the OEG-SAM as substrate covering layer very attractive. For generating the OEG-SAM, the oligo (ethylene glycol) alkanthiols are self assembled onto a gold-film, which is generally bound to a silicon substrate via a permalloy or chromium layer (Figure 1.12, ***(iii)***). Between the surface covering OEG-SAM and the membrane is a water inter-layer with a thickness of 10-40 Å. It has been suggested that the thickness of this water inter-layer can be tuned by using different sodium-chloride concentrations within the buffer solution.[133] However, the molecular mechanism for this tuning process is not understood yet, especially when considering the complexity of acting forces within the FFM sample system. There are several forces, which are thought to contribute to the desired floating state of the membrane: long range, weak van der Waals (vdW) forces cause an attraction between surface and membrane,[134] while entropic Helfrich fluctuation

forces [135] and hydration forces generate repulsive forces between surface and membrane.[136], [137] Additional electrostatic interactions can result in short range attractive or repulsive forces depending on the overall surface charge of the substrate surface and the floating membrane.[134], [138] Because of the solution reservoirs on both sides of the floating membrane and the lack of any anchoring or supporting material, the membranes exhibit unconstrained fluctuations that are similar to those observed in natural membranes.[95] Owing to these characteristics, the FFM sample system is highly suitable for a broad spectrum of applications in biophysical studies, biosensors and nanotechnology.[133]

In conclusion, all three sophisticated planar model membrane system, cushioned, tethered and free floating, reduce the unwanted surface influence on the membrane behaviour in comparison to the SLB system. Additionally, cushioned and tethered bilayers have been used successfully for studies of integral membrane proteins.[110], [139] While SLBs do not provide sufficient space for the cytosolic domain of many integral membrane proteins, polymer cushioned and tethered bilayers enabled the embedding of transmembrane proteins without deformation, binding or denaturing of the protein due to surface contact.[109], [110] In case of the free floating membrane system, further development and understanding is needed to provide the means for applications in membrane protein studies.

While common deposition methods via vesicle fusion and LB+LS deposition make the fabrication of native membrane composition difficult, recently methods have been developed for generating supported and cushioned planar model membranes of native composition.[140]–[142] Here, cell blebs are collected and directly deposited onto an SLB substrate providing native supported lipid bilayers.[140], [141] Mixing the cell blebs with vesicles containing polyethylene glycol during the deposition generates native cushioned bilayers of increased distance between bilayer and substrate surface.[142] Furthermore, integral membrane proteins can be expressed directly in the mammalian cells and therefore be natively present in membranes of the cell blebs, which circumvents any difficulties related to purification or vesicle inclusion of the proteins; as proteins are natively present in their natural membrane environment, any crucial protein/lipid interaction can be preserved, which makes these methods very attractive for studying integral protein/membrane interactions.[142] The production

of native membranes within the FFM system would provide a powerful approach for protein/membrane interaction studies, thereby forming a bridge between *in vitro* and *in vivo* studies.

1.2.2 Experimental Methods

The following section introduces some of the most common experimental, complementary techniques used for studying molecular interactions with planar, biological model membranes.

Neutron Reflectometry (NR)

In our studies the most extensively used experimental technique for investigating planar, biological model membranes, as well as their interaction with proteins, was neutron reflectometry (NR). Dedicated facilities use either nuclear fission or spallation processes to produce a neutron beam of reliable and consistent flux.[143] The ISIS neutron and muon source facility, where we undertook our measurements, is a proton-induced spallation source.[144] Here, a proton beam of 800 MeV is delivered to two tungsten targets (TS1 ans TS2), whereby TS1 receives 40 and TS2 10 proton pulses per second.[145], [146] When a high-energy proton collides with a heavy-metal nucleus, it can cause the nucleus to eject particles or clusters of particles, as well as split into two fragments that are excited. These fragments then release neutrons with energies of around 1 MeV as they de-excite, while the ejected particles may induce additional spallation reactions. At ISIS, this process leads to the production of approximately 10-15 neutrons for every proton incident.[145] To decrease the energy of the neutrons, moderators from solid methane/hydrogen surround the targets. Due to multiple collisions in the moderator the neutrons lose energy quickly and exit the moderator with energies in the range of meV-eV.[145] The exiting neutrons are channeled into different beamlines and are now usable for studying the molecular structure and function of matter from the microscopic down to the atomistic scale.

NR experiments generally make use of cold neutrons with wavelengths ranging from 1 to 20 Å.[143], [146] This wavelength range makes neutrons suitable for studying the molecular structure of samples at the nanoscale. Additionally, the moderate energy of cold neutrons make them nondestructive to biological samples, enabling long examination times. Furthermore, neutrons are well suited

for studying multi-layer systems like the planar model membrane systems as they penetrate deeply into material and provide the relative distribution of the different components along the axis of the membrane normal.[95] The deep sample penetration of neutrons is due to the fact that neutrons, as the name implies, have no charge and therefore are unaffected by the charge of orbital electrons. Thus, neutrons see matter mainly in the form of a vacuum and solely interact with the atomic nucleus via the strong nuclear force.[147] This enables the probing of buried samples inside complex layer systems, such as membranes and proteins in planar model membrane systems. Besides the nuclear scattering, magnetic scattering occurs with neutrons via a spin-based dipole-dipole interaction when magnetic atoms (having unpaired orbital electrons) are present. The significantly higher magnetic scattering rate of neutrons compared to electrons or X-ray photons made neutron-based methods the leading approach for studying magnetism at the atomic level.[147]

In NR experiments the ratio between specular reflected radiation intensity and incident radiation intensity of a neutron beam is measured. The geometry of a reflectometry experiment is shown in Figure 1.14.

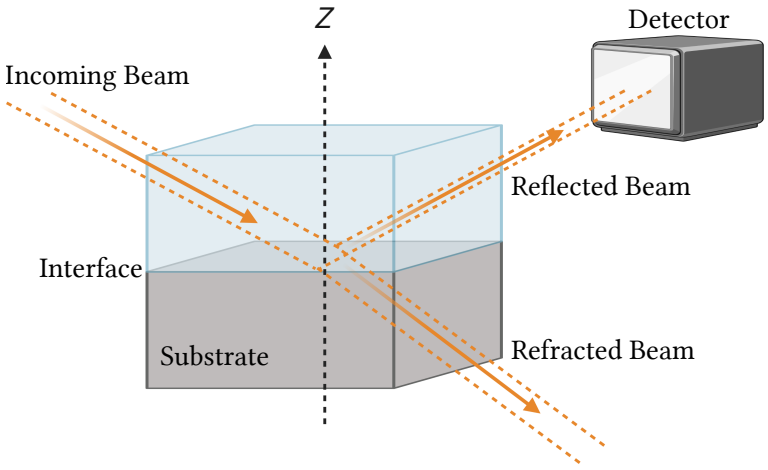


Figure 1.14 | General Set-up of NR Experiments. Schematic representation of a typical, experimental NR configuration. The incoming neutron beam gets reflected at interfaces within the sample and the reflected neutrons are detected for further analysis. NR experiments provide information about the structure perpendicular to the interface, here the z-dimension. Adapted from [143], created with *BioRender.com*.

At the ISIS facility an incoming neutron beam containing a spectrum of neutron wavelengths (called a white beam) is used at defined incident angles. Due to the fact that ISIS is a pulsed spallation neutron source, the time of neutron ejection from the target is known. As a result, it becomes

possible to measure the time taken for the neutron to reach the detector with a high degree of precision. Via the time and distance covered by the neutron between target and detector, the velocity and kinetic energy of the neutron is calculated using:

$$E_k = \frac{mv^2}{2}$$

with E_k being the kinetic energy, m the mass of the neutron and v the velocity of the neutron (distance/time). Then, E_k is used to determine the neutron wavelength by the de Broglie relation[148]:

$$E = \frac{\hbar v}{\lambda}$$

where $\hbar$ is the Planck constant and λ the neutron wavelength. This technique of assigning wavelengths to detected neutrons of a white neutron beam source is known as time-of-flight.[149]

The reflection of neutrons occurs solely at interfaces between layers which show a difference in the so called scattering length density (SLD). The SLD is the sum of the scattering length of each atom within the molecule divided by the volume of the molecule, with the scattering length quantifying the scattering magnitude of each element:

$$SLD = \frac{\Sigma_i \, b_i}{V_m}$$

where b_i is the scattering length of all i atoms in the molecule with the molecular volume of V_m. While the scattering strength of X-ray photons scales with the atomic number, a unique feature of neutrons is, that the scattering strength and therefore the scattering length is irregular to any atomic property. So far, there is no precise nuclear theory of neutron-nuclear interaction and the scattering strength must be experimentally determined. However, it is this variation of scattering length across the periodic table which makes neutrons very attractive for biological samples. Thus, the scattering length of protium (H) *versus* deuterium (D), the two stable isotopes of hydrogen, shows with -3.74 *versus* 6.67 Å a big difference, which causes the SLDs of H_2O and D_2O to flank the lower and upper limit of SLDs observed for organic molecules, respectively.[143] This allows to vary the SLD of

the buffer solution, generally surrounding biological samples by changing the ratio of H_2O:D_2O. By matching the SLD of the buffer solution with other system components, the neutron reflection between bulk solution and that respective component is disabled. Therefore, different parts of the system are made visible or invisible for the neutrons depending on the buffer solution SLD. This approach is known as isotopic contrast variation strategy and commonly used in NR measurements of biological samples to maximise the structural information gained by the experiment.[150], [151] An example for the application of multiple isotopic contrasts is shown in Figure1.15.

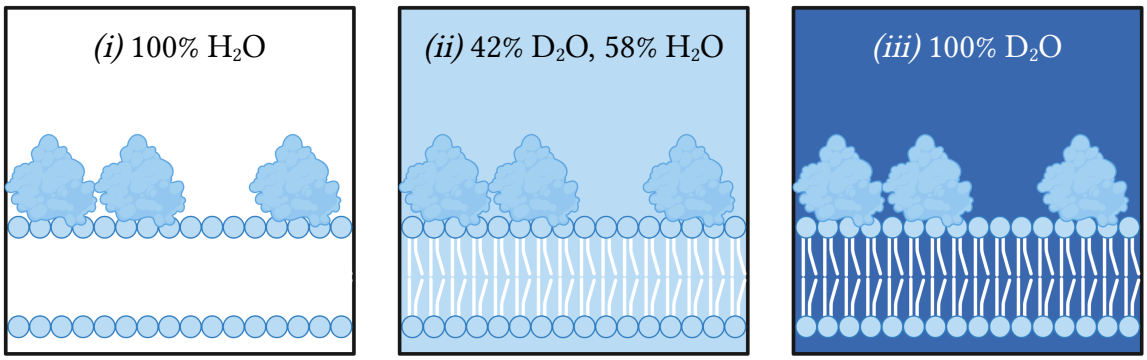


Figure 1.15 | Effect of Isotopic Contrast Variation with Neutrons. Shown are peripheral membrane proteins bound to a membrane at three different isotopic solution contrasts. Hereby, the scale from white to dark blue represents low to high SLD. ***(i)*** Lipid tails have a low SLD, close to H_2O. Therefore, lipid tails do not significantly contribute to the NR data of this sample at 100% H_2O solution contrast. Thus, this contrast is the primary source of structural information for lipid head groups and proteins. ***(ii)*** At a solution contrast of 42% D_2O, 58% H_2O the solution SLD is very close to both lipid head groups and proteins, making them invisible for NR. However, there is now a significant difference between lipid tail SLD and solution SLD, making lipid tails the dominant contributor to the collected NR data. Thus, this contrast is the primary source of structural information for lipid tails. ***(iii)*** At 100% D_2O solution contrast, the SLD of the proteins, lipid head groups and lipid tails differ significantly from the solution SLD. Thus, the overall shape of the multi-component sample is gained by the analysis of this contrast. This Figure was created with *BioRender.com*

However, not only the SLD of the buffer solution can be varied in order to increase or decrease the NR contribution of individual sample components. Especially in sample systems containing multiple biological molecules of interest with similar SLD, e.g. membranes of complex lipid composition or clusters of multiple proteins, it is beneficial to change the SLD of selected bio-molecules by replacing hydrogen with deuterium atoms within the bio-molecule.[152], [153] The deuterium labelling of bio-molecules can be achieved by chemical synthesis (e.g. for lipids) or by bacteria growing in

deuterated medium (e.g. for proteins). However, the final deuteration level and therefore the SLD of the bio-molecule depends on the percentage of solvent exchangeable hydrogens within the molecule and on the SLD of the surrounding buffer solution. Amine and hydroxyl groups are examples for groups with solvent exchangeable hydrgogens. Therefore, even though buried groups, not exposed to the solvent are not effected, proteins and carbohydrates can have a significantly varying SLD depending on the solvent SLD. In contrast, lipids with their high percentage of stable C-H/C-D bonds have an SLD which does not depend on the solvent isotopic contrast.[143]

The obtained reflectivity profiles from NR experiments show the reflected neutron intensity against Q_z, the scattering vector in the Z-direction (i.e. perpendicular to the reflecting interface). In general, the scattering vector Q describes the wavevector transfer, meaning the difference between the incident and final wavevector.

$$Q = k_i - k_f$$

where k_i is the incident and k_f the final wavevector (see Figure 1.16, **A** for the schematic presentation of a radiation scattering event).[147]

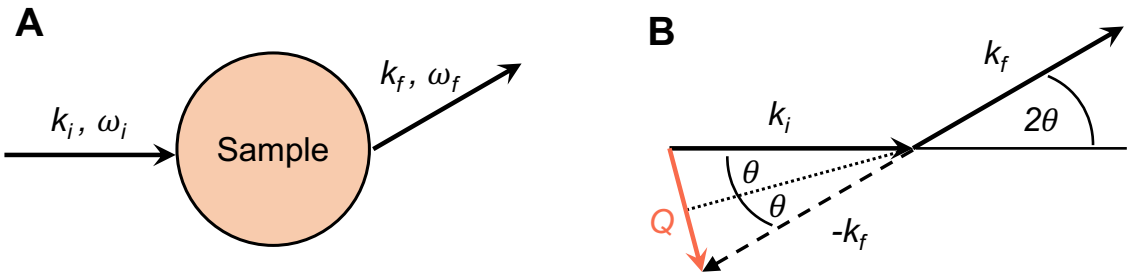


Figure 1.16 | Basic Principle of Neutron Scattering. **A** Schematic representation of the scattering of some probing radiation by a sample (orange circle) with incident k_i and final k_f wavevector of frequency ω_i and ω_f, respectively. **B** A vector diagram describing an elastic scattering event, where k_i is the incident, k_f the final wavevector, 2θ the scattering angle and Q the scattering vector (highlighted in red). Adapted from [147].

Given that only elastic scattering is being considered, the frequency of the radiation remains constant, i.e. $\omega_i = \omega_f$. Therefore, the wavevector k is the only variable that changes, i.e. $k_i \neq k_f$. Because elastic scattering preserves the frequency of the probing radiation, the wavelength λ of the radiation will also

remain constant. This implies that the moduli of the incident and final wavevector are equal:

$$|k_i| = |k_f| = \frac{2\pi}{\lambda}$$

Thus, the only variable that causes a change in the wavevector *k* is the direction of the wave, i.e. the angle θ of the wavevector. As illustrated in the vector diagram for elastic scattering (Figure 1.16, **B**), elementary trigonomemtry then leads to the following definition of Q:

$$Q = \frac{4\pi}{\lambda} sin(\theta)$$

with λ being the neutron wavelength and θ the incident angle of the incoming beam with respect to the reflecting interface. Therefore the scattering vector Q is reciprocally proportional to the wavelength and has unites of Å^{-1}.[147]

Figure 1.17, **A** shows a calculated example of NR data for a simple air/liquid interface (here D_2O for the liquid phase), as well as for the same interface including an additional 60 Å thin, homogeneous film of lower SLD in comparison to D_2O. The added film provides an additional interface resulting in an air/solid and solid/liquid interface. Thus, on both interfaces the neutrons get reflected leading to peaks and troughs in regions of Q_z, where it comes to constructive and destructive interference between the reflected neutron waves, respectively.[143] These interference fringes in the NR data caused by the reflection at multiple interfaces are called Kiessig fringes. The distance between single Kiessig fringes is directly linked to the distance between the reflecting interfaces, therefore to the thickness of the added film via:

$$Q_{z2} - Q_{z1} = \frac{2\pi}{d}$$

with Q_{z2} and Q_{z1} being the Q_z-positions of the Kiessig fringes (see Figure 1.17, **A**) and d the thickness of the interfacial film.[143]

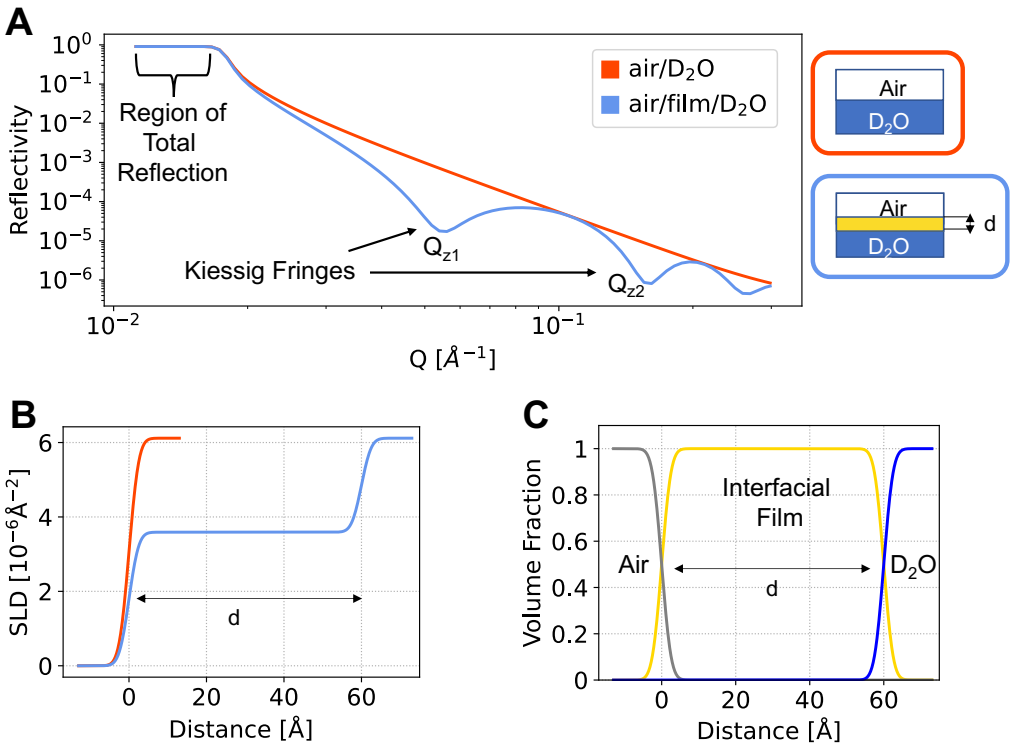


Figure 1.17 | Example of Calculated NR Data with SLD and VFP Analysis. A Calculated, hypothetical NR data showing the reflectivity intensity *versus* the scattering vector Q_z for an air/liquid interface (red) and for a consecutive air/solid and solid/liquid interface due to an additional interfacial film with a thickness of 60 Å (blue). The distance between the Kiessig fringes ($Q_{z2} - Q_{z1}$, highlighted with arrows) is inverse proportional to the thickness d of the interfacial film. **B** By fitting the parameters describing the different layers (SLD, thickness, roughness) until the calculated reflectivity profile approaches most closely the experimental profile, the profile of the scattering length density (SLD) along the interface normal (in general along Z-direction) is obtained (red: air/D_2O, blue: air/film/D_2O sample system). **C** The volume fraction plot (VFP) is an approach of visualization the results from the model fitting, which became recently more common. The VFP shows the volume fraction distribution of each sample component along the interface normal (in general along Z-direction) (grey: air, gold: film, blue: D_2O). In both SLD and VF plot, zero at the x-axis corresponds to the z-position of the first interface the incoming neutron beam gets reflected at (air/D_2O or air/film respectively).

To gain structural information from the NR profiles, mathematical models, which describe the reflectivity of layered interfaces, are used to fit the experimental reflectivity profiles. These models, produced by Parratt[154] or Abelès,[155], [156] differ in their specific mathematical approach. However, they all involve modelling the interfacial structure as a series of layers, each described via a thickness, surface roughness and an SLD.[143] Hereby, the roughness is defined by whether the transition between SLD layers is sharp or gradual and therefore often referred to as the grading or smoothness of the interface.[157], [158] Mathematically, the roughness is described via a height-height correlation

function across a layer boundary.[133] Features like Kiessig fringes enable conclusions about the thickness of the layers, while the magnitude of reflection provides information about the difference in SLD between layers.[143] The fitting parameters, including thickness, roughness and SLD of each layer, are adjusted until the calculated reflectivity profiles match the experimental data most closely. This process is implemented in a variety of reflectometry modelling software packages, such as refnx,[159] MOTOFIT,[160] RasCAL [161] and Aurore.[162] In general, the fitting software provides a goodness of fit parameter such as X^2 to indicate the similarity between the experimental and fitted reflectivity profile. The result of the fitting process is an SLD profile along the interface normal (in general along the *Z*-direction), which provides structural information perpendicular to the reflecting interfaces (Figure 1.17, **B**).[143] Another, recently more popular visualization of the fitting results is the volume fraction plot (VFP). In the VFP the contribution of each sample component along the interface normal is shown, which makes the interpretation of the NR results easier and requires no advanced experience in NR (Figure 1.17, **C**).

Different types of planar model membrane systems, from supported to free floating, assembled via LB-LS deposition or vesicle fusion (see section 1.2.1), are investigated with NR to gain structural insights.[133], [163]–[165] The specific sample holder contains inlets and outlets, through which the buffer solution can be exchanged, making the isotopic contrast strategy easy to apply (Figure 1.18). The combination of NR with the isotopic contrast strategy is increasingly being used to study structural aspects of membranes and membrane binding molecules like proteins along the membrane normal.[166]–[170] In terms of the model fitting, membranes are often treated slightly differently from simple layers. In general, membranes are fitted by area per molecule (APM), explicitly associated water (with the lipid head group region), coverage and roughness. The membrane coverage is fitted as the ratio between lipid and solvent SLD, taking possible membrane defects filled with water into account. The APM of the lipid head groups and lipid tails is set to be equal, so the number of lipid heads matches the number of lipid tails. The APM of e.g. the lipid tails is defined as:

$$APM_{tail} = \frac{V_{tail}}{d_{tail}}$$

where V_{tail} is the volume and d_{tail} the thickness of a lipid tail. Mostly, V_{tail} is kept constant while APM_{tail} is defined as fitting parameters, linked with d_{tail}; the same applies for the lipid head groups described by V_{head}, d_{head} and APM_{head}.

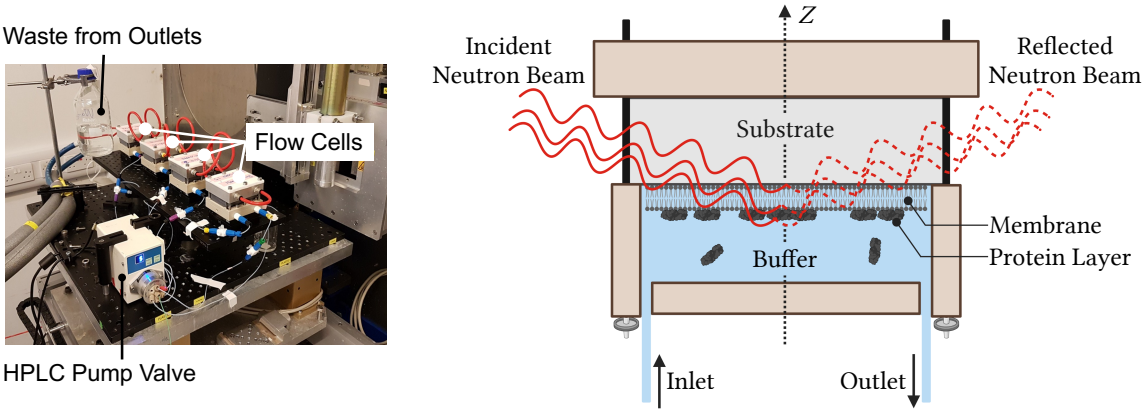


Figure 1.18 | NR Sample Setup for Membrane Studies. The left picture shows an experimental beamline setup for the consecutive measurement of four membrane sample flow cells with NR. The structure of each of these sample flow cells corresponds to the schematic presentation on the right. The flow-through cavity has a volume of around 3 mL and is filled with buffer solution during the measurements (blue). Through the in- and outlet the buffer solution can be easily changed (often via an HPLC pump, see left picture). The incoming neutrons get reflected on the interfaces normal to the Z-axis/membrane normal; in the given example on the substrate/membrane, lipid head group/lipid tail, membrane/protein and protein/water interface. The resulting reflectivity profile depends on the number of interfaces across Z, as well as the chemical composition, thickness and roughness (smoothness of transition between layers) of the layers flanked by interfaces. Adapted from [171].

Quartz Crystal Microbalance with Dissipation Monitoring (QCM-D)

Quartz crystal microbalance with dissipation monitoring (QCM-D) is a surface sensitive technique utilizing the piezoelectric effect for real-time measurements of surface interactions with a piezoelectric single crystal quartz sensor.[172], [173] A characteristic resonance frequency of the quartz sensor is achieved by applying an alternating electric field on the crystal. Any changes in the mass occurring at the surface interface of the crystal result in a shift of this primary resonance frequency (Δf) of the crystal (Figure 1.19). This makes QCM-D a highly sensitive method for measuring mass changes, enabling quantitative measurements to be made.[174]

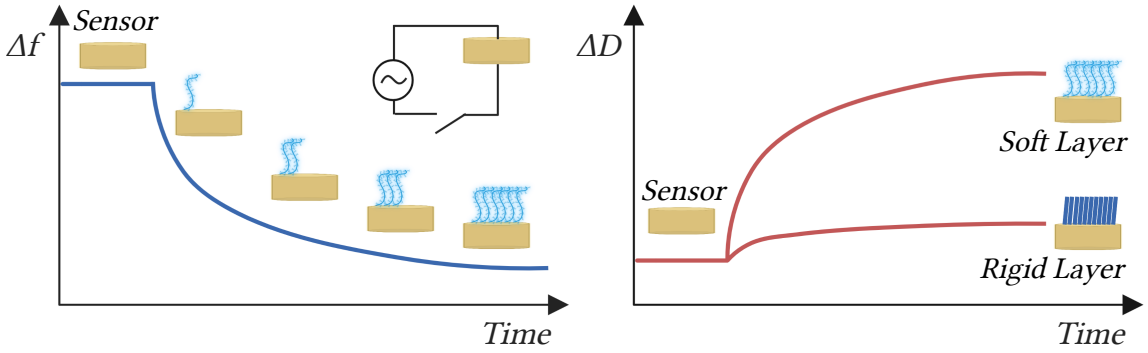


Figure 1.19 | QCM-D Provides Frequency (Δf) and Dissipation Energy Factor (ΔD) over Time. The higher the amount of bound material on the quartz crystal sensor (highlighted in gold), the lower is the frequency factor Δf measrured in real-time (left). Additionally, the higher the elasticity of the crystal bound material, the faster is the energy dissipation after switching off the alternating current, resulting in a higher dissipation energy factor ΔD (right). This Figure was adapted from [174] and created with *BioRender.com*

Simultaneously, the energy dissipation is monitored as well, providing insights about the viscoelastic properties of the material bound to the crystal quartz sensor.[173] For quantifying the energy dissipation, the crystal oscillation amplitude is recorded as a function of time upon switching off the alternating electric field. The oscillation amplitude decays exponentially, whereby the grade of the decay and therefore the energy dissipation factor depends on the viscoelastic properties of the crystal bound material. The less rigid the crystal bound material is, the faster is the decay time of the oscillation amplitude providing a larger shift in the dissipation factor (ΔD) (Figure 1.19).

For rigid layers with $\Delta D = 0$ and an air interface, the change in the resonant frequency (Δf) is directly proportional to the amount of mass interacting with the quartz sensor surface,[175], [176] as given by the Sauerbrey relation:

$$\Delta m = -C \frac{\Delta f_n}{n}$$

where n is an odd overtone number (n = 1, 3,...,13) and C is a sensor-dependent mass sensitivity constant. However, biological studies are generally conducted in liquid environments and mostly contain a layer of biological material, which shows a high energy dissipation factor ($\Delta D > 0$). Therefore, in this scenario the Sauerbrey equation is not valid anymore and the Voigt model has to be applied to relate Δf to mass changes and ΔD to viscosity.[177], [178] In the Voigt model the adsorbed layer

is described by a frequency-dependent complex shear modulus, defined by:

$$G^* = G' + iG'' = \mu_f + i2\pi f n_f$$

where G^* describes the complex shear modulus, G' the energy storage and G'' the energy dissipation. Furthermore, f is the oscillation frequency, μ_f the elastic shear modulus and n_f the shear viscosity.[179] Modern QCM-D devices have the capability to simultaneously measure Δf and ΔD for multiple harmonics, extending up to the 13$^{\text{th}}$ overtone. The combination of several overtones in the analysis process enables the extraction of viscoelastic properties of the material absorbed to the crystal sensor with greater accuracy.[174]

SLBs can be assembled on quartz crystal sensors via vesicle fusion.[95] The assembling process is directly observable in the QCM-D data (Figure 1.20). The initial adsorption of the water filled vesicles leads to an increase in the mass absorbed to the crystal sensor and therefore to a decreased resonance frequency. The energy dissipation is also increased due to the viscoelasticity of the water filled vesicles. Upon vesicle rupture, the comparatively rigid supported lipid bilayer causes slower energy dissipation and due to the loss of vesicle-trapped water a lower mass of crystal coupled material. This results in decreased values for dissipation and increased values for the resonance frequency. SLBs in combination with QCM-D have been used to study protein/membrane interactions, which enables a label-free method to detect and characterize the clustering of membrane-bound proteins.[180] Furthermore, by analysing the ratio of $\Delta D/\Delta f$ the intrinsic viscosity can be calculated. The intrinsic viscosity is a measure of the frictional interaction between a biomolecule and the surrounding solvent molecules in solution. This frictional interaction is directly related to the hydrodynamic volume and shape of the biomolecule.[181], [182] The relationship between intrinsic viscosity and volume/shape has been used to study conformational changes of intrinsically disordered proteins when bound to quartz crystal sensor coupled SLBs.[183]

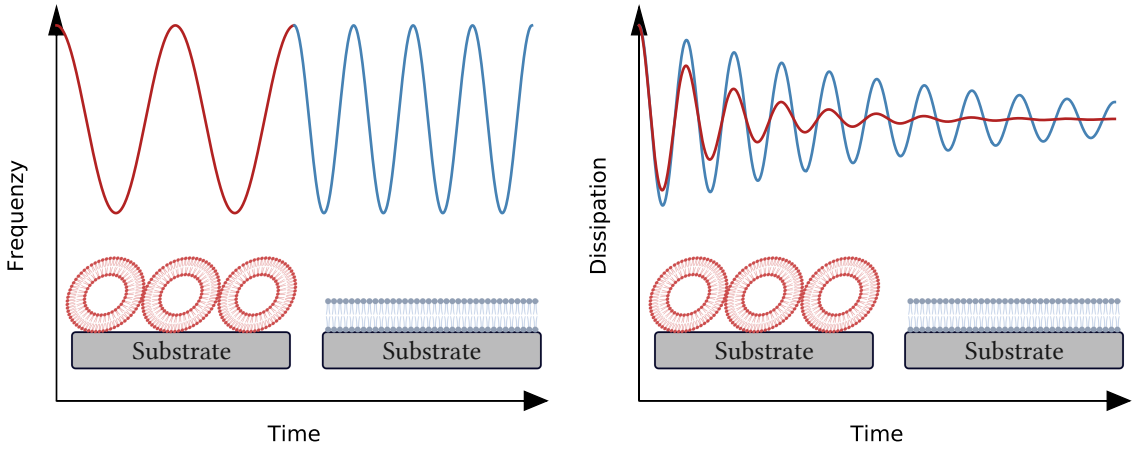


Figure 1.20 | SLB Deposition on QCM-D-Sensors. Shown is a schematic presentation (not to scale) of the resonance frequency (left) and the energy dissipation (right) data from QCM-D measurements during the SLB formation via vesicle fusion: Vesicle absorption onto the substrate, here identical with the QCM-D sensor (i.e. the quartz crystal), results in low resonance frequency of the piezoelectric OCM-D sensor (red, left) and fast decay of the oscillation amplitude once the electric field is switched off (right, red). After vesicle bursting and SLB formation, the crystal bound material is more rigid, reflected in the higher resonance frequency, as well as the slower energy dissipation (blue curves). Adapted from [95].

Attenuated Total Reflection Fourier Transform Infrared Spectroscopy (ATR-FTIR)

Infrared spectroscopy (IR) is the measurement of the interaction of infrared light with matter. The wavelengths of infrared light absorbed by a sample depend on the molecular vibrations of the molecules present within the sample. A molecule can have multiple vibration modes. Thus, for molecules with N number of atoms, geometrically non-linear molecules have 3N-6 and geometrically linear molecules have 3N-5 vibration modes (for linear molecules the rotation around the main axis of symmetry is not measurable). All of the molecular vibrations which cause a change in the dipole moment of the molecule interact with infrared light when the frequency of the infrared light matches the frequency of the molecular vibration mode.[184] Therefore, each IR active vibration mode provides an absorbance band in the IR absorbance spectrum, enabling insights in chemical and structural composition of the sample.

In attenuated total reflection Fourier transform infrared spectroscopy (ATR-FTIR) the IR beam is directed through an IR-transparent solid prism with a high refractive index, called the internal reflection element (IRE) (Figure 1.21). Most widely used are prisms made of zinc selenide, diamond, silicon or germanium.[185] At the surface of the IRE the sample of interest is positioned. The angle

of the incoming IR beam is greater than the critical angle of the IRE, so total internal reflection of the IR beam occurs in the IRE, often multiple times.[95] At the reflecting interface a standing wave, called an evanescent wave is produced for each reflection. These evanescent waves of IR light interact with the sample and attenuate the IR beam dependent on the molecular vibrations present in the sample. Therefore, the IR beam exiting the IRE contains chemical and structural information about the sample generated on the surface of the IRE.[185] Thus, variations in the chemical composition near or at the interface can be detected by observing changes in the IR absorption spectra. The penetration depth of the evanescent waves depends on the angle of incidence, the refractive indices of the IRE and the sample, as well as on the IR wavelength. The typical range of the exponentially decaying penetration depth is 0.5-2 µm.[185] These values follow the definition of the penetration depth to be equal to the depth at which the intensity of the evanescent waves is attenuated to 1/e.[186] However, the actual probing depth of the evanescent waves is deeper than this defined penetration depth. It has been reported that the IR spectra contain absorbance information of the sample reaching around three times deeper than the calculated penetration depth of the evanescent waves.[187] One main advantage of ATR-FTIR in comparison to the traditional, transmission FTIR is, that due to the interaction with only a several micrometer thick surface layer, the strong infrared absorbance by water is no longer an issue when studying aqueous samples.[185] This enabled insights into interactions of proteins with different surfaces in aqueous solution.[188]

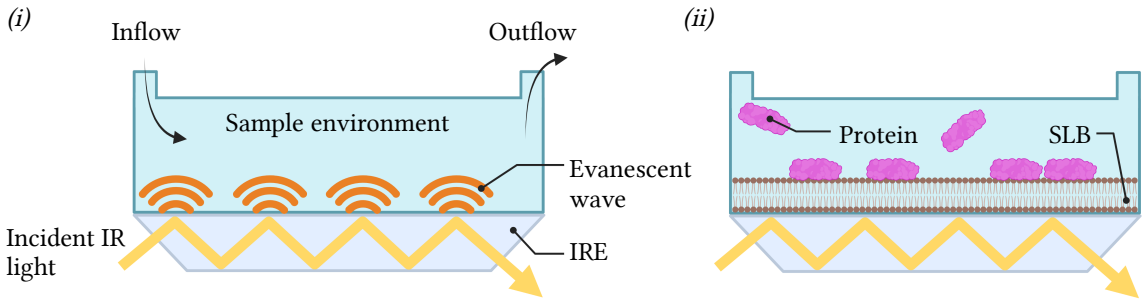


Figure 1.21 | Sample Cell of ATR-FTIR Measurements. ***(i)*** Shown is a schematic presentation of the ATR-FTIR sample cell consisting of an internal reflection element (IRE) and an adjacent sample environment. Total reflection of the incoming IR beam occurs within the IRE multiple times. At the points of total internal reflection evanescent waves are formed, penetrating several microns into the sample environment. ***(ii)*** Supported lipid bilayers (SLBs, brown) can be assembled onto the IRE. Structure and orientation of membrane binding proteins (pink) can be probed using ATR-FTIR. This Figure was created with *BioRender.com*

ATR-FTIR has been successfully used to study biophysical interactions with SLBs (Figure 1.21).[189] In general, SLBs are assembled on the IRE prism via vesicle fusion. Lipid phase states in SLBs, as well as time dependent changes in composition can be analysed by ATR-FTIR measurements.[190], [191] Hereby, changes in the position and width of lipid related IR absorption bands (e.g. the C=O stretching vibration of the glycerol-ester bond of the phospholipid head groups at $\sim$1731 cm^{-1}) provide conclusions on the local lipid environment.[190] Changes in the SLB composition are indicated by increasing or decreasing intensity of respective IR adsorption bands.[192] Furthermore, the binding event of peripheral membrane proteins, as well as structural changes in both membrane lipids and membrane protein resulting from protein/membrane interactions can be monitored using ATR-FTIR.[193], [194] Hereby, the protein size is not a concern as the relatively long decay length of the IR evanescent waves extend beyond the size of even the largest proteins.[189] Additionally, the utilization of polarized light in ATR-FTIR measurements provides a mean to assess the alignment of proteins relative to the membrane interface.[195], [196] A slight disadvantage of studying protein/lipid interactions with ATR-FTIR is the fact that usually these measurements have to be conducted in D_2O instead of H_2O. In H_2O the bending mode of water with a wavenumber of around 1644 cm^{-1} overlaps with the amide HNC=O stretching vibration (1650 cm^{-1}), as well as with other functional groups like carboxylic acids.[197] The interference between water and functional groups makes the analysis of these peaks and therefore the investigation of protein/membrane interactions via ATR-FTIR difficult. Fortunately, the bending mode of D_2O is located at lower frequency (1215 cm^{-1}), which makes it less likely to interfere with the detection of other functional groups in the IR spectrum.[95], [197]

1.2.3 Computational Methods

For assisting the analysis of experimental neutron data, there is a growing interest to use computational simulations.[163], [198] Due to the complexity of soft matter sample systems, classical simulations, often in combination with coarse-grained potential models, are necessary to simplify the calculations. In classical simulations, classical mechanics based on Newton's laws of motion are used to describe the physical behaviour of molecules withing the sample system. In our work, we used classical simulations

in terms of molecular dynamics (MD) simulations for assisting the analysis of our experimental NR data. Therefore, we introduce the underlying theory of this method in the following section.[199]

Classical MD Simulations

Classical MD simulations represent atoms as spheres with an atom type specific van der Waals (vdW) radius and point charge at the center of the sphere. This simplified representation of atoms is enabled by the Born-Oppenheimer approximation.[200] In brief, the Born-Oppenheimer approximation proposes that the motion of electrons and nucleus within an atom can be considered independently of each other. The approximation assumes that due to the large difference in mass, nuclei move much slower than the electrons, therefore allowing the electrons to adjust to the position of the nuclei before the nuclei move again. This means that the electronic degrees of freedom can be omitted and merged in one effective potential, which allows the description of atomic dynamics by the position of the nucleus moving in this electronic potential.[200] Due to this simplification of the complex quantum-mechanic nature of atoms and molecules, timescales and system sizes relevant for studying biological processes are easily accessible with present computational infrastructure. Furthermore, this spherical description of atoms allows the motions of single atoms to be calculated applying Newton's equations of motion. Thus, the acceleration a_i on a given atom i can be obtained by the force F_i acting on that atom, in agreement with Newton's second law of motion:

$$\frac{\overrightarrow{F_i}}{m_i} = \frac{\partial \overrightarrow{v_i}}{\partial t} = \overrightarrow{a_i}$$

with m_i being the mass of the atom i. The force F_i can be obtained from the derivative of the potential describing the interactions of the considered atom with respect to the atomic configuration:

$$\overrightarrow{F_i} = -\frac{\partial U\,(\overrightarrow{r})}{\partial \overrightarrow{r_i}}$$

where U represents the potential energy containing all interaction functions applying to the atom i, r_i the three dimensional vector of the position of atom i and r the three dimensional vectors of the positions of all N atoms involved in the interactions contained in U ($\overrightarrow{r} = \overrightarrow{r_1}, \overrightarrow{r_2}, \overrightarrow{r_3}, ... \overrightarrow{r_N}$). By calculating the integration of these equations of motion for all atoms within the system, velocities,

accelerations and therefore the production of the atomic coordinates are obtained. One of the most commonly used methods to solve the equations of motion is the Verlet integrator algorithm,[201] for which Hansen and McDonald provided a detailed description.[202] In brief, by using a Taylor expansion for the atom coordinates r_i at a time *t*, the following two equations are generated for the forward ($r_i(t+\Delta t)$) and backward ($r_i(t-\Delta t)$) expansion:

$$r_i(t+\Delta t) = r_i(t) + v_i(t)\,\Delta t + \frac{F_i(t)}{2m_i}(\Delta t)^2 + \frac{1}{3!}\dddot{r}_i(t)(\Delta t)^3 + \sigma(\Delta t)^4$$

$$r_i(t-\Delta t) = r_i(t) - v_i(t)\,\Delta t + \frac{F_i(t)}{2m_i}(\Delta t)^2 - \frac{1}{3!}\dddot{r}_i(t)(\Delta t)^3 + \sigma(\Delta t)^4$$

The addition of these two equations provides the new position of atom *i* at the time $t+\Delta t$:

$$r_i(t+\Delta t) \approx 2r_i(t) - r_i(t-\Delta t) + \frac{F_i(t)}{m_i}(\Delta t)^2$$

where $r_i(t+\Delta t)$ is the new, $r_i(t-\Delta t)$ the previous, $r_i(t)$ the present atomic position and $F_i(t)$ the present acting force. Thus, the Verlet algorithm allows the calculation of atomic trajectories over time. Since velocities are used to determine a temperature via the kinetic energy, they are reconstructed by subtraction of the backward from the forward expansion equation, leading to the following estimation:

$$v_i(t) \approx \frac{r_i(t+\Delta t) - r_i(t-\Delta t)}{2\Delta t}$$

In order to avoid discontinuities at the borders of the simulation system, so called periodic boundary conditions are used. Hereby, identical copies of the simulation system are indefinitely projected around the central simulation box, assembling a continuous system. Thus, a particle that exits the simulation system on one side of the simulation box re-enters on the opposite side of the box. By selecting an appropriate simulation box size and shape, interactions between molecules in the central simulation system and their projection must be prevented.

Most simulation systems are briefly equilibrated in an NVT ensemble (isothermal-isochoric conditions), then performed in an NPT ensemble (isothermal-isobaric conditions), with the latter reflecting experimental conditions. To preserve constant temperature and pressure in a simulation

system, a thermostat and barostat are applied. Simple thermostats like the Berendesn thermostat re-scale the velocities of all atoms within the simulation system.[203] Due to the relation between the kinetic energy and the temperature, changing the velocities is equivalent to an adjustment of the temperature. Barostats regulate the pressure often by re-scaling the box dimensions and coordinates of corresponding atoms.[203] Hereby, the scaling of the box dimensions depends on the compressibility, specified for each box dimension. In simulations containing membranes it is common to use semi-isotropic pressure coupling to avoid deformations of the membrane. Hereby, the x and y dimensions are scaled together, while the z dimension is scaled separately.

The potential energy functions describing all possible interactions between atoms are necessary for computing the forces F_i and collected together to form the so called force field of classical MD simulations.

Force Fields

The potential functions used in some popular force fields, can be subdivided into bonded and non-bonded interactions for each atom i. Thus, for a given atom i the potential U_i in classical MD simulations is calculated via:

$$U_i\left(r^N\right) = U_{i,bonded}\left(r^N\right) + U_{i,non-bonded}\left(r^N\right)$$

with $\left(r^N\right)$ providing the position of all atoms within the system. The potential for the bonded term contains potentials describing bonds, angles, dihedral angles and improper dihedral angles. In general, bonds, angles and improper dihedral angles are described with harmonic potentials and dihedral angles with an oscillating potential, leading to the following equation:

$$\begin{aligned} U_{i,bonded}\left(r^N\right) = & \sum_{bonds} \frac{1}{2} k_r \left(r - r_0\right)^2 \\ & + \sum_{angles} \frac{1}{2} k_\theta \left(\theta - \theta_0\right)^2 \\ & + \sum_{impropers} \frac{1}{2} k_\omega \left(\omega - \omega_0\right)^2 \\ & + \sum_{dihedrals} k_\varphi \left(1 + cos\left(n\varphi - \varphi_0\right)\right)^2 \end{aligned}$$

where the constants k_r, k_θ and k_ω are the force constants of harmonic potentials to describe the oscillation of a chemical bond (r) or angle (θ, ω) around an equilibrium bond length or angle value, given by r_0, θ_0, ω_0, respectively. In the last term *n* sets the periodicity of the oscillating potential for dihedral angles with the force constant k_φ and the equilibrium angle φ_0.

The potential for the non-bonded term contains the Coulomb potential for describing electrostatic interactions, as well as the Lennard-Jones (LJ) potential for describing vdW interactions. Both potentials are calculated over all non-bonded, interacting atoms *j*, leading to the following equation:

$$U_{i,non-bonded}\left(r^N\right) = \sum_j \frac{q_i q_j}{4\pi\varepsilon_0 r_{ij}} + \sum_j 4\varepsilon_{ij}\left[\left(\frac{\sigma_{ij}}{r_{ij}}\right)^{-12} - \left(\frac{\sigma_{ij}}{r_{ij}}\right)^{-6}\right]$$

where the first term of the equation, the Coulomb potential, describes the interaction energy between two charged atoms. Thus, the Coulomb potential is a function of the charges of the interacting atoms, q_i and q_j, as well as of the distance between them, r_{ij}. Also contained in the potential is the vacuum permittivity, ε_0, which is a fundamental constant that relates the electric field to the electric charge. In the second part of the equation, the LJ potential describes the interaction energy between uncharged atoms consisting of two terms: A short-range repulsion term ($\sim r^{-12}$) which arises from the Pauli exclusion principle and becomes dominant at very short distances between interacting atoms i and j. And a long-range attraction term ($\sim r^{-6}$), due to the dispersion force, which becomes dominant at intermediate distances. Hereby, ε_{ij} and σ_{ij} represent the depth of the minimum of the LJ energy profile and the distance at which the potential is zero, respectively.

The force field contains the force constants and equilibrium values for all possible bonds and angles, as well as the charges (and masses) of each atom type and the LJ parameters for all possible interaction pairs. The values of these parameters are chosen so results from simulations match experimentally and quantum-mechanically derived results best. This process of parametrisation is time consuming and done very carefully, resulting in different force fields, each parametrised separately and based on different selections of experimental data and theoretical calculations. Hence, each force field has its own version of different molecules. The selection of force field is a very critical point and not straightforward. Since most force fields have some limitations, it is essential to examine prior studies

related to the application, so one can eliminate force fields that have known deficiencies important to the problem of interest. While there is no universal cure-all for selecting an ideal force field, some of the important issues of recent force fields and how they influence different applications are provided in [204]. More simple selection criteria to assess are software compatibility, the availability of parameters for the molecules under investigation, as well as the desired resolution, with force fields parametrised at e.g. atomistic or coarse grained level.

In all atomistic (AA) force fields simulated particles are individual atoms, while in coarse grained (CG) force fields the simulated particles are representative beads containing several atoms. Common examples, also used in this work, are the CHARMM [205] and the Martini [206] force field for AA and CG resolution, respectively. In version 2 of the Martini force field, the beads represent groups of 4 heavy atoms (Figure 1.22).[207]

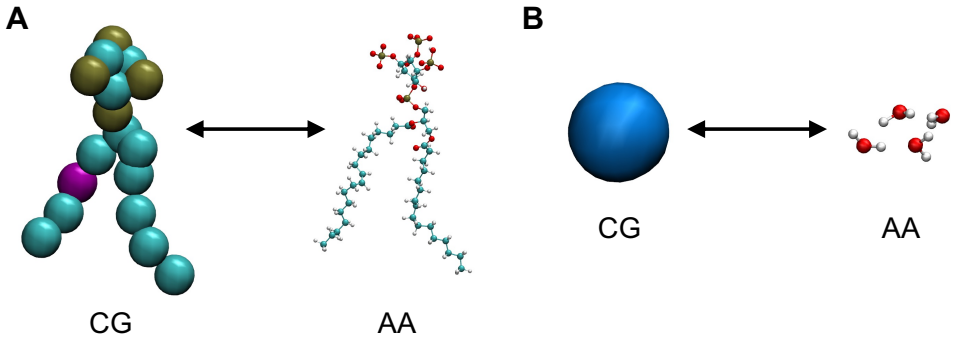


Figure 1.22 | Coarse Grained *versus* All Atomistic Presentation. In all atomistic (AA) force fields each atom is represented with a set of coordinates, while in coarse grained (CG) force fields several heavy atoms are combined in one bead. The atomistic CHARMM36 [205] and coarse grained Marini2 4-to-1 presentation [207] of a PIP3 lipid (**A**) and water (**B**) is shown as examples.

This 4-to-1 mapping was extended in version 3 of the Martini force field, with small and tiny beads of 3-to-1 and 2-to-1 mapping, respectively, being available.[206] The increased number of bead types makes the mapping of several chemical groups, e.g. ring-like or branched groups, more appropriate. As the release of version 3 was during the production of this work, both versions are used in our studies. In general, as force fields are continually refined and updated, it is important to keep up-to-date with the latest version of force fields. While AA force fields provide atomistic resolution, the advantage of CG

force fields is the accessibility of larger timescales and bigger system sizes to be simulated. For instance, the Martini force field improves the timescale by an order of 2-3 compared to AA force fields.[208] This improvement is caused by the decreased number of particles which leads to less degrees of freedom to be calculated. Additionally, as the particle mass is increased, the degree of motion slows down, which enables the use of larger simulation timesteps and potentials of shorter range. However, the speed-up comes at a price: The simplified description of electrostatic interactions leads to different limitations, e.g. an exaggerated protein stickiness.[209], [210] Also changes in protein conformation are not observable in CG simulations due to an elastic network applied for stabilising the secondary structure of proteins. Therefore, multi-scaling approaches are used, utilising the advantages from both resolutions, CG and AA.[45] The systems are rapidly sampled in CG, then converted into AA for further simulation to refine the molecular conformations at higher resolutions and in absence of a protein restricting elastic network.[211]–[213] For the conversion from the CG to the AA representation, the fragment-based protocol CG2AT is a straightforward and popular approach.[211] Here, AA fragments are fitted into the single CG beads. Then, each residue is minimised, followed by combining all residues and re-minimisation of the fully combined structure. The obtained *de novo* structure is either the final AA structure or in case the user supplies AA fragments of the CG molecule to be converted, the supplied fragments are rigid body fitted to the CG backbone and the missing residues, post-translational modifications are added from the *de novo* structure to gain a final AA structure. This multi-scale approach using initially CG then AA resolution was used frequently in the following studies.

The parametrisation of water is particularly important in force fields, due to its specific characteristics and the large amount of water being present in most biophysical simulations. In the CG Martini force field the 4-to-1 mapping applies also for water with four water molecules being represented by one Martini water bead (Figure 1.22, **B**). In AA simulations due to the computational cost of more advanced water models, the most widely used water models are "simple point charge" (SPC) and "transferable intermolceular potential" (TIP) models.[214] The most common members of the TIP family are the 3-point model TIP3P and the 4-point model TIP4P.[215], [216] The water model and force field are closely linked, and therefore, it is common to find that the most appropriate water model

for a given force field is the one that was originally employed to parametrize that force field.[214] Thus, in general the GROMOS force field is used with SPC,[217] the AMBER force field with TIP3P,[218] the OPLS force field with TIP4P [219] and the CHARMM force field with a modified version of the TIP3P water model, namely mTIP3P.[220] These rigid nonpolarizable water models, along with their force fields, use fixed charges where the partial charge on an atom cannot change over the course of a simulation. Therefore, the dielectric effects of water are not described properly and dipole moments are often underestimated in these rigid water models.[214], [221] Using polarizable water models offers a solution to this challenge. Polarizable force fields (e.g. the polarizable version of the CHARMM force field based on the classical Drude oscillator model [222], [223] or the AMOEBA force field based on an interactive atomic dipole induction scheme [224], [225]) use polarizable models such that the partial charge on an atom can change during a simulation in response to changes in its environment/interactions.[214] However, polarizable models are computationally expensive and so not feasible for large complex simulations. The electronic continuum correction (ECC) is a physically well justified, simplified 'correction' within which the atomic partial charges are scaled to account for the missing electronic polarizability in standard, non polarizable MD force fields.[226], [227]

Electronic Continuum Correction (ECC)

In standard, non polarizable MD force fields the electrostatic interactions of charged molecules like ions are calculated based on their integer charges, in essence treating these molecules as if they were in vacuum, isolated from any external interaction.[227] Thus, these force fields do not account for the electronic polarizability from surrounding molecules like solvents and therefore overestimate the charges of ions and other charged chemical groups. The electronic continuum correction (ECC) solves this overestimation by attenuating the charges based on the mean-field approach of charges moving in an uniform electronic continuum with an effective dielectric constant.[226], [227] Thus, the scaling factor of the charges is inversely proportional to the electronic (high-frequency) dielectric constant of the surrounding medium ε_{el} and is defined as:

$$f_q = \varepsilon_{el}^{-1/2}$$

Upon charge scaling also the LJ parameter σ has to be slightly decreased to ensure that the simulations keep matching the experimental oxygen radial distribution functions of the water molecules surrounding the ions or charged groups. Typical scaling factors f_σ for σ fall into the range of $0.72 < f_\sigma \leq 1$.[228] With an electronic dielectric constant ε_{el} of 1.78, water has a scaling factor f_q of around 0.75. The quantitative comparison between neutron scattering data and simulations showed that the usage of this 0.75 scaling factor considerably enhances the accuracy of simulations of solvated ions.[229]–[232] Furthermore, by comparing simulations with structural NMR results it has been shown that the structure of phospholipid membranes containing anionic lipids, as well as their interaction with cations like Ca^{2+} is significantly improved in simulations when using the ECC approach compared to the standard MD force fields.[226], [228] In our studies the interaction between phospholipid membranes and cations play a crucial role. Therefore, we used the ECC approach, as well as standard MD force fields to assess the controversial parametrization of ions within MD simulations.

1.2.4 Aim and Outline of this Thesis

Conventional planar model membrane systems, like supported lipid bilayers, have the disadvantage of the close contact with the adjacent substrate surface influencing membrane behaviour. The free floating model membrane (FFM) system provides with its water inter-layer between substrate surface and membrane a promising new generation of planar modem membrane systems in which the influence of adjacent substrate surface is decreased compared to previous sample systems. Therefore, we wanted to apply the FFM system to investigate the interactions of peripheral membrane proteins with their target membranes. The role of these interactions are of great interest as many diseases are associated with perturbed protein/membrane binding processes. The combination of neutron reflectometry (NR) experiments with molecular dynamics (MD) simulations is a great way for analysing these interactions, with NR providing a density distribution of each sample component (e.g. lipids, proteins) along the membrane normal and MD supplementing these results by providing all atomistic resolution of the structural binding modes of membrane lipids and proteins. Initial NR experiments with the FFM

system revealed that buffer salt conditions have a huge influence on membrane behaviour within the FFM system, suggesting the requirement of a better understanding of our experimental sample system.

In *Chapter 2* the effect of different salt buffer conditions on the membrane behaviour within the FFM system was probed using NR experiments. Hereby, present cations as well as the membrane lipid compositions were varied between sample systems. A strong correlation between cations present in the system and the distance between the floating membrane and the substrate sufrace, as well as the membrane roughness was observed. By calculating the free cation binding energies between different cations and the different layers within the FFM system, MD simulations provided possible explanations for the membrane behaviour we observed experimentally. Finally, quartz crystal microbalance with dissipation monitoring (QCM-D) was used as complementary experimentally method to confirm the results obtained by NR and MD, as well as to demonstrate the possible usage of the FFM system by a bench-top, easily accessible technique.

In *Chapter 3* a further understanding of the FFM system was obtained by studying the effect of pH on membrane behaviour within the FFM system. In *Chapter 2* the charge modulation of the substrate surface due to cation binding was suggested to be the main cause of the observed changes in distance between the floating membrane and the substrate surface upon cation addition in the buffer solution. Therefore, we expected to see similar effects by changing the substrate surface charge via pH of the surrounding buffer solution. Thus, floating membranes of different lipid composition were investigated at different pH values employing NR and MD. Furthermore, by simulating multi-layer systems the influence of the adjacent substrate surface on membrane dynamics and lipid conformation within the FFM system was investigated. Previous studies claimed that the FFM system decreases the influence of the adjacent substrate surface on lipid diffusion and membrane fluctuations compared to previous sample systems by the presence of the water layer between substrate surface and floating membrane. However, in the literature there was no quantitative investigation of this suggestion yet. Therefore, FFMs were simulated at different distances from the substrate surface, while lipid diffusion and lipid conformation were calculated in both membrane leaflets.

After understanding the processes and interactions within the FFM system, in *Chapter 4* the FFM system was applied for the investigation of the interaction between peripheral membrane proteins and their target membranes. The proteins of interest were kindlin-2 (K2), involved in integrin activation, and T-lymphoma invasion and metastasis 2 (TIAM2), a guanine nucleotide exchange factor. Both proteins contain a pleckstrin homology (PH) domain, known to be a membrane targeting domain by binding to phosphatidylinositol (PIP) lipids. Initially, simpler supported lipid bilayer systems were used in combination with Fourier transform infrared spectroscopy (ATR-FTIR), as well as with NR to find the best sample conditions to be used in the FFM system. Then, PIP containing membranes were generated in the FFM system and investigated before and after protein addition using NR. The final NR results were compared with MD simulations for gaining an all atomistic view of the protein binding modes supported by the experimental results.

Chapter 5 concludes this work by summarizing the key findings and outlines potential future research directions how the combination of neutron and simulation studies might enable us to continue to better understand the complex interactions between proteins and membranes.

2

The Effect of Salt Buffer Condition on Free Floating Model Membranes

Contents

2.1 Introduction 48
2.2 Results 51
2.2.1 NR Reveals Cation Induced Bilayer-to-SAM Distance Modulation 51
2.2.2 Complementary Analysis on QCM-D Sensor Surfaces 62
2.2.3 MD Simulations Reveal Differences in Ion Binding between OEG-SAM and FFM 64
2.3 Discussion 79
2.4 Materials and Methods 81
2.4.1 Materials 81
2.4.2 Neutron Reflectometry (NR) Measurements 82
2.4.3 Quartz Crystal Microbalance with Dissipation Monitoring (QCM-D) Measurements 86
2.4.4 Molecular Dynamics (MD) Simulations 88

2.1 Introduction

Different planar model membrane system were developed in order to study interactions between membrane associated proteins and membranes *in vitro*.[233] In simpler planar model membrane systems, the membrane is deposited directly onto a supporting substrate, mostly silicon (Figure 2.1).[107] However, the underlying, bound substrate influences the membrane dynamics and fluidity.[106] Therefore, more advanced model membrane systems try to decrease the interaction between the

membrane and the substrate. In cushioned model membrane systems, this is achieved by a hydrophilic polymer layer between the membrane and the substrate [234], whereas in tethered model membrane systems substrate attached polymeric membrane tethers enable a solution layer between the membrane and the substrate (Figure 1.12).[127] However, the model membrane system which reduces the influence of the substrate the most, is very likely the free floating model membrane system.[132] Here, a combination of attractive and repulsive forces between the membrane and the substrate causes a solution layer with a thickness of around 20 Å between the membrane and the substrate (Figure 2.1).[136], [235], [236] This leads to a free floating membrane (FFM), surrounded by 'bulk' solution on both sides without being tethered or in contact with substrate bound material. A previous study showed that FFBs can be produced via vesicle rupture adjacent to carboxylate terminated oligo (ethylene glycol) alkanthiol self-assembled monolayer surfaces (OEG-SAM) covering a gold-coated substrate.[133] This makes the FFM system even more attractive as it enables a fairly quick and easy generation of FFMs of high coverage without having to conduct a Langmuir-Blodgett/Langmuir-Schaefer deposition, which is time consuming and requires special equipment and expertise in order to generate high quality membranes.[132]

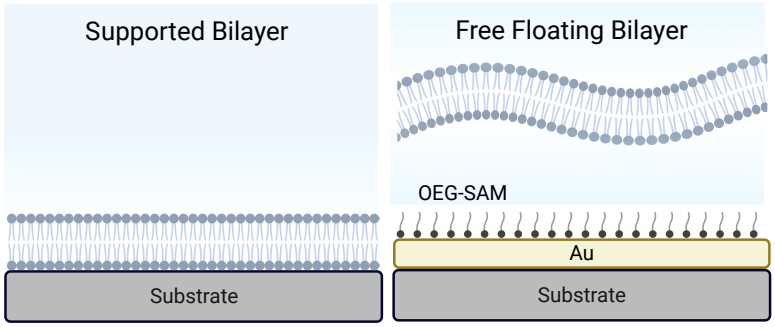


Figure 2.1 | Supported *versus* Free Floating Model Membrane System. Shwon is a schematic representation of the supported lipid bilayer sample system (left) compared to the free floating model memrane system (right). While the membrane is in direct contact with the adjacent substrate when supported, in the free floating bilayer system the membrane is on both sides surrounded by water. The carboxylate terminated oligo (ethylene glycol) alkanthiol self-assembled monolayer surfaces (OEG-SAM) formed on the gold surface cause an interplay of attractive and repulsive forces within the system, enabling the floating state of the membrane.

Although the FFM system seems like a very attractive planar membrane model system and promises an important step forward concerning mimicking natural membrane behaviour, the forces acting within this model system leading to the desired floating state of the membrane are not fully understood yet. It has

been previously shown, that 200 mM NaCl in the bulk solution reversibly increase the distance between OEG-SAM and FFM.[133] However, no cause for this effect has been identified. As electrolytes seem to influence the behaviour and position of the FFM in the sample system, the self-assembly process of the FFM adjacent to the OEG-SAM surface requires Ca^{2+} ions and in general experiments investigating the interactions between proteins and membranes need NaCl present in the buffer solution, the interactions of Ca^{2+} and Na^{+} ions alongside their effects on the FFM were of particular interest. Ca^{2+} and Na^{+} ions are known to interact with phospholipid membranes, in various amounts depending on the presence of anionic phospholipids within the membrane.[237], [238] However, in the FFM system the partly negatively charged OEG-SAM surface represents a competing layer for cation interactions. As the interactions of metal cations with OEG-SAMs and their resulting surface charge modulation have never been studied, we were interested in these interactions themselves as well as their effects in the FFM system. Besides, the water behaviour between OEG-SAM and FFM and its possible change resulting from the presence of cations were also a focus of our studies. The reason is, that OEG-SAMs are known for their repulsive hydration forces caused by tightly bound water layers to the oligo (ethylene glycol) (OEG) groups of the OEG-SAM molecules [239], [240], leading to their use in anti-fouling surface coatings.[241] Therefore, FFMs of different lipid compositions were investigated using neutron reflectometry (NR) measurements, each in the presence of no additional cations, Ca^{2+} and Na^{+}. NR was used as these multi-layer model membrane systems are perfectly suitable for nondestructive, deeply penetrating neutrons.[143] By varying the ratio of H_2O *versus* D_2O in the bulk solution or by deuterium labeling of the biomolecules in these sample system, the overall structure along the membrane normal and the relative distribution of single components can be resolved by NR.[242] This work was published in: John, L. H., Preston, G. M., Sansom, M. S., Clifton, L. A. (2021). Large scale model lipid membrane movement induced by a cation switch. *Journal of colloid and interface science*, 596, 297-311.

2.2 Results

2.2.1 NR Reveals Cation Induced Bilayer-to-SAM Distance Modulation

Self-assembled free floating membranes (FFMs) of different lipid compositions adjacent to OEG-SAMs were generated (Table 2.1). The complexity of the lipid composition was thereby step wise increased in order to investigate the usability of the FFM system for studies of membranes with biological complexity. Therefore, starting from a simple POPC membrane and a POPC/POPS mixture (8:2, mol:mol), a model of the inner leaflet of the mammalian plasma membrane (POPC/POPS/PIP3 7:2:1, mol:mol:mol)[2] and a model of the plant plasma membrane (POPC/POPS/Chol/DGDG 5:2:2:1, mol:mol:mol:mol)[6], [243] were produced. The self-assembling process of all FFMs required 2 mM $CaCl_2$ present in the buffer solution (which is also in agreement with physiological concentrations [244]). Furthermore, a previous study suggested a significant influence of cations being present in the buffer solution on the thickness of the solution layer between OEG-SAM surface and FFM.[133] Thus, the interactions of Ca^{2+} ions and their role in the observed large scale membrane movements were of particular interest. In order to remove the Ca^{2+} ions out of the buffer solution after the FFM assembly, each sample system was treated with 1 mM EDTA. Then, the FFM system was flushed with a 200 mM NaCl buffer solution in order to study the difference between the effects caused by divalent Ca^{2+} ions *versus* monovalent Na^{+} ions at physiological conditions.[133], [244] In the last step, the 2 mM $CaCl_2$ buffer solution was added back into the FFM system. For each FFM sample system, at each buffer solution condition NR measurements were carried out using three different isotopic contrasts (H_2O, AuMW, D_2O). By applying a single uniform layer model for each component in the sample system, the average relative distribution of all components, including OEG-SAM, FFM and buffer solution, were resolved for each sample system, at all buffer solution conditions. The full NR data sets, including reflectively profiles, data model fits and the resulting neutron scattering length density (nSLD) profiles, are shown for all model membranes in Figure 2.2, 2.3, 2.4 and 2.5. Resolved key structural parameters of all NR measurements are listed in Table 2.1 with further parameters in Table 2.2. Note, the FFM-to-SAM

distance is defined as the distance between the OEG-SAM/water interface and the water/lipid head group interface, therefore equivalent to the thickness of the solution layer between OEG-SAM and FFM.

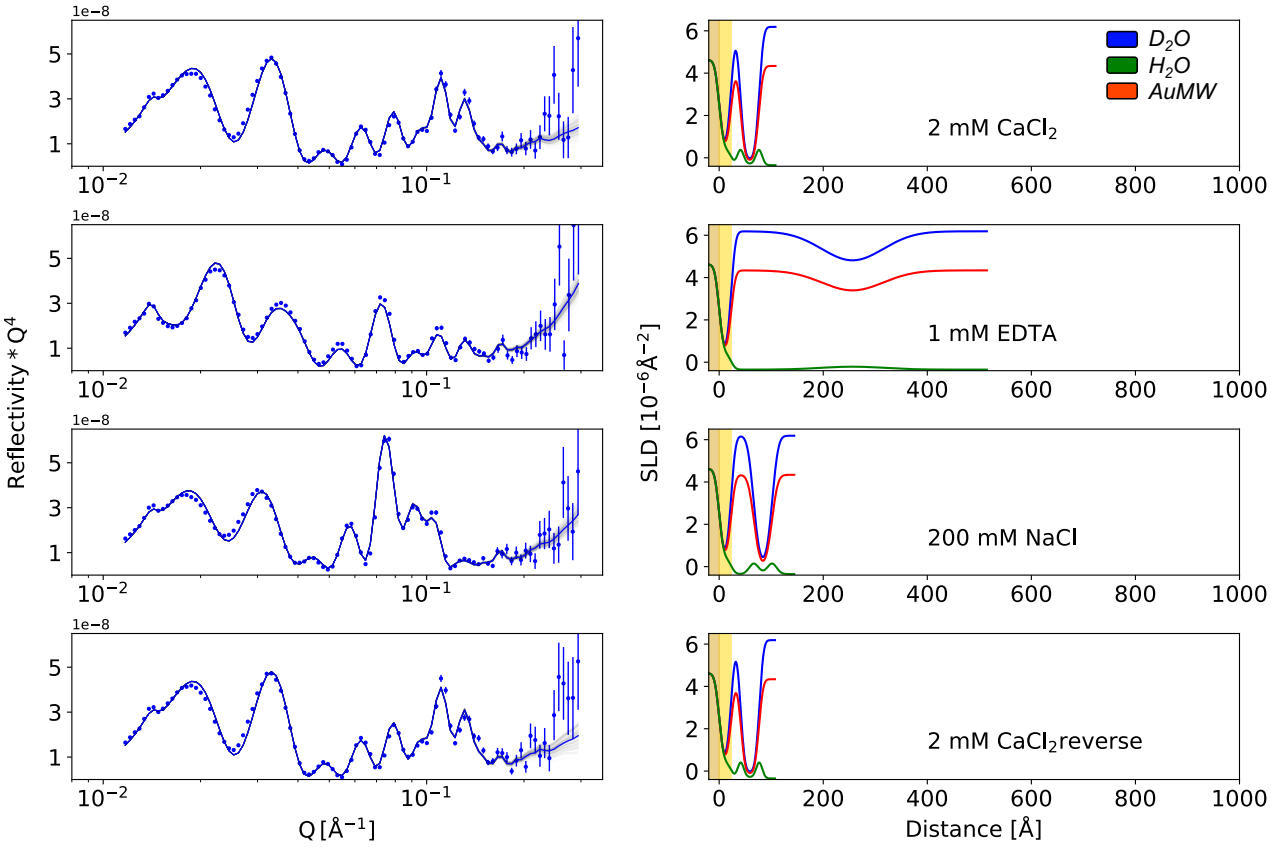


Figure 2.2 | Reflectivity and SLD Profiles of a POPC Membrane in Absence and Presence of Ca^{2+} and Na^{+} ions. Each row shows the reflectivity and the corresponding SLD profile for one of the buffer solution condition at which the POPC membrane was measured (see labels in SLD profiles). The SLD profiles are shown for the three applied isotopic contrasts, H_2O (green), AuMW (red), D_2O (blue). Here, zero at the x-axis is equal to the gold/OEG-SAM interface. For clarity the area of the gold layer is highlighted in light brown and the area of the OEG-SAM in yellow. The reflectivity profiles include the experimental data (dotted) and fits (solid), both for the D_2O isotopic contrast.

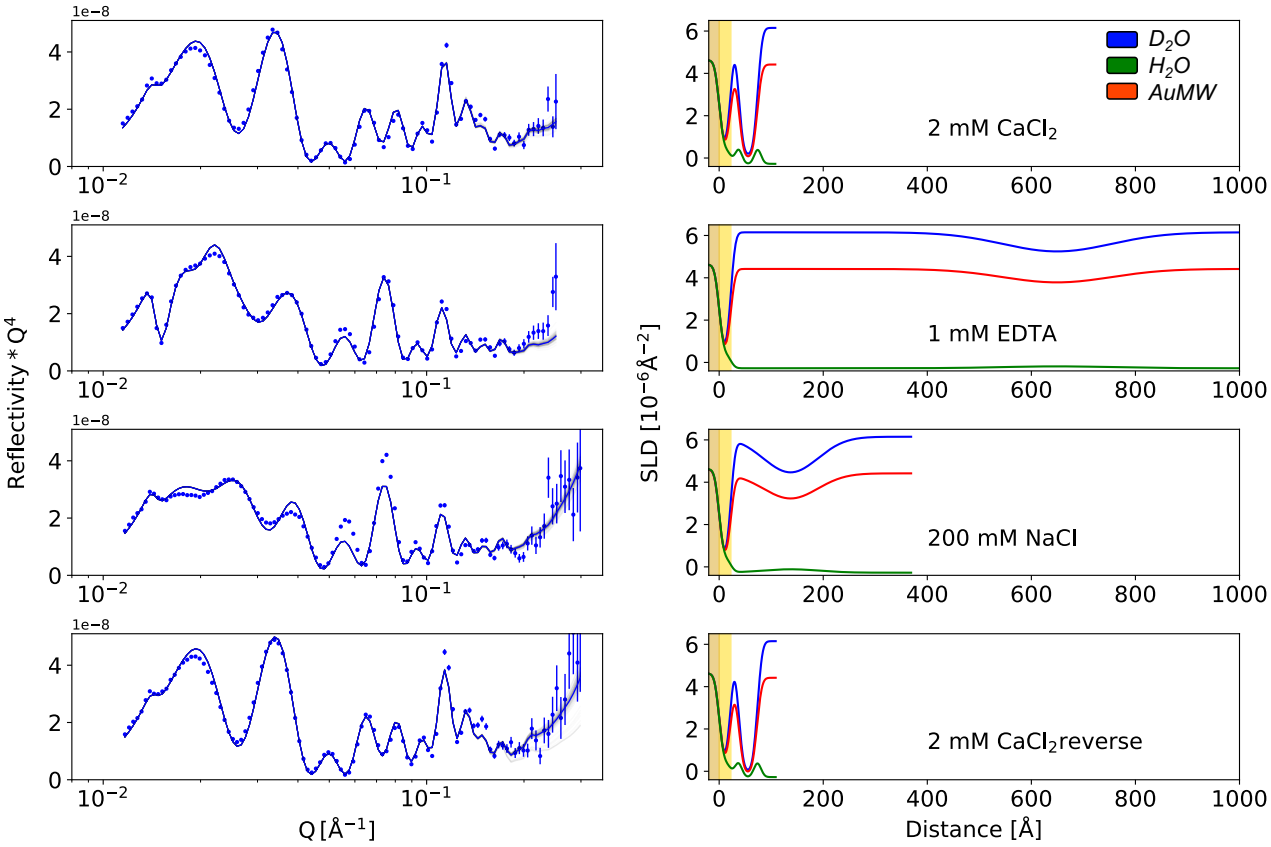


Figure 2.3 | Reflectivity and SLD Profiles of a POPC:POPS (8:2) Membrane in Absence and Presence of Ca^{2+} and Na^{+} ions. Each row shows the reflectivity and the corresponding SLD profile for one of the buffer solution condition at which the POPC:POPS (8:2, mol:mol) membrane was measured (see labels in SLD profiles). The SLD profiles are shown for the three applied isotopic contrasts, H_2O (green), AuMW (red), D_2O (blue). Here, zero at the x-axis is equal to the gold/OEG-SAM interface. For clarity the area of the gold layer is highlighted in light brown and the area of the OEG-SAM in yellow. The reflectivity profiles include the experimental data (dotted) and fits (solid), both for the D_2O isotopic contrast.

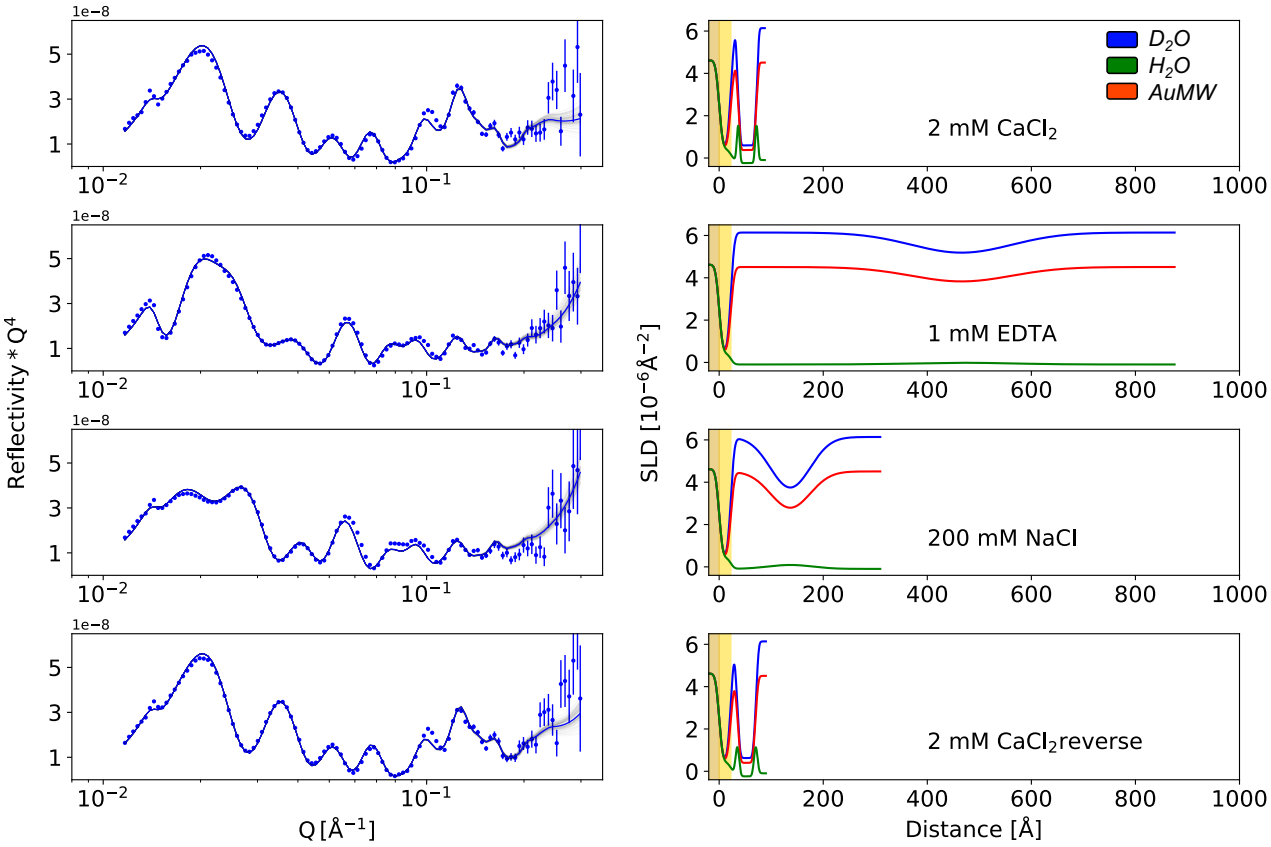


Figure 2.4 | Reflectivity and SLD Profiles of a Mammalian Plasma Model Membrane in Absence and Presence of Ca^{2+} and Na^{+} ions. Each row shows the reflectivity and the corresponding SLD profile for one of the buffer solution condition at which the POPC:POPS:DOPIP3 (7:2:1, mol:mol:mol) membrane was measured (see labels in SLD profiles). The SLD profiles are shown for the three applied isotopic contrasts, H_2O (green), AuMW (red), D_2O (blue). Here, zero at the x-axis is equal to the gold/OEG-SAM interface. For clarity the area of the gold layer is highlighted in light brown and the area of the OEG-SAM in yellow. The reflectivity profiles include the experimental data (dotted) and fits (solid), both for the D_2O isotopic contrast.

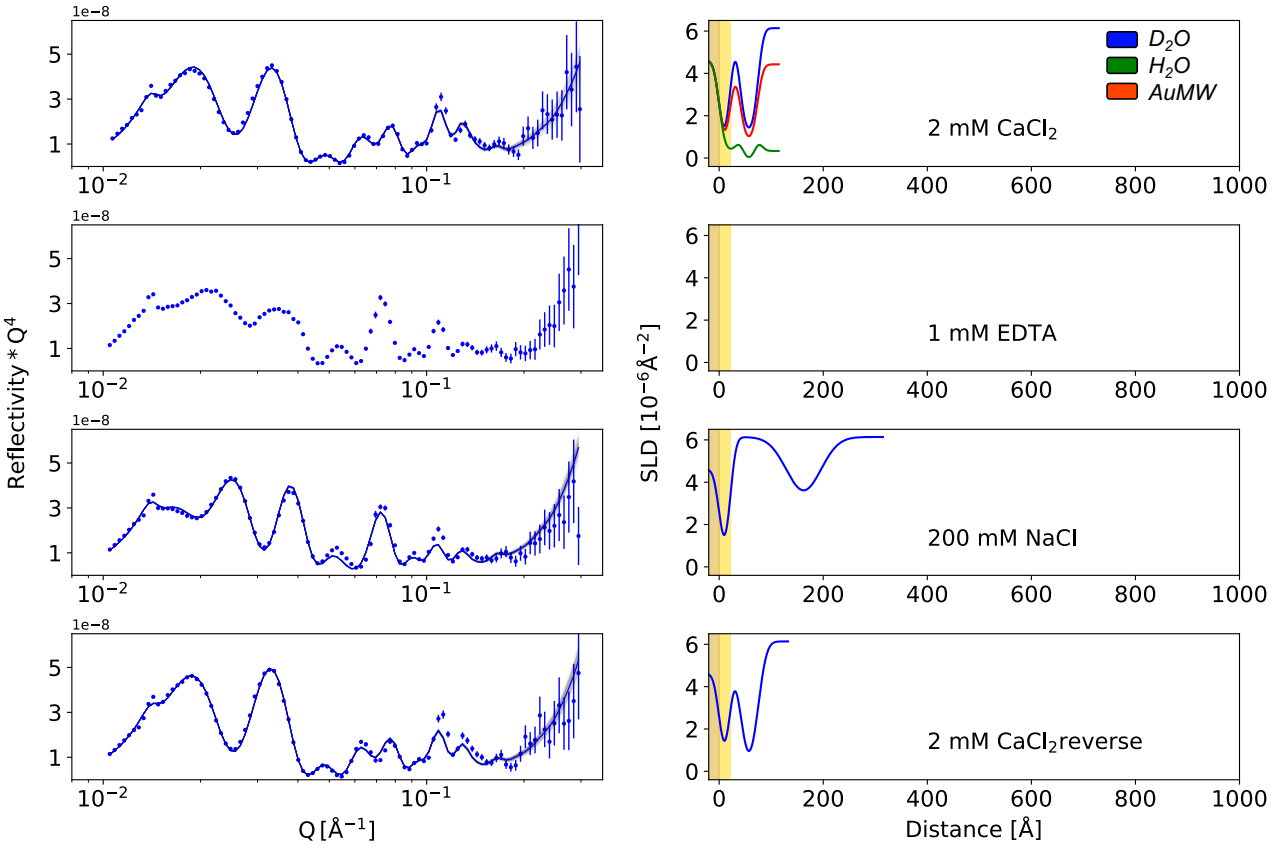


Figure 2.5 | Reflectivity and SLD Profiles of a Plant Plasma Model Membrane in Absence and Presence of Ca^{2+} and Na^{+} ions. Each row shows the reflectivity and the corresponding SLD profile for one of the buffer solution condition at which the POPC:POPS:Chol:DGDG (5:2:2:1, mol:mol:mol:mol) membrane was measured (see labels in SLD profiles). The SLD profiles are shown for the three applied isotopic contrasts, H_2O (green), AuMW (red), D_2O (blue). Here, only the initial membrane position at 2 mM $CaCl_2$ was measured at all three isotopic contrasts, the other buffer solution conditions only at D_2O. Zero at the x-axis is equal to the gold/OEG-SAM interface. For clarity the area of the gold layer is highlighted in light brown and the area of the OEG-SAM in yellow. The reflectivity profiles include the experimental data (dotted) and fits (solid), both for the D_2O isotopic contrast. Note, there was no reasonable fitting possible for the 1 mM EDTA buffer solution condition. However, the fringes in the experimental reflectivity profile show clearly that the FFM is far away from the OEG-SAM surface and in a rough state at this cation-free buffer solution condition.

Sample	FFM-to-SAM Distance [Å]				FFM Roughness [Å]			
	2 mM $CaCl_2$	*1 mM EDTA*	*200 mM NaCl*	*2 mM $CaCl_2$ reverse*	*2 mM $CaCl_2$*	*1 mM EDTA*	*200 mM NaCl*	*2 mM $CaCl_2$ reverse*
POPC	15 ± 1	212 ± 1	40 ± 1	15 ± 1	6 ± 1	58 ± 2	9 ± 1	6 ± 1
POPC:POPS (8:2)	12 ± 1	606 ± 3	93 ± 1	11 ± 1	7 ± 1	104 ± 1	51 ± 1	7 ± 1
POPC:POPS:PIP3 (7:2:1)	12 ± 1	423 ± 2	94 ± 1	10 ± 1	2 ± 1	96 ± 1	37 ± 1	3 ± 1
POPC:POPS:Chol: DGDG (5:2:2:1)	15 ± 1	-	120 ± 1	15 ± 1	8 ± 1	-	32 ± 1	12 ± 1

Table 2.1: | Resolved Structural NR Parameters. The distance between OEG-SAM and FFM, as well as the roughness of the FFM are given for all FFM samples at each measured buffer solution condition. The errors represent the 95% confidence intervals determined via MCMC sampling of the fitting parameters.

Sample	FFM Coverage [%]				SAM Thickness [Å]
	2 mM $CaCl_2$	*1 mM EDTA*	*200 mM NaCl*	*2 mM $CaCl_2$ reverse*	*All Conditions*
POPC	97 (96, 97)	87 (83, 91)	93 (92, 94)	96 (95, 97)	23 (22, 23)
POPC:POPS (8:2)	93 (93, 94)	100 (98, 100)	94 (92, 96)	96 (95, 96)	22 (22, 23)
POPC:POPS:PIP3 (7:2:1)	87 (86, 87)	100 (99, 100)	100 (99, 100)	86 (86, 87)	23 (22, 23)
POPC:POPS:Chol: DGDG (5:2:2:1)	77 (76, 78)	-	94 (92, 96)	98 (97, 99)	21 (21, 22)

Table 2.2: | Resolved Structural NR Parameters. The FFM coverage, as well as the thickness of the OEG-SAM are given for all FFM samples at each measured buffer solution condition. The errors represent the 95% confidence intervals determined via MCMC sampling of the fitting parameters.

All FFMs showed high membrane coverage after their generation adjacent to the OEG-SAM and their structural parameters were in good agreement with previous studies (see Table 2.1 and

2.2).[131], [133] Then, all FFMs showed the same dependence of the FFM-to-SAM distance and FFM roughness on the cations present in the buffer solution (see Figure 2.6). The initial bilayer-to-SAM distance in the presence of 2 mM $CaCl_2$ was at around 11 to 16 Å. EDTA mediated sequestration of Ca^{2+} resulted in a large increase of the FFM-to-SAM distance to above 200 Å. The addition of 200 mM NaCl reduced the FFM-to-SAM distance to an intermediate value, whilst returning the FFM into a 2 mM $CaCl_2$ containing buffer solution returned the FFM back to its initial position adjacent to the OEG-SAM ($\sim$9–16 Å). In all cases the reversible movement of the FFM away from and back to the OEG-SAM surface did not result in measurable loss of the total membrane coverage, suggesting these to be fully reversible processes (see Table 2.2).

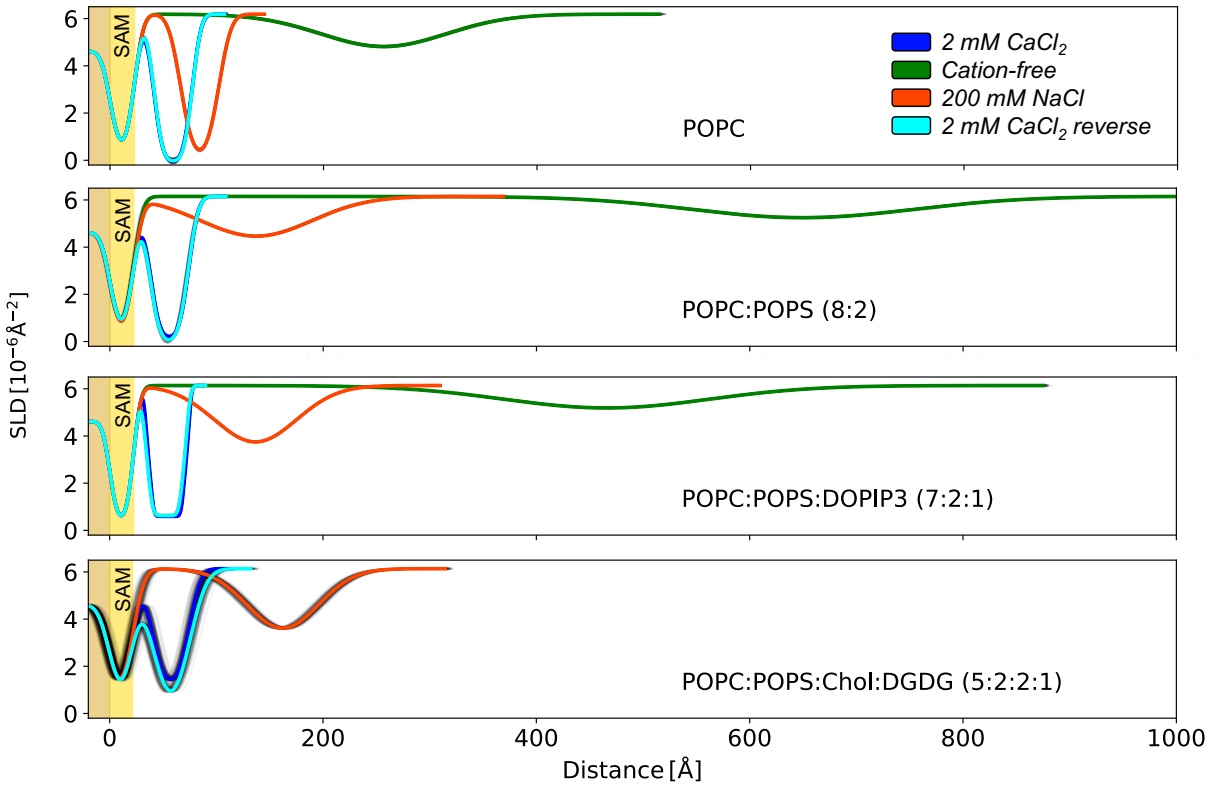


Figure 2.6 | SLD Profiles of FFMs at Different Buffer Solution Conditions. Each subplot shows the SLD profiles belonging to one respective FFM (see labels in subplots). Different colours of the profiles represent different additions to the buffer solution, which were present in each sample in following order: 2 mM $CaCl_2$ after the self-assembling process of the FFM (blue), no cations due to 1 mM EDTA mediated Ca^{2+} sequestration (green), 200 mM NaCl (red) and finally, again 2 mM $CaCl_2$ (cyan). Changes in the FFM-to-SAM distance can be seen through changes in the Gaussian distribution of the FFM (here equal to the not highlighted, second distribution next to the OEG-SAM in the SLD profiles). The largest changes caused the EDTA mediated Ca^{2+} sequestration, resulting in very rough FFMs, far away from the OEG-SAM surface. 200 mM NaCl returned the POPC bilayer almost completely, the anionic membranes only partly back towards their initial positions. All FFMs restored their initial position close to the OEG-SAM surface when the 2 mM $CaCl_2$ containing buffer solution was flushed back into the sample system (corresponding SLD profiles in cyan overlay with the profiles of the initial positions in blue). Experimental data and model data fits used to produce these SLD profiles are given in Figure 2.2, 2.3, 2.4 and 2.5.

Though the trends in FFM-to-SAM distance change against buffer solution conditions were similar, the magnitude differed between FFMs. For example, whilst after Ca^{2+} sequestration the POPC membrane moves to ∼200 Å from the OEG-SAM surface, the anionic eukaryotic membrane models (i.e. POPC:POPS and POPC:POPS:DOPIP3) were found to move to significantly higher distances away from the OEG-SAM surface in this buffer solution condition (∼600 Å and ∼400 Å respectively, see

Table 2.1). This suggested a correlation between membrane anionic character and the FFM-to-SAM distance change after Ca^{2+} sequestration. A similar trend was seen with 200 mM NaCl. Here, the POPC membrane returned to a close FFM-to-SAM distance ($\sim$40 Å, compared to $\sim$15 Å in 2 mM $CaCl_2$), whereas the anionic POPC:POPS and POPC:POPS:DOPIP3 membranes returned to a larger FFM-to-SAM distance of $\sim$94 Å. Interestingly, when comparing the two mammalian anionic membrane models with each other, the FFM-to-SAM distances for the POPC:POPS membrane during all applied salt solution buffer conditions were either greater or equal to those of the POPC:POPS:DOPIP3 membrane, although the latter had a higher net negative charge, see Table 2.1. The anionic plant plasma membrane model (POPC:POPS:Chol:DGDG, 5:2:2:1, mol:mol:mol:mol) showed the same behaviour as the mammalian plasma membrane models, starting with a close position to the OEG-SAM surface in the presence of Ca^{2+} ($\sim$15 Å), followed by dramatic changes in the reflectivity profile upon EDTA mediated Ca^{2+} sequestration (see Figure 2.5). However, the interfacial structure could not be adequately resolved for this cation-free state, most likely due to the roughness of the membrane being too high for analysis or high heterogeneity in the membrane position at this solution condition. This measurement points out the limitations of these measurements. Additionally, we observed increasing ambiguity in the fit at FFM-to-SAM distances above 200 Å. Therefore, the exact values obtained from the EDTA measurements have to be treated with care. Nevertheless, the FFM-to-SAM distance could be resolved once the sample was immersed into 200 mM NaCl, showing a distance of $\sim$120 Å (see Table 2.1). In all cases, the bilayer roughness, which describes the height-height correlation function across a layer boundary,[133] showed a proportional increase with FFM-to-SAM distance (see Table 2.1). In mathematical terms, the roughness is equivalent to the horizontal correlation length. This length defines the distance at which the average square difference in height *H(r)* starts to loose its correlation with the distance *r* and to be constant.[245] Therefore, the roughness describes the area in which a layer smears out and in which SLDs of adjacent layers mix. Therefore, it is not to be confused with the error of the layer thickness, defined by a single SLD. In a continuous planar material such as a supported lipid bilayer the largest and therefore overriding source of roughness is likely to be displacement of the bilayer from its mean averaged position due to the fluctuations along the

bilayer normal.[132], [235], [246] Therefore, this increase in the roughness value might be related to an increased fluctuation amplitude of the floating membrane as it moves away from the surface.

Finally, as the NR data suggested that Ca^{2+} brings the FFM much closer to the OEG-SAM surface than Na^{+}, the effect of Ca^{2+} on the FFM-to-SAM distance in the presence of physiological concentrations of Na^{+} was investigated. To this end, two independent repeats of a POPC FFM were sequentially examined in buffer solutions containing 100 mM NaCl with and without 1 mM $CaCl_2$. The solution without $CaCl_2$ contained 0.5 mM EDTA to remove any contaminating Ca^{2+} cations from the previous buffer solution. The NR analysis (see Figure 2.7) revealed that the FFM-to-SAM distance was significantly smaller with the buffer solution containing both Ca^{2+} and Na^{+} than in the presence of Na^{+} only ($\sim$25 vs. $\sim$43 Å). These data demonstrate the strong influence of divalent cations on the FFM-to-SAM distance, even in the presence of a one hundred times higher concentration of monovalent cations. Furthermore, these results suggested the possibility of fine-tuning the FFM-to-SAM distance by using combinations of mono- and divalent cations. Resolved structural parameters are given in Table 2.3.

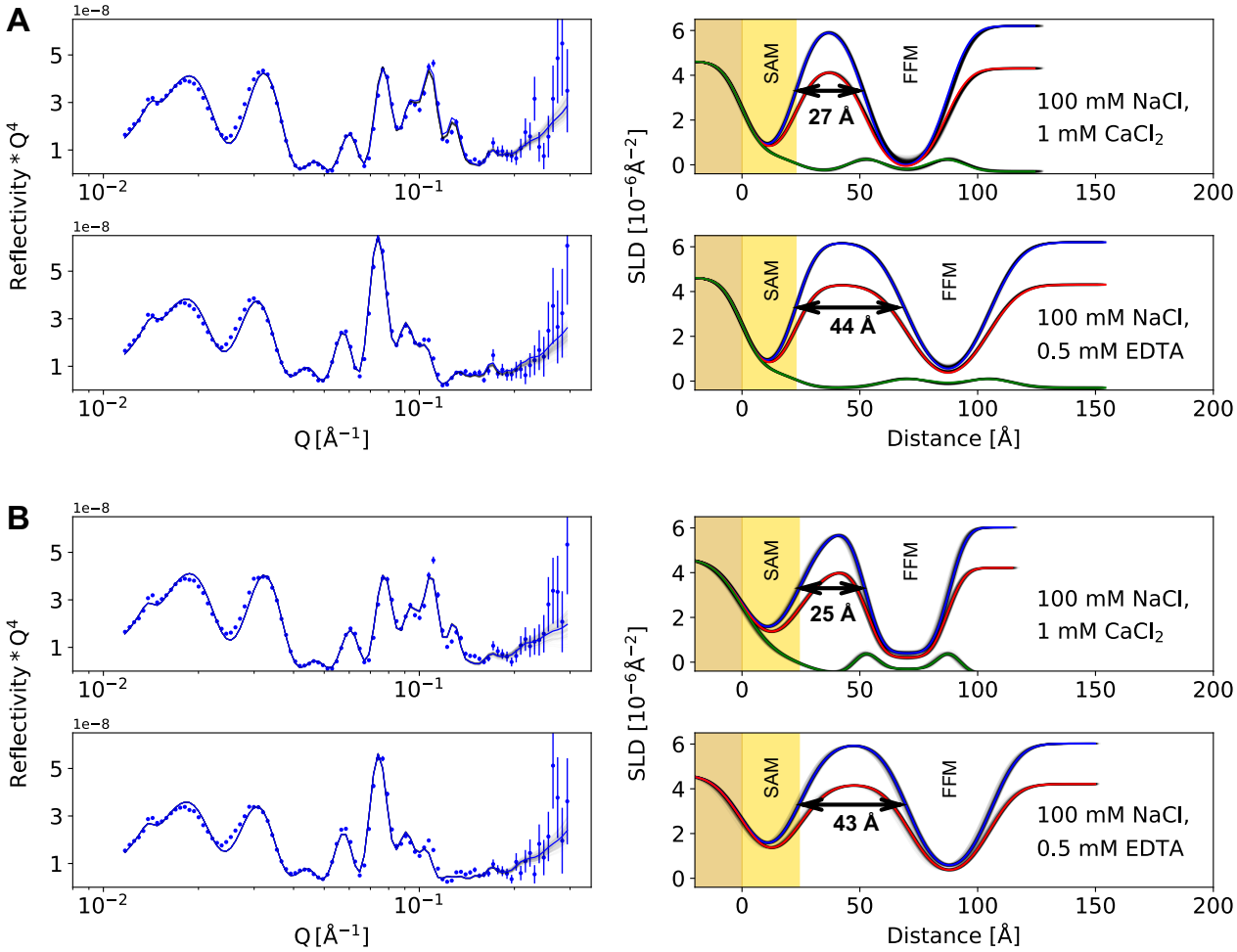


Figure 2.7 | Ca^{2+} Dependent Fine-tuning of FFM-to-SAM Distance in Presence of Na^{+}. **(A)** and **(B)** show two independent repeats of a POPC FFM, each measured with NR at two different buffer solution conditions: 100 mM NaCl / 1 mM $CaCl_2$ (top) and 100 mM NaCl / 0.5 mM EDTA (bottom). For each buffer solution condition three isotopic contrasts were applied, D_2O (blue), AuMW (red) and H_2O (green). The obtained reflectivity profiles, including model data fits, are shown for the D_2O contrast (left column). The corresponding SLD profiles these fits describe are shown for all three isotopic contrasts (right column; note: The H_2O contrast was not measured for repeat **B** at 100 mM NaCl / 0.5 mM EDTA). The resolved FFM-to-SAM distances are given, highlighting the difference in this caused by 1 mM $CaCl_2$ in the presence of 100 mM NaCl. Relevant parameters are given in Table 2.3.

Sample	FFM-to-SAM Distance [Å]		FFM Roughness [Å]		FFM Coverage [%]	
	100 mM NaCl, 1 mM $CaCl_2$	*100 mM NaCl, 0.5 mM EDTA*	*100 mM NaCl, 1 mM $CaCl_2$*	*100 mM NaCl, 0.5 mM EDTA*	*100 mM NaCl, 1 mM $CaCl_2$*	*100 mM NaCl, 0.5 mM EDTA*
POPC Repeat A	27 ± 1	44 ± 1	7 ± 1	10 ± 1	95 ± 1	94 ± 1
POPC Repeat B	25 ± 1	43 ± 1	5 ± 1	9 ± 1	90 ± 1	92 ± 1

Table 2.3: | Resolved Structural NR Parameters. The distance between OEG-SAM and FFM, as well as the roughness and coverage of the FFM are given for two POPC FFM repeats at each measured buffer solution condition. The errors represent the 95% confidence intervals determined via MCMC sampling of the fitting parameters.

2.2.2 Complementary Analysis on QCM-D Sensor Surfaces

Quartz crystal microbalance with dissipation monitoring (QCM-D) is a surface sensitive technique utilizing the piezoelectric effect for real-time measurements of surface interactions. The change in the resonant frequency (Δf) is inversely proportional to the amount of mass at the sensor surface, as given by the Sauerbrey equation.[175], [176] To complement NR measurements and to demonstrate utilization of this sample system in studies using benchtop analytical techniques, FFMs of POPC:POPS (8:2, mol:mol) were self-assembled onto a OEG-SAM coated QCM sensor chip surface. Measurements of changes in the frequency (Δf) and dissipation (Δd) were used to monitor the sample response after changing the buffer solution condition. These changes are caused by variations in the amount of trapped solution between the FFM and the OEG-SAM, which is part of the total layer mass. Hence, the changes in FFM-to-SAM distance will be associated with a decrease in Δf and an increase in Δd. This assumption is supported by the observation that the water inside a vesicle adsorbing onto a QCM sensor adds to the adsorbed mass measured and the loss can be measured during vesicle rupture.[176], [247]

The QCM-D results were complementary to those observed with NR, showing a large decrease in Δf and increase in Δd when the buffer condition was changed from 2 mM $CaCl_2$ to 0 mM $CaCl_2$ by EDTA mediated Ca^{2+} sequestration. This implies that a thicker water layer was trapped between the OEG-SAM and the FFM in case of the Ca^{2+} free state compared to the initial state given in the presence of Ca^{2+} (see Figure 2.8). Interestingly, Δf often after an initial decrease showed a slow increase, whereas Δd increased always to a plateau after Ca^{2+} sequestration. It is possible that this effect was due to the movement of the FFM to a large distance, which was outside the frequency depth sensitivity range of QCM-D (which is inversely proportional to the square of the resonant frequency) and/or at which the water was no longer mechanically coupled to the FFM. Besides the distance, increased membrane curvature and fluctuation amplitude of the FFM could have been another cause of the reduction in mechanically coupled water to the FFM. Immersing the FFM into 200 mM NaCl containing buffer solution seemed to bring the FFM partly back to the OEG-SAM surface, revealed by values of Δf and Δd between that observed in the presence of Ca^{2+} and the cation-free state. Finally, when the samples were exchanged back into 2 mM $CaCl_2$ containing buffer solution the Δf and Δd values returned to their initial values. This suggested, like the NR data indicated, a reversible process of FFM-movement away from and back to a close position to the OEG-SAM surface. The solution exchange process was repeated twice and showed good reversibility, as well as robustness of the biomimetic sample system to repeated large distance changes (see Figure 2.8). The QCM-D measurements were conducted by Dr. Luke Clifton.

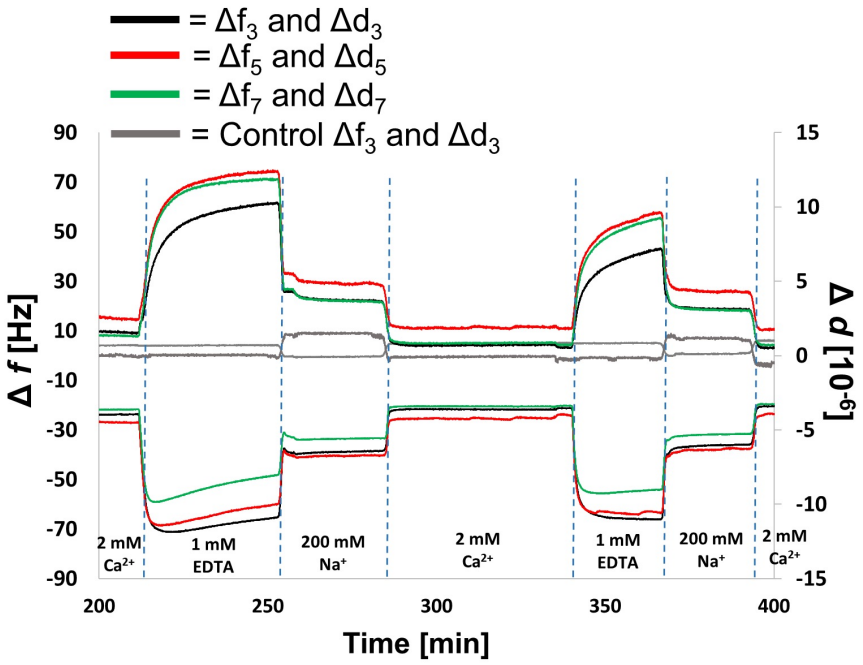


Figure 2.8 | QCM-D Measurements of a Free Floating POPC:POPS Membrane (8:2, mol:mol) in Absence and Presence of $CaCl_2$ and NaCl. The changes in frequency (Δf) and dissipation (Δd) at different solution salt conditions are given for the 3rd (black), 5th (red) and 7th (green) overtones. For the control data set with no membrane adjacent to the OEG-SAM only the 3rd overtone is given (grey line). This Figure was produced by Dr. Luke Clifton.

2.2.3 MD Simulations Reveal Differences in Ion Binding between OEG-SAM and FFM

Taken together, the NR and QCM-D results indicated that Ca^{2+} reversibly moves the FFM closest to the OEG-SAM surface, followed by Na^+. These results raised the question what the difference is between Na^+- and Ca^{2+}-interactions within the system. In particular, we wished to understand which layer preferentially interacts with cations, and how strongly the different cationic species interact. This information would enable us to understand the observed substantive, reversible movements of the FFM away from the surface in response to changes in cation concentrations. MD simulations of the OEG-SAM and of the different lipid bilayers used in the NR experiments were performed at different $CaCl_2$ and NaCl concentrations. Coarse grained (CG) simulations were used to generate initial model structures, using the well-established Martini force field.[207], [248] For the CG model of the OEG-SAM a range of initial lattice constants (a_0) of the hexagonal OEG-SAM-grid (0.1 Å intervals between 4.9 and 5.6 Å) were

defined for a set of OEG-SAMs differing in the percentage of charged SAM-COO$^-$ molecules present (0, 5, 10, 20, 39 and 50%). Figure (2.9) shows a schematic of a partly negatively charged OEG-SAM.

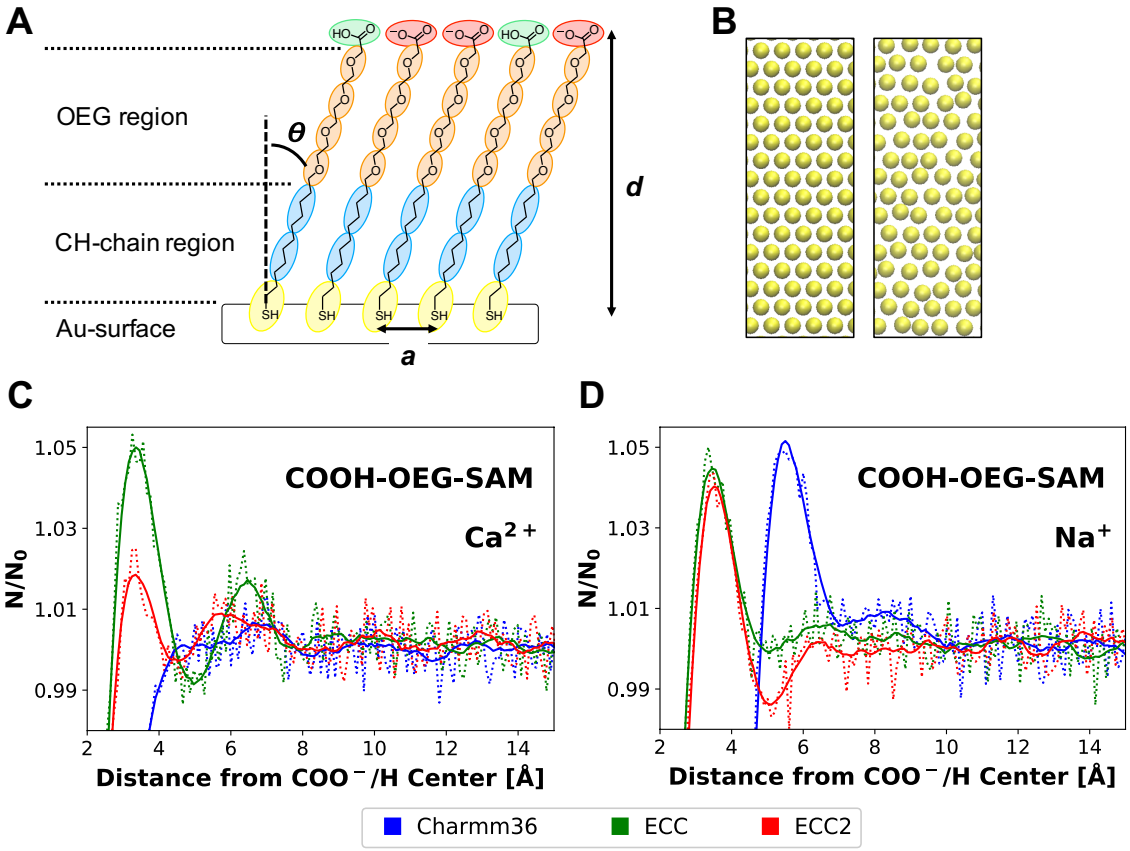


Figure 2.9 | Structure of OEG-SAM and Water Distribution Profiles Adjacent to an All Atom (AA) Model of OEG-SAM:. (A) Schematic structure of OEG-SAM, assembled onto the gold-sputtered surface, including the chemical structure and CG mapping schemes of the SAM molecules. Colours represent different Martini beads. Yellow: SC5, blue: C1, orange: SN0, red: SQn, green: SP2. Calculated parameters like thickness (d), lattice constant (a) and tilt angle (θ) of the OEG-SAM are indicated. **(B)** Bottom view of the initial positioning of the SC5-beads of the SAM-molecules along a hexagonal grid (left), as well as after a 60 ns CG production simulation (right). **(C, D)** N/N_0 water molecules along surface normal with N being the number of molecules at given z-position and N_0 the bulk concentration as average of number density above 4 nm away from the surface. **(C)** Results for samples with 400 mM Ca^{2+} and **(D)** with 400 mM Na^+. Different colours represent three applied CHARMM36 force field parameters (see methods for details): Standard (blue), ECC (green), ECC2 (red). Zero on the x-axis is equal to the centre of mass of the OEG-SAM carboxyl groups.

Three replicas each of 60 ns production time for 48 different initial configurations were carried out. The lattice constant <a>, tilt angle θ of the alkane thiol chain (estimated via order parameters between the thiol-bead and the upper CH-chain-bead <$S_{THI\text{-}C1B}$>), the monolayer thickness <d> and the surface hydrophilicity <η> were monitored to characterize the resultant OEG-SAM compared to experiments.

The averaged results of the last 50 ns of the CG production simulations are shown in Figure 2.10, with the errors representing the standard deviation between the three independent simulations of each system.

Charged SAM-COO^- and uncharged SAM-COOH molecules showed negligible differences in order parameters $<S_{THI\text{-}C1B}>$ within all OEG-SAM compositions (Figure 2.10, **A/B**). This explains why $<a>$ and $<d>$ seemed to be independent of the percentage of charged OEG-SAM molecules (Figure 2.10, **C/D**). Thus, for further simulations the 39% charged OEG-SAM was chosen, corresponding to the OEG-SAM used in NR at pH 7.2 employing the pKa value of carboxyl terminated SAMs predicted by previous studies.[249] However, $<d>$ and $<S_{THI\text{-}C1B}>$ showed a high dependency on a_0. Previous studies showed that with the Martini bead definition it is not possible to reproduce the experimental alkane thiol chain tilt angle of 20-35° [250], [251] while matching the experimental lattice constant of 4.97 Å [252] on gold (111).[253] This was resolved when converting the CG presentation into an all-atom (AA) representation by rescaling the *xy* coordinates by 0.93 $\times$. A tilt angle of 20-35° corresponds to 0.51–0.82 $<S_{THI\text{-}C1B}>$ which needed a_0 to be bigger than 5.1 Å (Figure 2.10, **A/B**). An initial lattice constant of 5.2–5.3 Å agreed well with the OEG-SAM thickness observed in NR (21–23 Å, Table 2.2 and Figure 2.10, **D**). The averaged $<a>$ showed the overall structural stability of the packing (Figure 2.10, **C**) and revealed that both a_0 of 5.2 and 5.3 Å converged due to minor rearrangements to 5.3 Å. Thus, an a_0 of 5.3 Å was chosen for further simulations. The hydrophilicity of the OEG-SAM seemed to be almost independent of a_0 (Figure 2.10, **E**).

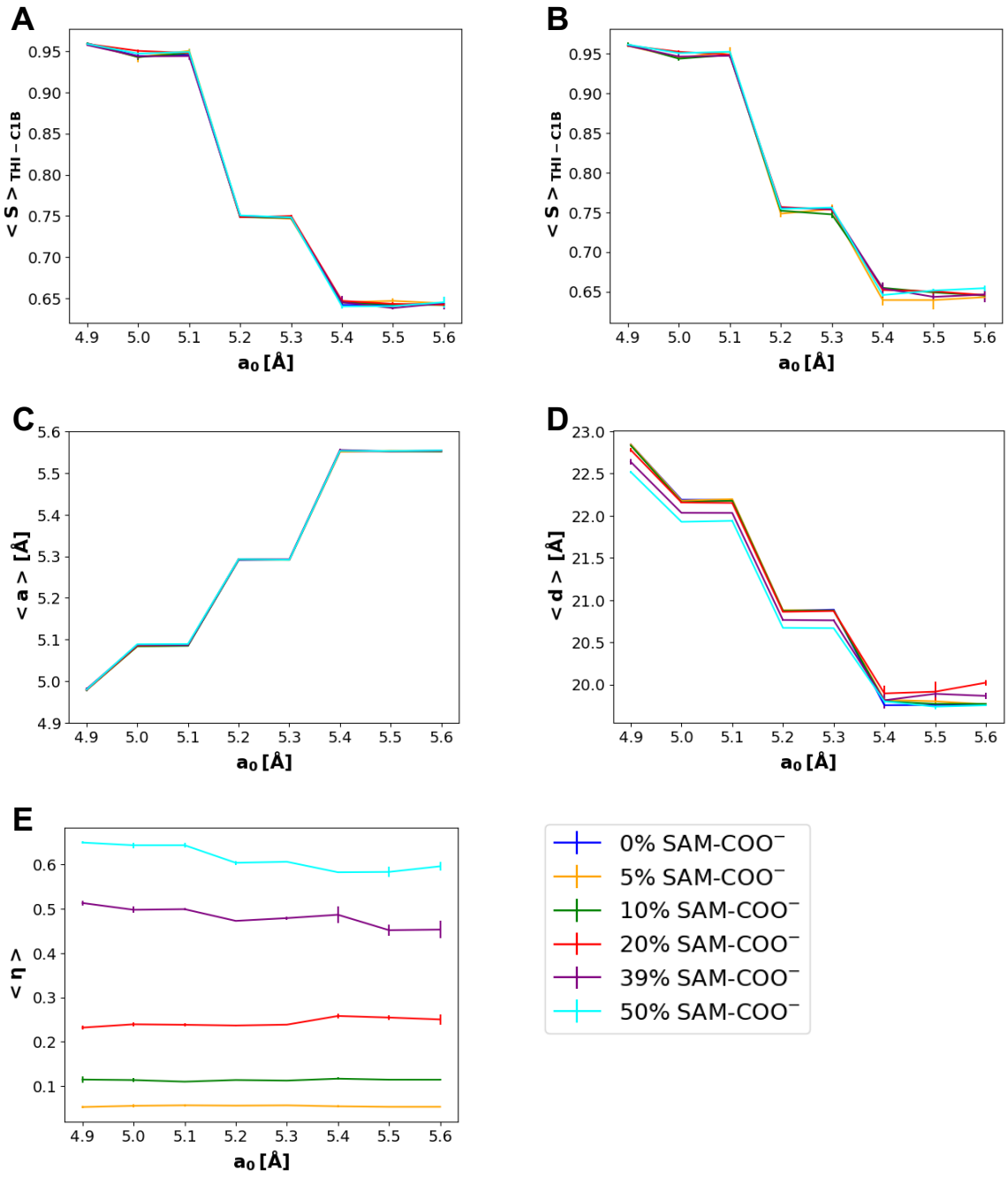


Figure 2.10 | Characterization of Coarse Grained (CG) OEG-SAM. Time and ensemble average of order parameters between thiol-bead and upper CH-chain-bead <$S_{THI\text{-}C1B}$> of the charged (COO^-) **(A)** and the uncharged (COOH) **(B)** SAM molecules in dependency of the initial lattice constant a_0. Time and ensemble average of the lattice constant <a> **(C)**, the thickness <d> **(D)** and the hydrophilicity <η> of the OEG-SAM **(E)** in dependency of a_0. All parameters were monitored for OEG-SAMs different in charge (see legend for percentage of charged (COO^-) SAM molecules). The colour code is identical between plots. The surface hydrophilicity was calculated using the GROMACS command SASA with Martini vdW-radii and a probe radius of 0.26 nm. For the calculation of the order parameters, the Martini Python script *do-order-gmx5.py* was used and for the SAM-molecule accordingly edited. As indicated in Figure 2.9 the thickness was defined as distance between the centre of mass of the thiol-beads (SC5) and the centre of mass of the carboxyl-beads (SQn and SP2).

The CG OEG-SAM was converted into an AA representation and simulated for up to 100 ns in the presence of different Na^+ and Ca^{2+} concentrations (see Figure 2.9 for the CG *versus* AA mapping schemes of the OEG-SAM molecules; see Figure 2.11 for an exemplary CG and AA frame of the OEG-SAM).

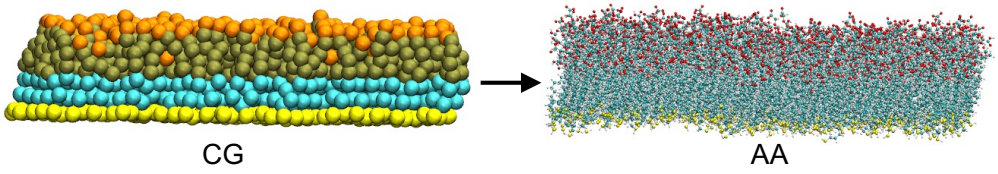


Figure 2.11 | Exemplary CG and AA Frame of OEG-SAM. The OEG-SAM was converted from CG (left) to AA (right) resolution. In the CG representation the bead containing the thiol-group is highlighted in yellow; the CH-region and the OEG-region is highlighted in cyan and brown, respectively; the terminating COO^-/H-group is colored in orange. For clarity the AA representation is colored by element: sulfur (yellow), carbon (cyan), hydrogen (light grey), oxygen (red).

To explore the robustness of our results to the parametrization of these ions we explored a number of variations, namely: CHARMM36 [254], the electronic continuum correction (ECC) within CHARMM36 [227], and a modified ECC version developed using CHARMM36, here called ECC2 [255]. In both, ECC and ECC2 the atomic lipid head group charges are scaled down to account for the missing electronic polarizability in the standard CHARMM36 force field. Additionally, in ECC2 also the lipid head group Lennard-Jones (LJ) potential is scaled (see methods for details). In order to maintain a finite cation concentration in the water phase during all conditions, the cation concentration was raised to 400 mM (see Figure 2.12). As anticipated, we observed oscillations in the water density close to the OEG-SAM surface, extending approximately four molecular water diameters away from the surface (Figure 2.9, **C/D**), in agreement with previous studies on OEG-SAMs.[256], [257]

The free energy profiles of Na^+ and Ca^{2+} binding at an all atom POPC membrane are very similar for the different force field parametrizations used, namely the ECC-, ECC2- and the standard CHARMM36-force field parametrization (Figure 2.13). However, with increasing amount of negatively charged lipids within the membrane the standard CHARMM36 force field caused stronger cation-binding compared to the ECC and ECC2 parametrization resulting in deeper minima of the free energy functions (Figure 2.13, **C-F**). ECC and ECC2 provided very similar free energy profiles across

all the different membranes. Therefore, the scaling of the head group charge seemed to override the effects caused by scaling the head group LJ potential.

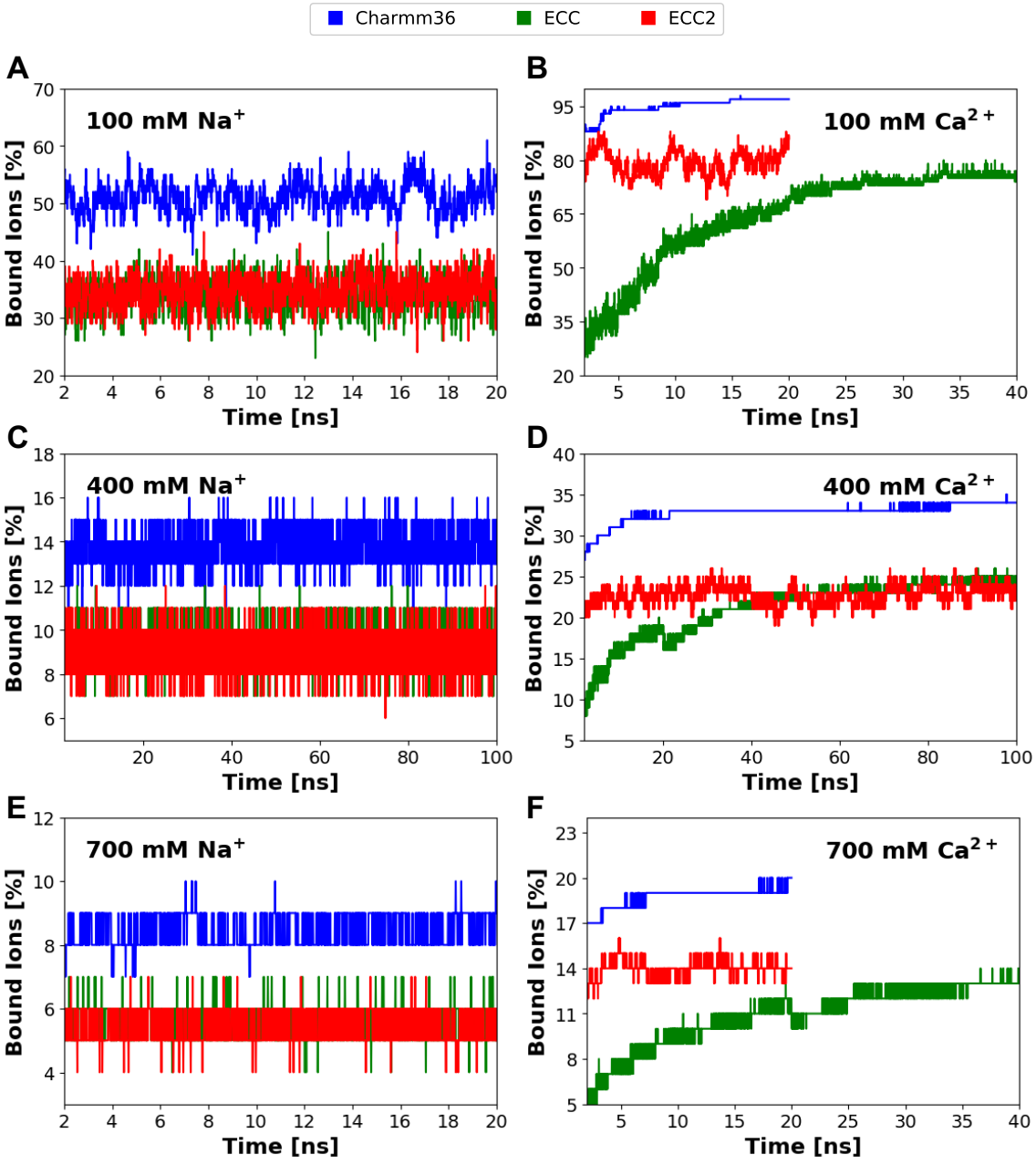


Figure 2.12 | Bound Cations to All Atom (AA) OEG-SAM over Time. Percentage of bound cations over simulation time for three applied CHARMM36 force field parameters: Standard (blue), ECC (green) and ECC2 (red). Cation concentration present in simulation box is given in each subplot. The cut-off set to define bound *versus* unbound states was 3.5 Å. Note the different scaling of axes between subplots. Profiles suggested significant stronger Na^+ and Ca^{2+} binding to the OEG-SAM in case of standard CHARMM36 compared to ECC and ECC2, whereas ECC and ECC2 seemed to be very similar in terms of ion affinity. The time necessary for obtaining the ion binding equilibrium was longer for ECC in comparison to ECC2. As shown in **(B)**, 100 mM Ca^{2+} bind almost completely to the OEG-SAM in case of standard CHARMM36. Therefore, simulations with 400 mM ion concentration, showing an equilibrium between bound and unbound ions, were used for calculating free binding energy profiles. Convergence was ensured by calculating the free binding energy profile over simulation time.

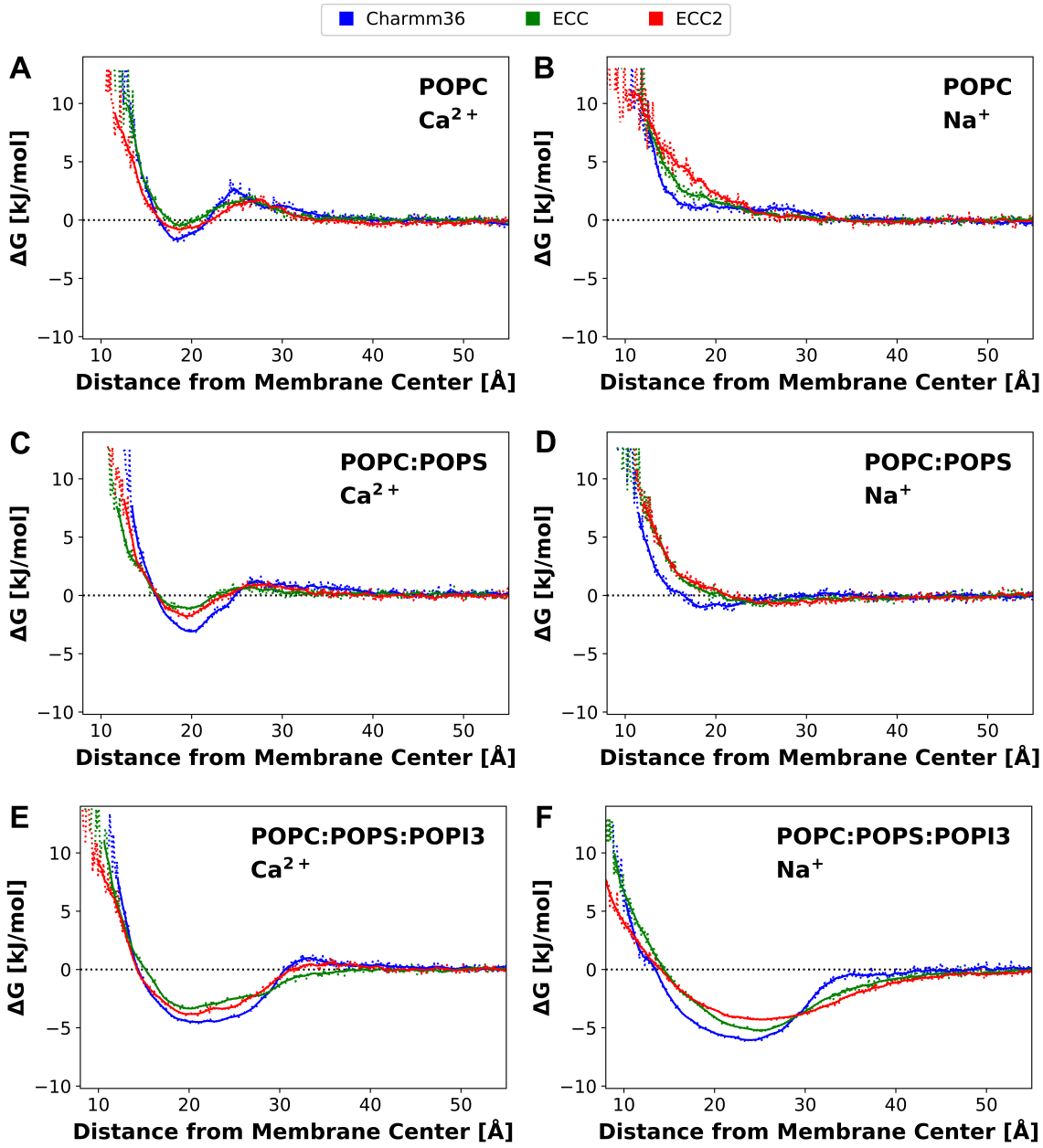


Figure 2.13 | Free Energy of Cation-Binding at All Atom (AA) Membranes. Calculated free energy profiles obtained by applying the Boltzmann equation to simulations in the presence of 400 mM Na^+ (right column) and 400 mM Ca^{2+} (left column) surrounding different membranes: **(A, B)** POPC, **(C, D)** POPC:POPS (8:2, mol:mol), **(E, F)** POPC:POPS:POPIP3 (7:2:1, mol:mol). Different colours represent three applied CHARMM36 force field parameters: Standard (blue), ECC (green) and ECC2 (red). Zero on the x-axis is equal to the membrane's centre of mass.

It is known that the binding of cations on phospholipids influence the net dipolar direction and potential of the membrane by changing the head group conformation.[258], [259], [238] Furthermore, it has been shown that these conformational changes in the head group can be related to cation

affinity.[228] Thus, in order to investigate which lipid species show differences in their cation affinity between the different force field parametrizations and therefore cause the differences we saw in the free energy cation-binding profiles (Figure 2.13), we determined the head group tilt angle for each lipid species, in each membrane and for the three different force field parametrizations (Figure 2.15, 2.16, 2.17). The head group tilt angle θ was defined as angle between the membrane normal (labelled as Z-axis) and a head group vector. For POPC and POPS the widely used P→N vector was defined as head group vector, which connects the phosphorus and nitrogen atoms in the head group moiety (Figure 2.14, **A/B**). Additionally, for POPS the P→C vector was defined as second head group vector, which connects the phosphorus and the carboxyl carbon atoms in the head group moiety (Figure 2.14, **B**). For POPIP3 the vector connecting the carbon atoms at position 1' and 4' of the inositol ring was defined as head group vector C1→C4 (Figure 2.14, **C**).

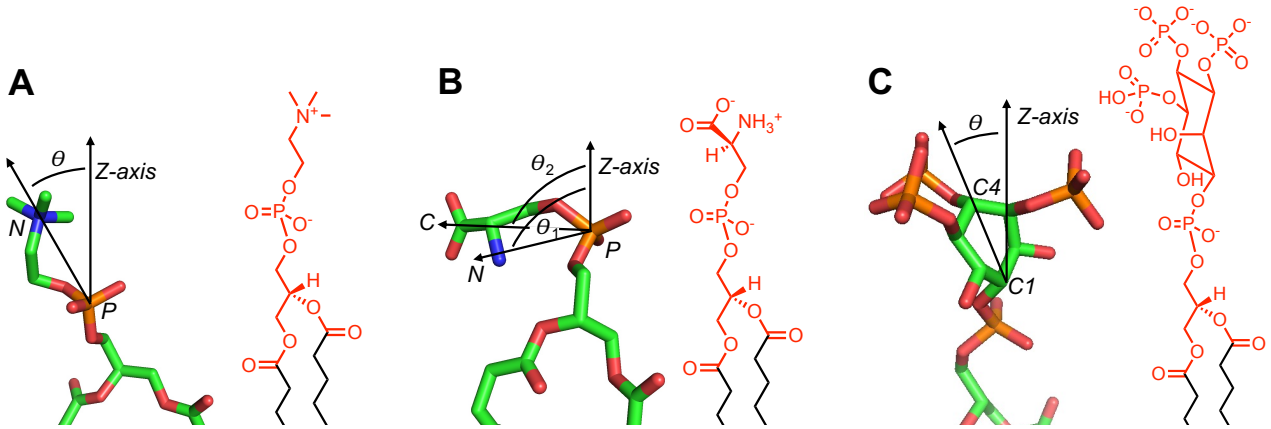


Figure 2.14 | Definition of Head Group Tilt Angles. The head group tilt angle θ was defined as angle between the membrane normal (Z-axis) and the head group vector. For POPC and POPS (**A, B**) the head group vector corresponds to the P→N vector, for POPIP3 (**C**) to the C1→C4 vector. A second head group vector P→C was defined for POPS (**B**). The red parts of the chemical head group structures represent the respective parts of the lipid species which were differently paramterized bewteen CHARMM36, ECC and ECC2.

POPC showed with a tilt angle of ∼55° (here the mode of the density distribution) in the presence of Ca^{2+} and of ∼65° in the presence of Na^{+} in POPC, POP:POPS (8:2, mol:mol) and POPC:POPS:POPIP3 (7:2:1, mol:mol:mol) no significant difference between the three force field parametrizations (Table 2.4, Figure 2.15). These values are in well agreement with previous studies.[228], [260] For POPS we observed in all membranes and all salt conditions a shift of both tilt angles towards higher values

for the CHARMM36 force field compared to the ECC and ECC2 (Figure 2.16, Table 2.5). This observation indicates that in a POPC/POPS membrane only the force field parametrization of the POPS lipids cause a difference in the cation-binding affinity of the membrane.

Membrane	**Lipid**	**Cation**	θ **P→N [°]**		
			CH36	**ECC**	**ECC2**
POPC	POPC	Ca^{2+}	55 ± 26	55 ± 28	49 ± 27
POPC:POPS (8:2)	POPC	Ca^{2+}	56 ± 26	56 ± 28	55 ± 28
POPC:POPS:POPIP3 (7:2:1)	POPC	Ca^{2+}	56 ± 26	55 ± 27	55 ± 27
POPC	POPC	Na^{+}	65 ± 27	64 ± 28	64 ± 28
POPC:POPS (8:2)	POPC	Na^{+}	67 ± 26	64 ± 28	65 ± 28
POPC:POPS:POPIP3 (7:2:1)	POPC	Na^{+}	65 ± 26	65 ± 28	65 ± 28

Table 2.4: | POPC Head Group Tilt Angles. Calculated mode of the head group tilt angle density distributions (Figure 2.15) for different membranes and different force field parametrizations, each system in presence of Ca^{2+} and Na^{+}. The errors correspond to the standard deviation. The head group tilt angle θ is defined as the angle between the bilayer normal and a head group vector. For POPC the head group vector P→N connects the phosphorus and nitrogen atoms in the phsophorylcholine moiety (Figure 2.14).

Looking at the tilt angle of the POPIP3 inositol ring in the POPC:POPS:POPIP3 (7:2:1, mol:mol:mol) membrane, the difference between CHARMM36 and the ECC-parametrizations became even more significant (Figure 2.17, Table 2.6). Especially in the presence of Na^{+} the head group tilt angle showed with 55° for the CHARMM36 force field *versus* 29° for the ECC-parametrizations a huge difference. In agreement with that, the free energy profiles of the Na^{+}-binding had the largest differences between the force fields for the POPC:POPS:POPIP3 membrane. The larger tilt angles of POPS and POPIP3 when using CHARMM36 seemed to lead to the higher cation-binding affinities, reflected in the deeper energy dips compared to the ECC-parametrizations (Figure 2.13).

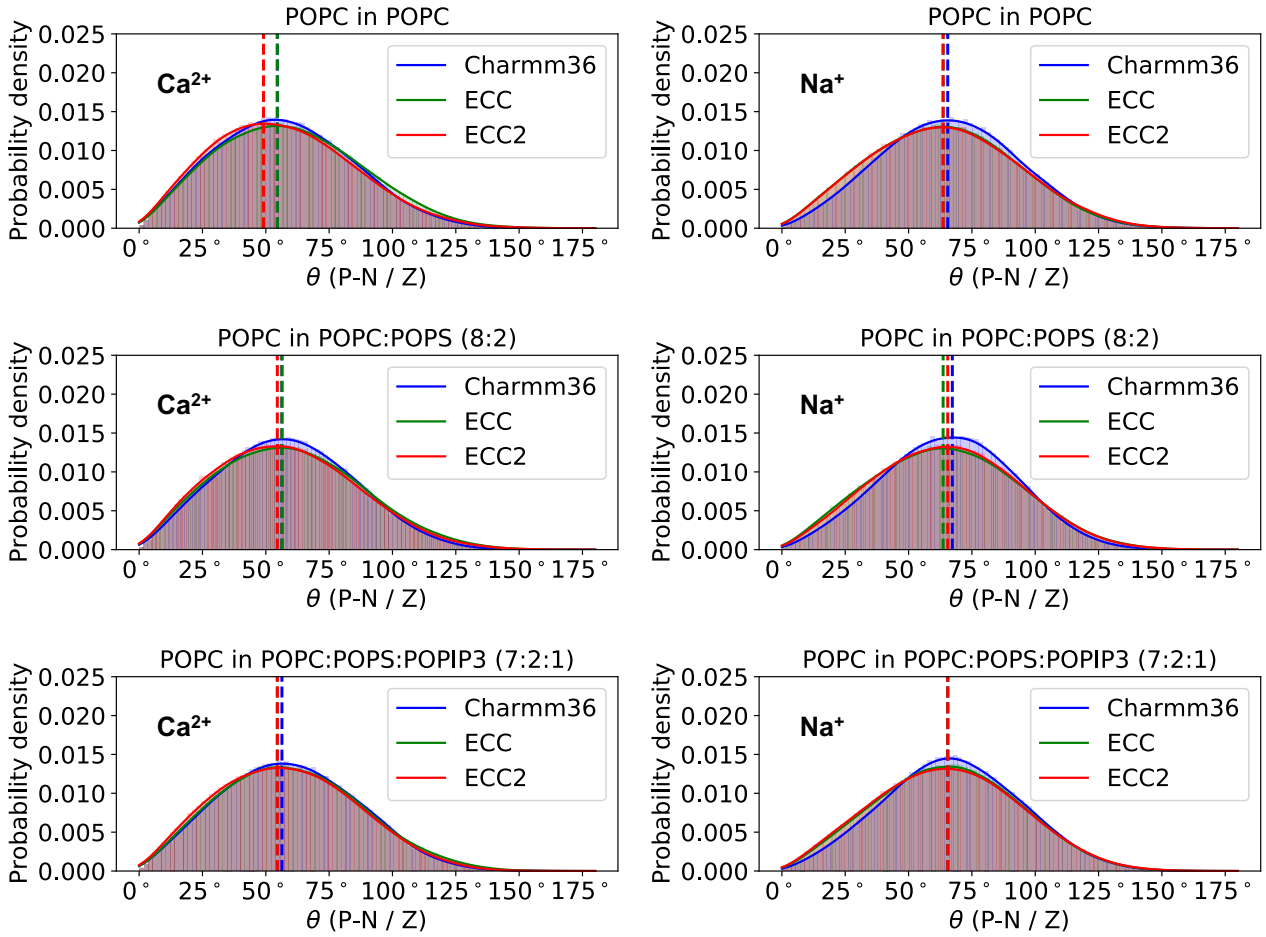


Figure 2.15 | POPC Head Group Tilt Angle Density Distributions. The probability density distributions for the tilt angle θ of POPC in the POPC, POPC:POPS (8:2, mol:mol) and the POPC:POPS:POPIP3 (7:2:1, mol:mol:mol) membrane were calculated as ensemble and time average over the final 5 ns of the production run. Shown are the distributions in the presence of Ca^{2+} (left column) and Na^{+} (right column). Different colours represent three applied CHARMM36 force field parameters: Standard (blue), ECC (green) and ECC2 (red). The vertical, dashed lines show the mode of the corresponding distribution (for values see Table 2.4).

Membrane	Lipid	Cation	θ P→N [°]			θ P→C [°]		
			CH36	ECC	ECC2	CH36	ECC	ECC2
POPC:POPS (8:2)	POPS	Ca^{2+}	58 ± 28	67 ± 28	65 ± 27	69 ± 21	51 ± 24	56 ± 24
POPC:POPS: POPIP3 (7:2:1)	POPS	Ca^{2+}	75 ± 28	56 ± 27	67 ± 28	69 ± 25	53 ± 24	60 ± 25
POPC:POPS (8:2)	POPS	Na^{+}	76 ± 26	67 ± 27	73 ± 27	55 ± 20	51 ± 22	51 ± 22
POPC:POPS: POPIP3 (7:2:1)	POPS	Na^{+}	71 ± 26	62 ± 27	69 ± 28	55 ± 20	47 ± 23	51 ± 23

Table 2.5: | POPS Head Group Tilt Angles. Calculated mode of the head group tilt angle density distributions (Figure 2.16) for different membranes and different force field parametrizations, each system in presence of Ca^{2+} and Na^{+}. The errors correspond to the standard deviation. The head group tilt angle θ is defined as the angle between the bilayer normal and a head group vector. For POPS there were two head group vectors defined: P→N, which connects the phosphorus and nitrogen atoms, and P→C which connects the phosphorus and the carboxyl carbon atoms in the head group moiety (Figure 2.14).

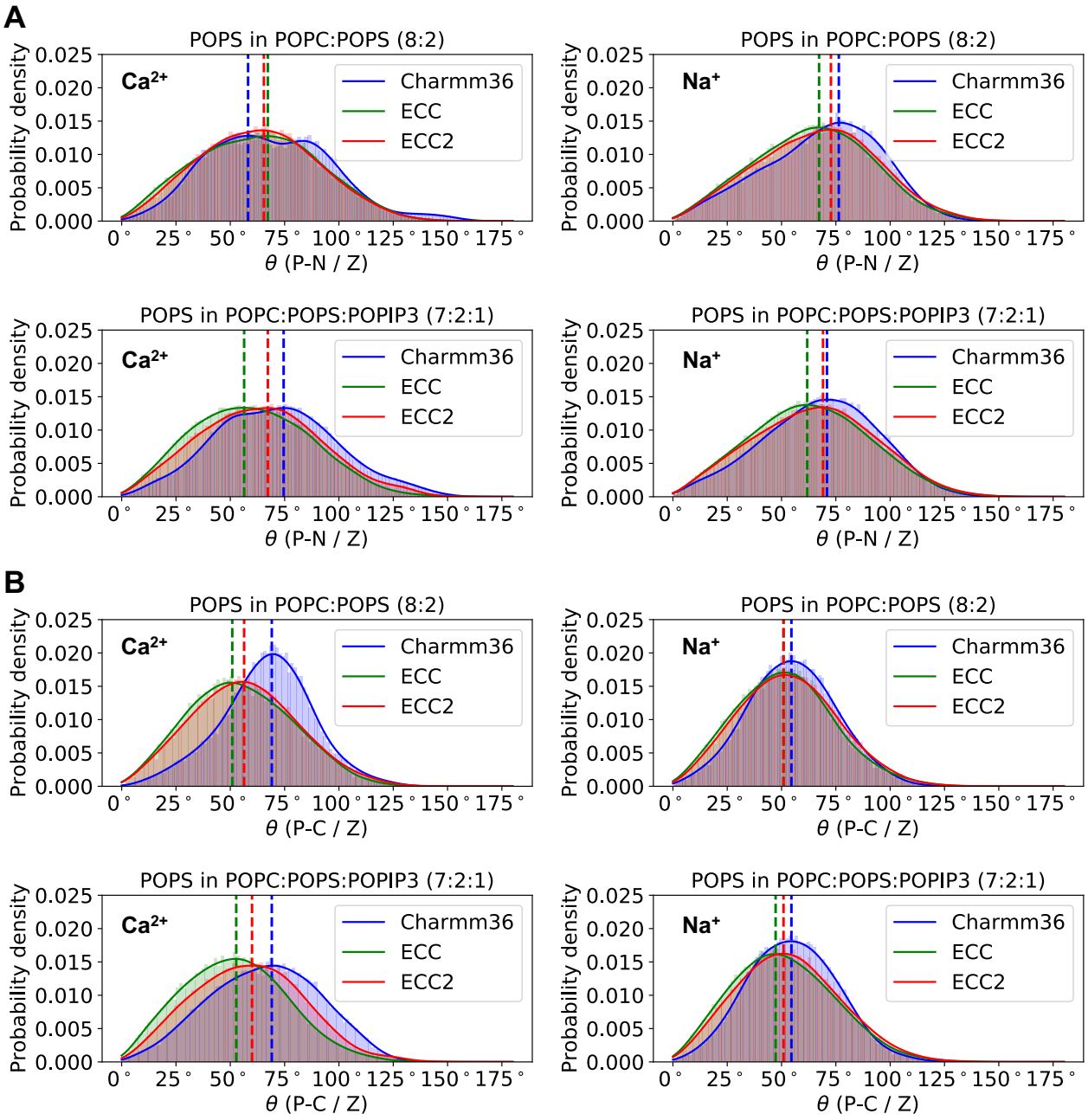


Figure 2.16 | POPS Head Group Tilt Angle Density Distributions. The probability density distributions for the tilt angle θ of POPS in the POPC:POPS (8:2, mol:mol) and POPC:POPS:POPIP3 (7:2:1, mol:mol:mol) membrane were calculated as ensemble and time average over the final 5 ns of the production run. **A** displays the distributions belonging to the P→N head group vector, **B** the distributions belonging to the P→C head group vector. Shown are the distributions in the presence of Ca^{2+} (left column) and Na^{+} (right column). Different colours represent three applied CHARMM36 force field parameters: Standard (blue), ECC (green) and ECC2 (red). The vertical, dashed lines show the mode of the corresponding distribution (for values see Table 2.5).

Membrane	Lipid	Cation	θ C1→C4 [°]		
			CH36	ECC	ECC2
POPC:POPS: POPIP3 (7:2:1)	POPIP3	Ca^{2+}	47 ± 20	31 ± 17	36 ± 21
POPC:POPS: POPIP3 (7:2:1)	POPIP3	Na^{+}	55 ± 21	29 ± 18	29 ± 17

Table 2.6: | POPIP3 Head Group Tilt Angles. Calculated mode of the head group tilt angle density distributions (Figure 2.17) for different membranes and different force field parametrizations, each system in presence of Ca^{2+} and Na^{+}. The errors correspond to the standard deviation. The head group tilt angle θ is defined as the angle between the bilayer normal and a head group vector. For POPIP3 the head group vector C1→C4 connects the carbon atoms at position 1' and 4' of the inositol ring (Figure 2.14).

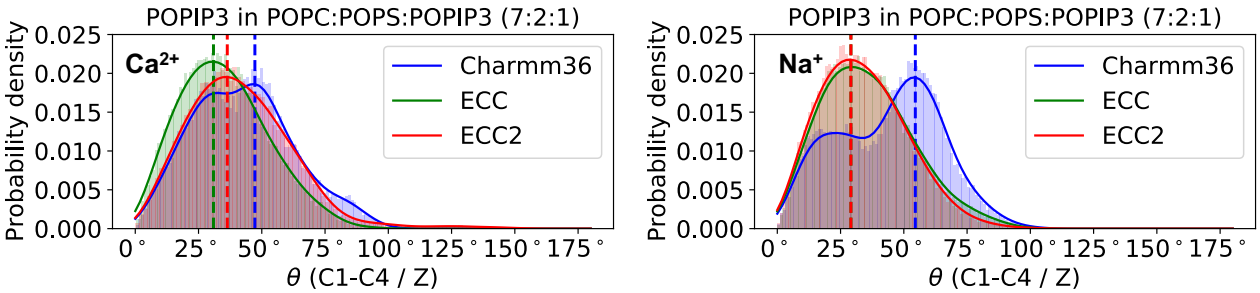


Figure 2.17 | POPIP3 Head Group Tilt Angle Density Distributions. The probability density distributions for the tilt angle θ of POPIP3 in the POPC:POPS:POPIP3 (7:2:1, mol:mol:mol) membrane were calculated as ensemble and time average over the final 5 ns of the production run. Shown are the distributions in the presence of Ca^{2+} (left column) and Na^{+} (right column). Different colours represent three applied CHARMM36 force field parameters: Standard (blue), ECC (green) and ECC2 (red). The vertical, dashed lines show the mode of the corresponding distribution (for values see Table 2.6).

.

But which one of the force field parametrizations came experimental values closest and was therefore recommended to use for further analysis of our experimental system? In a previous study the ECC-parametrization was applied to the Amber Lipid 17 force field.[228] In a direct comparison with NMR experiments, their ECC-lipid parameters gave much better results than the standard Lipid 17 force field. In their ECC-simulations of a POPC:POPS (5:1, mol:mol) membrane, the P→N vector of POPS was in the presence of 200 mM Na^{+} around 67° and in the presence of 200 mM Ca^{2+} around

64°. In both cases the standard Lipid 17 force field showed higher tilt angles but significant less agreement with NMR measurements.[228] These values agree well with our ECC- and ECC2-results (Figure 2.5). Furthermore, we observed the same pattern, the standard CHARMM36 force field had higher tilt angles compared to the ECC-parametrizations. Thus, based on these results we assumed that the standard CHARMM36 force field overestimates the cation-binding affinity to phosphilipid bilayers like the standard Lipid 17 force field does and that an ECC-parametrization provides significant improvement. With ECC and ECC2 showing very similar results, we decided to continue our analysis using the ECC2-parametrization as the time necessary for obtaining the ion binding equilibrium was significantly longer for ECC in comparison to ECC2 (Figure 2.12).

The minima of the free energy landscapes for Na^+ and for Ca^{2+} ions above the OEG-SAM, calculated with the ECC2-parametrization, were comparable with values of ∼6.7 and ∼6.8 kJ/mol (Figure 2.18, **A**), but with closer approach for Ca^{2+} (d_{MIN} = ∼2.3 Å for Ca^{2+} and ∼3.9 Å for Na^+). In each case there was a shoulder at ∼-1 Å suggesting a degree of penetration of cations between the OEG-carboxyl groups, as can be seen from the corresponding density profiles in Figure 2.19. However, for Ca^{2+} the potential well is steeper such that cation density extends for ∼7 Å from the carboxylates at the surface of the SAM, whereas for Na^+ the potential well is broader and bulk cation concentration is not reached until > 15 Å from the SAM surface. We carried out similar calculations for interactions of the cations with the various lipid bilayer surfaces (Figure 2.18, **B/C**). Two trends are seen: as was observed with the SAM, Ca^{2+} ions are more strongly localized at the surface than are Na^+ ions, corresponding to clear energy minima near the bilayer head groups and a steeper potential well for Ca^{2+}. Furthermore, a clear trend was observed in terms of the depth of the energy well for Ca^{2+} when comparing a zwitterionic POPC membrane with a modestly anionic POPC/POPS membrane and with a more markedly anionic POPC/POPS/POPIP3 membrane. With increasing average surface charge density from 0 e/nm^2 for the POPC, 0.3 e/nm^2 for the POPC/POPS to 1.2 e/nm^2 for the POPC/POPS/POPIP3 bilayer, the depth of the energy well intensified for Ca^{2+}. In agreement with this trend, the SAM showed, with a surface charge density of 1.9 e/nm^2, the deepest energy well for Ca^{2+} compared to the various bilayers. Significant Na^+ binding was only observed in the presence

of the highly negatively charged POPIP3 within the membrane. POPIP3 seemed to cause for Na^+, as well as for Ca^{2+} an intensified breadth of the energy well, suggesting strongly fluctuating binding. So, in the case of the POPIP3 containing bilayer, a clear Ca^{2+} ion density extending 10 Å and a clear Na^+ ion density extending 20 Å from the bilayer surface were observed.

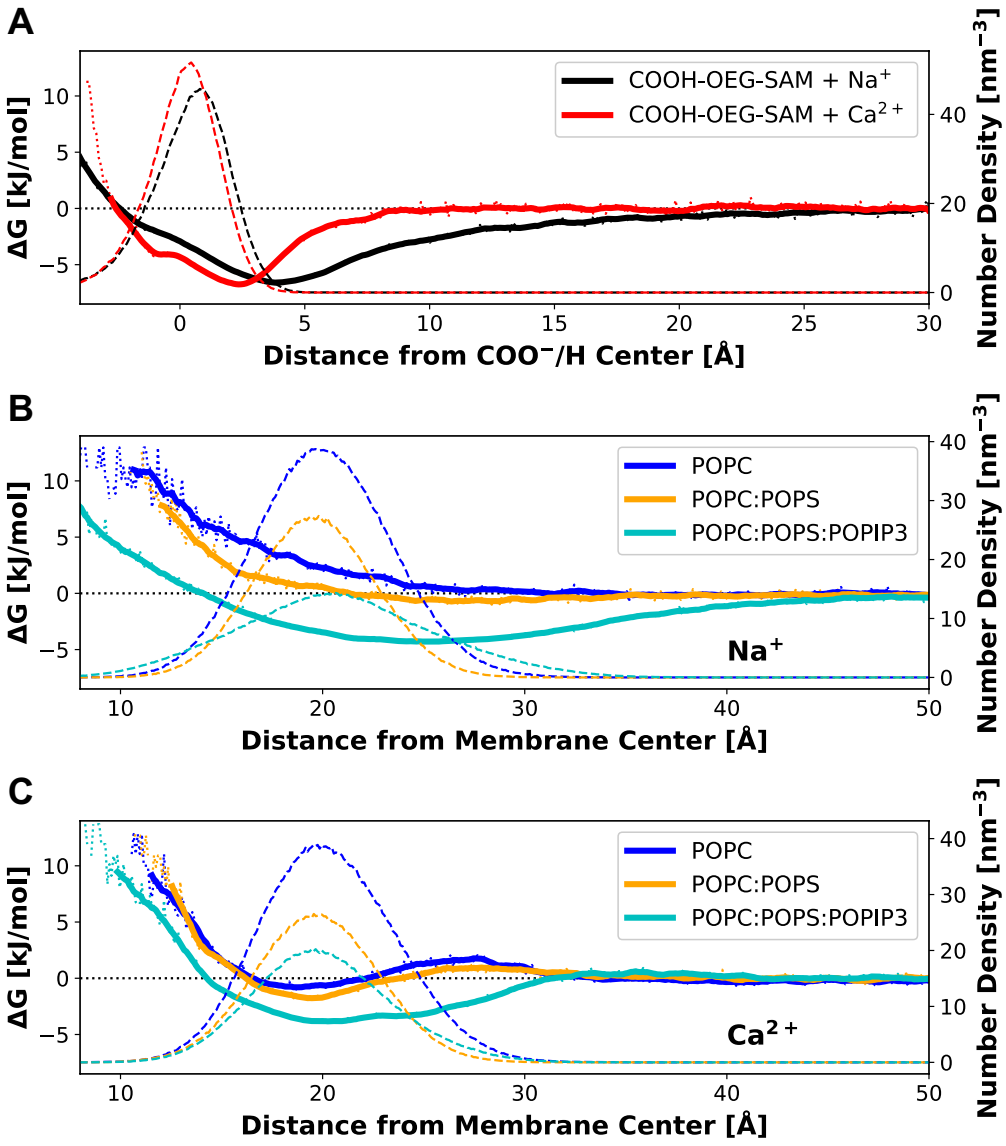


Figure 2.18 | Free Energy of Ion-Binding in All Atom (AA) Simulations of OEG-SAM and of Lipid Bilayer Membranes. **(A)** Free energy profiles for cation interactions with the OEG-SAM (solid lines). These were evaluated in the presence of 400 mM Ca^{2+} (red) and 400 mM Na^+ (black) using the ECC2 force field. Zero on the x-axis is equal to the centre of mass of the OEG-SAM carboxyl groups. Dashed lines represent the corresponding number density profiles of the terminal COO^-/H groups of the SAM molecules. **(B, C)** Free energy profiles for Na^+ **(B)** and Ca^{2+} **(C)** interactions with phospholipid bilayers (solid lines). The different colours represent the different bilayers: Blue: POPC, orange: POPC:POPS (8:2, mol:mol), cyan: POPC:POPS:POPIP3 (7:2:1, mol:mol:mol). Zero on the x-axis is equal to the centre of mass of the respective bilayer. Dashed lines represent the corresponding number density profiles of the lipid head groups, including the inner phosphates.

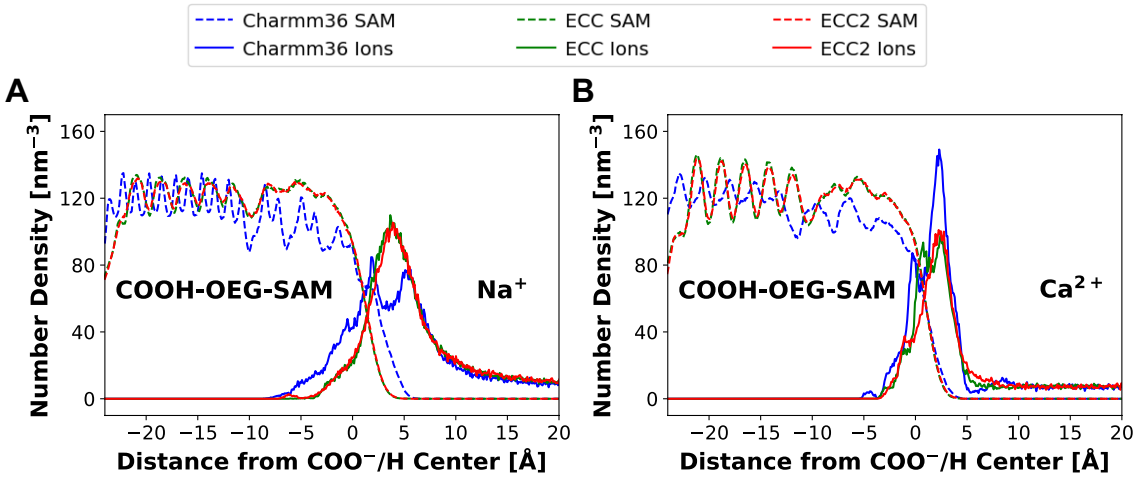


Figure 2.19 | Partial Densities of All Atom (AA) OEG-SAM. Number density profiles of OEG-SAM (dashed lines) and respective cations (solid lines; **(A)** 400 mM Na^+, **(B)** 400 mM Ca^{2+}) along surface normal. Different colours represent three applied CHARMM36 force field parameters: Standard (blue), ECC (green) and ECC2 (red). Zero on the x-axis is equal to centre of mass of the SAM carboxyl groups. In order to visualize the density profiles of the ions, their density was multiplied by 40. Zero on the x-axis is equal to the centre of mass of the SAM carboxyl groups. ECC and ECC2 provided very similar cation number density profiles. By contrast, the standard CHARMM36 force field revealed stronger Ca^{2+}-binding and deeper penetration of Na^+-cations resulting in a higher peak for Ca^{2+} and a broader distribution for Na^+ compared to ECC and ECC2.

2.3 Discussion

The NR results reveal a clear trend in bilayer-to-SAM distance depending on the salt solution present between the OEG-SAM and the lipid bilayer. These trends were similar for a simple POPC and more complex and biologically relevant POPC:POPS, POPC:POPS:DOPIP3, and POPC:POPS:Chol:DGDG free floating membranes (FFMs). All four samples yielded a close approach of the FFM to the OEG-SAM surface in the presence of 2 mM $CaCl_2$. In the absence of additional cations, a separation of > 200 Å was observed. In the presence of 200 mM NaCl an intermediate separation distance was observed, this being greater for the anionic membranes and less for the zwitterionic POPC membrane. These results suggest attraction between bilayer and OEG-SAM is greatest in the presence of Ca^{2+}, with a weaker attraction in the presence of an elevated concentration of Na^+.

The interplay of four main intermolecular forces is thought to control the distance between the FFMs and the OEG-SAM surface: van der Waals (vdW) forces give rise to weak yet long range attraction

between the bilayer and the surface [134], whilst entropic Helfrich fluctuational forces [135], as well as hydration forces can produce a repulsion between the OEG-SAM and the FFM.[136], [137] Electrostatic forces can produce short range attractive or repulsive interactions depending on the surface charge of the SAM and the FFM.[134], [138] As both the membrane head groups and the OEG-SAM surface contained ionizable groups and given the salt solution effects it was inferred that the predominant cause of these effects were changes in electrostatics interactions of the system under differing conditions.

The MD results allow us to integrate these experimental results with an underlying molecular model of the OEG-SAM/FFM system (Figure 2.20). Simulations showed a layer of increased Ca^{2+} concentration above the SAM surface with a thickness of around 7 Å and above various FFMs with a thickness of 5 to 10 Å (Figure 2.18). Therefore, the full width of the aqueous layer between the SAM and the bilayer surfaces observed by NR (11 to 16 Å) will contain an elevated concentration of Ca^{2+}. Note that this would accommodate the three to four water layers seen at the SAM surface (Figure 2.9). A coarse grained model of this resultant system is shown in Figure 2.20, **B**. From this integrative model it is evident that the Ca^{2+} ions are potentially able to bridge between the anionic carboxyl groups at the OEG-SAM surface and phospholipid head groups. In the absence of any cations, the attractive vdW forces seem to be large enough to stay in equilibrium with the repulsive electrostatic, entropic and hydration forces, and therefore to prevent the membrane from floating away. We suggest that due to multiple interacting, aligned dipoles in a FFM system, the effective range of induced dipole-dipole forces, resulting in attractive vdW forces is increased, allowing even unexpectedly large distances between FFM and OEG-SAM. It will be of interest to examine the dynamic behaviour of water and Ca^{2+} ions within this nanoconfined salt solution layer in more detail by all atom MD simulations. Applying hereby different ion parametrizations, as well as different water models will be of particular interest. In the case of Na^{+} the much weaker binding, especially to the membrane surfaces suggests a less intensified bridging effect of the interlayer cations, too small to overcome the repulsion force between the OEG-SAM and FFM resulting in the intermediate position of the FFM (Figure 2.20, **A**). Additional all atom MD simulations comparing the behaviour of Na^{+} with that of Ca^{2+} within the area between OEG-SAM and FFM will be necessary to confirm the predicted molecular

model. Nevertheless, our model and results promise an important step forward in gaining a precise understanding of the complex forces which control this novel sample system and in uncovering the elegant mechanism for membrane-to-surface distance control described here.

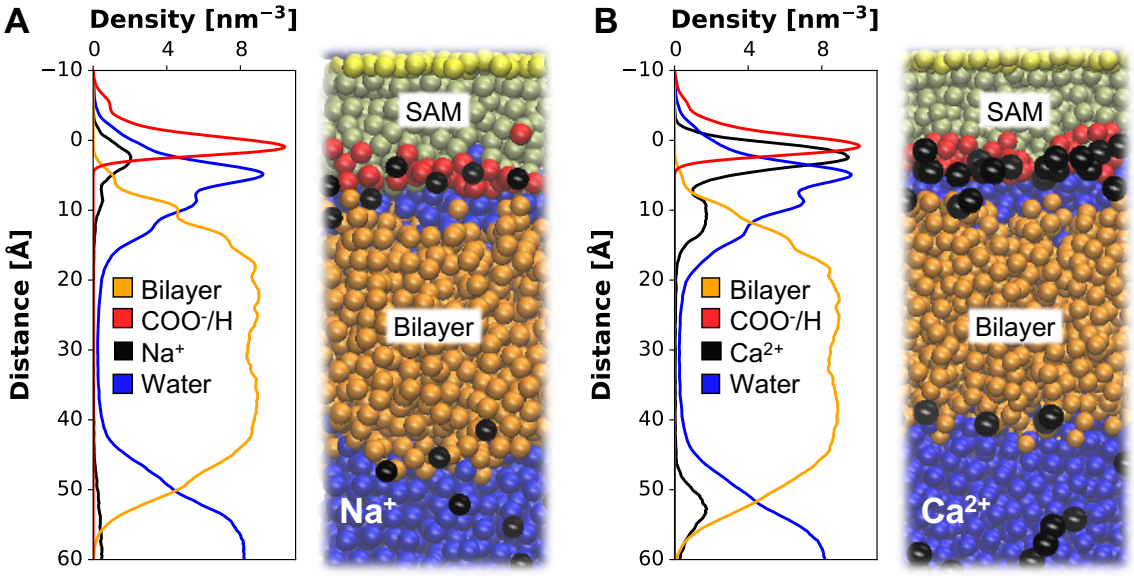


Figure 2.20 | Coarse Grained Free Floating Bilayer System. OEG-SAM and a POPC:POPS (8:2) membrane were initially separated by a 12 Å water layer in the presence of 400 mM Na^+ **(A)** or Ca^{2+} **(B)**, respectively. The bilayer had a hole with a diameter of 2 nm through which ions and water could pass the membrane. After 1 µs production run the number density profiles of the cations and water were determined. Zero on the y-axis is equal to the centre of mass of the OEG-SAM carboxyl groups. In order to visualize the density profiles of the ions, their density was multiplied by 10. The Ca^{2+} showed a significantly stronger binding to both SAM and bilayer in comparison to Na^+. The density profile of Ca^{2+} (**B**, black) suggests that Ca^{2+} ions bridge between the anionic OEG-SAM and the phospholipid surface. However, the week binding of Na^+, especially to the bilayer (**A**, black), might cause a too small bridging effect in order to overcome the repulsive force between the anionic SAM and an anionic membrane. Again, the hydration layers above the SAM are observable in both cases (**A/B**, blue).

2.4 Materials and Methods

2.4.1 Materials

POPC (1-palmitoyl-2-oleoyl-*sn*-glycero-3-phosphocholine), POPS (1-palmitoyl-2-oleoyl-*sn*-glycero-3-phospho-L-serine), DOPIP3 (1,2-dioleoyl-*sn*-glycero-3-phospho-(10-myo-inositol-3',4',5'-trisphosphate) and DGDG (digalactosyldiacylglycerol, plant origin) were obtained from Avanti polar lipids (Alabaster, AL, USA) and used without further purification. OEG-SAM (HS-C_{11}-EG_3-OCH_2-COOH) was

obtained from ProChimia surfaces (Gdansk, Poland). The chemical structure of the OEG-SAM molecule is given in Figure 2.21. D_2O (Deuterium oxide), Chol (cholesterol, from sheep's wool) and HEPES sodium salt (N-(2-Hydroxyethyl)piperazine-N'-(2-ethanesulfonic acid) sodium salt) were sourced from Sigma-Aldrich (Gillingham, UK). $CaCl_2$ (Calcium chloride), NaCl (sodium chloride) and EDTA (Ethylenediaminetetraacetic) were sourced from Fisher Scientific (Loughborough, UK). Silicon substrates were obtained from Crystran (Poole, UK) as a bespoke request.

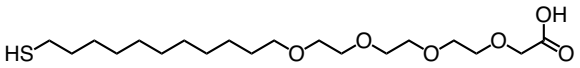


Figure 2.21 | Chemical Structure of OEG-SAM Molecule.

2.4.2 Neutron Reflectometry (NR) Measurements

NR measurements were carried out using the white beam SURF [261] and CRISP [262] reflectometers at the ISIS Spallation Neutron Source, Rutherford Appleton Laboratory (Oxfordshire, UK), which use neutron wavelengths from 0.5 to 7 Å and 0.5 to 6.5 Å, respectively. The reflected intensity was measured at glancing angles of 0.35°, 0.65° and 1.5° for both instruments. Reflectivity was measured as a function of the momentum transfer Q_z, with $Q_z = (4\pi sin\theta) \ / \ \lambda$ where λ is the neutron wavelength and θ the incident angle. Data were obtained at a nominal resolution $(dQ \ / \ Q)$ of 3.5%. The total illuminated sample length was $\sim$ 60 mm on both instruments. Details of the liquid flow and liquid chromatography setup used in the experiments describe here are described in a previous article.[263] Briefly, solid liquid flow cells were placed onto the instrument sample position and connected to instrument controlled HPLC pumps (either a Hitachi L-7100 on SURF or a Knauer Smartline 1000 on CRISP) which control the change of solution isotopic contrast in the flow cell, as well as the change in solution counter ion concentration and type.

Gold and Permalloy Coating of Silicon Crystals

Piranha acid cleaned silicon crystals (50 $\times$ 80 $\times$ 15 mM) with a polished 80 $\times$ 50 mm surface (111 orientation, root mean square surface roughness of $\sim$ 3 Å) were sequentially sputter coated with

permalloy ($Ni_{80}Fe_{20}$) and gold at the NIST centre for Nanoscience and Technology, Gaithersburg, MD, USA, in a Denton Discovery 550 sputtering chamber. Permalloy was used to bind the gold layer to the silicon substrate as its high neutron scattering length density (SLD) benefits the analysis of the NR data.[264]

Self-Assembled Monolayer Coating of Gold Surfaces

Gold and permalloy coated silicon substrates were cleaned by UV-ozone cleaning followed by washing with ultra-pure water, drying and a second UV-ozone cleaning procedure. Solutions of OEG-SAM molecules were prepared by dissolving this material in absolute ethanol (> 99.8% purity) to a concentration of 70 mM. The cleaned substrates were then incubated in this solution for 48 h in a low light environment at room temperature. After this time the substrates were removed from the thiol containing solution and sequentially washed with ethanol and water before drying under nitrogen. The OEG-SAM coated substrates were assembled into ISIS facility standard solid/liquid flow cells while completely submerged in water to prevent air entrapment. Images and a description of this process and the cells used can be found in this review.[143] Once assembled, the cells were stored at 4 °C prior to analysis of the solid/liquid interface by NR.

Surface Structure Measurements

Initially NR measurements of the OEG-SAM/gold/permalloy coated substrates were conducted under two solution isotopic contrast conditions (H_2O and D_2O). Upon confirmation of homogenous OEG-SAM coated gold surfaces with suitable surface coverage (> 95%), free floating membrane (FFM) fabrication took place.

Free Floating Membrane (FFM) Fabrication

Small unilammelar vesicles (SUVs) were prepared by dissolving phospholipids in $CHCl_3$ and evaporating the solvent under a stream of nitrogen to produce a lipid cake of 6 mg of lipid mass which was further dried under vacuum for 12 h. The dry lipid cake was then immersed in the deposition buffer solution (20 mM HEPES, 2 mM $CaCl_2$ pH/D 7.2) and bath sonicated to produce a vesicle suspension with

a lipid concentration of 1 mg/mL. This suspension was then ultrasonicated to produce SUVs. The formation of FFMs by vesicle rupture onto OEG-SAMs has been described previously.[133] Briefly, the concentration of the SUV suspension was reduced to 0.2 mg/mL and again ultrasonicated. This last step of sonication was always conducted less than 15 min before the SUV suspension was injected into the solid/liquid flow cells using prewashed disposable syringes at room temperature ($\sim$ 20 °C). The flow of the solution was reversed after two cell volumes were injected into the solid/liquid cell and ran in reverse for another two cell volumes ($\sim$ 6 mL assuming a 3 mL liquid volume in the solid/liquid flow cells). This process was iterated at least twice. The formation of the bilayers adjacent to the OEG-SAM coated gold surface was monitored by NR, specifically looking for changes in the Kiessig fringe spacing in the low Q regime (less than 0.05 $Å^{-1}$). A new set of fringe spacings, with a new minimum at $\sim$ 0.03 $Å^{-1}$ signified the formation of the FFM adjacent to the SAM/water interface. Upon FFM formation, the samples were flushed with deposition buffer (20 mM HEPES, 2 mM $CaCl_2$ pH/D 7.2) to remove non-surface bound material and heated to 38 °C. Then, the vesicle suspension was reinjected, and the sample incubated for $\sim$ 2 h at 38 °C. Finally, deposition buffer solution was flushed through the cells to remove the excess vesicles, followed by the structural examination of the resulting interfacial assemblage by NR.

Isotopic Contrast Variation Strategy

The samples measured are composed of hydrogenous lipids adjacent to hydrogenous SAMs grafted onto a gold surface. To gain maximum information on the membrane coverage and position relative to the OEG-SAM/water interface it was therefore necessary to measure the samples in D_2O buffer solutions, as this produced a series of layer interfaces, SAM/water-, water/membrane- and membrane/bulk water-interlayer, which had high SLD differences. These interfaces encoded high amplitude fringes in the experimental data and allowed for unambiguous resolution of the interfacial architecture upon data analysis. It has been previously shown that the idealized labelling strategy of a hydrogenous SAM, deuterated water interlayer, hydrogenous membrane and deuterated bulk water allowed for the solution interlayers between the OEG-SAMs and FFMs to be adequately resolved.[133]

Therefore, here, for every sample condition the surface assemblage was measured in D_2O and 75% D_2O / 25% H_2O (gold matched water, AuMW) buffer solutions, with both solution contrast conditions being highly sensitive to the overall FFM and OEG-SAM structure, as well as the water interlayer between them. Additionally, a H_2O solution isotopic contrast was obtained for each experimental condition measured, as under this solution condition the OEG-SAM molecules, lipid tails and the water interlayer are essentially contrast matched, meaning the position of the lipid head groups can be resolved independently. Due to the large amount of data obtained in this study, only the D_2O data sets are shown for all samples as these are most sensitive to the FFM-to-SAM distance.

Neutron Reflectivity Data Analysis

Neutron reflectometry data were analysed using the Python library refnx (v.0.1.16.).[159], [265] Refnx enables to define custom models of interfacial structures, from which parameters feed into the Abelès reflectivity model.[154], [266] The model consisted of six slab objects, describing the four layers of the substrate (Si, SiO_2, permalloy, gold), the OEG-SAM and the water interlayer between OEG-SAM and membrane. Each slab was characterized by its SLD, thickness and roughness, with the Névot–Croce approach used to describe the roughness.[267] To estimate the coverage of the OEG-SAM, there was an additional flexible parameter defined for the slab of the OEG-SAM, modelling the intercalated volume fraction of solvent. The slab objects had a calculated SLD, which was fixed except for the slab of SiO_2, permalloy and the water interlayer. To define the membrane in the model, two LipidLeaflet objects were used. Each LipidLeaflet was made of two slabs, describing a lipid head group and a lipid tail layer. One head group layer formed an interface with the water gap, facing towards the surface, the other an interface with the bulk water, facing away from the surface. The head and tail components had a fixed SLD and volume parameter, summarized in Table 2.7. These parameters provided head and tail layers with a given thickness, whereby its roughness and intercalated volume fraction of solvent depended on the modelled area per molecule. To ensure that the number of head and tail components were equal, the area per molecule was set to be the same for the head and tail layers.

Throughout the analyses, the instrument resolution, as well as the parameters of the substrate (Si, SiO_2, permalloy, gold) and the OEG-SAM were set to be equal across all data sets obtained for one membrane sample, meaning across varying salt solution conditions and different isotopic contrasts. Therefore, to further constrain the fitting of the substrate and OEG-SAM, reflectivity data sets were obtained for the OEG-SAM/gold/permalloy coated silicon surfaces without the presence of the bilayer at the bulk interface. Each of these OEG-SAM/substrate only data sets was simultaneously fitted with the data sets, in which the membrane was present above the respective OEG-SAM/gold/permalloy coated silicon surface at varying salt solution conditions. Only the presence and position of the membrane was varied between the simultaneously fitted data sets, leading to unique, low ambiguity solutions for the interfacial structures. Note, each membrane data set included three (H_2O, D_2O, AuMW) and each OEG-SAM/substrate only data set two (H_2O, D_2O) solution isotopic contrasts, which were also fitted simultaneously. The fitting parameters across the different isotopic contrasts of each data set were set to be equal. Only the SLD of the solvent, the scale factor and the background were allowed to vary for each isotopic contrast independently.

The best fit to the data was obtained by applying the differential evolution method, provided to refnx by the scipy library.[268] Then, the probability distribution function for each parameter was estimated via the MCMC sampling method available to refnx from the emcee library.[269] Hereby, 200 walkers were used over 8000 iterations of equilibration and 100000 iterations of sampling. The sampled MCMC chain was thinned by 10000 steps, equivalent to the iteration number at which the autocorrelation function of the parameters reached zero.

2.4.3 Quartz Crystal Microbalance with Dissipation Monitoring (QCM-D) Measurements

QCM-D was performed using a Q-sense Q4 Analyzer QCM-D system (Gothenburg, Sweden). Sensors were washed with 0.5% sodium dodecyl sulphate solution, ultra-pure water and ethanol before being dried with a stream of nitrogen and UV-ozone cleaned for 25 min. The sensors were then incubated in a 60 mM solution of OEG in absolute ethanol ($\geq$ 99.8% purity)[274] for 48 h at room temperature,

Parameter	POPC	POPS	DOPIP3	POPIP2	Chol	DGDG
V_{head} [Å^3]	319 [265]	244 [270]	429 [271]	386 [271]	-	391 [271]
V_{tail} [Å^3]	944 [265], [272]	944 [265], [272]	944 [272]	944 [265], [272]	612 [273]	944 [272]
SL_{head} [Å]	6.00778e^{-4}	8.45773e^{-4}	15.59044e^{-4}	13.33594e^{-4}	-	10.28344e^{-4}
SL_{tail} [Å]	-2.66688e^{-4}	-2.66688e^{-4}	-0.7557e^{-4}	-2.66688e^{-4}	1.32910e^{-4}	0.90734e^{-4}

Table 2.7: Invariant lipid parameters within the model.

under low light conditions. The surfaces were washed with ethanol, ultra-pure water, dried with N_2 and mounted into the temperature controlled QCM flow cells at 20 °C, which were attached to a calibrated peristaltic pump and initially filled with 20 mM HEPES pH 7.2 buffer. A flow rate of 0.25 mL$\times$min^{-1} was used throughout, unless otherwise stated. Frequency and dissipation changes (Δf and Δd) were monitored using multiple harmonics (n = 3, 5, 7, 9, 11, 13) of the resonant frequency. However, for clarity, data are reported using the 3rd, 5th and 7th harmonics only (3rd only for the control measurements). A baseline was acquired for 5 min into 20 mM HEPES pH 7.2 buffer before the measurement was started. Buffer was exchanged into 20 mM HEPES, 2 mM $CaCl_2$ pH 7.2 prior to the injection of a 0.2 mg/mL POPC: POPS 8:2 (mol/mol) vesicle suspension in the same buffer. Vesicles were prepared in the same way as described for neutron reflectometry measurements. Once the Δf_3 (change in frequency of the 3rd harmonic) reached around -70 Hz the surface was washed with 20 mM HEPES, 2 mM $CaCl_2$ pH 7.2 buffer to remove excess vesicles leaving a membrane coated sensor surface. A final change in f_3 of ~ -25–30 Hz was observed for the formation of the FFB coated gold surface, in good agreement with previous observations on planar membrane systems.[176] One sensor was not incubated in the presence of vesicles but ran through the same changes of solution salt conditions as the membrane containing samples to act as a control in order to assess the frequency and dissipation response to changes in solution conditions. After bilayer formation the changes in frequency and dissipation upon changing the solution salt conditions between 2 mM $CaCl_2$, 1 mM EDTA and 200 mM NaCl were measured. Like with NR measurements, the membranes were first measured in 2 mM $CaCl_2$

containing 20 mM HEPES pH 7.2 buffer, then 1 mM EDTA, 200 mM NaCl and finally back into 2 mM $CaCl_2$ containing 20 mM HEPES pH 7.2 buffer. The process was repeated on the same samples at least twice to show repeatability. Experiments were repeated in triplicate and conducted by Dr Luke Clifton.

2.4.4 Molecular Dynamics (MD) Simulations

Coarse Grained (CG) Simulation Protocol

CG simulations were run using GROMACS 2019.1.[275] and the CG Martini force field, using the open beta 3.0.b.3.2 version.[207], [248] The systems were minimized with the steepest decent method, followed by 10 ps simulation in the canonical (NVT) ensemble and 200 ns in the isothermal-isobaric (NPT) ensemble with v-rescale temperature coupling at 308 K.[276] Semi-isotropic Berendsen pressure coupling was used for the NPT ensemble coupling at 1 bar with a time constant of 4 ps, normal compressibility of 4.5×10^{-5} bar^{-1} and lateral compressibility of 0 bar^{-1} for the OEG-SAM system or of 4.5×10^{-5} bar^{-1} for the various bilayer systems.[203] Finally, a 60 ns production simulation was run with v-rescale temperature coupling at 308 K and semi-isotropic Parrinello-Rahman barostat coupling at 1 bar with a time constant of 12 ps, normal compressibility of 3.0×10^{-4} bar^{-1} and lateral compressibility of 0 bar^{-1} for the OEG-SAM system or of 3.0×10^{-4} bar^{-1} for the various bilayer systems.[277] Van der Waals (vdW) interactions were shifted from 9 to 11 Å and electrostatics were described by the reaction field method, using a potential shift modifier with a cut-off of 11 Å. Bonds were constrained with the LINCS algorithm. The first 10 ns of the production simulation were considered as additional equilibration and therefore not included in the analysis. Data were analysed using VMD[278] or GROMACS[279]. Force field files are accessible via https://doi.org//10.5281/zenodo.4434613.

All Atom (AA) Simulation Protocol

AA simulations were performed using GROMACS 2019.1.[275] and three different force fields: standard (i.e. non-scaled) CHARMM36 [254], scaled ECC- [227] and ECC2-CHARMM36 [255] (for details see below). A force-switch modifier was used for the van der Waals forces and the Particle-Mesh-Ewald method for the electrostatics.[280] Dispersion corrections were turned off. First,

5000 steps of steepest decent minimization were performed. Second, the systems were equilibrated for 10 ps in the NVT ensemble and for 2 ns in the NPT ensemble. Finally, production simulations with 2 fs time step and virtual-sites on the SAM-molecules were run for up to 100 ns. V-rescale temperature coupling at 308 K [276] using a time constant of 0.1 ps and semi-isotropic Parrinello-Rahmen pressure coupling at 1 bar [277] with a time constant of 2 ps, normal compressibility of 4.5×10^{-5} bar^{-1} and lateral compressibility of 0 bar^{-1} for the OEG-SAM system or of 4.5×10^{-5} bar^{-1} for the various bilayer systems were applied. For the analysis the final 5 ns of the production simulations were considered. Data were analysed using VMD[278] or GROMACS[279]. Force field files are accessible via https://doi.org//10.5281/zenodo.4434613.

CG Simulation Setup

The implementation of the negatively charged COO^--SAM and neutral COOH-SAM molecule within the Martini3 force field [248] was achieved by fitting the results from CG MD simulations (bond length and bond angle distributions) to AA MD simulations with the CHARMM36 force field.[254], [281] The initial topology for the CHARMM36 was generated by using the CHARMM-GUI Ligand Reader and Modeler.[282] The provided parameter estimation from 1 μs AA simulations of COO^-/H-SAM in water (TIP3P) were taken for the CG simulations and refined if necessary (see Figure 2.22). Obtained parameters are listed in Table 2.8. Using standard Martini3 beads the mapping scheme between CG and AA resulted for both molecules in a SC5 bead for the thioethyl tail group, SN0 beads for the C-O-C-groups and C1 beads for each nbutyl group. The carboxyl head group was mapped into a SP2 bead for the neutral and into a SQn bead for the negatively charged state (see Figure 2.9).

Assembling the CG SAMs was based on an approach of a previous study.[253] Monolayers out of the implemented SAM molecules were built with a modification of the Python tool *insane.py* in a $105 \times 105 \times 130$ Å box.[283] The modifications of the script involved the introduction of the COOH-SAM and COO^--SAM matrix, as well as the positioning of the molecules onto a hexagonal lattice with a defined lattice constant. For the representation of the gold surface a flat surface model, used successfully earlier, was applied.[253], [284] Thus, the thioethyl tail beads of the SAM molecules

(SC5) were restrained to a plane with a harmonic force constant of 5000 kJ/(mol nm^2). The percentage of the randomly distributed negatively charged SAM-COO$^-$-molecules was either 0, 5, 10, 20, 39 or 50%. Only the required number of counter-ions in form of sodium and no additional salt concentration was added. For each differently charged system the initial lattice constant was varied between 4.9 and 5.9 Å in intervals of 0.1 Å, resulting in 48 different initial system setups. Each of these system setups was built and simulated three times independently.

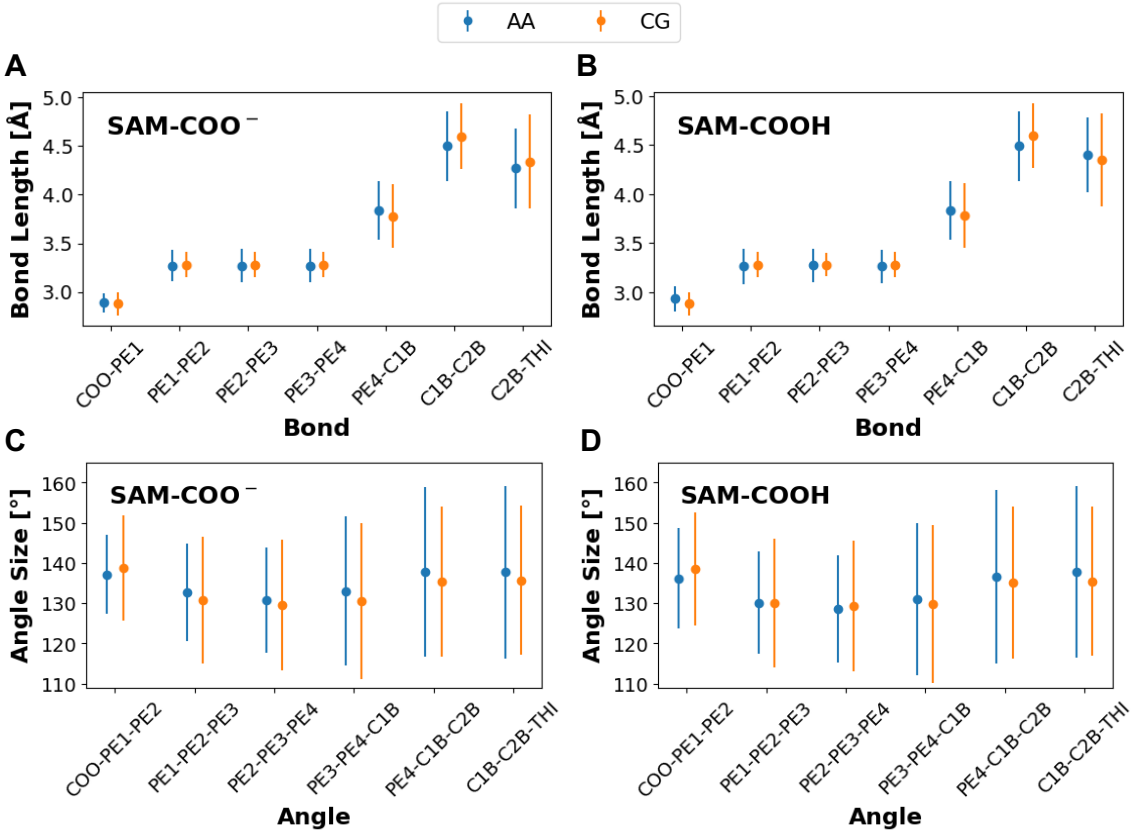


Figure 2.22 | Mapped Bond Length and Angle Distributions. Mean and standard deviation of bond length distributions of Martini3-CG (orange) and CHARMM36-AA (blue) charged (COO$^-$) **(A)** and uncharged (COOH) SAM-molecules **(C)**. Mean and standard deviation of angle distributions of CG (orange) and AA (blue) charged (COO$^-$) **(B)** and uncharged (COOH) SAM molecules **(D)**.

Group	Name	Bead-type	Ref.
carboxyl	COO	SQn or SP2*	[207], [248]
oxydimethylene 1	PE1	SN0	[253], [285]
oxydimethylene 2	PE2	SN0	[253], [285]
oxydimethylene 3	PE3	SN0	[253], [285]
oxydimethylene 4	PE4	SN0	[253], [285]
n-butyl 1	C1B	C1	[207]
n-butyl 2	C2B	C1	[207]
thioethyl	THI	SC5	[207], [248], [253]

Bond	r_0 [nm]	k_B [kJ/mol nm^2]	Ref.
COO-PE1	0.29	20000	this work
PE1-PE2	0.33	17000	[253], [285]
PE2-PE3	0.33	17000	[253], [285]
PE3-PE4	0.33	17000	[253], [285]
PE4-C1B	0.39	2500	this work
C1B-C2B	0.47	2500	this work, [207]
C2B-THI	0.45	1250	this work

Angle	θ_0 [°]	k_B [kJ/mol rad^2]	Ref.
COO-PE1-PE2	140	70	this work
PE1-PE2-PE3	130	50	[253], [285]
PE2-PE3-PE4	130	50	[253], [285]
PE3-PE4-C1B	140	25	this work
PE4-C1B-C2B	150	25	this work
C1B-C2B-THI	150	25	this work

Table 2.8: | Coarse Grained MD Simulation Parameters. Parameters for the charged SAM-COO^-- and uncharged SAM-COOH-molecule. *Bead type of carboxyl group depended on protonation state: for negatively charged, unprotonated carboxyl group SQn and for neutral, protonated carboxyl group SP2. Besides this difference charged and uncharged SAM-molecules were equal in their coarse grained parametrization.

The lipid bilayers were generated in a 105 × 105 × 200 Å box using the unmodified Python tool *insane.py*.[283] An exception was the membrane containing phosphatidylinositol (3,4,5)-triphosphate (DOPIP3). Here, the CHARMM-GUI Martini Bilayer Maker was used providing a box of 155 × 155 × 200 Å.[283] Simulations were performed for pure 1-palmitoyl-2-oleoylsn-glycero-3-phosphocholine (POPC), its mixture with 1-palmitoyl-2-oleoyl-sn-glycero-3-phospho-L-serine (POPS) (POPC/POPS 8:2, mol:mol) as well as its mixture with POPS and 1-palmitoyl-2-oleoyl-sn-glycero-3-phosphatidylinositol-(3,4,5)-triphosphate (POPIP3) (POPC/POPS/POPIP3 7:2:1, mol:mol:mol). Again, only the required number of counter-ions in form of sodium and no additional salt concentration was added.

For the multilayer system (Figure 2.20) the POPC:POPS (8:2 mol:mol) bilayer was first run separately in the presence of 400 mM Na^+ and of 400 mM Ca^{2+}. Hereby, the bilayer had a hole with a diameter of around 2 nm produced by a cylindric force constant of 1000 kJ/(mol nm^2), which only was applied to beads C3A and C3B of POPC and POPS being in a 2 nm environment around a chosen point at x = 35 Å and y = 35 Å. Then the OEG-SAM layer was run separately in the presence of 400 mM Na^+ and of 400 mM Ca^{2+}. Hereby, the x/y-dimensions of the box were set to be equivalent to the x/y-dimensions of the final frame of the bilayer simulation. Both layers were then added together

into a box with the given x/y-dimensions and z = 450 Å, separated by ∼12 Å. After solvating and evenly distributing 400 mM Na^+ or 400 mM Ca^{2+} across the water the system ran for 1 µs with a time step of 1 fs, lateral and normal compressibility of 0 and 3.0 × 10^{-4} bar^{-1}, respectively. The cation concentrations were calculated as [salt] = N_c × [water]/N_w, where N_c is the number of cations, [salt] the desired salt concentration, N_w the number of water molecules and [water] = 55.5 M.[228] The respective number of chloride ions was added for neutralization.

AA Simulation Setup

Following the CG production simulations AA simulations were performed in case of the individual layers. The conversion of the structure from CG to AA resolution was carried out with the Python tool *cg2at.py*.[211] Thereby the counter-ions were replaced with water. As there is no evidence of a favoured protonation site in case of POPIP3, equal amounts of the three different protonation states were included. Then, several calcium and sodium concentrations with respect to the number of water molecules present in the simulation box, were added, evenly distributed across the water. The cation concentrations were calculated as [salt] = N_c × [water]/N_w, where N_c is the number of cations, [salt] the desired salt concentration, N_w the number of water molecules and [water] = 55.5 M.[228] Finally, the number of chloride ions necessary for neutralization was added.

Besides the non-scaled standard CHARMM36 force field [254], two scaled CHARMM36 force fields with tuned charges and van der Waals radii were applied for each system. For the scaled ECC-CHARMM36 force field, the ECC-parameters were applied to the CHARMM36 POPC, POPS, POPIP3 and ion parameters.[226] Additionally, the ECC parametrization was expanded to the SAM molecules. Therefore, the SAM molecules were treated like ECC-lipids and the carboxyl-group together with the polyethylene-groups considered as the tuneable SAM head group (see Figure 2.23). The scaling factors of the SAM head group charges and LJ-sigma-parameters were set to be equal to the ECC-lipid scaling factors (f_q = 0.75, f_σ = 0.89). For the scaled ECC2-CHARMM36 force field only the van der Waals radii of the ions changed compared to ECC-CHARMM36. Here, in a previous study for CHARMM36 developed ECC-ion-parameters were applied.[255]

All ECC and ECC2 ion parameters are given in Table 2.9. Table 2.10 and 2.11 summarize the composition of all simulated AA SAM and AA membrane systems. The free energy landscapes were received by applying the Boltzmann equation. Firstly, N/N_0 was calculated using the number density profiles and calculating N_0 as average of number density above 40 Å away from the surface. Then, the free energy ΔG was calculated using following equation:

$$\Delta G = -RT \times In\,(N/N_0)$$

where R is the gas constant and T the temperature (here 308 K).

	ECC-force field			**ECC2-force field**		
	Ca^{2+}	**Na^{+}**	**Cl^{-}**	**Ca^{2+}**	**Na^{+}**	**Cl^{-}**
q	1.5	0.75	-0.75	1.5	0.75	-0.75
σ [Å]	2.16779	2.23717	3.17160	3.11814	2.86869	3.17160
ε [kJ/mol]	unchanged	unchanged	unchanged	0.0729968	0.0303006	unchanged

Table 2.9: | Ion-Parameters for ECC and ECC2 Force Field Parametrization. Values for charge (q), Lennard-Jones (LJ) -sigma (σ) and LJ-epsilon (ε) used in respective force field. Unchanged means that the standard CHARMM36 value was used.

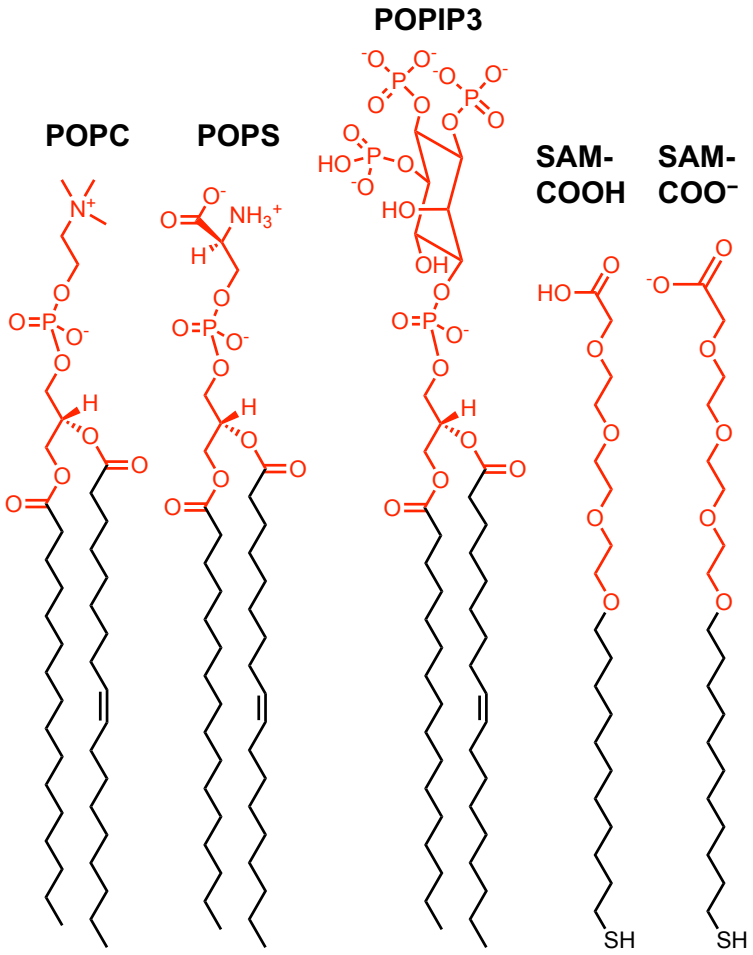


Figure 2.23 | ECC/ECC2-Parametrization of Lipids and SAM-Molecules. Parts of the molecules considered as head group and therefore scaled in their charge and van der Waals radii are shown in red. Unchanged tails of the molecules across the force field parametrizations, meaning standard CHARMM36 parameters were used, are shown in black. The scaling factors were: POPC ($f_q = 0.8, f_\sigma = 0.89$), POPS ($f_q = 0.75, f_\sigma = 0.89$), POPIP3 ($f_q = 0.75, f_\sigma = 0.89$), COOH-SAM ($f_q = 0.75, f_\sigma = 0.89$), COO^--SAM ($f_q = 0.75, f_\sigma = 0.89$). Structures were produced with ChemDraw.

	POPC		POPC:POPS (8:2)		POPC:POPS:POPIP3 (7:2:1)	
Ca^{2+} [mM]	400	-	400	-	400	-
Na^{+} [mM]	-	400	-	400	-	400
POPC	392	392	312	312	546	546
POPS	-	-	78	78	156	156
POPIP3	-	-	-	-	3×26	3×26
Water	57853	58264	57935	58346	133273	134213
Neutralizing cations	-	-	39	78	312	624
Additional cations	417	420	378	342	646	343
All cations	417	420	417	420	958	967
Cl^{-}	834	420	756	342	1292	343

Table 2.10: | Composition of Simulated AA Membrane Systems. The first two rows show the concentration of Ca^{2+} and Na^{+} ions with respect to the number of water molecules. The number of molecules and ions present in the respective system are given in the rows below. The number of POPIP3 lipids includes three equal amounts of the three different protonation states.

	OEG-SAM (39% Charged)					
Ca^{2+} [mM]	700	-	400	-	100	-
Na^{+} [mM]	-	700	-	400	-	100
SAM-COO^{-}	171	171	171	171	171	171
SAM-COOH	269	269	269	269	260	269
Water	94453	46190	46961	94221	47729	94905
Neutralizing cations	171	86	86	171	86	171
Additional cations	1020	513	256	513	-	-
All cations	1191	599	342	684	86	171
Cl^{-}	1020	1027	513	513	1	-

Table 2.11: | Composition of Simulated AA OEG-SAM Systems. The first two rows show the concentration of Ca^{2+} and Na^{+} ions with respect to the number of water molecules. The number of molecules and ions present in the respective system are given in the rows below.

3

Influence of pH Condition and Substrate on Free Floating Model Membranes

Contents

3.1 Introduction 98
3.2 Results 100
3.2.1 Influence of pH Condition on the FFM System 100
3.2.2 Influence of OEG-SAM Substrate on Free Floating Membranes 114
3.3 Discussion 123
3.4 Materials and Methods 126
3.4.1 Materials 126
3.4.2 Neutron Reflectometry (NR) Measurements 126
3.4.3 Molecular Dynamics (MD) Simulations 127
3.4.4 Appendix 132

3.1 Introduction

According to the classic Evans-Sackmann model, increasing the extent of a water layer between a substrate and an adjacent membrane leads to higher mobility of the membrane, therefore mimicking better natural membrane behaviour.[286] This inverse relationship between distance to the substrate and lipid diffusion of the adjacent membrane makes the previously observed easy manipulation of this distance very attractive.[287] As described in *Chapter 2*, in the free floating membrane (FFM) system the distance between the substrate, covered with a carboxylate terminated oligo (ethylene glycol) self-assembled monolayer (OEG-SAM), and the floating membrane can be varied by changing the

salt buffer condition. We suggested that the modulation of the OEG-SAM surface charge by cation binding is the main cause of the significant different lengths of the SAM-to-FFM distances observed at different salt buffer conditions and neutral pH (see *Chapter 2*). The cation binding to the OEG-SAM surface decreased the repulsion force between the anionic OEG-SAM and the anionic phospholipid membrane. Additionally, the accumulation of cations in the water inter-layer between OEG-SAM and floating membrane was suggested to cause an attractive bridging effect between the membrane and the OEG-SAM, which was more pronounced for Ca^{2+} than for Na^{+}. This electrostatic attraction, together with long range, attractive van der Waals (vdW) forces [136], stays in equilibrium with repulsive hydration [288] and membrane fluctuation forces [135]. The interplay of these attractive and repulsive forces lead to close membrane positions to the OEG-SAM in the presence of cations, while at the same time preventing contact between them and maintaining the water inter-layer. To test our hypothesis we wanted to investigate the effect of changing the pH in the buffer solution on the FFM-to-SAM distance at fixed salt buffer conditions. According to our hypothesis, changing the ionisation of the acidic groups on both the OEG-SAM and the membrane head groups by applying different pH conditions will alter the FFM-to-SAM distance in a controlled fashion due to OEG-SAM/membrane surface charge modulation. For instance, at chosen low (pH 3), medium (pH 7) and high (pH 10) pH the OEG-SAM is fully protonated (neutral), partly protonated (28% negatively charged) and fully deprotonated (100% negatively charged), respectively (see Table 3.2). Furthermore, we were particularly interested to see if there is indeed in addition to the decreased repulsion an attractive bridging effect emerging between the OEG-SAM and the membrane due to cation accumulation at the OEG-SAM surface. There is no electrostatic repulsion force between OEG-SAM and floating membrane at low pH of 3, but also no additional attractive bridging force between them. So, in accordance with our hypothesis, we expect short, but longer FFM-to-SAM distances at low pH compared to the very short FFM-to-SAM distances in the presence of Ca^{2+}. By using neutron reflectometry (NR) measurements we examined a POPC only and an anionic POPC:POPS (8:2 mol:mol) floating membrane adjacent to an OEG-SAM in the presence of 2 mM $CaCl_2$ and of 150 mM NaCl at pH 3, 7 and 10. Then, coarse grained (CG) molecular dynamics (MD) simulations of these layers at the

different salt and pH conditions were performed to gain further understanding of the effects observed in the NR experiments. These studies either agree with our current model of FFM-to-SAM distance tuning or provide tangible clues to unravel the mechanism of distance modulation.

Besides the use of OEG-SAMs in the FFM-system, there is a substantial interest in OEG-SAMs, owing to their versatile applications, including their application in biological microelectromechanical systems, used for biosensing, artificial organ generation or drug delivery [289], [290], as well as their application in formulation of biosurfaces and antifouling surface coatings.[241], [291], [292] Thus, our study of structural effects on OEG-SAMs caused by different pH conditions are important to several fields including biochemistry, material science and biomedicine.

We are able to tune the distance between OEG-SAM and the floating membranes in the FFM-system, but the ultimate questions are: Does the substrate, covered with the OEG-SAM, have an effect on biophysical properties of the floating membrane despite having a water inter-layer between the OEG-SAM and the membrane? If so, is there a FFM-to-SAM distance above which the influence of the OEG-SAM surface on membrane properties becomes negligible; and does that distance vary between different salt conditions? Therefore, multi-layer coarse grained FFM systems were simulated, consisting of an OEG-SAM separated from different phospholipid membranes by a varying initial distance. Of particular interest was the lateral lipid diffusion in the upper and lower leaflet of the floating membranes, often used as analytical parameter for membrane fluid-phase behavior.[293]

3.2 Results

3.2.1 Influence of pH Condition on the FFM System

NR Reveals pH Dependency of FFM-to-SAM Distance

While the effect on free floating membrane (FFM) behaviour at different salt conditions was intensively studied (*Chapter 2*), here we investigate another important variable within the FFM system: the pH of the buffer solution. Modulated electrostatic surface charges of the OEG-SAM were identified as the main cause of large membrane movements within the FFM system (*Chapter 2*). The modulation was

caused by cation binding to the OEG-SAM surface, which changes the repulsion between phospholipid membrane and OEG-SAM to a tunable attraction, the strength of which depends significantly on the type of cation.[287] Therefore, the question arose, how different pH conditions, which alter the charge of the OEG-SAM surface and of the lipid head groups, influence the membrane behaviour at different salt conditions? Is there an attractive bridging effect emerging between the OEG-SAM and the FFM due to the enhanced cation concentration in the water inter-layer or is the cause of the observed membrane movements purely down to decreased repulsion between the two layers? To tackle these questions, we performed neutron reflectometry (NR) experiments on two different FFM systems, one of which contained a POPC, the other a POPC:POPS (8:2, mol:mol) membrane. Both systems were measured at pH 3, 7 and 10 of the 20 mM HEPES buffer solution, containing 2 mM $CaCl_2$, 150 mM NaCl or no additional salt. Note, the expected surface charges of the membranes and the OEG-SAM at selected pH values are discussed in the following section and listed in Table 3.2. Table 3.1 shows an overview of the measured systems, their resulting FFM-to-SAM distance, FFM roughness and coverage. Corresponding scattering length density (SLD) and reflectivity profiles are shown in Figure 3.1 and 3.2.

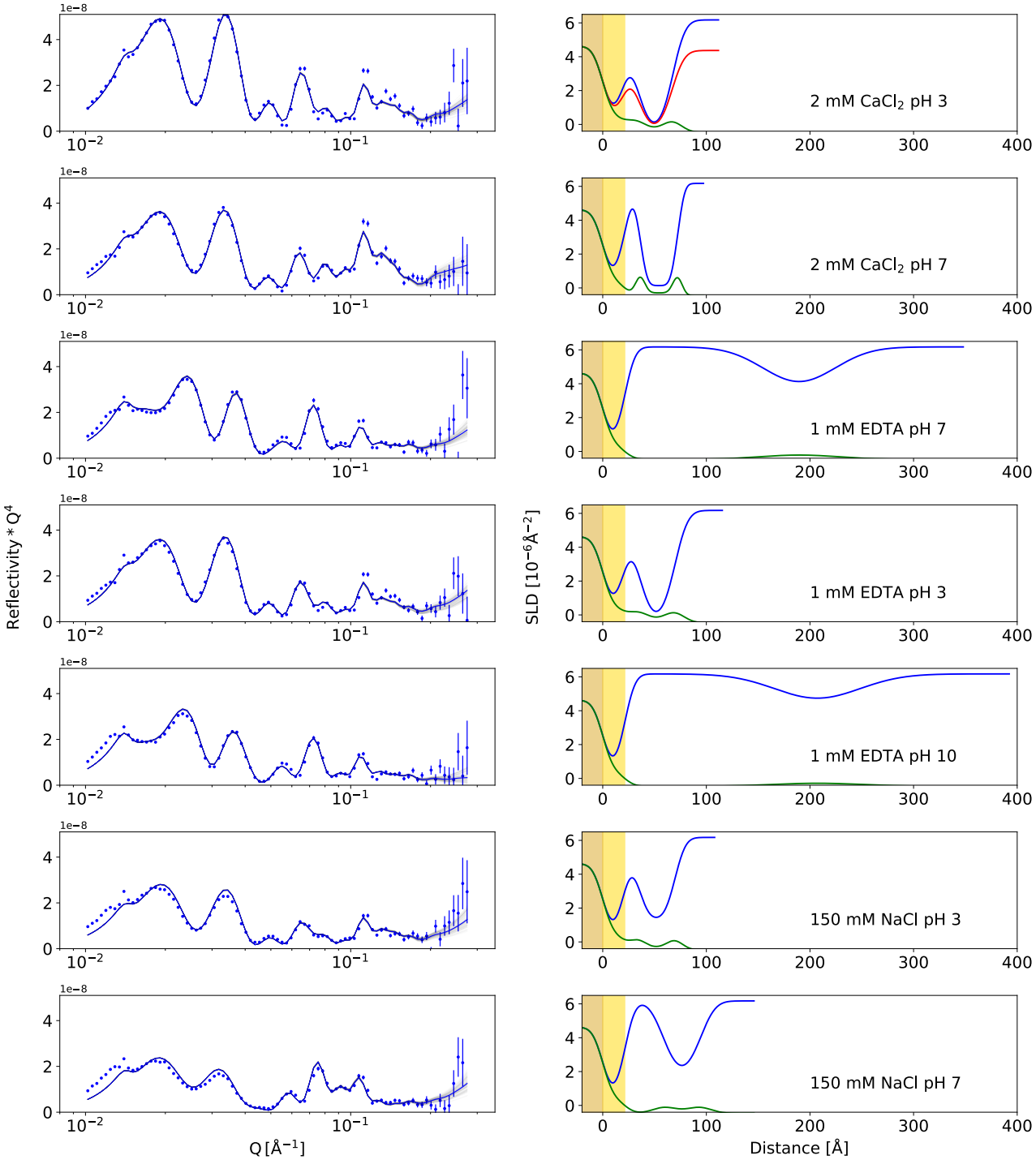


Figure 3.1 | Reflectivity and SLD Profiles of a POPC (8:2) Membrane in Absence of Cations, in Presence of Ca^{2+} and Na^{+} ions, at pH 3, 7 and 10. Each row shows the reflectivity and the corresponding SLD profile for one of the buffer conditions at which the POPC membrane was measured (see labels in SLD profiles). The standard buffer to which the listed salts were added, was 20 mM HEPES. The SLD profiles are shown chronologically (top to bottom) for the applied isotopic contrasts: 100% water (H_2O, green), 100% deuterium oxide (D_2O, blue) and 75% D_2O / 25% H_2O (gold matched water, AuMW, red). Here, zero at the x-axis is equal to the gold/OEG-SAM interface. For clarity the area of the gold layer is highlighted in light brown and the area of the OEG-SAM in yellow. The reflectivity profiles include the experimental data (dotted) and fits (solid), both for the D_2O isotopic contrast.

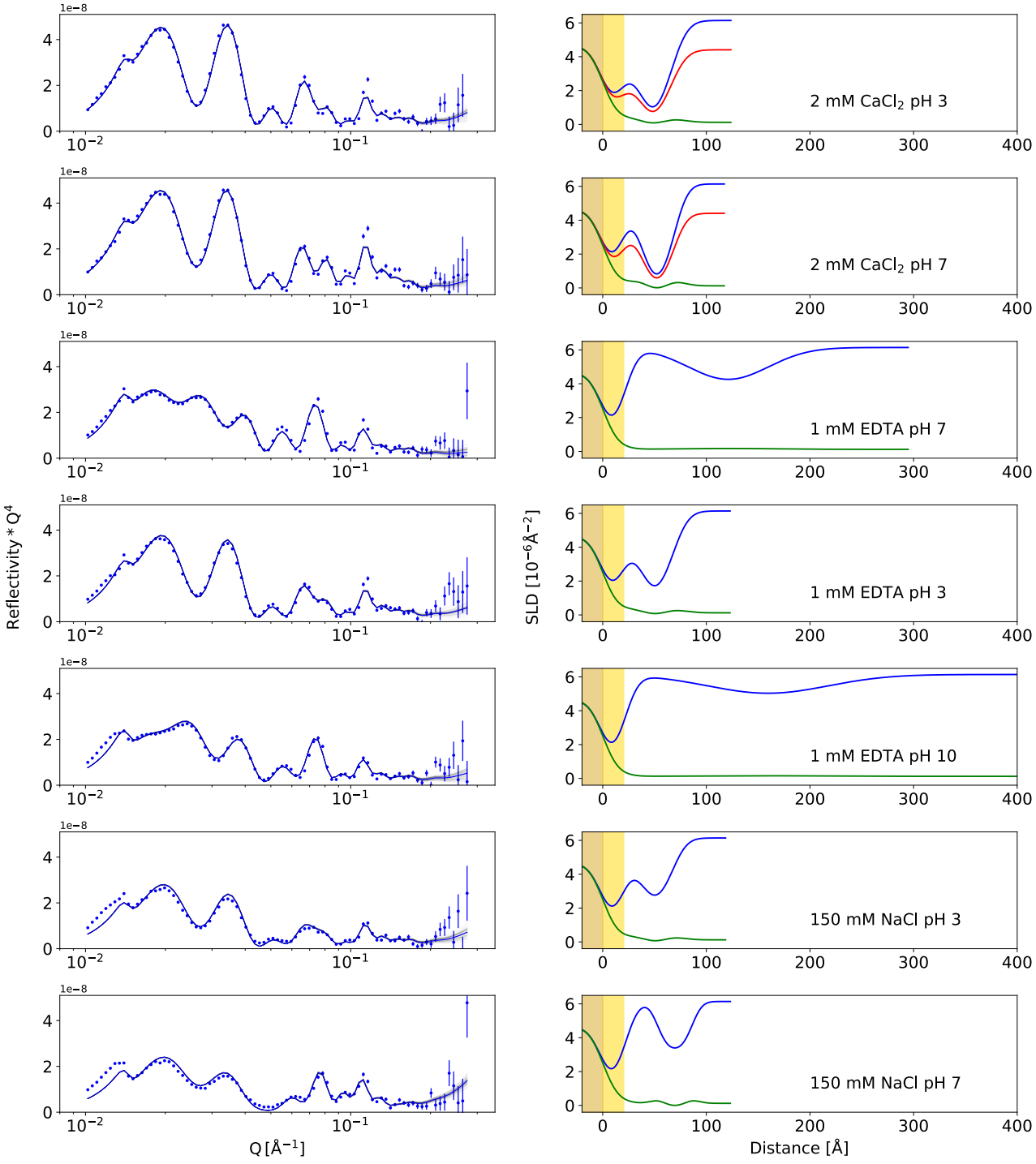


Figure 3.2 | Reflectivity and SLD Profiles of a POPC:POPS (8:2) Membrane in Absence of Cations and in Presence of Ca^{2+} and Na^{+} ions, at pH 3, 7 and 10. Each row shows the reflectivity and the corresponding SLD profile for one of the buffer solution condition at which the POPC:POPS (8:2, mol:mol) membrane was measured (see labels in SLD profiles). The standard buffer to which the listed salts were added, was 20 mM HEPES. The SLD profiles are shown chronologically (top to bottom) for the applied isotopic contrasts, H_2O (green), AuMW (red), D_2O (blue). Here, zero at the x-axis is equal to the gold/OEG-SAM interface. For clarity the area of the gold layer is highlighted in light brown and the area of the OEG-SAM in yellow. The reflectivity profiles include the experimental data (dotted) and fits (solid), both for the D_2O isotopic contrast.

	FFM-to-SAM Distance [Å]						
Chronology ⟼	*2 mM $CaCl_2$ pH 3*	*2 mM $CaCl_2$ pH 7*	*1 mM EDTA pH 7*	*1 mM EDTA pH 3*	*1 mM EDTA pH 10*	*150 mM NaCl pH 3*	*150 mM NaCl pH 7*
POPC	7 ± 1	12 ± 1	147 ± 1	9 ± 1	165 ± 2	9 ± 1	34 ± 1
POPC/POPS	10 ± 1	13 ± 1	83 ± 1	12 ± 1	121 ± 3	12 ± 1	31 ± 1
	FFM Roughness [Å]						
POPC	9 ± 1	4 ± 1	33 ± 2	9 ± 1	40 ± 2	8 ± 1	11 ± 1
POPC/POPS	13 ± 1	10 ± 1	38 ± 1	12 ± 2	57 ± 3	11 ± 1	8 ± 1
	FFM Coverage [%]						
POPC	99 (97, 100)	94 (92, 95)	76 (72, 80)	99 (97, 100)	63 (60, 67)	75 (73, 77)	66 (64, 68)
POPC/POPS	99 (98, 100)	94 (92, 96)	86 (83, 90)	84 (82, 86)	76 (70, 83)	61 (59, 63)	44 (43, 46)

Table 3.1: | Resolved Structural NR Parameters. The distance between OEG-SAM and FFM, the roughness of the FFM and the FFM coverage are given for all FFM systems at each measured buffer solution condition. The standard buffer to which the listed salts were added, was 20 mM HEPES. The columns follow the chronological order of the measurements form the left to the right. Measurements undertaken at pH 7 and pH 10 are shaded in teal and red, respectively. The errors of the FFM-to-SAM distance and the FFM roughness represent the 95% confidence intervals determined via MCMC sampling of the fitting parameters. The FFM coverage was calculated using the area per lipid of the membrane via: $V_{\text{tail}} \,/\, (apm \times t_{\text{tail}})$ with V_{tail} being the volume of the lipid tail, apm the fitted area per lipid and t_{tail} the thickness of the lipid tail. The errors correspond to the 95% confidence intervals of the area per lipid determined via MCMC sampling.

We reproduced our previous findings at pH 7 (*Chapter 2*), with both membranes showing short FFM-to-SAM distances of around 13 Å in the presence of Ca^{2+}, an intermediate FFM-to-SAM distance in the presence of Na^{+} (34 ± 1 Å for POPC and 31 ± 1 Å for POPC/POPS) and a long FFM-to-SAM distance in the absence of cations (147 ± 1 Å for POPC and 83 ± 1 Å for POPC/POPS) (Table 3.1, Figure 3.1 and 3.2). Also the membrane roughness was again significantly larger at the long

FFM-to-SAM distances in absence of cations compared to the short FFM-to-SAM distances in the presence of Ca^{2+}: for POPC around 8 fold and for POPC/POPS around 4 fold bigger. Interestingly, we observed for both membranes at pH 3 short FFM-to-SAM distances of 7 to 12 Å across all salt conditions. At pH 3 the POPC membrane is around 1% and the POPC/POPS (8:2, mol:mol) membrane around 6.4% positively charged, whereby the OEG-SAM is fully protonated, therefore uncharged (see Table 3.2-3.5 for pK_a values and calculations). These findings show that the lack of electrostatic repulsion between the OEG-SAM surface and the membrane at low pH leads to a close approach of the membrane towards the OEG-SAM surface caused by long range attractive vdW interactions. In agreement with this, at higher pH where membranes and OEG-SAM become negatively charged, the membrane moved further away from the OEG-SAM surface. Hereby, the extent of the movement strongly depended on the salt present in the buffer. So, in the presence of Ca^{2+} the difference between the membrane position at pH 3 and pH 7 was around 5 Å for POPC and 3 Å for POPC/POPS, in the presence of Na^+ 25 Å (POPC) and 19 Å (POPC/POPS) and in the absence of any salt 138 Å (POPC) and 71 Å (POPC/POPS). Therefore cations decrease the repulsion forces between the two negatively charged layers, leading to shorter FFM-to-SAM distances than without the presence of cations, an effect that is more pronounced for divalent Ca^{2+} than monovalent Na^+. The salt-free system was also measured at the very high pH of 10, showing with 165 ± 1 for POPC and 121 ± 1 for POPC/POPS the longest FFM-to-SAM distances. This again confirms that higher OEG-SAM surface charge and membrane head group charge result in a larger distance between the two caused by increased electrostatic repulsion forces. Note that we lost significantly on membrane coverage over time, especially after the harsh treatment with pH 10 (see Table 3.1).

In summary, the NR experiments showed that the pH condition modulates the FFM-to-SAM distance in a controlled manner, as was expected by our previous hypothesis (see *Chapter 2*). However, the observed very short distances at low pH, without cations present were unexpected and do not support the previously proposed attractive bridging force of divalent Ca^{2+} cations being necessary to approach these close membrane positions to the OEG-SAM surface.

MD Confirms Absence of Cation Induced Attractive Bridging Effect

The NR results raised the question how strongly the surface charge modulations caused by different pH conditions alter the Na^+ and Ca^{2+} interactions with the OEG-SAM and the floating membrane. Previously we showed that at pH 7 both Na^+ and Ca^{2+} energetically favour the interaction with the OEG-SAM over the interaction with different phospholipid membranes (see *Chapter 2*). But does the OEG-SAM stay the energetically most favorable layer in the FFM system to interact with cations across the different pH conditions? To gain further understanding of the cation interactions within the FFM system and the role of pH conditions, MD simulations of the OEG-SAM and of the different lipid bilayers used in the NR experiments were performed at pH 3, 7 and 10, each in the presence of 200 mM $CaCl_2$ and 200 mM NaCl. CG simulations were used to generate model structures, using the well-established Martini force field.[206] To represent the different pH conditions, the protonation probability of each molecule corresponding to the different pH conditions was calculated and according to these probabilities charged and uncharged versions of each molecule were randomly distributed in the corresponding layer.

The protonation probabilities of each lipid species and the OEG-SAM molecule were calculated by using the following correlation between the protonation free energy and the protonation probability:

$$\Delta G_{\text{prot}} = -RTln\left[\frac{\langle x\rangle}{1-\langle x\rangle}\right]$$

where ΔG_{prot} is the protonation free energy, $\langle x\rangle$ the protonation probability of the examined molecular group, R the gas constant and T the temperature. This equation was combined with the correlation between pK_a and the protonation free energy:

$$pK_{\text{a}}\,(pH) = pH - \frac{\Delta G_{\text{prot}}\,(pH)}{RTln10}$$

where R is the gas constant, T the temperature and ΔG_{prot} the protonation free energy. Thus, the protonation probabilities at different pH conditions were calculated via the following equation:

$$RTln10 \cdot (pH - pK_{\text{a}}) = -RTln\left[\frac{\langle x\rangle}{1-\langle x\rangle}\right]$$

Therefore, for a pK_a value of 7.4 for the OEG-SAM-carboxyl group, the amount of negatively charged OEG-SAM-molecules across the OEG-SAM is 0, 28 and 100% at pH 3, 7 and 10, respectively.

For POPC the pK_a value of the negatively charged phosphate group PO_4^- is 1. Thus, at pH 7 and pH 10 the POPC lipid is neutral. However, at pH 3 a small amount of 1% of the POPC lipids is positively charged due to the protonation of the phosphate group, resulting in PO_3-OH. For the POPS lipid the situation becomes more complex due to three different protonation groups within the POPS lipid which have to be considered. The pK_a value of the phosphate group (PO_4^-) is 2.6, of the carboxyl group (COO^-) 5.5 and of the amino group (NH_3^+) 11.55. This results in a positively charged amino group (NH_3^+), protonated carboxyl group (COOH) and 28% protonated (PO_3-OH) and 72% unprotonated (PO_4^-) phosphate group for pH 3. Therefore, at pH 3 POPS is overall 72% neutral and 28% positively charged. At pH 7 the amino group is positively charged (NH_3^+), the phosphate group negatively charged (PO_4^-) and the carboxyl group has a protonation probability of 3%. Therefore, at pH 7 POPS is overall 97% singly negatively charged and 3% neutral. At pH 10 both the phosphate and the carboxyl group are negatively charged, whereby the protonation probability of the amino group drops to 97%, resulting in 97% singly and 3% twice negatively charged POPS lipids. Table 3.2 summarizes the protonation probabilities of the different functional groups within the different molecules at pH 3, 7 and 10. Therefore, a positively charged POPC lipid, as well as a positively, twice negatively charged and neutral POPS lipid were parameterized (see Method section 3.4.3). Then, the OEG-SAMs and phospholipid membranes were assembled for the different pH conditions with a charged *vs.* uncharged molecule ratio according to the protonation probabilities (see Method section 3.4.3, Tables 3.4 and 3.5).

Molecule	pK_a(funct. gr.)	pH3 $\langle x \rangle$	pH7 $\langle x \rangle$	pH10 $\langle x \rangle$
SAM	(COO^-) = 7.4	1	0.72	0
POPC	(PO_4^-) = 1	0.01	0	0
POPS	(PO_4^-) = 2.6	0.28	0	0
POPS	(COO^-) = 5.5	1	0.03	0
POPS	(NH_3^+) = 11.55	1	1	0.97

Table 3.2: | Protonation Probabilities. Given are the protonation probabilities $\langle x \rangle$ at pH 3, 7 and 10 for the different functional groups (funct. gr.) within the OEG-SAM, POPC and POPS molecule. Also provided are the pK_a values based on which the protonation probabilities were calculated.

For gaining insights in the OEG-SAM behaviour in dependency of the pH condition, the time and ensemble average of the thickness $<d>$, the lattice constant $<a>$ of the OEG-SAM, order parameters between thiol-bead and upper CH-chain-bead $<S_{THI\text{-}C1B}>$ of the charged (COO^-) (called SPA) and the uncharged (COOH) (called SPU) OEG-SAM molecules, as well as the surface accessible area (SASA) along the hydrophilicity $<\eta>$ of the OEG-SAM was observed for the different pH and different salt conditions (Figure 3.3). Besides minor differences for most of the parameters, we observed a significant trend for the SASA: the SASA increases with the charge and therefore hydrophilicity $<\eta>$ of the OEG-SAM. Especially the difference in SASA between pH 7 and 10 is large and might find its cause in the equally big increase of the order parameter $<S_{THI\text{-}C1B}>$ of the charged OEG-SAM molecules (SPA). The change in this order parameter corresponds to a change in tilt angle of the charged OEG-SAM molecules from around 26° to 15°. Hence the charged OEG-SAM molecules (SPA) seem to be more upright with increased pH. Combined with the slightly higher lattice constant for pH 10 compared to pH 7, this might explain why the SASA is bigger for pH 10 compared to pH 7. The water distribution profiles on top of the OEG-SAM confirm this suggestion as water penetrates deeper into the OEG-SAM with increasing pH value (Figure 3.4).

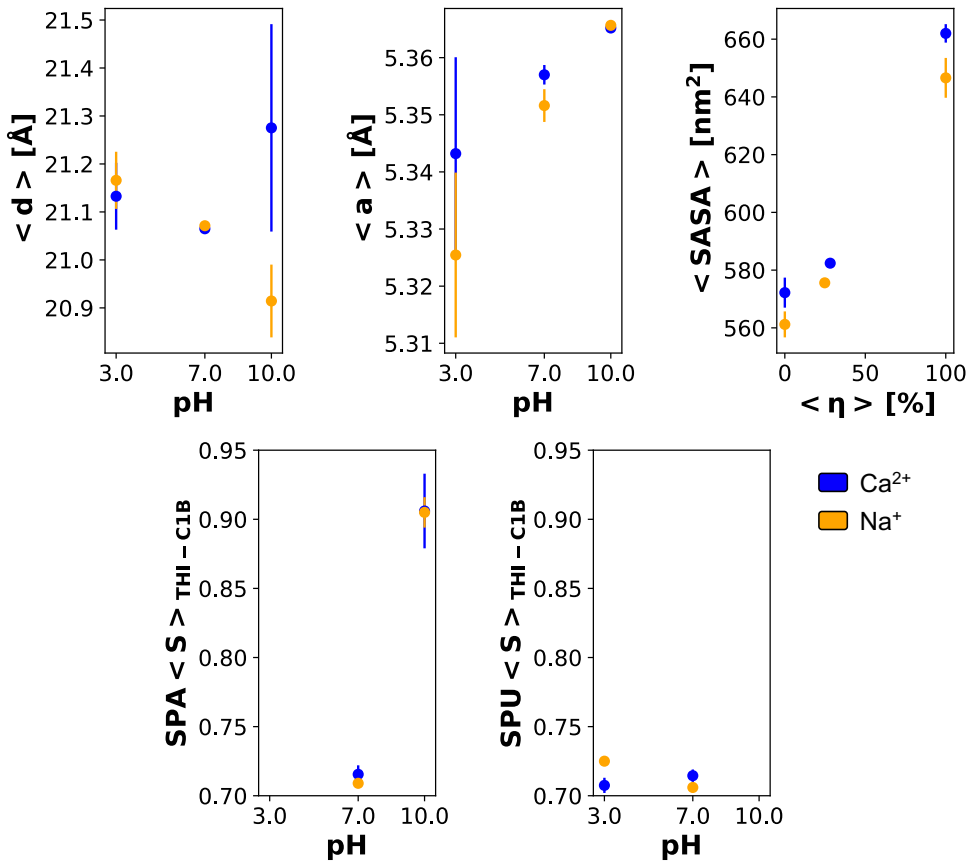


Figure 3.3 | Characterization of CG OEG-SAM at Different pH Conditions, in the Presence of Na^+ and Ca^{2+}. Time and ensemble average of order parameters between thiol-bead and upper CH-chain-bead <$S_{THI\text{-}C1B}$> of the charged (COO^-) (called SPA) and the uncharged (COOH) (called SPU) OEG-SAM molecules in dependency of the pH condition are shown. Also, time and ensemble average of the lattice constant <*a*> and the thickness <*d*> of the OEG-SAM in dependency of the pH value, as well as the surface accessible area <*SASA*> in dependency of the hydrophilicity <η> are shown. The colour code is identical between plots, blue for 200 mM Ca^{2+} and orange for 200 mM Na^+ being present in the system. The surface hydrophilicity was calculated using the GROMACS command SASA with Martini vdW-radii and a probe radius of 0.26 nm. For the calculation of the order parameters, the Martini Python script *do-order-gmx5.py* was used and for the OEG-SAM-molecules edited accordingly. As indicated in Figure 2.9 the thickness was defined as distance between the centre of mass of the thiol-beads (SC5) and the centre of mass of the carboxyl-beads (SQn and SP2).

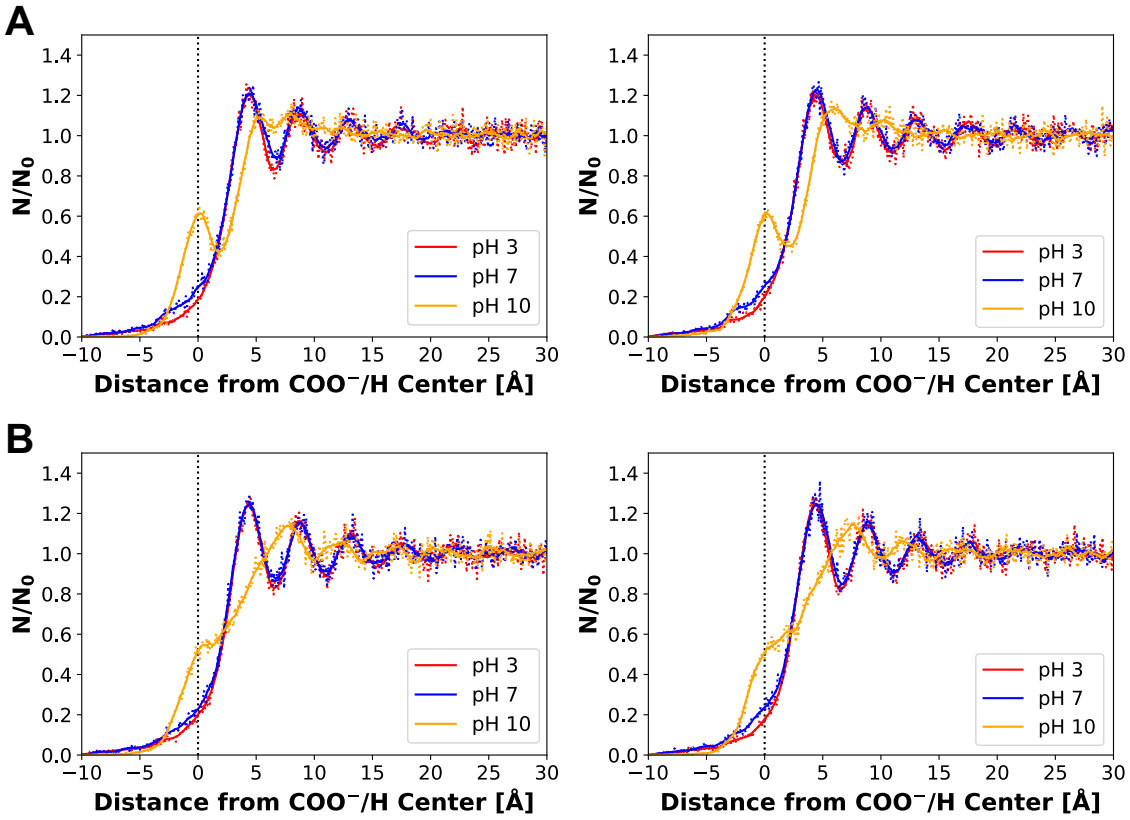


Figure 3.4 | Water Density Profiles in CG Simulations of OEG-SAM at Different pH and Salt Buffer Conditions. The water density profiles on top of the OEG-SAM show N/N_0 water molecules along surface normal with N being the number of molecules at given z-position and N_0 the bulk concentration as average of number density above 4 nm away from the surface. Results are shown for two independent repeats containing 200 mM Ca^{2+} **(A)** and for two independent repeats containing 200 mM Na^+ **(B)**. Different colours represent three applied pH conditions: orange (pH 10), blue (pH 7) and red (pH 3). Zero on the x-axis is equal to the centre of mass of the OEG-SAM carboxyl groups.

To investigate how the pH condition influences the interaction between cations and the OEG-SAM, free cation binding energy profiles were calculated for Na^+ and Ca^{2+} at pH 3, 7 and 10 (Figure 3.5) as described previously (Methods 2.4.4). Not surprisingly, the cation binding affinity of the OEG-SAM increases with increasing pH value from almost no affinity (0.8 ± 0.2 kJ/mol for Na^+ and 0.6 ± 0.1 kJ/mol for Ca^{2+}) to strong ion binding affinity at pH 7 and 10. Hereby, the free binding energy is in case of Ca^{2+} with 6.9 ± 0.1 and 12.4 ± 0.1 kJ/mol for pH 7 and pH 10, respectively, significantly higher than for Na^+ with a free energy of 5.0 ± 0.1 and 7.4 ± 0.1 kJ/mol for pH 7 and 10, respectively. Note, the free energy binding of Na^+ at pH 10 is likely even lower than 7.4 kJ/mol. The cation concentration was always kept to 200 mM, except for the system containing the OEG-SAM

at pH 10 in the presence of Na^+. Here, a Na^+ concentration of 400 mM was necessary to ensure neutralization of the system (see Method section 3.4.3).

Also, the free energy profiles reveal that the cations are able to penetrate deeper into the OEG-SAM with increasing pH value, again this being more pronounced for Ca^{2+} than for Na^+. This goes in line with the water also being able to penetrate deeper into the OEG-SAM with higher pH value of the surrounding solvent, forming a defined layer within the OEG-SAM carboxyl head group area (Figure 3.4). As anticipated, the water density profiles also show oscillations close to the OEG-SAM surface, extending approximately five molecular water diameters (2.8 Å) away from the surface, in agreement with previous studies on OEG-SAMs.[256], [257] Interestingly, these oscillations seem to decrease significantly at high pH conditions (see Figure 3.4, pH 10).

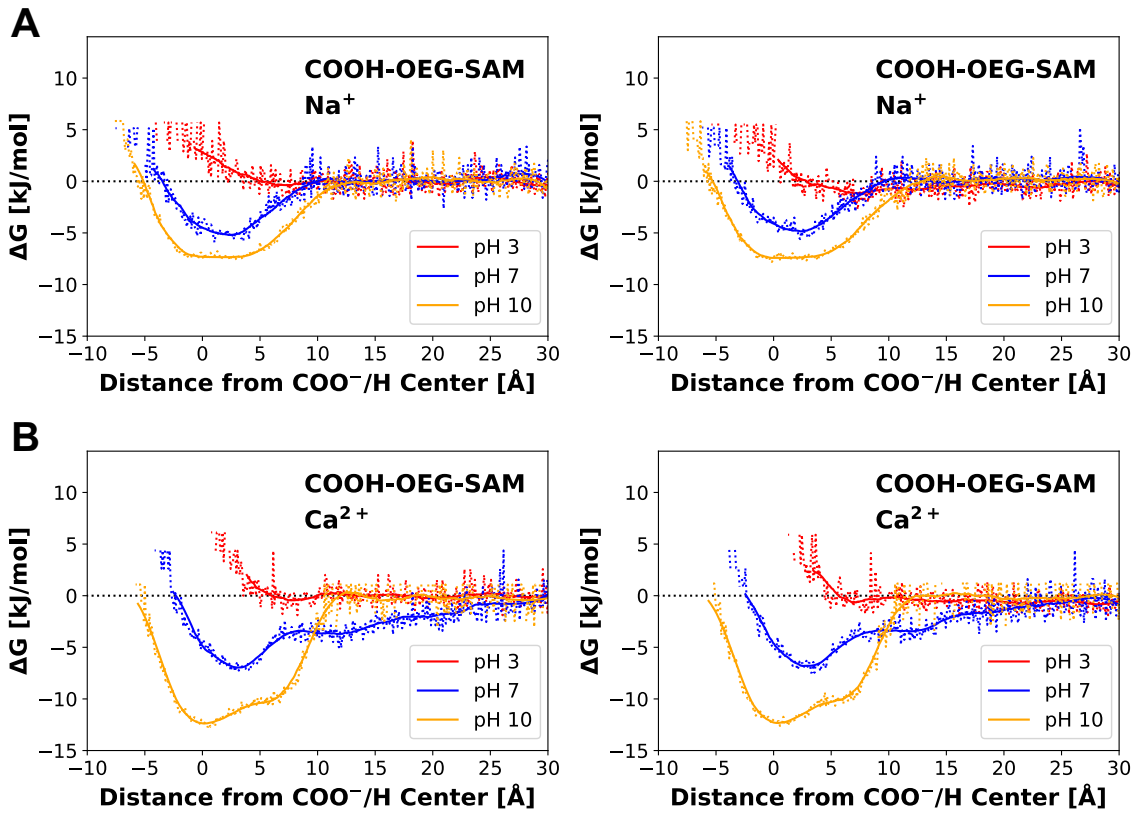


Figure 3.5 | Free Energy Profiles of Ion-Binding in CG Simulations of OEG-SAM at Different pH and Salt Buffer Conditions. Free energy profiles for cation interactions with the OEG-SAM at pH 3 (red), 7 (blue) and 10 (orange), which correspond to a 0%, 28% and 100% negatively charged $COOH^-$/H-OEG-SAM, respectively. These were evaluated in the presence of 200 mM Na^+ for two independent repeats **(A)** and in the presence of 200 mM Ca^{2+} for two independent repeats **(B)** using the Martini3 force field.[206] Zero on the x-axis is equal to the centre of mass of the OEG-SAM carboxyl groups.

For the quantification of the cation binding to different phospholipid membranes at different pH conditions, a POPC only and a POPC:POPS (8:2, mol:mol) membrane were charged in conformity with protonation probabilities representing pH 3, 7 and 10 (see Table 3.2) and simulated in the presence of 200 mM Ca^{2+} and 200 mM Na^{+}. The calculated free cation binding energy profiles showed that there is no significant cation binding to the POPC membrane for both cations, at all pH conditions (see Figure 3.6, blue profiles). In the case of Na^{+} there is also no energetically preferred cation binding to the POPC/POPS membrane for all pH conditions, although cations start to penetrate deeper into the lipid head group region of the POPC/POPS membrane with increasing pH (see Figure 3.6, **B**). In contrast, there is energetically favoured Ca^{2+} binding at pH 7 and 10 to the POPC/POPS membrane with the minimum of the free energy profiles being below zero in the lipid head group region (see Figure 3.6, **A**). Interestingly, only for these two systems where Ca^{2+} showed some binding, the penetration of the Ca^{2+} cations was similar in depths to the penetration Na^{+} showed for the same conditions. For all other systems, where no cation binding was observable, the Na^{+} cations were able to come closer to the lipid head group region than the Ca^{2+} cations, indicated by the earlier rising of the free energy profiles in case of Ca^{2+} when approaching the lipid head group region.

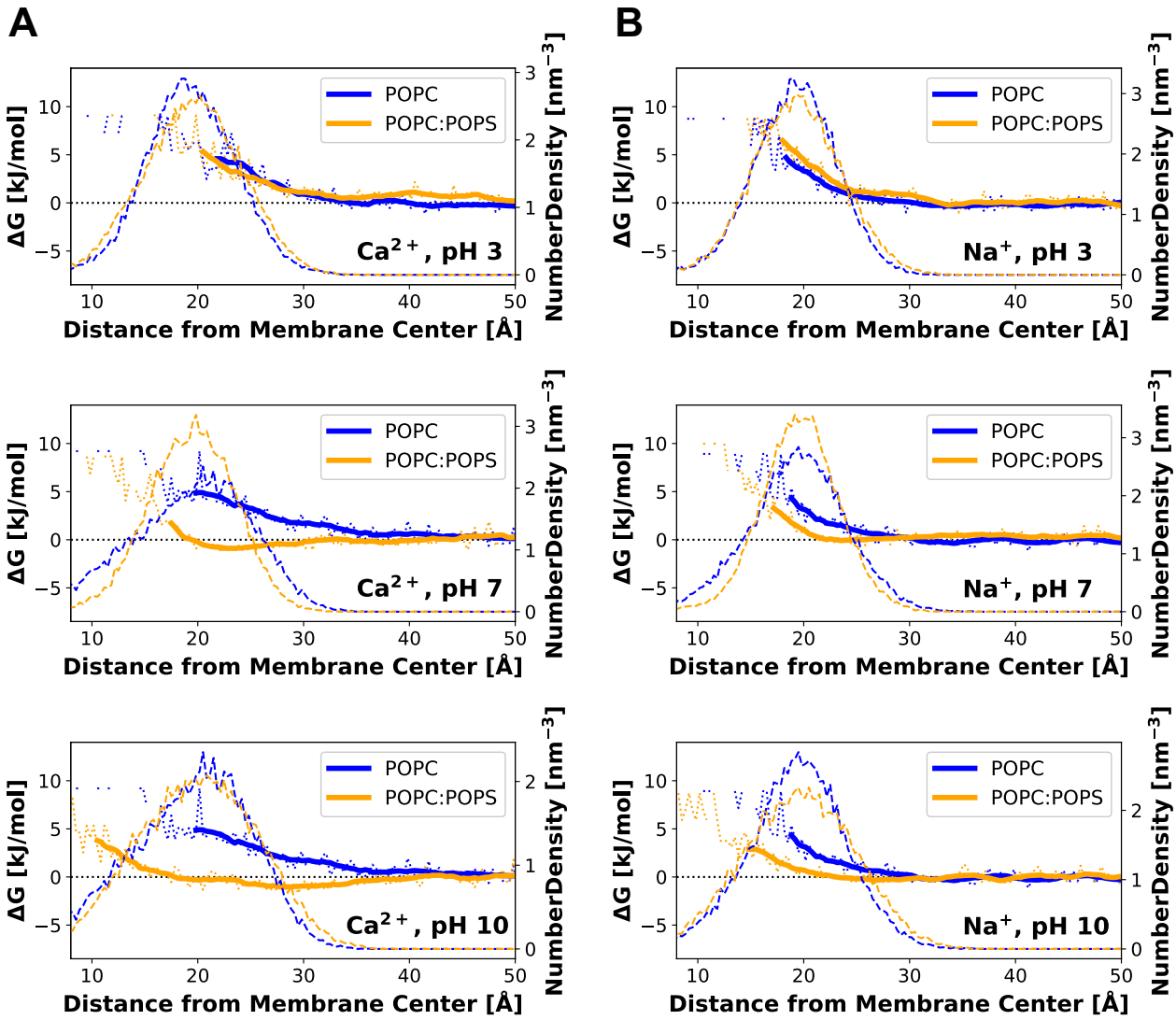


Figure 3.6 | Free Energy of Ion-Binding in CG Simulations of Phospholipid Membranes at Different pH and Salt Buffer Conditions. Free energy profiles for Ca^{2+} (**A**) and Na^{+} (**B**) interactions with a POPC (blue) and a POPC/POPS (8:2, mol:mol) (orange) membrane at pH 3 (top), 7 (middle) and 10 (bottom), which correspond to differently charged membranes (see Table 3.5 and 3.2). Zero on the x-axis is equal to the centre of mass of the respective bilayer. Dashed lines represent the corresponding number density profiles of the lipid head groups.

In summary, the MD results show a structural effect on the OEG-SAM caused by pH, leading to smaller tilt angles of the negatively charged OEG-SAM molecules with increasing pH. This change allows water and cations to penetrate deeper into the OEG-area of the SAM with increasing pH. Also, higher pH results in stronger cation binding affinities towards OEG-SAMs with Ca^{2+} showing significantly higher free binding energies compared to Na^{+}. In contrast, there is no cation affinity towards neutral POPC and anionic POPC/POPS membranes at low and high pH. Solely Ca^{2+} shows

some minor binding to the POPC/POPS membrane above neutral pH. These findings are in agreement with the NR results and suggest the role of cations in the FFM system is only to reduce the repulsion between OEG-SAM and floating membrane by binding to the OEG-SAM surface and not to cause an additional attractive force between the two layers.

3.2.2 Influence of OEG-SAM Substrate on Free Floating Membranes

Lateral Lipid Diffusion in Lower Leaflet Reduced by OEG-SAM

In order to investigate what effect the adjacent OEG-SAM has on biophysical properties of a free floating phospholipid membrane in the free floating membrane (FFM) system, membranes with different lipid compositions were simulated at different distances above the OEG-SAM, in the presence of 200 mM Na^+ and 200 mM Ca^{2+} (see Table 3.3 for overview). The membranes used were a simple POPC membrane, followed by a POPC/POPS mixture (8:2, mol:mol) and a model of the inner leaflet of the mammalian plasma membrane mimic (POPC:POPS:POPIP3, 7:2:1, mol:mol:mol). The initial distances between these membranes and the OEG-SAM surface were set to be 15, 30 and 90 Å, representing the range of distances we observed experimentally in the presence of Ca^{2+}, Na^+ and a mixture of the two cations (see Table 2.3 and 2.1). The FFM-to-SAM distances of the equilibrated FFM systems, averaged over the last 200 ns of the 2 µs coarse grained (CG) simulations are shown in Table 3.3. For this work the newly developed version of the Martini force field, Martini 3, was used.[206] Therefore, a new parametrization of the coarse grained OEG-SAM molecules was needed (see Method section 3.4.3).

FFM-System	15 Å	30 Å	90 Å
POPC Ca^{2+}	8 ± 1	25 ± 1	81 ± 1
POPC Na^{+}	9 ± 1	23 ± 1	84 ± 1
POPC:POPS (8:2) Ca^{2+}	9 ± 1	25 ± 1	85 ± 1
POPC:POPS (8:2) Na^{+}	9 ± 1	26 ± 1	83 ± 1
POPC:POPS:POPIP3 (7:2:1) Ca^{2+}	12 ± 1	23 ± 1	85 ± 1
POPC:POPS:POPIP3 (7:2:1) Na^{+}	14 ± 1	29 ± 1	83 ± 1

Table 3.3: | FFM-to-SAM Distance in CG Multi-Layer Simulations. Shown are the distances between the OEG-SAM surface and the bottom of the phospholipid bilayers, averaged over the final 200 ns of the 2 μs simulations. The top row shows the initial FFM-to-SAM distance, set at the beginning of the simulations. The OEG-SAM surface was defined as centre of mass of the OEG-SAM carboxyl groups and the bottom of the membrane as the center of mass of the phospholipid head groups of the lower leaflet. For Ca^{2+}, as well as for Na^{+}, the cation concentration was 200 mM.

The equilibrated FFM-to-SAM distances vary from the initial distances as a small hole in the floating membrane with a diameter of around 2 nm allowed ions and water to pass the phospholipid membrane. Therefore the extent of the water inter-layer between OEG-SAM and FFM varied throughout the simulations. There was no additional intention to mimic experimental membrane defects by implementing the membrane hole. Nevertheless, as an experimentally used floating membrane always contains a certain level of defects like holes, the presence of the hole might have the potential to make experimental and computational membrane systems more alike. Furthermore, the simulation of the multi-layer system including a gold-surface with bound OEG-SAM molecules required the lateral compressibility to be set to zero (see Method section 3.4.3). Therefore, for comparison the phospholipid membranes were also simulated without the adjacent OEG-SAM present, without a hole included, as well as with the lateral compressibility switched on; basically plain standard membrane MD simulations. Then, in order to observe if the absence of the lateral compressibility or the constraints forming the hole in the membrane have an effect on membrane properties, these settings were successively included in separate sets of simulations. So, in an additional set of simulations the

hole was included into the different phospholipid membranes, whereby the lateral compressibility was still switched on. Then, in further simulations of the phospholipid membranes including the hole, the lateral compressibility was set to zero. Thus, we could observe which effects on membrane properties resulted from the specific simulation settings rather than the presence of the adjacent OEG-SAM. An overview of the differently simulated systems can be seen in Figure 3.7.

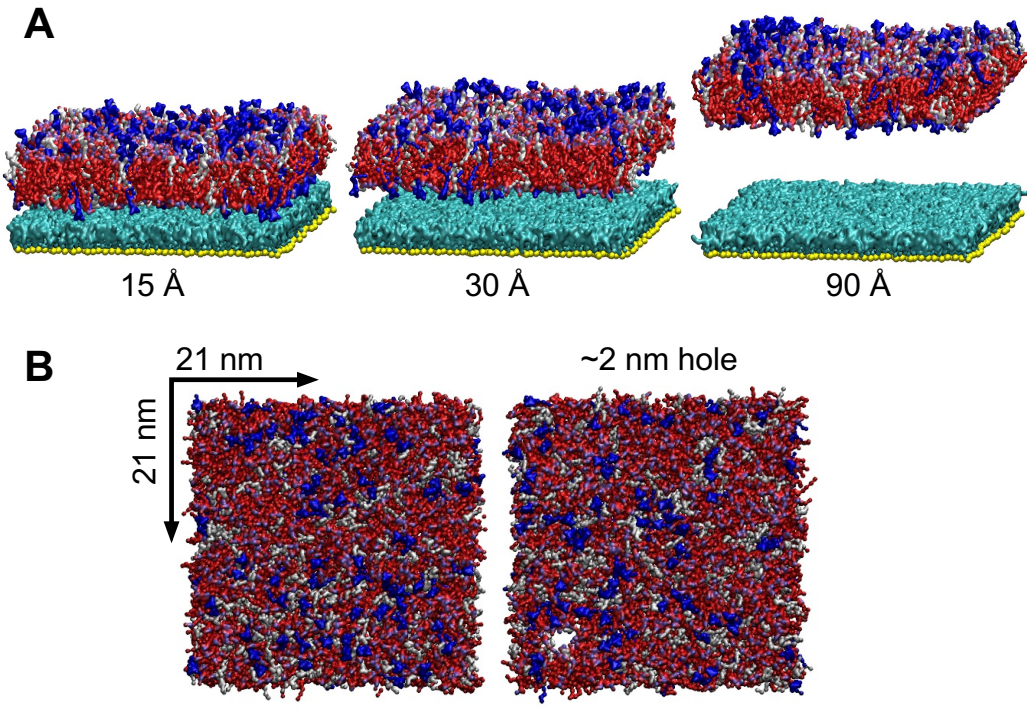


Figure 3.7 | Overview of Simulated Systems. The exemplary membrane shown here consists of a POPC:POPS:POPIP3 (7:2:1, mol:mol:mol) lipid mixture. Panel **A** shows the simulated multi-layer FFM-systems with the phospholipid membrane starting at 15, 30 and 90 Å distance above the OEG-SAM (cyan with thiol-beads shown in yellow). Panel **B** clarifies the hole dimensions by showing the top view of the membrane, simulated without (left) and with a hole (right). The diameter of the hole was kept to around 2 nm via cylindrical position restrains.

We were particularly interested in the potential influence of the OEG-SAM on membrane dynamics in terms of the lateral lipid diffusion. For the investigation of the lateral lipid diffusion it was not possible to use standard analysis tools. The reason for this was that for the lipid diffusion investigation the area around the hole in which the lipids were influenced by the cylindrical constraints forming the hole had to be excluded. Therefore, we generated our own script with the following approach: For each lipid the center of mass (COM) movement between current and previous lipid position was

calculated for each time step across the final 200 ns of the 2 µs CG simulations, except the lateral distance between the center of the hole and the lipid was smaller than 5 nm at the considered time step. The resulting vectors describe the COM movement for each lipid at each considered time step. By generating the cumulative sum of the x- and y-values of these vectors the length of the x/y-vector between the position of the lipid at each time step and the origin can be calculated. The square root of the latter represents the lateral mean square displacement (MSD) of the lipid at each considered time step. Then, the MSD *versus* time was fitted by a straight line for each lipid, with the slope representing the diffusion coefficient of the respective lipid. The mean of the single lipid diffusion coefficients across all lipids corresponding to the same lipid species was calculated to represent the averaged lipid diffusion coefficient of a lipid species within a membrane. To facilitate the inspection of the resulting lipid diffusion coefficients across the different phospholipid membranes, the lipid diffusion coefficients were visualized in Figure 3.8. Detailed values can be found in the Appendix, Table 3.6, 3.7, 3.8 .

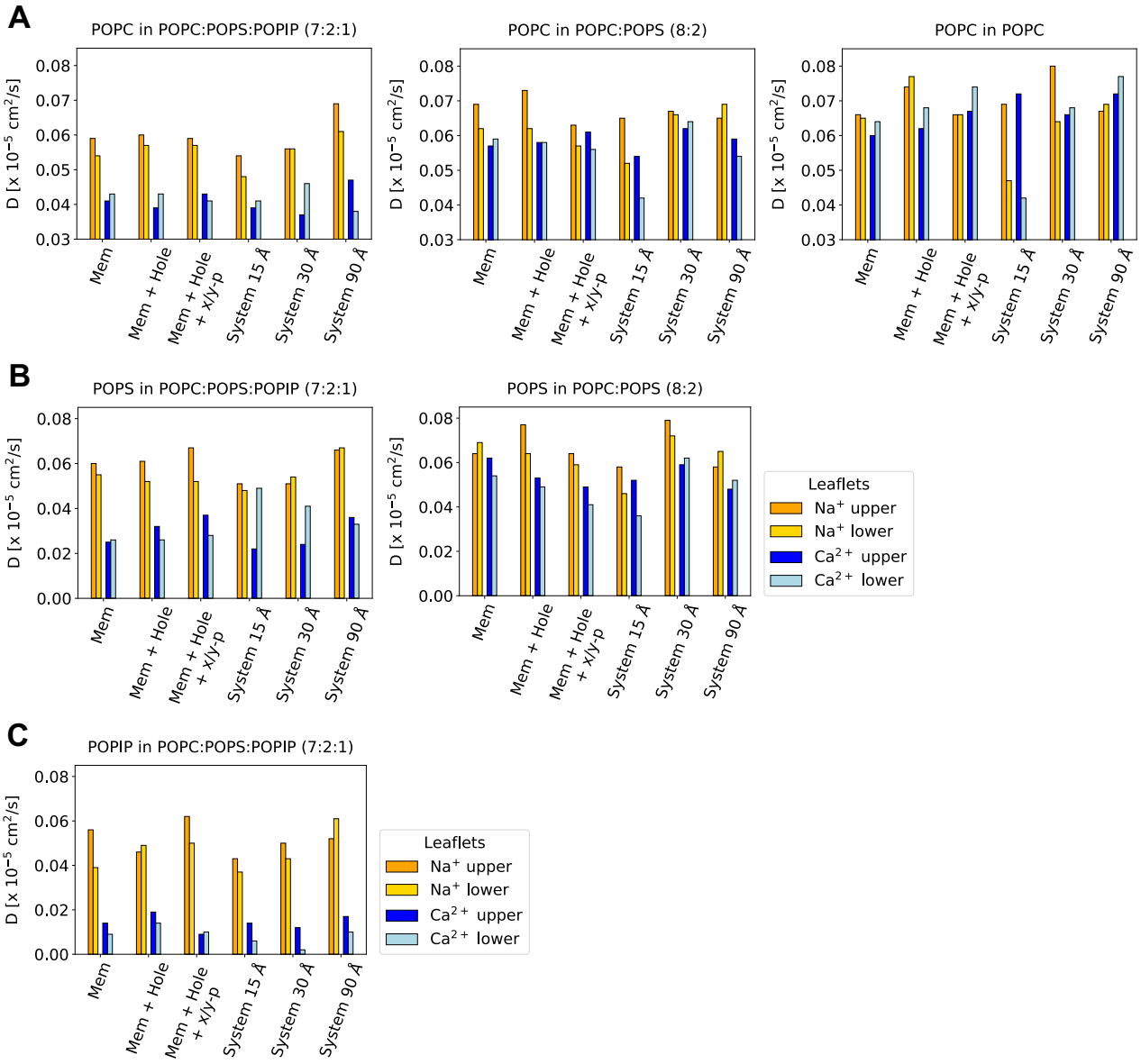


Figure 3.8 | Lateral Lipid Diffusion Coefficients in CG Phospholipid Membranes and FFM-Systems. The lateral lipid diffusion coefficients were calculated as ensemble average across the lipids corresponding to the same lipid species. The left column shows the results for the POPC:POPS:POPIP3 (7:2:1, mol:mol:mol), the central column for the POPC:POPS (8:2, mol:mol) and the right column for the POPC membrane. Panel (**A**) shows the lipid diffusion coefficients for POPC, Panel (**B**) for POPS and Panel (**C**) for POPIP3 within the different membranes. The different system setups are given along the x-axis: standard compressibility (Mem), standard compressibility and a hole introduced (Mem + Hole), with a hole and a lateral compressibility of zero (Mem + Hole + x/y-p), multi-layer FFM-Systems with the membrane initially set to a FFM-to-SAM distance of 15 (System 15 Å), 30 (System 30 Å) and 90 Å (System 90 Å). Different colors represent the two different leaflets of the respective membrane and different salt buffer conditions (see legend): the upper (orange) and lower (yellow) leaflet in the presence of 200 mM Na^+, the upper (dark blue) and lower (light blue) leaflet in the presence of 200 mM Ca^{2+}. Lower leaflet was defined as the leaflet facing towards the OEG-SAM surface in the multi-layer FFM-Systems, the upper leaflet was facing the bulk water. For the simulations without the OEG-SAM present (Mem, Mem + Hole, Mem + Hole + x/y-p) the lower and upper leaflet are interchangeable. Note the different length scale in Panel **A** compared to Panel **B** and **C** along the y-axis.

The addition of a hole into the membrane, as well as the deactivation of the lateral compressibility showed no effect on the later lipid diffusion across all the different membranes and different salt buffer conditions (see Figure 3.8, Mem, Mem + Hole, Mem + Hole + x/y-p). These findings were beneficial for our studies, as potential changes from natural membrane fluidity are then attributable to the presence of the OEG-SAM. The only lipid species showing some minor trend with the addition of the cylindrical hole constraints and the change in lateral compressibility was the POPS in the POPC/POPS (8:2, mol:mol) membrane in the presence of Ca^{2+} (see Figure 3.8, **B**); here, compared to the standard membrane simulation the diffusion coefficient decreased from around 0.058 to 0.051 $\times$ 10^{-5} cm^2/s when the hole was added and further down to around 0.045 $\times$ 10^{-5} cm^2/s with the lateral compressibility additionally set to zero.

Looking at the multi-layer FFM-systems, where the membrane was adjacent to the OEG-SAM with an equilibrium FFM-to-SAM distance of around 9 Å, we observed a significant difference in lateral diffusion coefficient between upper and lower leaflet for POPC in the POPC membrane in the presence of 200 mM Na^+ and Ca^{2+} (see Figure 3.8, **A**, System 15 Å). Thus, the adjacent OEG-SAM at a FFM-to-SAM distance of around 9 Å (see Table 3.3) seems to decrease the lateral POPC diffusion in the leaflet facing towards the OEG-SAM. Interestingly, this effect does not reach far enough to also effect the POPC diffusion in the upper leaflet, facing towards the bulk. Although slightly smaller, the same effect has been observed with lateral diffusion of POPC, as well as POPS in the POPC:POPS (8:2, mol:mol) membrane (see Figure 3.8, **A**, **B**). Furthermore, in the case of the POPC/POPS membrane the lateral lipid diffusion coefficients were smaller in the presence of Ca^{2+} compared to Na^+ across all system setups. This effect becomes even more pronounced in the highly negatively charged POPC:POPS:POPIP3 (7:2:1, mol:mol:mol) membrane. Here, Ca^{2+} decreases the lateral lipid diffusion of all the lipid species drastically (see Figure 3.8, left column). Also, the difference we observed in the lipid diffusion between the upper and lower leaflet for the POPC and POPC/POPS membranes in case of the System at 15 Å distance, was not consistently and significantly shown by the POPC/POPS/POPIP3 membrane. In case of lateral POPS diffusion within POPC/POPS/POPIP3, in the presence of Ca^{2+} the

lateral diffusion was even higher in the lower leaflet compared to the upper leaflet, thus reversed to what we observed for the POPC and POPC/POPS membranes (see Figure 3.8, **B**, System 15 Å).

In summary, the specific simulation settings our multi-layer system requires (hole in membrane and absence of lateral compressibility) conveniently have no effect on membrane fluidity. However, at short FFM-to-SAM distances of around 9 Å the presence of the OEG-SAM seems to influence membrane dynamics despite the presence of the water inter-layer. Thus, the presence of the OEG-SAM reduces the lateral lipid diffusion in the lower leaflet of the floating POPC and POPC/POPS membrane. This influence on membrane dynamics by the substrate becomes negligible at FFM-to-SAM distances above $\sim$25 Å. Also, the more negatively charged the membrane is, the smaller is this reduction in lipid diffusion caused by the OEG-SAM at short FFM-to-SAM distances, with the POPC/POPS/POPIP3 membrane showing no such reduction. At the same time, with increasing negative charge of the membrane the reduction in lipid diffusion caused by the presence of Ca^{2+} increases drastically, independent of the FFM-to-SAM distance. Therefore strongly anionic phospholipid membranes can be used in the FFM system without having to take substrate effects on membrane dynamics into account, especially in the presence of Ca^{2+}. However, with more neutral phospholipid membranes, a FFM-to-SAM distance above $\sim$25 Å is advisable to avoid surface influence.

Lipid Conformation Unaffected by Presence of OEG-SAM

In order to see if there is also an effect of the adjacent OEG-SAM on the lipid tail conformation, we calculated the ensemble average of the lipid tail carbon chain order parameters $< S >$ for the different lipid species in the simulated phospholipid membranes in the presence of 200 mM Na^+ and 200 mM Ca^{2+} (see Appendix, Tables 3.9, 3.10, 3.11 for detailed values). For an easier investigation the order parameters were converted into the corresponding tilt angle of the lipid tails and visualized in Figure 3.9. Hereby, the lipid tilt angle Θ was defined as the angle between the membrane normal and the lipid tail vector, averaged over both lipid tails (see Figure 3.9, **D**). The results show that the addition of the cylindrical hole constraints, as well as the deactivation of the lateral compressibility did not show an effect on the lipid tilt angle across all membranes. Furthermore, the addition of the

OEG-SAM showed no effect on the POPC tilt angle in all membranes in the presence of Na^+ and Ca^{2+}, with the tilt angle staying around 40°. Also, POPS in the POPC:POPS (8:2, mol:mol) membrane showed no significant or consistent trend of the lipid tilt angle in dependence of the presence of the OEG-SAM, neither of the salt condition. In contrast, the POPS tilt angle was in the presence of Ca^{2+} consistently bigger in the lower leaflet of the POPC:POPS:POPIP3 (7:2:1, mol:mol:mol) membrane, showing a difference of 1.1, 2.5 and 1.6° between the leaflets for the 15, 30 and 90 Å FFM-System, respectively. However, the differences in the tilt angles between the leaflets were with 1.1° (for POPS) and 2.7° (for POPIP3) in the presence of Ca^{2+} and with 2.3° (for POPS) and 1.8° (for POPIP3) in the presence of Na^+ substantially larger for the standard POPC/POPS/POPIP3 membrane simulations than for the other standard membrane simulations (see "Mem" on x-axis in Figure 3.9, **B/C**, left column). These values show the inherent variability of lipid order parameters within the POPC/POPS/POPIP3 membrane, suggesting the trend observed with POPS as being insignificant. In summary, as desired, the presence of the OEG-SAM seems to have no effect on the lipid tail conformation, making the sample system usable for mimicking natural membrane behaviour.

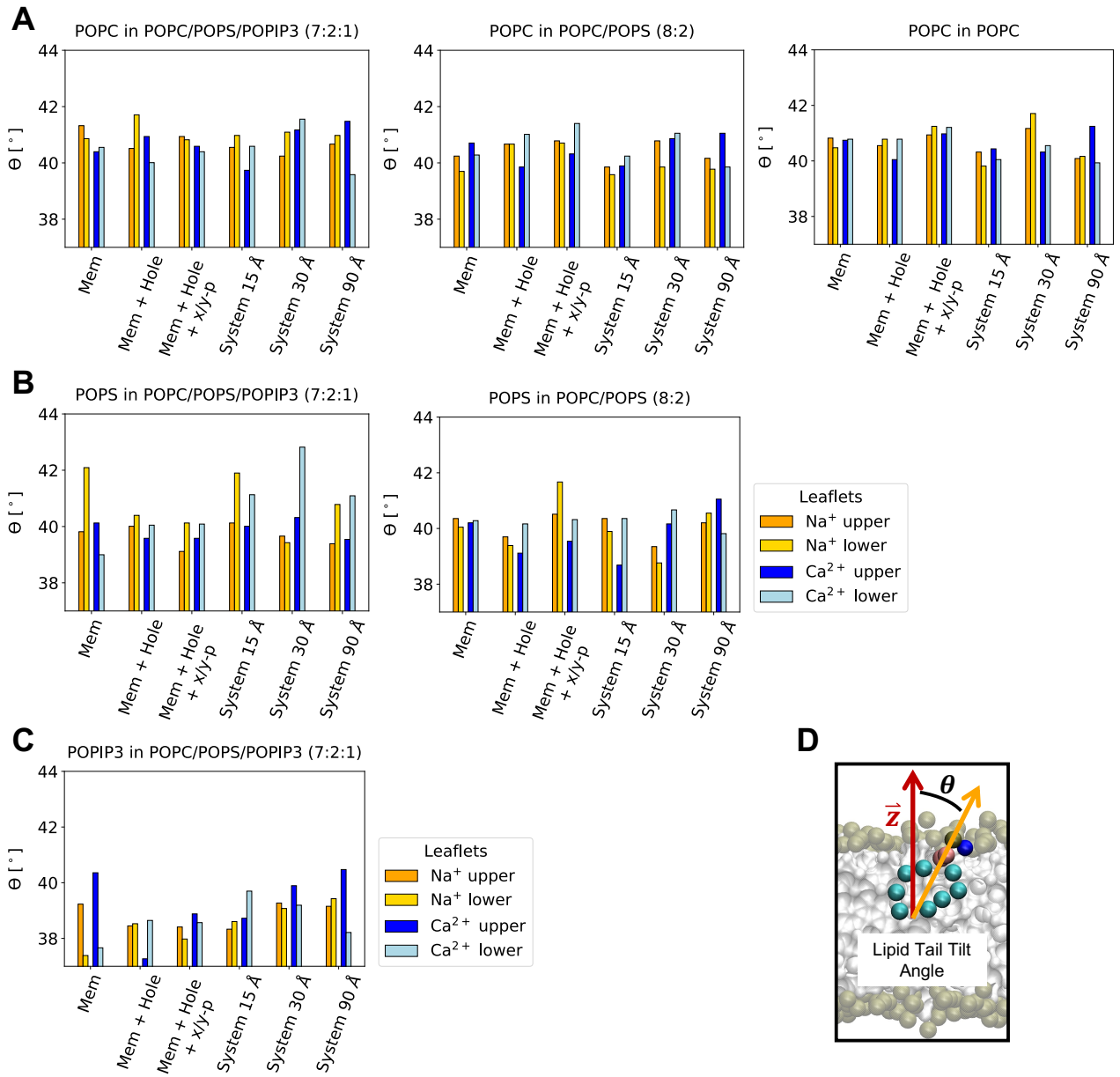


Figure 3.9 | Lipid Tail Tilt Angle for CG Phospholipid Membranes and FFM-Systems. The lipid tail tilt angles were calculated from the lipid carbon chain order parameters $< S >$ (see Table 3.9, 3.10, 3.11). As visualized in **D**, the lipid tail angle Θ was defined as angle between the membrane normal z (red) and the lipid tail vector (orange), averaged over both lipid tails (beads in cyan). The left column shows the results for the POPC:POPS:POPIP3 (7:2:1, mol:mol:mol), the central column for the POPC:POPS (8:2, mol:mol) and the right column for the POPC membrane. Panel (**A**) shows the tilt angles for POPC, Panel (**B**) for POPS and Panel (**C**) for POPIP3 within the different membranes. The different system setups are given along the x-axis: standard compressibility (Mem), standard compressibility and a hole introduced (Mem + Hole), with a hole and a lateral compressibility of zero (Mem + Hole + x/y-p), multi-layer FFM-Systems with the membrane initially set to a FFM-to-SAM distance of 15 (System 15 Å), 30 (System 30 Å) and 90 Å (System 90 Å). Different colors represent the two different leaflets of the respective membrane and different salt buffer conditions (see legend): the upper (orange) and lower (yellow) leaflet in the presence of 200 mM Na^+, the upper (dark blue) and lower (light blue) leaflet in the presence of 200 mM Ca^{2+}. The lower leaflet was defined as the leaflet facing towards the OEG-SAM surface in the multi-layer FFM-Systems, the upper leaflet was facing the bulk water. For the simulations without the OEG-SAM present (Mem, Mem + Hole, Mem + Hole + x/y-p) the lower and upper leaflet are interchangeable.

3.3 Discussion

In the free floating membrane (FFM) sample system different pH conditions cause different OEG-SAM and membrane surface charges. In order to probe the effect of different surface charges on the floating membrane behaviour, we examined POPC only and anionic POPC:POPS (8:2, mol:mol) membranes floating adjacent to an OEG-SAM surface in the FFM system at pH 3, 7 and 10 with neutron reflectometry (NR) measurements. Each of the NR measurements, performed at different pH conditions, were conducted at three different salt conditions: in absence of additional cations, as well as in presence of 2 mM $CaCl_2$ and 150 mM NaCl. We were able to reproduce previous NR results at pH 7 [287], showing a small distance between OEG-SAM and floating membranes of around 12-13 Å in the presence of 2 mM $CaCl_2$, an intermediate distance of around 31-34 Å in the presence of 150 mM NaCl and a very large distance after removing any cations via EDTA treatment ($\sim$147 Å for POPC only and $\sim$83 Å for POPC/POPS membrane). Our previous hypothesis was that the cause of these distance modulations is mainly due to the surface charge modulation of the OEG-SAM resulting from cation binding. Additionally, we suggested that an attractive bridging effect between OEG-SAM and membrane caused by the enhanced cation concentration in the water inter-layer is more pronounced for Ca^{2+} than for Na^{+}. This explains the close membrane positions in the presence of Ca^{2+} and the intermediate positions in the presence of Na^{+}.

However, in contrast to our previous hypothesis, both membranes POPC and POPC/POPS showed very short distances between OEG-SAM and floating membrane for all applied salt buffer conditions at pH 3. Here, the FFM-to-SAM distance lays with 7-12 Å in the FFM-to-SAM distance regime we previously observed only in the presence of Ca^{2+} (see Table 3.1). At pH 3 the carboxyl groups of the OEG-SAM are protonated, making the OEG-SAM surface neutral. At the same time the POPC membrane is 1% and the POPC/POPS membrane 6.4% positively charged (see Table3.2-3.5), meaning there is no electrostatic attraction present between the two layers. Therefore, the absence of the repulsion between membrane and OEG-SAM alone is responsible for short FFM-to-SAM distances, caused by attractive, long range vdW forces.[235] No additional attractive bridging effect between

membrane and OEG-SAM seems necessary for reaching FFM-to-SAM distances of around 10 Å. These results agree with our previous model on the prediction that the OEG-SAM surface charge modulation is the main driving force behind the large membrane movements in the FFM system. However, our results disagree with the predicted additional attractive bridging effect caused by the enhanced cation density in the water inter-layer we postulated earlier.[287] The cations seem to be solely another instrument for decreasing the repulsion between the layers, not causing any additional attraction force though, with Ca^{2+} attenuating the repulsion force more pronounced than Na^{+}.

The molecular dynamics (MD) simulations of the different layers at pH 3, 7 and 10, in the presence of 200 mM Ca^{2+} and 200 mM Na^{+}, support the new conclusion that cations reduce the repulsion force between OEG-SAM and floating membrane, while not causing an additional attractive bridging effect between them. Both cations show no binding to both POPC and POPC/POPS membrane at different pH conditions. Only Ca^{2+} shows a small binding affinity to the POPC/POPS membrane at pH 7 and 10 (Figure 3.6). In contrast, both cations show strong affinity towards the OEG-SAM at pH 7 and 10, with Ca^{2+} showing larger free cation binding energies than Na^{+} (Figure 3.5). These findings agree on the model suggesting that the cations decrease the repulsion between OEG-SAM and membrane due to binding onto the OEG-SAM surface, while at the same time not applying an attractive bridging force towards the floating membrane as the extent of cation affinity towards phospholipid membranes seems negligible.

Additionally, our simulations showed structured water layers of around five molecular water diameters (2.8 Å) on top of the OEG-SAM surface for both salt buffer conditions (Figure 3.4). This was expected and in agreement with previous findings, making us confident in interpreting our simulations.[256], [257] Interestingly, the oscillations in the water density, which indicate the structured water layers, disappeared at high pH for both salt conditions. This change was accompanied by an increase in SASA and decrease of the molecular tilt angle of the charged molecules in the OEG-SAM (Figure 3.3). The stable structure of an OEG-SAM is based on a delicate interplay between several interactions: bonded interactions between gold and thiol group of OEG-SAM molecules, intermolecular non-bonded interactions between OEG-SAM molecules - electrostatic (between terminal carboxyl groups) and vdW forces (chain-chain interactions) - and intramolecular interactions (bond

stretches, angle bend, torsions).[251] Therefore, the structural changes we observed are likely caused by increased electrostatic repulsion between the terminal carboxyl groups, which are negatively charged at high pH. The less tilted conformation of the OEG-SAM allows water to penetrate deeper into the OEG-SAM (Figure 3.3), which at the same time might cause the structural rearrangement of the water on top ot the OEG-SAM surface. Notably, it has been experimentally shown that the character of the thiol-gold binding depends on the pH condition: with increasing pH the bond type shifts from coordinate bond to covalent bond.[294] It is very likely that the altered thiol-gold bond influences the tilt angle of the OEG-SAM. However, our CG simulations are unable to capture such changes and more advanced all atomistic simulations, including polarizable force-fields, would be needed to determine the specific effects of pH on the tilt angle of OEG-SAMs under different conditions. OEG-SAMs have a variety of applications, such as generating biofunctionalized and antifouling surfaces [241], [292]. Understanding the factors that influence the orientation of the OEG-SAM molecules is important for these applications as it affects the surface properties.

Due to its unique properties such OEG-SAMs are a key component of the FFM system. Therefore, we wanted to investigate to what extent the presence of the OEG-SAM effects the biophysical properties of a floating phospholipid membrane in the FFM system. For this investigation we simulated membranes of different lipid compositions at varying distances away from the OEG-SAM. At close distances of around 9 Å we observed decreased lateral lipid diffusion of POPC and POPS in the leaflet facing towards the OEG-SAM (lower leaflet) of POPC and POPC:POPS (8:2, mol:mol) membranes. This decreased lipid dynamics solely in the lower leaflet is in agreement with previous findings: Here, an even smaller distance between a solid scaffold and a dioleoylphosphatidylethanolamine (DOPC) of 2 Å was simulated and showed only decreased dynamics in the lower leaflet, while the upper leaflet facing towards the bulk water was not affected.[295] Considering that the vdW interactions were shifted from 9 to 11 Å and electrostatics were described by the reaction field method, using a potential shift modifier with a cut-off of 11 Å, it is no surprise that we were not able to observe any significant changes in lipid dynamics at the larger distances between OEG-SAM and floating membrane. Interestingly, in the anionic POPC/POPS membrane the lateral lipid diffusion was smaller

in the presence of Ca^{2+} compared to Na^{+} for both lipid species. This effect got even more pronounced in the highly negatively charged POPC:POPS:POPIP3 (7:2:1, mol:mol) membrane for all three lipid species, with POPIP3 showing the most drastic difference between lipid diffusion coefficients in the presence of Ca^{2+} compared to Na^{+}. These findings agree well with previous studies suggesting cross-bridging between lipids in negatively charged phospholipid membranes by Ca^{2+}, thus slowing down lipid diffusion.[244], [296] In conclusion, for highly negatively charged membranes the effect an adjacent OEG-SAM might have on the lipid diffusion of the floating membrane is overridden by cations and for less charged or neutral membranes the effects seem to become negligible at distances above ∼25 Å. While the lipid dynamics show some impact by the OEG-SAM, there was no consistent change in lipid tail conformation caused by the presence of the OEG-SAM (see Figure 3.9). Taking together these findings, they seem to promise indeed that the FFM-system represents a planar model membrane system, in which the membrane can be tuned by suitable pH conditions and/or salt buffer conditions to a FFM-to-SAM distance of ∼25 Å above which the floating membrane feels basically no influence by the substrate concerning membrane-fluidity and lipid conformation.

3.4 Materials and Methods

3.4.1 Materials

See section 2.4.1.

3.4.2 Neutron Reflectometry (NR) Measurements

The same process was undertaken as previously described in section 2.4.2. Modifications to the previous protocol are given here: Specular neutron reflectometry (NR) measurements were carried out using the white beam INTER reflectometer at the ISIS Spallation Neutron Source, Rutherford Appleton Laboratory (Oxfordshire, UK), using neutron wavelengths from 1.0 to 18.0 Å. The reflected intensity was measured at glancing angles of 0.7° and 2.3°. Reflectivity was measured as a function of the momentum transfer Q_z, with $Q_z = (4\pi sin\theta) \,/\, \lambda$ where λ is wavelength and θ is the incident

angle. Data were obtained at a nominal resolution $(dQ\ /\ Q)$ of 3.5%. The total illuminated sample length was ∼60 mm on an ∼80 mm substrate.

3.4.3 Molecular Dynamics (MD) Simulations

Coarse Grained (CG) Simulation Setups

This chapter employed the newly released version 3 of the Martini force field [206] (note, in *Chapter 2* we used the interim version beta 3.0.b.3.2 [248]). Using standard Martini3 beads the mapping scheme between CG and AA resulted in a SC5 bead for the thioethyl tail group, SN3a beads for the C-O-C-groups and C1 beads for each nbutyl group for both molecules. The carboxyl head group was mapped into a SP2 bead for the neutral and into a SQ5n bead for the negatively charged state. Note, compared to the previous parametrization of *Chapter 2* this means a switch from SN0 to SN3a for the C-O-C-groups and from SQn to SQ5n for the negatively charged carboxyl group. Therefore, a new implementation of the negatively charged COO^--SAM and neutral COOH-SAM molecule within the Martini3 force field [206] was needed. This was again achieved by fitting the results from CG MD simulations (bond length and bond angle distributions) to AA MD simulations with the CHARMM36 force field.[254], [281] The initial topology for the CHARMM36 was generated by using the CHARMM-GUI Ligand Reader and Modeler.[282] The provided parameter estimations from 1 µs AA simulations of COO^--/COOH-SAM in water (TIP3P) were taken for the CG simulations and refined if necessary (see Figure 3.10). The previously obtained parameters worked well for the new bead mapping in the new force field and were used in the following (parameters are listed in Table 2.8).

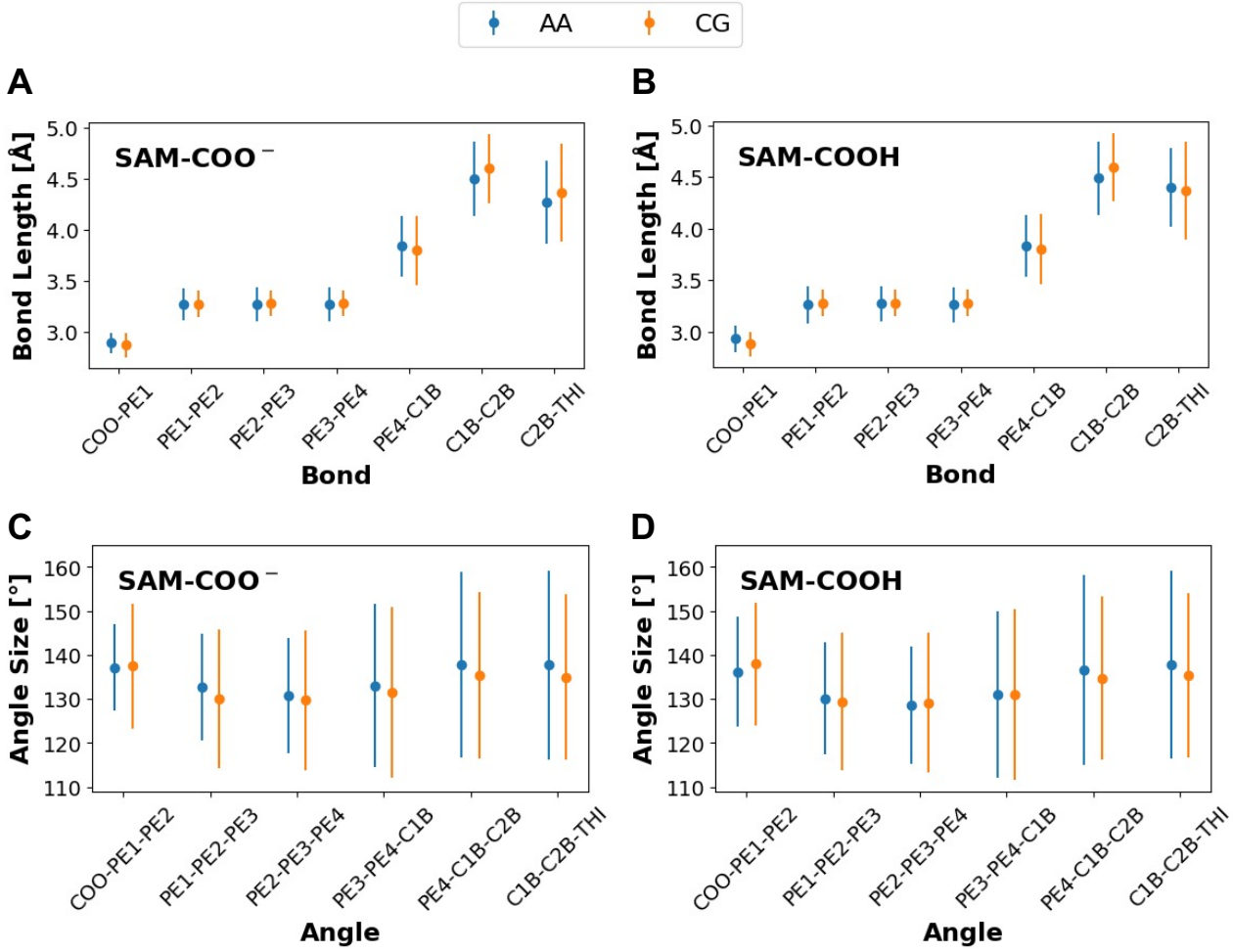


Figure 3.10 | Mapped Bond Length and Angle Distributions. Mean and standard deviation of bond length distributions of Martini3-CG (orange) and CHARMM36-AA (blue) charged (COO^-) (**A**) and uncharged (COOH) SAM-molecules (**B**). Mean and standard deviation of angle distributions of CG (orange) and AA (blue) charged (COO^-) (**C**) and uncharged (COOH) SAM molecules (**D**).

.

The simulations of phospholipid membranes and OEG-SAMs at different pH conditions required the parameterized of POPC and POPS lipids with different head group charges: For generating the positively charged, protonated POPC lipid, the negatively charged Q5 bead of the POPC head group was converted into a neutral P6 bead (Table 3.4). In case of POPS, three additional POPS lipid versions had to be generated, a positively, twice negatively charged and neutral POPS lipid. For the positively charged POPS, the CNO bead was converted from a neutral P6 to a positively charged Q5p bead, as well as the PO4 bead from a negatively charged Q5 bead to a neutral P6 bead. Following this scheme, for the neutral POPS only the CNO bead was converted from a neutral P6 to a positively charged

Q5p bead. And finally for the twice negatively charged POPS only the CNO bead was converted from a neutral P6 to a negatively charged Q5n bead (Table 3.4).

Then, the phospholipid membranes and OEG-SAMs were generated for the different pH conditions with a charged *vs.* uncharged molecule ratio provided by the protonation probabilities using a modification of the Python tool *insane.py* [283]. The modifications of the script involved the introduction of the COOH-SAM, COO^--SAM and newly defined POPC, POPS lipid matrix, as well as the positioning of the OEG-SAM molecules onto a hexagonal lattice with a defined lattice constant of 5.3 Å. The lipid bilayers were initially generated in a 200 $\times$ 200 $\times$ 300 Å box, while the initial x/y-dimensions of the OEG-SAMs corresponded to the x/y-dimensions of the final frame of the membrane simulation and a z-dimension of 200 Å. As previously described (Methods 2.4.4), the thioethyl tail beads of the SAM molecules (SC5) were restrained to a plane with a harmonic force constant of 5000 kJ/(mol nm^2). The molecule definitions, as well as the membrane and OEG-SAM compositions can be found in detail in Tables 3.4 and 3.5. The systems were each simulated separately in the presence of 200 mM Ca^{2+} and 200 mM Na^+, with the cation concentrations being calculated as previously stated (Methods 2.4.4). Note, in this concentration the counter-ions for neutralizing the simulation systems are included, except for the OEG-SAM system at pH 10 and in the presence of Na^+. Here, due to the fully negatively charged surface, a final sodium concentration of 400 mM was needed for fulfilling neutralization of the simulation system.

Molecule	State of Funct. Grps.	Bead Definition
POPC positive = POPU	PO_3-OH	PO4: Q5 –> P6
POPS neutral = POPT	PO_4^-, COOH, NH_3^+	CNO: P6 –> Q5p
POPS twice negative = POPN	PO_4^-, COO^-, NH_2	CNO: P6 –> Q5n
POPS positive = POPP	PO_3-OH, COOH, NH_3^+	CNO: P6 –> Q5p PO4: Q5 –> P6
OEG-SAM negative = SPA	COO^-	COO: SQ5n
OEG-SAM neutral = SPU	COOH	COO: SP2

Table 3.4: | Molecule and Bead Definition. Defined names, as well as the state of the respective functional groups and corresponding changes in the CG Martini bead definition are given for all used molecules.

Layer	pH	Composition
POPC	pH 3	POPC (99%): POPU (1%)
POPC	pH 7	POPC (100%)
POPC	pH 10	POPC (100%)
POPC:POPS (8:2)	pH 3	POPC (79.2%) : POPU (0.8%) : POPP (5.6%): POPT (14.4%)
POPC:POPS (8:2)	pH 7	POPC (80%) : POPS (19.4%) : POPT (0.6%)
POPC:POPS (8:2)	pH 10	POPC (80%) : POPS (19.4 %) : POPN (0.6%)
OEG-SAM	pH 3	SPU (100%)
OEG-SAM	pH 7	SPU (72%) : SPA (28%)
OEG-SAM	pH 10	SPA (100%)

Table 3.5: | Membrane and OEG-SAM Compositions at Different pH Conditions. Given are all membrane and OEG-SAM compositions in detail at the different pH conditions. Note, in the compositions the names POPC and POPS were given for the standard lipids given in Martini 3, so for the neutral POPC and simple negatively charged POPS.

For the multilayer system studies we followed the procedure described previously (Methods2.4.4) with some differences as follows: We used a POPC only, POPC:POPS (8:2, mol:mol) and a POPC:POPS:POPIP3 (7:2:1, mol:mol:mol) membrane. The concentration of both cations Na^+ and Ca^{2+} was 200 mM and the initial z-dimension set to 300 Å. The initial distance between OEG-SAM and membrane surface was set to 15, 30 and 90 Å for each system.

Coarse Grained (CG) Simulation Protocols

For the pH studies, the same protocol as presented in *Chapter 2* was applied (Method section, CG Simulation Protocol) with the following differences: Martini force file version 3 was used.[206] There was no NVT equilibration step.

For the multi-layer systems the same protocol was applied for the separate layers. After combining the layers and solvating the system with water and evenly distributed 200 mM Na^+ or 200 mM Ca^{2+} across the water, the system ran for 2 µs with a time step of 1 fs, lateral and normal compressibility of 0 and 3.0×10^{-4} bar^{-1}, respectively.

3.4.4 Appendix

POPC, Na^+	No SAM, no hole, no x/y-p	No SAM, with hole, no x/y-p	No SAM, with hole, with x/y-p	FFM 15 Å to SAM	FFM 30 Å to SAM	FFM 90 Å to SAM
POPC Diffusion *top* [x10^{-5} cm^2/s] Mean (Mode)	0.066 +/- 0.040 (0.020)	0.074 +/- 0.047 (0.020)	0.066 +/- 0.037 (0.021)	0.069 +/- 0.046 (0.018)	0.080 +/- 0.054 (0.029)	0.067 +/- 0.045 (0.020)
POPC Diffusion *bottom* [x10^{-5} cm^2/s] Mean (Mode)	0.065 +/- 0.039 (0.022)	0.077 +/- 0.045 (0.023)	0.066 +/- 0.039 (0.021)	0.047 +/- 0.027 (0.015)	0.064 +/- 0.043 (0.023)	0.069 +/- 0.045 (0.021)

POPC, Ca^{2+}	No SAM, no hole, no x/y-p	No SAM, with hole, no x/y-p	No SAM, with hole, with x/y-p	FFM 15 Å to SAM	FFM 30 Å to SAM	FFM 90 Å to SAM
Lateral Diffusion *top* [x10^{-5} cm^2/s] Mean (Mode)	0.060 +/- 0.040 (0.023)	0.062 +/- 0.038 (0.019)	0.067 +/- 0.041 (0.024)	0.072 +/- 0.040 (0.022)	0.066 +/- 0.038 (0.023)	0.072 +/- 0.047 (0.026)
Lateral Diffusion *bottom* [x10^{-5} cm^2/s] Mean (Mode)	0.064 +/- 0.044 (0.019)	0.068 +/- 0.039 (0.024)	0.074 +/- 0.047 (0.024)	0.042 +/- 0.025 (0.014)	0.068 +/- 0.044 (0.024)	0.077 +/- 0.049 (0.030)

Table 3.6: | Lateral Lipid Diffusion Coefficients in CG POPC Membranes. Calculated lateral lipid diffusion coefficients of POPC within a POPC membrane in the presence of 200 mM Na^+ and 200 mM Ca^{2+}. Different system setups were used: Standard compressibility (Mem), standard compressibility and a hole introduced (Mem + Hole), with a hole and a lateral compressibility of zero (Mem + Hole + x/y-p), multi-layer FFM-Systems with the membrane initially set to a FFM-to-SAM distance of 15, 30 and 90 Å (FFM 15, 30, 90 Å to SAM). Shown is the mean of the single lipid diffusion coefficients (see Figure 3.8 for visualisation). The modes of the same distributions are given in parenthesis. The errors represent the standard deviation of the distribution, estimated by $(full\ width\ at\ half\ maximum \times 2.355)$. The lower leaflet was defined as the leaflet facing towards the OEG-SAM surface in the multi-layer FFM-Systems, the upper leaflet was facing the bulk water. For the simulations without the OEG-SAM present (Mem, Mem + Hole, Mem + Hole + x/y-p) the lower and upper leaflet are interchangeable.

.

POPC:POPS (8:2, mol:mol), Na^+	No SAM, no hole, no x/y-p	No SAM, with hole, no x/y-p	No SAM, with hole, with x/y-p	FFM 15 Å to SAM	FFM 30 Å to SAM	FFM 90 Å to SAM
POPC Diffusion *top* [x10^{-5} cm^2/s] Mean (Mode)	0.069 +/- 0.041 (0.024)	0.073 +/- 0.046 (0.027)	0.063 +/- 0.045 (0.019)	0.065 +/- 0.043 (0.019)	0.067 +/- 0.048 (0.021)	0.065 +/- 0.039 (0.019)
POPC Diffusion *bottom* [x10^{-5} cm^2/s] Mean (Mode)	0.062 +/- 0.043 (0.022)	0.062 +/- 0.040 (0.022)	0.057 +/- 0.036 (0.017)	0.052 +/- 0.035 (0.022)	0.066 +/- 0.040 (0.024)	0.069 +/- 0.048 (0.026)
POPS Diffusion *top* [x10^{-5} cm^2/s] Mean (Mode)	0.064 +/- 0.047 (0.022)	0.077 +/- 0.050 (0.036)	0.064 +/- 0.049 (0.029)	0.058 +/- 0.046 (0.027)	0.079 +/- 0.055 (0.033)	0.058 +/- 0.045 (0.023)
POPS Diffusion *bottom* [x10^{-5} cm^2/s] Mean (Mode)	0.069 +/- 0.053 (0.026)	0.064 +/- 0.039 (0.022)	0.059 +/- 0.043 (0.015)	0.046 +/- 0.032 (0.027)	0.072 +/- 0.051 (0.031)	0.065 +/- 0.042 (0.023)

POPC:POPS (8:2, mol:mol), Ca^{2+}	No SAM, no hole, no x/y-p	No SAM, with hole, no x/y-p	No SAM, with hole, with x/y-p	FFM 15 Å to SAM	FFM 30 Å to SAM	FFM 90 Å to SAM
POPC Diffusion *top* [x10^{-5} cm^2/s] Mean (Mode)	0.057 +/- 0.040 (0.020)	0.058 +/- 0.038 (0.019)	0.061 +/- 0.040 (0.020)	0.054 +/- 0.030 (0.018)	0.062 +/- 0.041 (0.024)	0.059 +/- 0.039 (0.019)
POPC Diffusion *bottom* [x10^{-5} cm^2/s] Mean (Mode)	0.059 +/- 0.036 (0.021)	0.058 +/- 0.037 (0.020)	0.056 +/- 0.037 (0.018)	0.042 +/- 0.027 (0.013)	0.064 +/- 0.039 (0.021)	0.054 +/- 0.036 (0.019)
POPS Diffusion *top* [x10^{-5} cm^2/s] Mean (Mode)	0.062 +/- 0.039 (0.025)	0.053 +/- 0.040 (0.020)	0.049 +/- 0.036 (0.020)	0.052 +/- 0.037 (0.022)	0.059 +/- 0.037 (0.023)	0.048 +/- 0.041 (0.019)
POPS Diffusion *bottom* [x10^{-5} cm^2/s] Mean (Mode)	0.054 +/- 0.040 (0.032)	0.049 +/- 0.043 (0.012)	0.041 +/- 0.029 (0.019)	0.036 +/- 0.026 (0.017)	0.062 +/- 0.042 (0.024)	0.052 +/- 0.044 (0.020)

Table 3.7: | Lateral Lipid Diffusion Coefficients in CG POPC:POPS (8:2, mol:mol) Membranes. Calculated lateral lipid diffusion coefficients of POPC and POPS within a POPC/POPS membrane in the presence of 200 mM Na^+ and 200 mM Ca^{2+}. Different system setups were used: Standard compressibility (Mem), standard compressibility and a hole introduced (Mem + Hole), with a hole and a lateral compressibility of zero (Mem + Hole + x/y-p), multi-layer FFM-Systems with the membrane initially set to a FFM-to-SAM distance of 15, 30 and 90 Å (FFM 15, 30, 90 Å to SAM). Shown is the mean of the single lipid diffusion coefficients (see Figure 3.8 for visualisation). The modes of the same distributions are given in parenthesis. The errors represent the standard deviation of the distribution, estimated by $(full\ width\ at\ half\ maximum \times 2.355)$. The lower leaflet was defined as the leaflet facing towards the OEG-SAM surface in the multi-layer FFM-Systems, the upper leaflet was facing the bulk water. For the simulations without the OEG-SAM present (Mem, Mem + Hole, Mem + Hole + x/y-p) the lower and upper leaflet are interchangeable.

.

POPC:POPS:POPIP3 (7:2:1, mol:mol:mol), Na^+	No SAM, no hole, no x/y-p	No SAM, with hole, no x/y-p	No SAM, with hole, with x/y-p	FFM 15 Å to SAM	FFM 30 Å to SAM	FFM 90 Å to SAM
POPC Diffusion *top* [x10^{-5} cm^2/s] Mean (Mode)	0.059 +/- 0.041 (0.019)	0.060 +/- 0.039 (0.019)	0.059 +/- 0.039 (0.020)	0.054 +/- 0.036 (0.019)	0.056 +/- 0.036 (0.021)	0.069 +/- 0.042 (0.023)
POPC Diffusion *bottom* [x10^{-5} cm^2/s] Mean (Mode)	0.054 +/- 0.035 (0.023)	0.057 +/- 0.036 (0.021)	0.057 +/- 0.033 (0.022)	0.048 +/- 0.031 (0.016)	0.056 +/- 0.037 (0.018)	0.061 +/- 0.042 (0.024)
POPS Diffusion *top* [x10^{-5} cm^2/s] Mean (Mode)	0.060 +/- 0.046 (0.023)	0.061 +/- 0.039 (0.026)	0.067 +/- 0.049 (0.033)	0.051 +/- 0.033 (0.017)	0.051 +/- 0.034 (0.021)	0.066 +/- 0.046 (0.031)
POPS Diffusion *bottom* [x10^{-5} cm^2/s] Mean (Mode)	0.055 +/- 0.044 (0.018)	0.052 +/- 0.034 (0.020)	0.052 +/- 0.034 (0.025)	0.048 +/- 0.038 (0.018)	0.054 +/- 0.036 (0.021)	0.067 +/- 0.046 (0.021)
POPIP3 Diffusion *top* [x10^{-5} cm^2/s] Mean (Mode)	0.056 +/- 0.040 (0.024)	0.046 +/- 0.033 (0.020)	0.062 +/- 0.052 (0.032)	0.043 +/- 0.028 (0.020)	0.050 +/- 0.046 (0.028)	0.052 +/- 0.030 (0.021)
POPIP3 Diffusion *bottom* [x10^{-5} cm^2/s] Mean (Mode)	0.039 +/- 0.028 (0.028)	0.049 +/- 0.034 (0.026)	0.050 +/- 0.040 (0.023)	0.037 +/- 0.028 (0.018)	0.043 +/- 0.038 (0.034)	0.061 +/- 0.048 (0.025)

POPC:POPS:POPIP3 (7:2:1, mol:mol:mol), Ca^{2+}	No SAM, no hole, no x/y-p	No SAM, with hole, no x/y-p	No SAM, with hole, with x/y-p	FFM 15 Å to SAM	FFM 30 Å to SAM	FFM 90 Å to SAM
POPC Diffusion *top* [x10^{-5} cm^2/s] Mean (Mode)	0.041 +/- 0.025 (0.013)	0.039 +/- 0.025 (0.015)	0.043 +/- 0.026 (0.014)	0.039 +/- 0.025 (0.014)	0.037 +/- 0.022 (0.011)	0.047 +/- 0.028 (0.016)
POPC Diffusion *bottom* [x10^{-5} cm^2/s] Mean (Mode)	0.043 +/- 0.029 (0.017)	0.043 +/- 0.029 (0.017)	0.041 +/- 0.026 (0.015)	0.041 +/- 0.026 (0.015)	0.046 +/- 0.027 (0.013)	0.038 +/- 0.029 (0.010)
POPS Diffusion *top* [x10^{-5} cm^2/s] Mean (Mode)	0.025 +/- 0.019 (0.011)	0.032 +/- 0.025 (0.011)	0.037 +/- 0.026 (0.014)	0.022 +/- 0.015 (0.007)	0.024 +/- 0.018 (0.008)	0.036 +/- 0.026 (0.010)
POPS Diffusion *bottom* [x10^{-5} cm^2/s] Mean (Mode)	0.026 +/- 0.019 (0.010)	0.026 +/- 0.017 (0.008)	0.028 +/- 0.022 (0.010)	0.049 +/- 0.032 (0.015)	0.041 +/- 0.032 (0.013)	0.033 +/- 0.020 (0.009)
POPIP3 Diffusion *top* [x10^{-5} cm^2/s] Mean (Mode)	0.014 +/- 0.010 (0.005)	0.019 +/- 0.013 (0.007)	0.009 +/- 0.008 (0.003)	0.014 +/- 0.010 (0.004)	0.012 +/- 0.008 (0.004)	0.017 +/- 0.013 (0.005)
POPIP3 Diffusion *bottom* [x10^{-5} cm^2/s] Mean (Mode)	0.009 +/- 0.007 (0.002)	0.014 +/- 0.009 (0.007)	0.010 +/- 0.009 (0.004)	0.006 +/- 0.005 (0.004)	0.002 +/- 0.003 (0.001)	0.010 +/- 0.010 (0.002)

Table 3.8: | Lateral Lipid Diffusion Coefficients in CG POPC:POPS:POPIP3 (7:2:1, mol:mol:mol) Membranes. Calculated lateral lipid diffusion coefficients of POPC, POPS and POPIP3 within a POPC/POPS/POPIP3 membrane in the presence of 200 mM Na^+ and 200 mM Ca^{2+}. Different system setups were used: Standard compressibility (Mem), standard compressibility and a hole introduced (Mem + Hole), with a hole and a lateral compressibility of zero (Mem + Hole + x/y-p), multi-layer FFM-Systems with the membrane initially set to a FFM-to-SAM distance of 15, 30 and 90 Å (FFM 15, 30, 90 Å to SAM). Shown are the mean of the single lipid diffusion coefficients (see Figure 3.8 for visualisation). The modes of the same distributions are given in parenthesis. The errors represent the standard deviation of the distribution, estimated by $(full\ width\ at\ half\ maximum \times 2.355)$. Lower leaflet was defined as the leaflet facing towards the OEG-SAM surface in the multi-layer FFM-Systems, the upper leaflet was facing the bulk water. For the simulations without the OEG-SAM present (Mem, Mem + Hole, Mem + Hole + x/y-p) the lower and upper leaflet are interchangeable.

.

Membrane + 200 mM Ca^{2+}	***Leaflet***	**Mem**	**Mem + Hole**	**Mem + Hole + x/y-p**	**FFM-System 15 Å**	**FFM-System 30 Å**	**FFM-System 90 Å**
POPC	*top*	0.361	0.379	0.355	0.369	0.372	0.348
POPC	*bottom*	0.360	0.360	0.349	0.379	0.366	0.382
POPC/POPS	*top*	0.362	0.384	0.372	0.383	0.358	0.353
POPC/POPS	*bottom*	0.373	0.354	0.344	0.374	0.353	0.384
POPC/POPS/POPIP3	*top*	0.370	0.356	0.365	0.387	0.350	0.342
POPC/POPS/POPIP3	*bottom*	0.366	0.380	0.370	0.365	0.340	0.391
Membrane + 200 mM Na^{+}	***Leaflet***	**Mem**	**Mem + Hole**	**Mem + Hole + x/y-p**	**FFM-System 15 Å**	**FFM-System 30 Å**	**FFM-System 90 Å**
POPC	*top*	0.359	0.366	0.356	0.372	0.350	0.378
POPC	*bottom*	0.368	0.360	0.348	0.385	0.336	0.376
POPC/POPS	*top*	0.374	0.363	0.360	0.384	0.360	0.376
POPC/POPS	*bottom*	0.388	0.363	0.362	0.391	0.384	0.386
POPC/POPS/POPIP3	*top*	0.346	0.367	0.356	0.366	0.374	0.363
POPC/POPS/POPIP3	*bottom*	0.358	0.336	0.359	0.355	0.352	0.355

Table 3.9: | POPC Order Parameters in CG Phospholipid Membranes and FFM Systems. Time (last 3 time steps) and ensemble average for POPC carbon chain order parameters $< S >$ of the top and bottom leaflets of different phospholipid membranes, in the presence of 200 mM Ca^{2+} and 200 mM Na^{+}. The bottom leaflet was defined as the leaflet facing towards the OEG-SAM surface in the multi-layer FFM-Systems, the top leaflet was facing the bulk water. For the simulations without the OEG-SAM present (Mem, Mem + Hole, Mem + Hole + xy/-p) the bottom and top leaflet are interchangeable. The phospholipid membranes itself were simulated with standard compressibility (column: Mem), then with standard compressibility and a hole introduced (column: Mem + Hole) and finally also with a hole and a lateral compressibility of zero (column: Mem + Hole + x/y-p). For the multi-layer FFM-Systems the membranes were initially set to a FFM-to-SAM distance of 15, 30 and 90 Å (columns: FFM-System 15, 30, 90 Å).

Membrane + 200 mM Ca^{2+}	***Leaflet***	**Mem**	**Mem + Hole**	**Mem + Hole + x/y-p**	**FFM-System 15 Å**	**FFM-System 30 Å**	**FFM-System 90 Å**
POPC/POPS	*top*	0.375	0.403	0.392	0.414	0.376	0.353
POPC/POPS	*bottom*	0.373	0.376	0.372	0.371	0.363	0.385
POPC/POPS/POPIP3	*top*	0.377	0.391	0.391	0.380	0.372	0.392
POPC/POPS/POPIP3	*bottom*	0.406	0.379	0.378	0.351	0.307	0.352
Membrane + 200 mM Na^{+}	***Leaflet***	**Mem**	**Mem + Hole**	**Mem + Hole + x/y-p**	**FFM-System 15 Å**	**FFM-System 30 Å**	**FFM-System 90 Å**
POPC/POPS	*top*	0.371	0.388	0.367	0.371	0.397	0.375
POPC/POPS	*bottom*	0.379	0.396	0.337	0.383	0.412	0.366
POPC/POPS/POPIP3	*top*	0.385	0.380	0.403	0.377	0.389	0.396
POPC/POPS/POPIP3	*bottom*	0.326	0.370	0.377	0.331	0.395	0.360

Table 3.10: | POPS Order Parameters in CG Phospholipid Membranes and FFM Systems. Time (last 3 time steps) and ensemble average for POPS carbon chain order parameters $< S >$ of the top and bottom leaflets of different phospholipid membranes, in the presence of 200 mM Ca^{2+} and 200 mM Na^{+}. The bottom leaflet was defined as the leaflet facing towards the OEG-SAM surface in the multi-layer FFM-Systems, the top leaflet was facing the bulk water. For the simulations without the OEG-SAM present (Mem, Mem + Hole, Mem + Hole + xy/-p) the bottom and top leaflet are interchangeable. The phospholipid membranes itself were simulated with standard compressibility (column: Mem), then with standard compressibility and a hole introduced (column: Mem + Hole) and finally also with a hole and a lateral compressibility of zero (column: Mem + Hole + x/y-p). For the multi-layer FFM-Systems the membranes were initially set to a FFM-to-SAM distance of 15, 30 and 90 Å (columns: FFM-System 15, 30, 90 Å).

Membrane + 200 mM Ca^{2+}	***Leaflet***	**Mem**	**Mem + Hole**	**Mem + Hole + x/y-p**	**FFM-System 15 Å**	**FFM-System 30 Å**	**FFM-System 90 Å**
POPC/POPS/POPIP3	*top*	0.400	0.420	0.421	0.423	0.399	0.402
POPC/POPS/POPIP3	*bottom*	0.447	0.418	0.432	0.416	0.404	0.395
Membrane + 200 mM Na^{+}	***Leaflet***	**Mem**	**Mem + Hole**	**Mem + Hole + x/y-p**	**FFM-System 15 Å**	**FFM-System 30 Å**	**FFM-System 90 Å**
POPC/POPS/POPIP3	*top*	0.371	0.450	0.409	0.413	0.383	0.368
POPC/POPS/POPIP3	*bottom*	0.440	0.415	0.417	0.388	0.401	0.426

Table 3.11: | POPIP3 Order Parameters in CG Phospholipid Membranes and FFM Systems. Time (last 3 time steps) and ensemble average for POPIP3 carbon chain order parameters $< S >$ of the top and bottom leaflets of different phospholipid membranes, in the presence of 200 mM Ca^{2+} and 200 mM Na^{+}. The bottom leaflet was defined as the leaflet facing towards the OEG-SAM surface in the multi-layer FFM-Systems, the top leaflet was facing the bulk water. For the simulations without the OEG-SAM present (Mem, Mem + Hole, Mem + Hole + xy/-p) the bottom and top leaflet are interchangeable. The phospholipid membranes itself were simulated with standard compressibility (column: Mem), then with standard compressibility and a hole introduced (column: Mem + Hole) and finally also with a hole and a lateral compressibility of zero (column: Mem + Hole + x/y-p). For the multi-layer FFM-Systems the membranes were initially set to a FFM-to-SAM distance of 15, 30 and 90 Å (columns: FFM-System 15, 30, 90 Å).

4

Applying the FFM System to Study Peripheral Membrane Proteins

Contents

4.1 Introduction 138
4.2 Results 141
4.2.1 NR Experiments Reveal Crucial Conditions for Studying PMPs 141
4.2.2 MD Simulations Provide Further Insights in Binding Conformations 160
4.3 Discussion 179
4.4 Methods 184
4.4.1 Materials 184
4.4.2 Protein Constructs 185
4.4.3 ATR-FTIR Experiments 188
4.4.4 Neutron Reflectometry Experiments 189
4.4.5 MD Simulations 194
4.5 Appendix 198

4.1 Introduction

The interaction between cytoplasmic peripheral membrane proteins (PMPs) and membranes is a key element for many cellular processes, such as vesicle trafficking, cytoskeleton reorganization, cell growth, chemotaxis, DNA synthesis, signalling and apoptosis.[297]–[301] Therefore, the investigation of binding processes between individual peripheral proteins and membranes are of great importance, albeit often poorly understood. By providing a fully atomistic resolution of the interacting membrane and protein, molecular dynamics (MD) simulation is a powerful technique for these investigations.

However, the approximations made in the MD force fields require experimental data for justifying the results. The problem is that for many membrane-targeting protein domains there is still only limited experimental evidence for their penetration, orientation, and position at the membrane interface. Various model membrane systems which mimic natural characteristics as closely as possible were developed to investigate the conformational changes in protein and membranes due to their interaction.[95] The most advanced model membrane system for this is probably the free floating membrane (FFM) system. Here, a water layer between the membrane and the subjacent substrate decreases the influence of the substrate on the membrane dynamics (see *Chapter 2* and *3*).[133] In this chapter we used this FFM system together with neutron reflectometry (NR) measurements to investigate the orientation and penetration of peripheral membrane proteins at the membrane interface. NR measurements provide insights in the contribution and distribution of the protein and the lipid components across the membrane-protein-complex and is therefore able to complement our MD results.[302]

Many cytoplasmic peripheral membrane proteins, like GDP/GTP exchange factors (e.g. Grp1), cytoskeleton regulator proteins (e.g. Rac), protein kinases (e.g. Akt1, PDK1) and lipid kinases (e.g. PI3K), use polybasic binding domains to bind on negatively charged phospholipids, which are enriched in the cytoplasmic leaflet.[32] Aside from POPS (1-palmitoyl-2-oleoyl-*sn*-glycero-3-phospho-L-serine), the by far principal anionic phospholipid present in the cytoplasmic leaflet, the most important protein recruiting anionic lipids are the PIPs (phosphatidylinositols).[33], [34], [42] Besides the FYVE, PX, ENTH, CALM, PDZ, PTB and FERM domains,[25] with more than 250 human proteins, one of the largest family of PIP binding domains is the pleckstrin homology (PH) domain.[48], [303] It is known that some of the PH domains show a degree of selectivity to one of the various phosphorylated derivatives of phosphatidylinositol, therefore enabling spatial and temporal docking of the PIP's parent protein.[304] One of the best studied representative of this group is the PH domain of the general receptor for phosphoinositides 1 (Grp1), which binds to POPI(3,4,5)P_3 with unusually high selectivity and affinity.[62], [63] The proteins which were investigated within this work are mMkindlin-2 (K2) and mMT-lymphoma invasion and metastasis 2 (TIAM2) and contain both a PIP binding PH domain.

The PH domain of K2 (K2-PH) is known to bind POPI(4,5)P_2 (1-palmitoyl-2-oleoyl-*sn*-glycero-3-phospho-(1'-myo-inositol-4',5'-bisphosphate), POPIP2) and POPI(3,4,5)P_3 (1-palmitoyl-2-oleoyl-*sn*-glycero-3-phospho-(1'-myo-inositol-3',4',5'-trisphosphate), POPIP3) with POPIP2 being a weaker ligand for K2-PH (for structural overview of PIPs see Methods, Figure 4.25).[86] Upon membrane binding, K2 undergoes protein-protein interactions with integrin or epidermal growth factor receptor (EGFR), leading to its roles as co-activator of talin mediated integrin activation and EGFR stabilizer.[305], [306] However, due to a lack of structural information, the molecular mechanism of POPIP-species specific K2-PH binding and how it may regulate the kindlin function is still controversial. The complexity of K2-PH binding to PIP containing membranes is reflected by a recent simulation study which suggested an influence of the PIP 4′ phosphate protonation state on the membrane bound conformation of K2-PH.[87]

TIAM2 is a guanine nucleotide-exchange factor and essential for Rac activation and therefore for membrane ruffling. It is speculated that the PH domain of TIAM2 (TIAM2-PH) mediates its membrane localization. The adjacent CC-Ex (coiled coil and extra) domain then enhances specific cellular localization by binding to integral membrane proteins (see Figure 4.1 for structural overview). Besides this, the CC-Ex domain seems to be crucial for stabilizing the adjacent PH domain, as well as for increasing the overall TIAM2 membrane affinity.[72] Nevertheless, the precise mechanism by which the PH domain together with the CC-Ex domain binds to the membrane remains unknown.

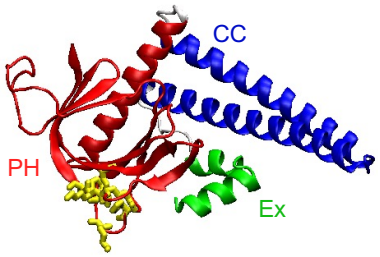


Figure 4.1 | Structural Overview of the PH-CC-Ex Domain of TIAM2. Shown is the structure of the PH-CC-Ex domain of TIAM2 (in the following referred to TIAM2-PH) with the N-terminal PH domain colored in red (residues 504-625), the coiled coil region in blue (CC, residue 630-700) and the Extra domain in green (Ex, residues 707-741). Connecting loop regions are shown in light grey. The previously predicted PIP binding site of the N-terminal PH domain is highlighted with the stick model in yellow and includes K514, R531, K532, W533, H579 and K581.[72]

4.2 Results

4.2.1 NR Experiments Reveal Crucial Conditions for Studying PMPs

Neutron reflectometry (NR) is known to be able to help predicting binding conformations of peripheral membrane proteins (PMPs) bound to their target membrane. So far this has been mainly done by using tethered lipid bilayers.[307], [308] We were curious to see if we can also use the more advanced, recently developed free floating model membrane (FFM) system [133] in order to study binding conformations of peripheral membrane proteins. Therefore, we conducted NR experiments using the FFM system to study the binding conformation of TIAM2-PH and K2-PH to their respective POPIP-containing membrane. Hereby, our results from molecular dynamics (MD) simulations served as comparison and validation.

Phospholipid Membrane Binding of Grp1-PH as Test System for Model Fit Development

First, the well studied PH domain of the Grp1 protein (Grp1-PH), which has a strong affinity towards PIP-containing membranes, was used as a test sample system to evaluate our fitting model. To simplify the system and therefore the model fits, we used a supported lipid bilayer (these initial measurements were conducted in collaboration with Dr. Luke Clifton and Tao Ni). Grp1-PH was added to a POPC:POPS:SAPIP3 (6:3:1, mol:mol:mol) and a POPC:POPS:DOPIP2 (6:3:1, mol:mol:mol) supported lipid bilayer (at a concentration of 0.05 mg/mL, 3.3 μM). In both cases we observed significant membrane binding of Grp1-PH. A model fit, describing the protein layer with a simple slab next to the outer membrane leaflet, revealed fits which describe the reflectivity data well (Figures 4.2, 4.3). The protein coverage resulting from these model fits was 25 $\pm$ 1% and 11 $\pm$ 1% for the 10% DOPIP2 and 10% SAPIP3 containing membrane, respectively.

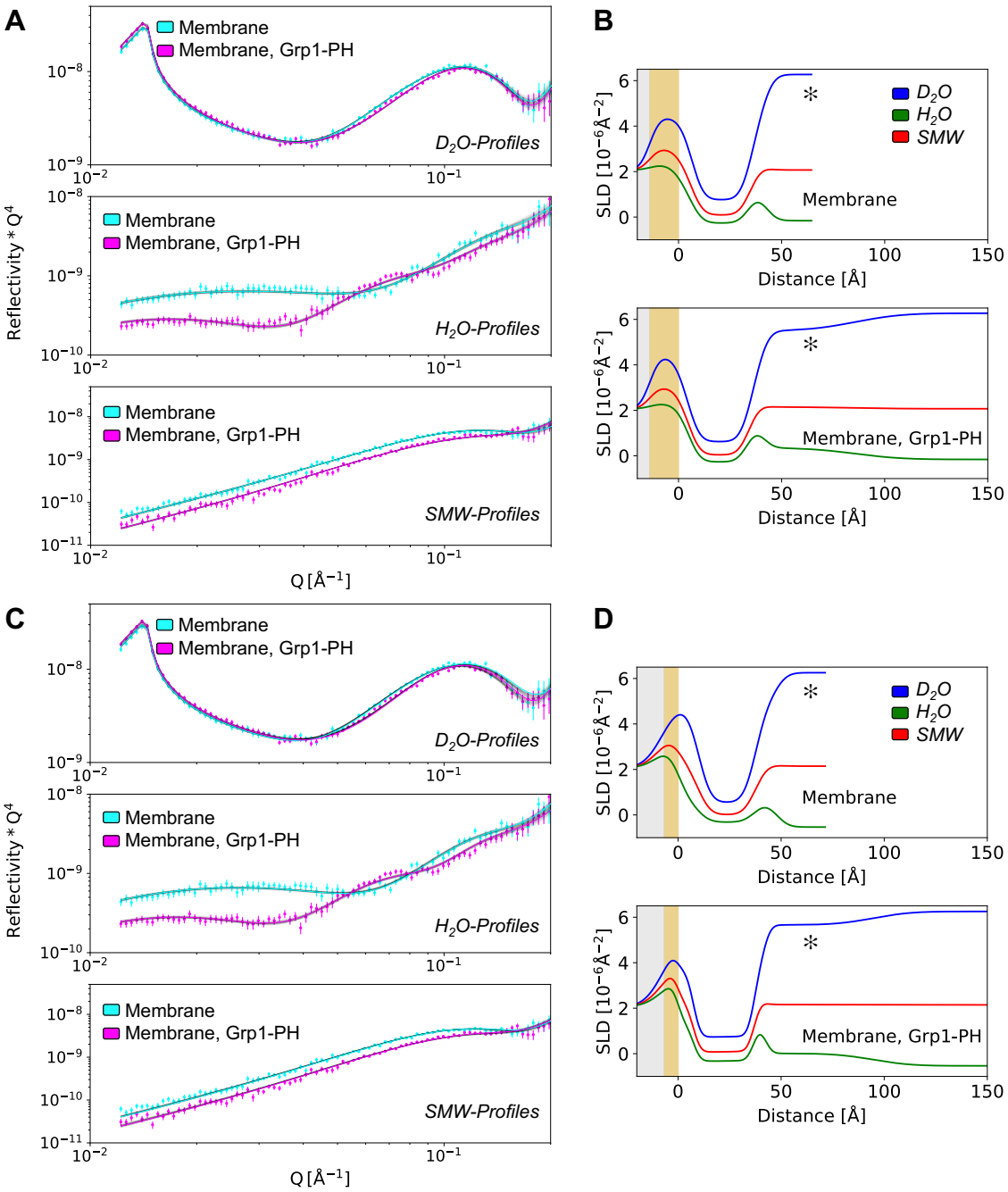


Figure 4.2 | NR of Grp1-PH Interacting with a 10% DOPIP2 Supported Lipid Bilayer. A, C The NR data (dots and error bars) of the POPC:POPS:DOPIP2 (6:3:1, mol:mol:mol) supported lipid bilayer before (cyan) and after Grp1-PH binding to the membrane (magenta) is shown for all three isotopic contrasts: D_2O (top), H_2O (middle), SMW (38% D_2O and 62% H_2O; bottom). For each reflectivity profile 500 samples from the posterior distribution of the model fit are shown in grey and the median of the distribution as solid line in the same color as the corresponding reflectivity data. In **A** a slab on top of the membrane was used for representing the protein layer in the model fit. In **C** additionally to the protein slab, a mixed layer of protein and lipids was used for describing the outer membrane leaflet in the model fit. **B, D** The resulting SLD profiles are shown for all three isotopic contrasts: D_2O (blue), H_2O (green), SMW (red). The upper SLD profiles correspond to the bilayer before and the lower to the bilayer after the Grp1-PH addition. Zero at the x-axis corresponds to the SiO_2/membrane interface. For clarity the area of the Si layer is highlighted in grey, the area of the SiO_2 layer in brown and the area of the protein marked with an asterisk.

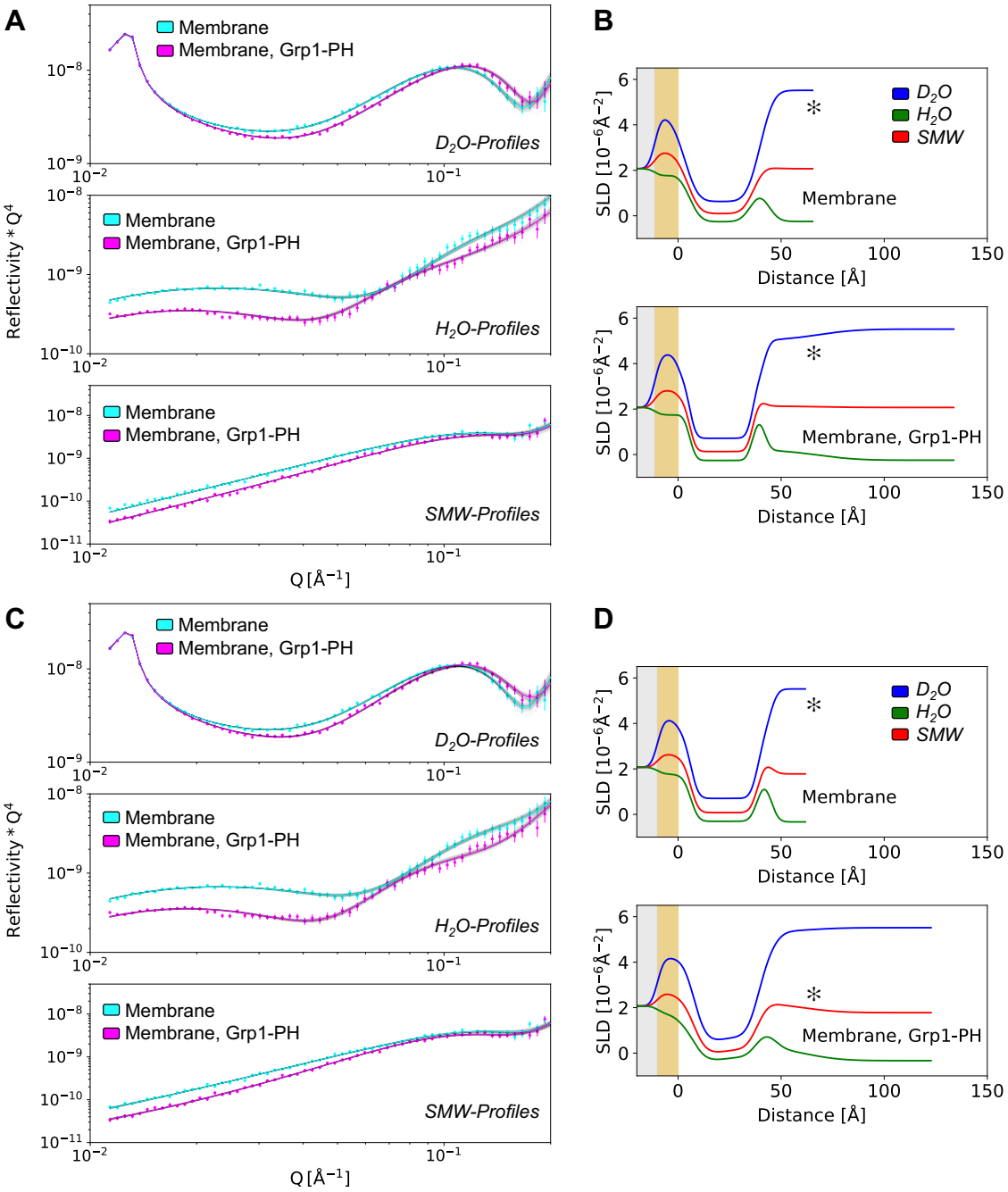


Figure 4.3 | NR of Grp1-PH Interacting with a 10% SAPIP3 Supported Lipid Bilayer. A, C The NR data (dots and error bars) of the POPC:POPS:SAPIP3 (6:3:1, mol:mol:mol) supported lipid bilayer before (cyan) and after Grp1-PH binding to the membrane (magenta) is shown for all three isotopic contrasts: D_2O (top), H_2O (middle), SMW (38% D_2O and 62% H_2O; bottom). For each reflectivity profile 500 samples from the posterior distribution of the model fit are shown in grey and the median of the distribution as solid line in the same color as the corresponding reflectivity data. In **A** a slab on top of the membrane was used for representing the protein layer in the model fit. In **C** additionally to the protein slab, a mixed layer of protein and lipids was used for describing the outer membrane leaflet in the model fit. **B, D** The resulting SLD profiles are shown for all three isotopic contrasts: D_2O (blue), H_2O (green), SMW (red). The upper SLD profiles correspond to the bilayer before and the lower to the bilayer after the Grp1-PH addition. Zero at the x-axis corresponds to the SiO_2/membrane interface. For clarity the area of the Si layer is highlighted in grey, the area of the SiO_2 layer in brown and the area of the protein marked with an asterisk.

In order to get information about the extent of the penetration of the protein into the membrane, a more advanced model fit was developed. Here, both the head group and the tail layer of the outer membrane leaflet facing towards the bulk water were described as mixed layers containing protein and lipid. The proportion of protein and lipid within this area was calculated by fitting the scattering length density (SLD) of the mixed layers as a mixture of protein-SLD and lipid head group- or lipid tail-SLD for the head group and lipid tail layer, respectively. Additionally, membrane coverage across both leaflets was used as a fitting parameter to account for membrane defects. For the external membrane part of the protein the layer thickness and coverage of the protein were used as fitting parameters. At the same time the external membrane coverage of the protein was linked with the internal membrane coverage of the protein by setting the internal membrane coverage of the protein to be equal or smaller than the external membrane coverage of the protein. This advanced fitting model revealed fits which described the reflectivity data well (Figures 4.2, 4.3).

In comparison to the simpler slab model fits, the mixed layer model fits showed mostly lower chi-square values for the H_2O and silicon matched water (SMW) contrasts, while the slab model fits showed lower chi-square values for the D_2O contrast. As the H_2O contrast is the contrast which changes the most when a peripheral protein binds to a supported lipid bilayer and therefore contains most of the information, the mixed layer model fit is likely a better choice for these sample systems. With a protein coverage of 23 $\pm$ 1% and a protein thickness of 53 $\pm$ 2 Å for the 10% DOPIP2 containing membrane the fitting model showed good agreement with the slab fitting model (25 $\pm$ 1% and 46 $\pm$ 3 Å for coverage and thickness, respectively, see Table 4.1). Also other key fitting parameters of both fitting models were in good agreement in case of the 10% DOPIP2 membrane, within expected variance (see Table 4.1). The main difference between the slab fitting model and our mixed layer fitting model are the additional fitting parameters describing the protein coverage within the outer membrane leaflet. Therefore, with the Grp1-PH protein basically not penetrating the 10% DOPIP2-membrane (the inner membrane coverage of Grp1-PH was 1 $\pm$ 1%), the similar results of both fitting models demonstrate, that our mixed layer fitting model is a reliable model. With an increased inner membrane coverage of the Grp1-PH protein when bound to the 10% SAPIP3-membrane (5 $\pm$ 3%), there are

significant differences in the fitting parameters describing the protein distribution, as expected (see Table 4.1). The protein distribution above and within the membrane can be seen best in a volume fraction plot (VFP) rather than an SLD plot (Figure 4.4). The VFPs show clearly that the Grp1-PH protein penetrates significantly the outer leaflet of the 10% SAPIP3 membrane, while there was little penetration in the presence of the 10% DOPIP2 membrane. Thus, we used our mixed layer fitting model for the following experiments and generated VFP additionally to the SLD plots.

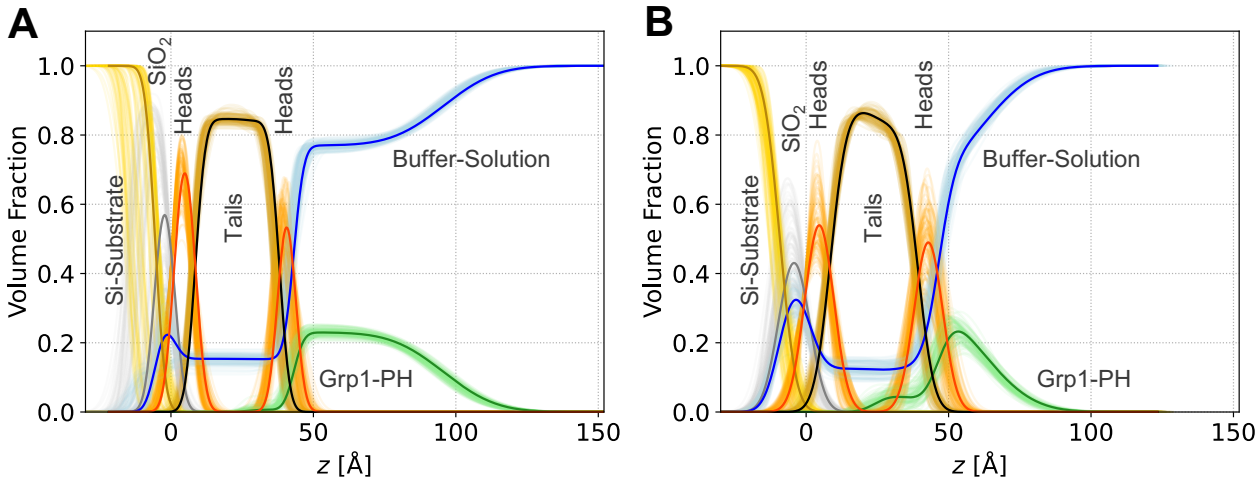


Figure 4.4 | Grp1-PH Binds to Supported Lipid Bilayers Containing PIPs. The volume fraction plots (VFPs) of the NR experiments with Grp1-PH interacting with a supported lipid bilayer containing a lipid ratio of POPC:POPS:DOPIP2 (6:3:1, mol:mol:mol) or POPC:POPS:SAPIP3 (6:3:1, mol:mol:mol) are shown in **A** and **B**, respectively. The corresponding data and model fits are shown in Figure 4.2, **C** and 4.3, **C**. For each component of the system 500 samples from the posterior distribution of the model fit are shown in light-shades and the median of the distribution as solid, dark-shaded line. The different components shown are as followed: Si-substrate (yellow/gold), SiO_2-surface (light grey/grey), lipid head groups (orange/red), lipid tails (brown/black), Grp1-PH protein (light green/green), buffer solution (light blue/blue). Zero at the x-axis corresponds to the SiO_2/membrane interface.

NR Parameter	10% DOPIP2				10% SAPIP3			
	Slab		Mixed Layer		Slab		Mixed Layer	
	-	*Grp1*	-	*Grp1*	-	*Grp1*	-	*Grp1*
apm inner leaflet [Å^2]	79 ± 1	75 ± 1	68 ± 2	54 ± 2	70 ± 1	74 ± 1	58 ± 1	60 ± 8
apm outer leaflet [Å^2]	79 ± 1	75 ± 1	68 ± 2	79 ± 1	70 ± 1	74 ± 1	58 ± 1	63 ± 8
membrane roughness [Å]	5 ± 1	4 ± 1	5 ± 1	3 ± 1	5 ± 1	3 ± 1	3 ± 1	5 ± 1
membrane coverage [%]	84 (83, 85)	86 (85, 88)	87 ± 2	84 ± 2	85 (83, 86)	83 (82, 84)	85 ± 1	84 ± 4
protein thickness [Å]	-	46 ± 3	-	53 ± 2	-	26 ± 4	-	15 ± 2
protein roughness [Å]	-	18 ± 2	-	15 ± 1	-	15 ± 2	-	14 ± 1
inner protein coverage [%]	-	-	-	1 ± 1	-	-	-	5 ± 3
outer protein coverage [%]	-	25 ± 1	-	23 ± 1	-	21 ± 3	-	35 ± 4
water per lipid head group	-	-	13 ± 1	3 ± 1	-	-	2 ± 1	5 ± 2
chi-square H_2O	92	108	74	88	72	50	42	53
chi-square SMW	91	127	88	104	54	46	46	34
chi-square D_2O	65	79	85	105	75	75	76	79

Table 4.1: | Resolved Structural NR Parameters. All key NR fitting parameters are given for the supported 10% DOPIP2 and 10% SAPIP3 membrane (both with a lipid ratio of POPC:POPS:DO/SAPIP, 6:3:1, mol:mol:mol) in the presence (right sub-column) and absence (left sub-column) of Grp1-PH. For each sample system the slab (left) and the mixed layer fitting model (right) was applied. In case of the slab fitting model the membrane coverage was calculated using the area per lipid of the membrane via: $V_{\text{tail}} \; / \; (apm \times t_{\text{tail}})$ with V_{tail} being the volume of the lipid tail, apm the fitted area per molecule and t_{tail} the thickness of the lipid tail. All errors correspond to the 95% confidence intervals determined via Markov chain Monte Carlo (MCMC) sampling of the fitting parameters.

K2-PH Binding to Floating DOPIP-Membranes Demonstrated Limits of Fitting Model

To investigate experimentally the PIP-dependency of K2-PH membrane binding and the ability of the FFM system to study the binding conformation of peripheral membrane proteins, we initially added 0.05 mg/mL (4.5 μM) K2-PH to three different membranes containing either 0, 5 or 10% DOPIP3, next to 20% POPS and 80, 75 or 70% POPC, respectively. As expected, with increasing DOPIP3 concentration in a POPC/POPS membrane, we observed an increased membrane affinity of K2-PH. Figure 4.5 shows that the higher the DOPIP3 concentration was, the further the difference between the reflectivity profiles of the membrane alone and the membrane in presence of the K2-PH expanded down towards lower Q-values (see difference of reflectivity plots in Q-range below 0.05 $Å^{-1}$). This means, the higher the DOPIP3 concentration was in the floating membrane, the more pronounced was the additional K2-PH protein layer on top of the floating membrane.

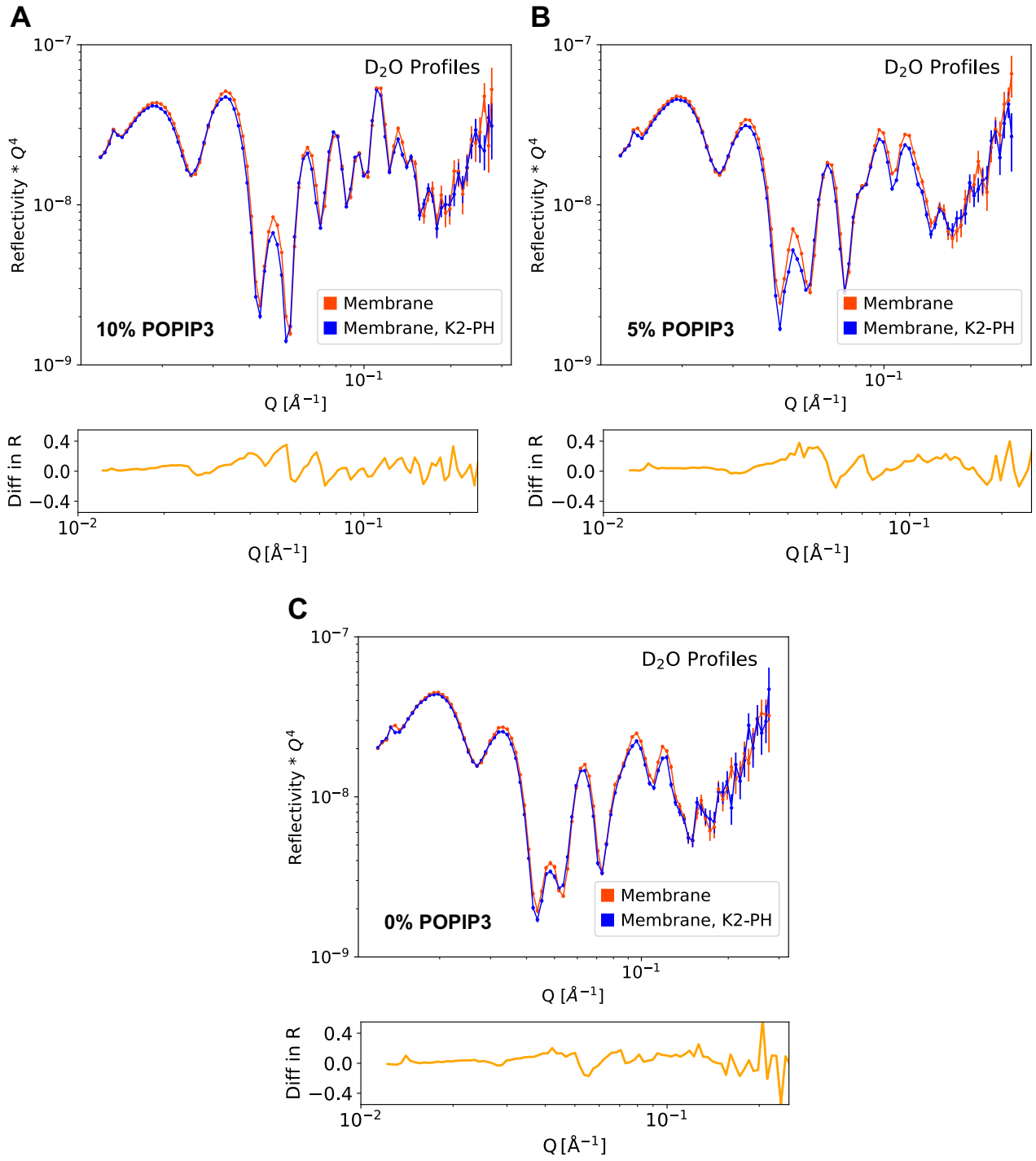


Figure 4.5 | DOPIP3 Dependency of K2-PH Interaction with Phospholipid Membranes. Raw neutron reflectivity data from a free floating membrane system containing a POPC:POPS:DOPIP3 membrane with a lipid ratio of 70:20:10, 75:20:5 and 80:20:0 (mol:mol:mol) is given in **A**, **B** and **C**, respectively. The samples were measured at four contrasts: 100% H_2O, AuMW (75% D_2O, 25% H_2O), PrMW (42% D_2O, 58% H_2O) and 100% D_2O. Shown are the raw data of the D_2O reflectivity profiles for the membranes alone (in red) and for the membranes after the addition of 0.05 mg/mL (4.5 µM) K2-PH (in blue). The orange profiles in the lower plots represent the difference in reflectivity caused by the addition of the protein K2-PH.

However, while we clearly see this trend in the reflectivity data, capturing the observed statistical relevant but small shifts in the Kiessing fringes with a fitting model in a validated way is challenging. By applying our mixed layer fitting model, we were not able to fit for the 5% DOPIP3 and the DOPIP3-free membrane a K2-PH layer on top of the membrane in a validated way. Here, the thickness of the external protein layer expanded in both model fits to meaninglessly high values of 140-180 Å. Also the roughness of the external protein layer expanded in the model fit always as much as it was allowed to by the settings of the fitting model, even when the upper end of the range was set to extremely high values of > 30 nm. The same uncertain behaviour of the roughness of the external protein layer was given for the 10% DOPIP3 membrane. In contrast, here a defined thickness of 68 $\pm$ 4 Å for the external protein layer was provided by the mixed layer fitting model. According to the model fit, there was an external protein coverage of 35 $\pm$ 1% and no inner protein coverage, meaning none of the protein penetrated into the membrane (see VFP and model fits in Figure 4.6). However, considering the uncertainty in the protein roughness, as well as the very high chi-square values, these results have to be treated with care (see full list of NR fitting parameter results in Table 4.2, **II**). These initial reflectivity profiles of a peripheral membrane protein binding to floating model membranes showed that there are limits in our fitting procedures to be able to capture small shifts in Kiessing fringes in a validated way. There are different options to gain more pronounced changes in the data resulting from protein binding: Increasing the size of the protein, increasing the amount of protein bound to the membrane by increasing the percentage of POPIP within the floating membrane or changing the underlying reflectivity profile given by the substrate.

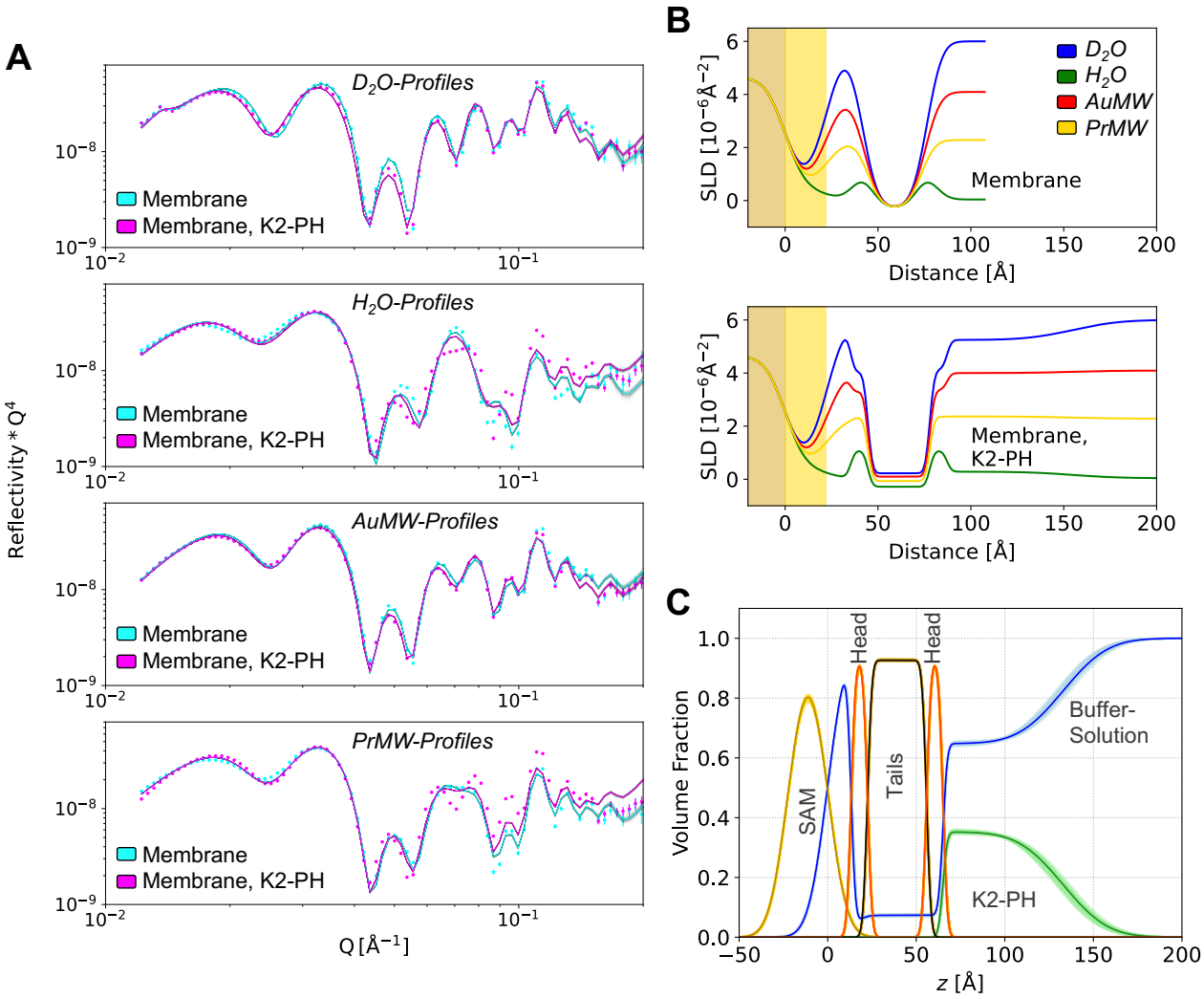


Figure 4.6 | NR of K2-PH Interacting with DOPIP3 Free Floating Membranes. **A** The NR data (dots and error bars) of the POPC:POPS:DOPIP3 (7:2:1, mol:mol:mol) floating membrane before (cyan) and after K2-PH addition (magenta) is shown for all isotopic contrasts: D_2O, H_2O, AuMW, PrMW (from top to bottom). For each reflectivity profile 500 samples from the posterior distribution of the model fit are shown in grey and the median of the distribution as solid line in the same color as the corresponding reflectivity data. For the representation of the protein distribution in the model fit a protein slab next to the outer membrane leaflet was used, as well as mixed layers of protein and lipids for the layers describing the lipid head groups and lipid tails of the outer membrane leaflet. **B** The resulting SLD profiles are shown for all isotopic contrasts: D_2O (blue), H_2O (green), AuMW (red), PrMW (gold). The upper SLD profiles correspond to the bilayer before and the lower to the bilayer after the K2-PH addition. Zero at the x-axis corresponds to the gold/OEG-SAM interface. For clarity the area of the gold layer is highlighted in light brown and the area of the OEG-SAM in yellow. **C** The resulting VFP: For each component of the system 500 samples from the posterior distribution of the model fit are shown in light-shades and the median of the distribution as solid, dark-shaded line. The different components shown are as followed: OEG-SAM (yellow/gold), lipid head groups (orange/red), lipid tails (brown/black), K2-PH protein (light green/green), buffer solution (light blue/blue). Zero at the x-axis corresponds to the OEG-SAM/water interface.

Figure 4.7 shows calculated D_2O NR model fits with identical membrane-, water inter-layer- and protein-parameters for two different substrates. One substrate (left column) contains a silicon, silicon dioxide, permalloy, gold and OEG-SAM layer forming all together the substrate we applied for the K2-PH experiments shown in Figure 4.5. The other substrate contains a chromium layer rather than a permalloy layer (right column). The advantage of the latter is that there is one reflectivity layer less contributing to the reflectivity profile due to silicon dioxide and chromium having almost identical SLDs. For both substrates the theoretical reflectivity profiles were calculated for an outer protein coverage of 0, 16 and 32%, while the inner protein coverage was set to be equal to the outer protein coverage (inner protein coverage = 1) or zero (see header for each subplot in Figure 4.7). All parameter sets were applied for a 30 Å and a 60 Å thick external protein layer. The resulting reflectivity profiles show that the permalloy containing substrate used in the FFM system needs either a thick protein layer or a reasonable amount of protein penetrating the membrane to show significant enough changes in the reflectivity profile for analysing the protein binding conformation. In contrast, the chromium containing substrate used in the FFM system shows much better sensitivity concerning a protein bound to the floating membrane. Even with a small protein and no membrane penetration of the protein the changes in the reflectivity profiles are significant and should be well detectable with our fitting model (Figure 4.7, **B**).

In summary, the first usage of the FFM system to study the membrane binding position and orientation of PMPs, here K2-PH, revealed limits concerning protein thickness and protein coverage which are analyzable with the FFM system we used so far. However, our model fit calculations showed that the change to a substrate with a lower number of reflecting interfaces overcomes these limitations.

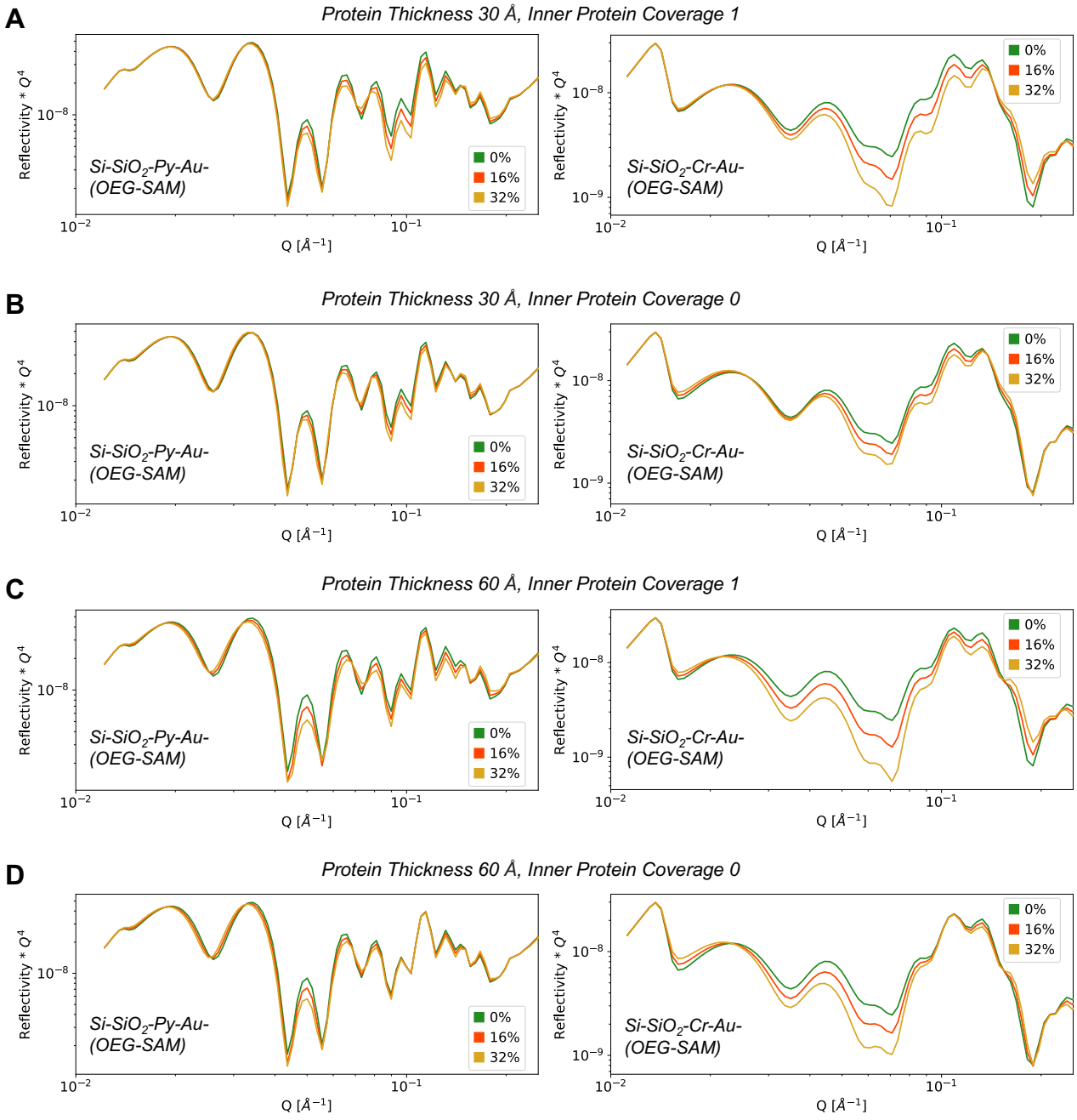


Figure 4.7 | Theoretical NR Model Fits for Different Substrates. Shown are the calculated reflectivity profiles for a 30 Å (**A, B**) and 60 Å (**C, D**) thick protein interacting with a floating model membrane (see header for each subplot). The substrate of the FFM system consisted of a silicon (Si), silicon dioxide (SiO_2), gold (Au) and OEG-SAM layer and contained between the SiO_2 and Au layer either a permalloy (Py, left column) or chromium (Cr, right column) layer. The different colors represent 0, 16 or 32% hypothetical external protein coverage. The inner protein coverage was either set to be zero (**B, D**) or one (**A, C**), with one meaning the inner protein coverage is equal to the external protein coverage given in respective parameter set (see header for each subplot).

Phospholipid Membrane Binding of Grp1-PH as Test System for Data Quality Development

Having seen that the Grp1-PH binding works well with the supported bilayer system and the higher sensitivity of the chromium containing substrate, we decided to use again Grp1-PH, together with the chromium substrate as a test system to see if the FFM system is indeed suitable to investigate membrane bound conformations of peripheral membrane proteins. Unfortunately, by adding 0.05 mg/mL Grp1-PH to a POPC:POPS:DOPIP2 (7:2:1, mol:mol:mol) floating membrane, we observed no changes in the reflectivity profile caused by the addition of Grp1-PH (Figure 4.8, **A**). This raised the question, why this experiment worked well with the supported lipid bilayer system and not with the FFM system? One of the key differences between the membrane preparation procedures is the presence of Ca^{2+}. The self assembling process of the membrane in the FFM system requires a small amount of Ca^{2+} (2 mM) present, while the assembling process in the supported lipid bilayer system requires no Ca^{2+}. Therefore, we repeated the experiment with a floating POPC:POPS:DOPIP3 (7:2:1, mol:mol:mol) membrane and sequestered the Ca^{2+} out of the FFM system by flushing the flow cell with 1 mM EDTA buffer solution immediately after the membrane deposition. Now, we observed significant changes in the reflectivity profile due to the protein addition (Figure 4.8, **C**). Our mixed-layer fitting model suggested a protein thickness of 30 $\pm$ 8 Å with an external and internal protein coverage of 16 $\pm$ 2% and 15 $\pm$ 2%, respectively (see Table 4.2 for all key NR parameters and Figure 4.8, **D** for VFP).

Taken together, these findings seem to promise indeed that the FFM-system represents a planar model membrane system, which is well suitable for investigating the membrane binding process of PMPs. Furthermore, they showed that the level of Ca^{2+} in the surrounding buffer solution might play a critical role concerning membrane recruitment of PH domains.

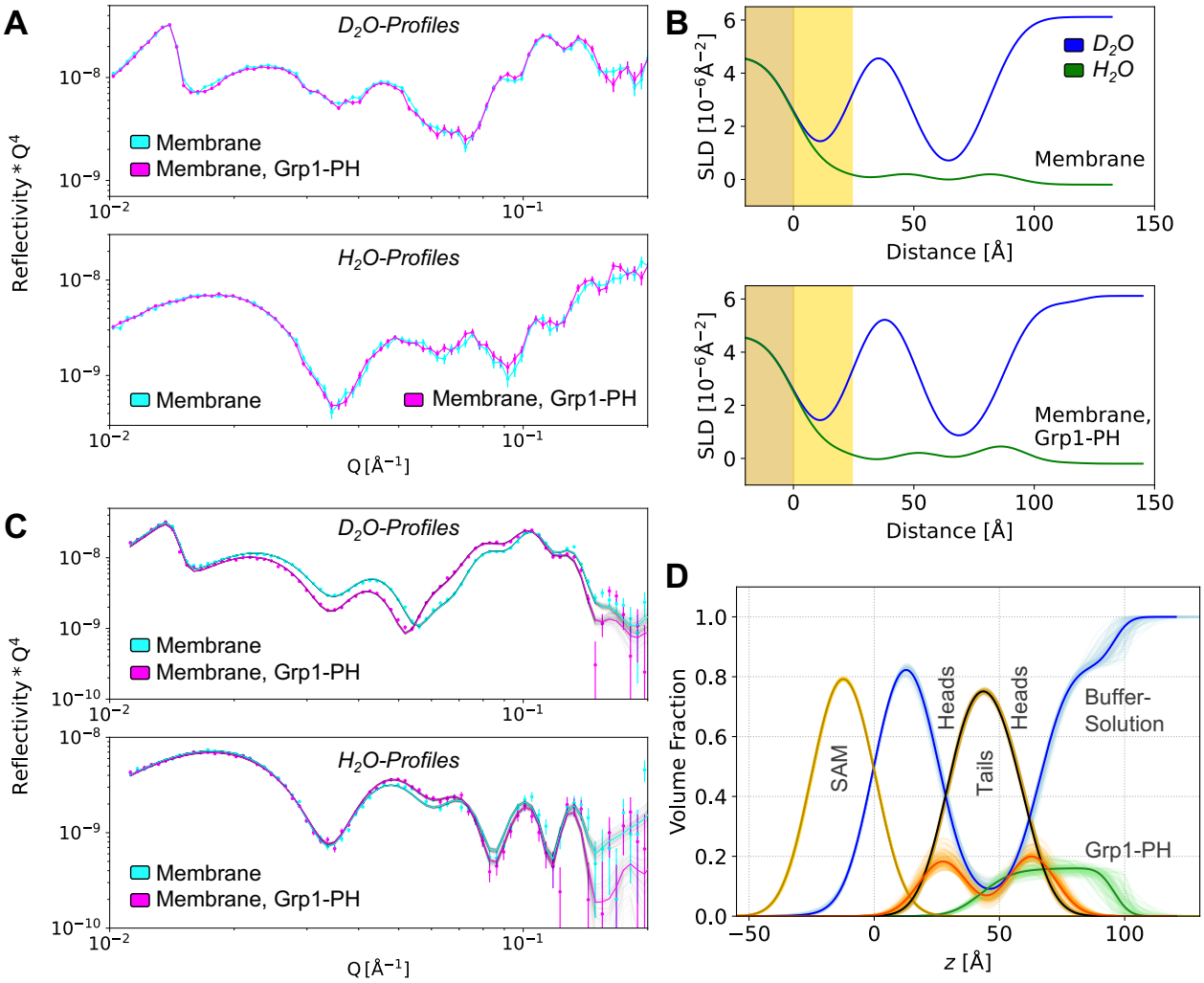


Figure 4.8 | Grp1-PH Binds to Free Floating Membranes Containing PIPs. The NR data (dots and error bars) of the POPC:POPS:DOPIP2 (7:2:1, mol:mol:mol) floating membrane in the presence of 2 mM Ca^{2+} and of the POPC:POPS:DOPIP3 (7:2:1, mol:mol:mol) floating membrane in the absence of Ca^{2+} are shown in **A** and **C**, respectively. Both systems were examined before (cyan) and after Grp1-PH addition (magenta). Results are shown for both isotopic contrasts: D_2O (top), H_2O (bottom). In **C** for each reflectivity profile 500 samples from the posterior distribution of the model fit are shown in grey and the median of the distribution as solid line in the same color as the corresponding reflectivity data. For the representation of the protein distribution in the model fit a protein slab next to the outer membrane leaflet was used, as well as mixed layers of protein and lipids for the layers describing the lipid head groups and lipid tails of the outer membrane leaflet. **B** The resulting SLD profiles corresponding to the data presented in **C** are shown for both isotopic contrasts: D_2O (blue), H_2O (green). The upper SLD profiles correspond to the bilayer before and the lower to the bilayer after the Grp1-PH addition. Zero at the x-axis corresponds to the gold/OEG-SAM interface. For clarity the area of the gold layer is highlighted in light brown and the area of the OEG-SAM in yellow. **D** The resulting VFP corresponding to the data presented in **C**. For each component of the system 500 samples from the posterior distribution of the model fit are shown in light-shades and the median of the distribution as solid, dark-shaded line. The different components shown are as followed: OEG-SAM (yellow/gold), lipid head groups (orange/red), lipid tails (brown/black), Grp1-PH protein (light green/green), buffer solution (light blue/blue). Zero at the x-axis corresponds to the OEG-SAM/water interface.

Calcium Restricts Membrane Binding of TIAM2-PH and K2-PH

To investigate the calcium dependency of the TIAM2-PH and K2-PH phospholipid membrane binding, we used attenuated total reflection (ATR) Fourier transform infrared (FTIR) spectroscopy (ATR-FTIR). In brief, FTIR spectroscopy provides insights about the chemical bonds present in a sample by analysing their characteristic bond vibrational frequencies. We used an ATR flow through top-plate assembly, a sample holder which mimics the NR floating cell. It holds a substrate in place and allows via inlet and outlet ports the introduction and removal of solutions. Flushing lipid vesicles onto the SiO_2-surface of a single-crystal silicon ATR substrate leads to vesicle deposition. By switching the surrounding buffer solution from high salt to no salt containing buffer solution the vesicles rupture due to osmotic shock and form a supported lipid bilayer. We confirmed the success of this deposition method by NR experiments previously (see e.g. Figure 4.3). The glycerol ester C=O stretching vibration, the asymmetric and symmetric stretching vibrations of the lipid acyl tail's C-H_2 groups, as well as the asymmetric stretching vibration of the lipid acyl tail's C-H_3 groups at 1731, 2924, 2855 and 2958 cm^{-1}, respectively, indicated the presence of the supported lipid bilayer. Protein binding to a supported lipid bilayer can be observed by the appearance of the unique protein amide HNC=O stretching vibration at around 1650 cm^{-1} in the ATR-FTIR spectrum. The more protein binds, the bigger the absorbance band gets at 1650 cm^{-1}. In the absence of Ca^{2+} in the buffer solution a clear increase of the protein amide stretching vibration band was observed over time for the interaction of 10 µM TIAM2-PH with a POPC:POPS:DOPIP2 (7:2:1, mol:mol:mol) membrane (Figure 4.9, **A**). In contrast, in the presence of 2 mM $CaCl_2$ in the buffer solution there was significantly less increase of the protein amide stretching vibration band over time for the interaction of 10 µM TIAM2-PH with either a POPC:POPS:DOPIP2 (7:2:1, mol:mol:mol) or POPC:POPS:DOPIP3 (7:2:1, mol:mol:mol) supported membrane (Figure 4.9, **B** and **C**, respectively). The same observation was made for 10 µM K2-PH interacting with DOPIP-containing supported membranes: The increase of the protein amide stretching vibration band over time was substantially more pronounced in the absence of Ca^{2+} compared to buffer conditions with Ca^{2+} present (Figure 4.10).

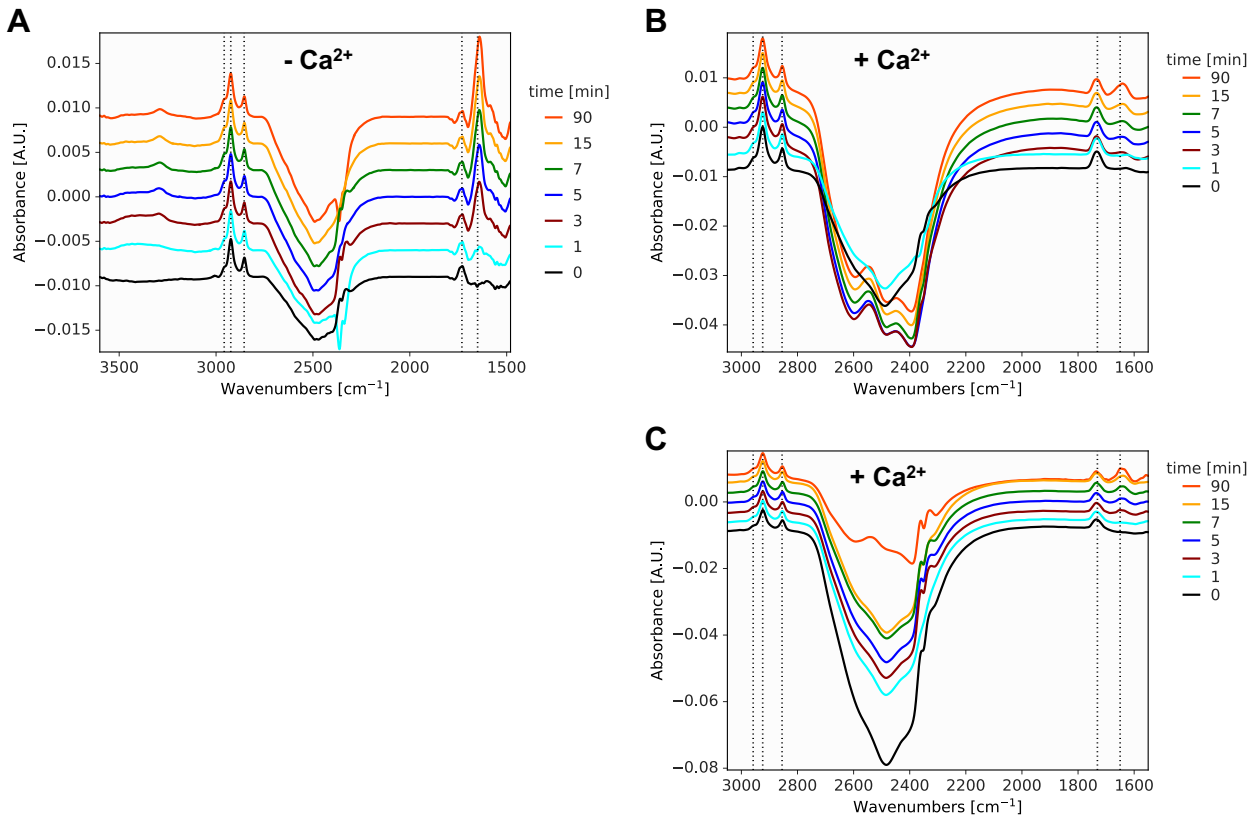


Figure 4.9 | Ca^{2+} Reduces the Binding of TIAM2-PH to Membranes Containing PIPs. ATR-FTIR spectra of a Si-absorbed supported POPC:POPS:DOPIP2 (7:2:1, mol:mol:mol) membrane in the presence of buffer lacking Ca^{2+} (**A**; 20 mM HEPES, 150 mM NaCl, pD 7.1) and Ca^{2+}-containing buffer (**B**; 20 mM HEPES, 150 mM NaCl, 2 mM $CaCl_2$, pD 7.1), both in the presence of 10 µM TIAM2-PH. Section **C** shows the ATR-FTIR spectra of a Si-absorbed supported POPC:POPS:DOPIP3 (7:2:1, mol:mol:mol) membrane in the presence of Ca^{2+}-containing buffer and 10 µM TIAM2-PH. All of the spectra displayed were taken at the time points indicated in the legends, with time zero being equal to the start of the protein being injected into the flow cell. The dashed vertical black lines highlight the absorbance wavenumbers corresponding to the symmetric stretching vibrations of C-H_2 groups (∼2855 cm^{-1}) and the asymmetric stretching vibrations of C-H_2 (∼2924 cm^{-1}) and C-H_3 groups (∼2958 cm^{-1}). These groups are primarily present in the lipid acyl tails. The absorbance at ∼1731 cm^{-1} corresponds to the C=O stretching vibration of the glycerol-ester bond of the phospholipid head groups. A growing absorbance band at around 1650 cm^{-1} indicates protein binding to the membrane, corresponding to the amide HNC=O stretching vibration. The strong negative absorbance band at ∼2500 cm^{-1} is caused by the fewer O-D bonds from the D_2O buffer being present in the penetration depth of the infrared effervescent wave after the membrane deposition relative to the background spectra collected on bare Si substrate.

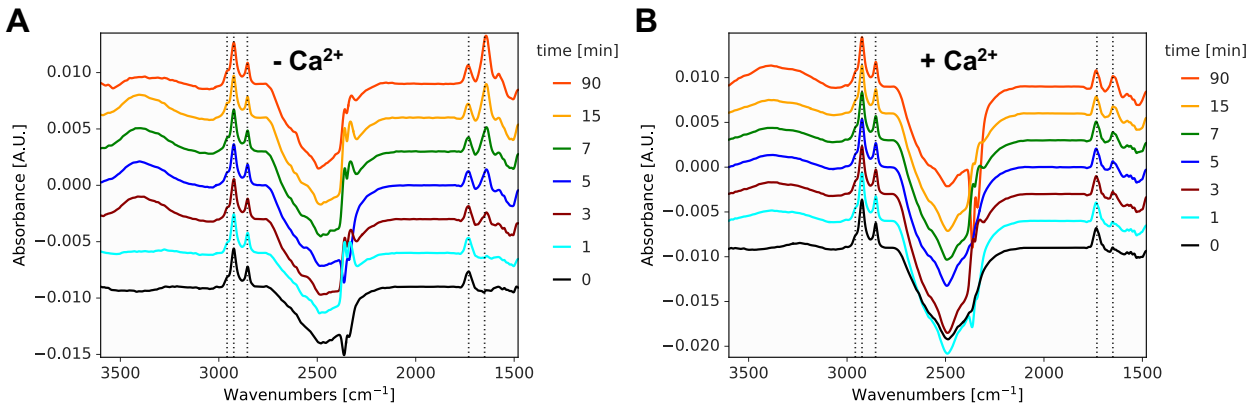


Figure 4.10 | Ca^{2+} Reduces the Binding of K2-PH to Membranes Containing PIPs. Panel **A** shows the ATR-FTIR spectra of a Si-absorbed supported POPC:POPS:DOPIP2 (7:2:1, mol:mol:mol) membrane in the presence of buffer lacking Ca^{2+} (20 mM HEPES, 150 mM NaCl, pD 7.1) and 10 µM K2-PH. Panel **B** shows the ATR-FTIR spectra of a Si-absorbed supported POPC:POPS:DOPIP3 (7:2:1, mol:mol:mol) membrane in the presence of Ca^{2+}-containing buffer (20 mM HEPES, 150 mM NaCl, 2mM $CaCl_2$, pD 7.1) and 10 µM K2-PH. All of the spectra displayed were taken at the time points indicated in the legends, with time zero being equal to the start of the protein being injected into the flow cell. The dashed vertical black lines highlight the absorbance wavenumbers corresponding to the symmetric stretching vibrations of C-H_2 groups (∼2855 cm^{-1}) and the asymmetric stretching vibrations of C-H_2 (∼2924 cm^{-1}) and C-H_3 groups (∼2958 cm^{-1}). These groups are primarily present in the lipid acyl tails. The absorbance at ∼1731 cm^{-1} corresponds to the C=O stretching vibration of the glycerol-ester bond of the phospholipid head groups. A growing absorbance band at around 1650 cm^{-1} indicates protein binding to the membrane, corresponding to the amide HNC=O stretching vibration. The strong negative absorbance band at ∼2500 cm^{-1} is caused by the fewer O-D bonds from the D_2O buffer being present in the penetration depth of the infrared effervescent wave after the membrane deposition relative to the background spectra collected on bare Si substrate.

These results strongly suggest that the presence of Ca^{2+} in the buffer solution restricts the binding of K2-PH and TIAM2-PH to PIP-containing phospholipid membranes. To explore this further, we performed NR experiments with the TIAM2-PH protein interacting with a POPC:POPS:DOPIP2 (7:2:1, mol:mol:mol) supported lipid bilayer, surrounded by a Ca^{2+}-free buffer solution. There were clear shifts in the reflectivity data of the D_2O contrast after protein addition and our mixed layer fitting model provided well fitted model fits with low chi-square values (Figure 4.11 and Table 4.2). The model fit suggested a protein thickness of 29 ± 4 Å with an external and internal protein coverage of 17 ± 1% and 9 ± 3%, respectively.

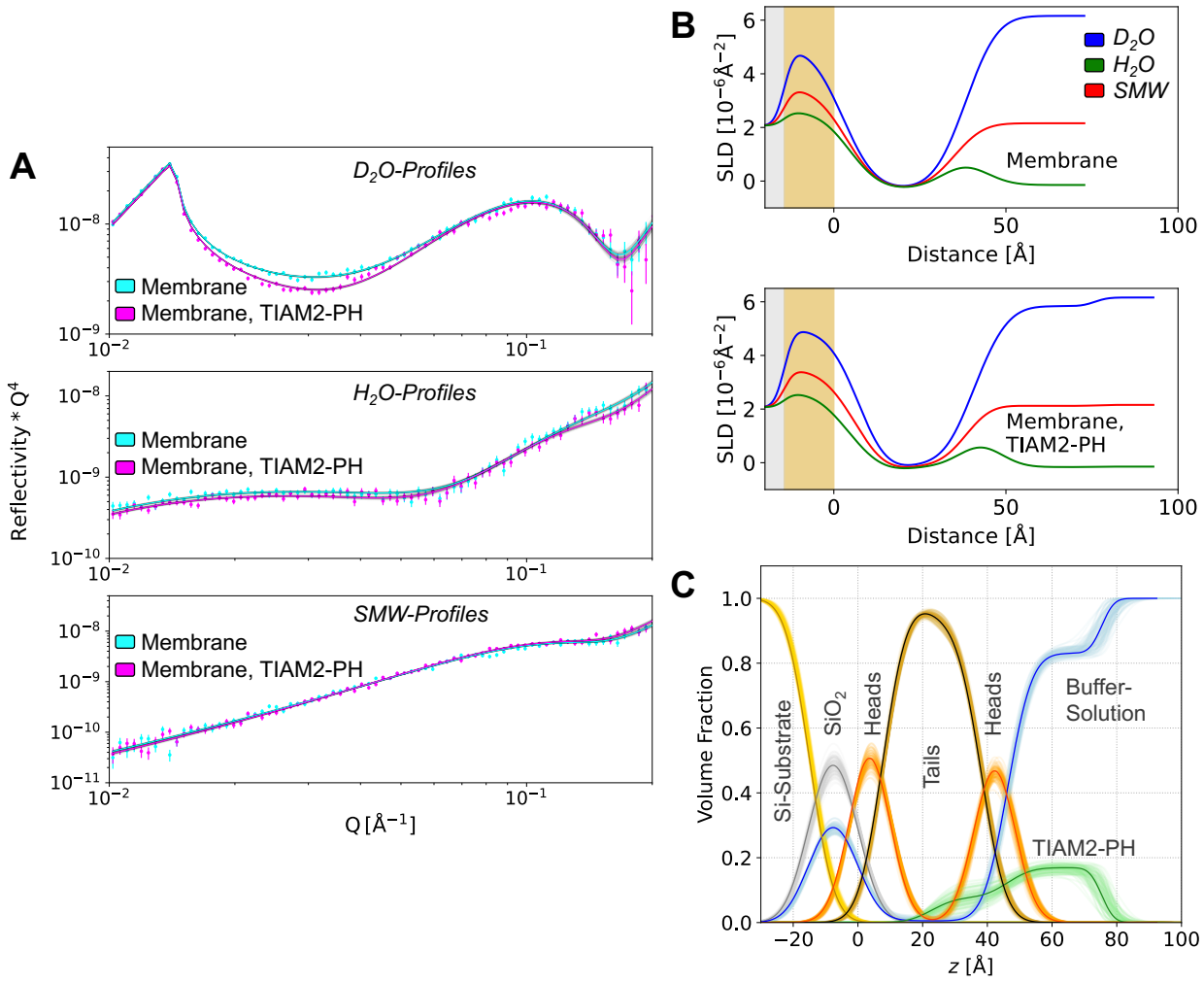


Figure 4.11 | TIAM2-PH Binds to a Supported Lipid Bilayer Containing DOPIP2 in the Absence of Ca^{2+}. **A** The NR data (dots and error bars) of the POPC:POPS:DOPIP2 (7:2:1, mol:mol:mol) supported lipid bilayer before (cyan) and after TIAM2-PH addition (magenta) is shown for all isotopic contrasts: D_2O, H_2O, SMW (from top to bottom). For each reflectivity profile 500 samples from the posterior distribution of the model fit are shown in grey and the median of the distribution as solid line in the same color as the corresponding reflectivity data. For the representation of the protein distribution in the model fit a protein slab next to the outer membrane leaflet was used, as well as mixed layers of protein and lipids for the layers describing the lipid head groups and lipid tails of the outer membrane leaflet. **B** The resulting SLD profiles are shown for all isotopic contrasts: D_2O (blue), H_2O (green), SMW (red). The upper SLD profiles correspond to the bilayer before and the lower to the bilayer after the TIAM2-PH addition. Zero at the x-axis corresponds to the SiO_2/membrane interface. For clarity the area of the Si layer is highlighted in light grey and the area of the SiO_2 layer in light brown. **C** The resulting VFP: For each component of the system 500 samples from the posterior distribution of the model fit are shown in light-shades and the median of the distribution as solid, dark-shaded line. The different components shown are as followed: Si (yellow/gold), SiO_2 (light grey/grey), lipid head groups (orange/red), lipid tails (brown/black), TIAM2-PH protein (light green/green), buffer solution (light blue/blue). Zero at the x-axis corresponds to the SiO_2/membrane interface.

NR Parameter	I		II		III	IV	
	10% DOPIP3 SiCrAu		10% DOPIP3 SiPyAu		Model Fit SiCrAu, SiPyAu	10% DOPIP2 Si	
	-	*Grp1*	-	*K2*	*Hypothetical*	-	*TIAM2*
apm inner leaflet [Å^2]	67 ± 2	72 ± 10	65 ± 1	57 ± 1	66	63 ± 1	62 ± 1
apm outer leaflet [Å^2]	67 ± 2	56 ± 8	65 ± 1	57 ± 1	66	63 ± 1	62 ± 1
membrane roughness [Å]	11 ± 2	9 ± 2	6 ± 1	2 ± 1	5	7 ± 1	6 ± 1
membrane coverage [%]	98 ± 2	79 ± 2	99 ± 1	93 ± 1	93/78/63*	99 ± 1	90 ± 3
protein thickness [Å]	-	30 ± 8	-	68 ± 4	30/60	-	29 ± 4
protein roughness [Å]	-	5 ± 6	-	20 ± 1	5	-	3 ± 1
inner protein coverage [%]	-	15 ± 2	-	0	0/16/32	-	9 ± 3
outer protein coverage [%]	-	16 ± 2	-	35 ± 1	0/16/32	-	17 ± 1
water per lipid head group	2 ± 2	1 ± 1	1 ± 1	7 ± 1	2	1 ± 1	7 ± 1
water inter-layer thickness [Å]	20 ± 2	25 ± 1	18 ± 1	13 ± 1	12	-	-
chi-square H_2O	178	110	4900	8565	-	89	81
chi-square D_2O	202	425	3306	4042		76	204
chi-square AuMW	-	-	1427	1455		-	-
chi-square PrMW	-	-	2468	9987		-	-
chi-square SMW	-	-	-	-		108	69

Table 4.2: | Resolved Structural NR Parameters. Fitting parameters are given for the floating POPC:POPS:DOPIP3 (7:2:1, mol:mol:mol) membrane in the presence (right sub-column) and absence (left sub-column) of Grp1-PH and K2-PH in **I** and **II**, respectively. For **I** a Si/SiO_2/Cr/Au/OEG-SAM and for **II** a Si/SiO_2/Py/Au/OEG-SAM substrate was used (see second row). **IV** shows the fitting parameters for the supported POPC:POPS:DOPIP2 (7:2:1, mol:mol:mol) membrane in the presence (right sub-column) and absence (left sub-column) of TIAM2-PH. All errors correspond to the 95% confidence intervals determined via MCMC sampling of the fitting parameters. **III** provides the parameters used for the model fit calculations presented in Figure 4.7. (*) Depending on the inner protein coverage the membrane coverage is different.

4.2.2 MD Simulations Provide Further Insights in Binding Conformations

CG Simulations Reveal Canonical and Non-canonical Binding Conformations

The NR results provided insights in the protein thickness and membrane penetration for K2-PH and TIAM2-PH interacting with POPIP-containing membranes. To gain further insights in the binding conformations, coarse grained (CG) MD simulations were performed for K2-PH and TIAM2-PH binding to a POPIP3 and POPIP2 containing phospholipid membrane. As in the NR experiments, two simple models of a cytoplasmic membrane composed of POPC:POPS:POPIP3 (7:2:1, mol:mol:mol) and POPC:POPS:POPIP2 (7:2:1, mol:mol:mol), as well as a control membrane containing POPC:POPS (8:2, mol:mol) were used. For both proteins ten repeats of 1.5 µs CG simulation were performed for each membrane composition. Each repeat had a randomly selected starting orientation of the protein with respect to the membrane. The initial distance between the center of mass (COM) of the protein and membrane was 9 nm for K2-PH and 11 nm for TIAM2-PH. The minimum distance between the protein and the membranes was calculated as a function of time for each simulation (Figure 4.12 and 4.15).

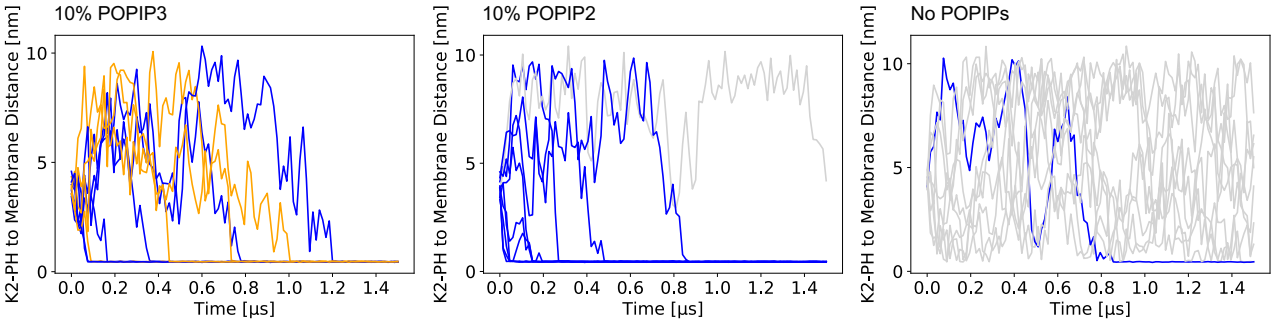


Figure 4.12 | Canonical Membrane Binding of CG K2-PH Depends on Presence and Type of PIPs. Minimum distance between the K2-PH and the Membrane, composed of POPC:POPS:POPIP3 (7:2:1, mol:mol:mol, left), POPC:POPS:POPIP2 (7:2:1, mol:mol:mol, middle) and POPC:POPS (8:2, mol:mol, right), for each of the 10 repeats over the 1.5 µs CG simulation time period. The colors represent the different binding modes: orange (binding with non-canonical conformation), blue (binding with canonical conformation) and grey (no binding).

In 10/10 repeats the K2-PH domain bound to the POPIP3 containing membrane within the 1.5 µs of the CG simulations (Figure 4.12). By converting the final CG binding conformations of K2-PH into an all atomistic (AA) representation and rotating the resulting system only around the membrane normal until the protein-RMSDs are minimal, the protein binding conformations were visually clustered into

canonical and non-canonical binding modes (Figure 4.13). For 6 of the binding events, the K2-PH bound in the canonical binding conformation, meaning being similar to the previously predicted binding conformation of the NMR structure obtained from the PDB entry 2LKO.[86] Figure 4.18 shows one of the POPIP3 canonical binding events, with the previously suggested POPIP binding residues highlighted in yellow.[86] In this binding event, six POPIP3 lipids were in contact with these residues (meaning within 5 Å, shown in orange). The other 4 POPIP3 binding events showed a non-canonical binding conformation with 3 being very similar in their binding pose (Figure 4.13). The non-canonical binding mode, which occurred just once showed similarity to the previously identified non-canonical binding conformation of K3.[309] For the POPIP2 containing membrane 9/10 repeats showed binding between the K2-PH and the membrane within the 1.5 µs of the CG simulations (Figure 4.12). In one repeat the K2-PH domain did not approach close enough to the membrane to experience an electrostatic interaction and so no binding event occurred. Here, for all nine binding events the K2-PH bound in the canonical binding conformation (Figure 4.13). In case of the control membrane, which contained no POPIPs, in only 1/10 repeat the K2-PH domain bound to the membrane and stayed bound (Figure 4.12). In several repeats the protein came close to the membrane, interacted briefly with the membrane, then dissociated back into the solution. Interestingly, in the only significant binding event the conformation of K2-PH matched the canonical binding conformation (Figure 4.13).

In summary, K2-PH showed almost no membrane binding affinity without PIPs being present in the membrane and more often canonical binding in the presence of POPIP2 than in the presence of POPIP3.

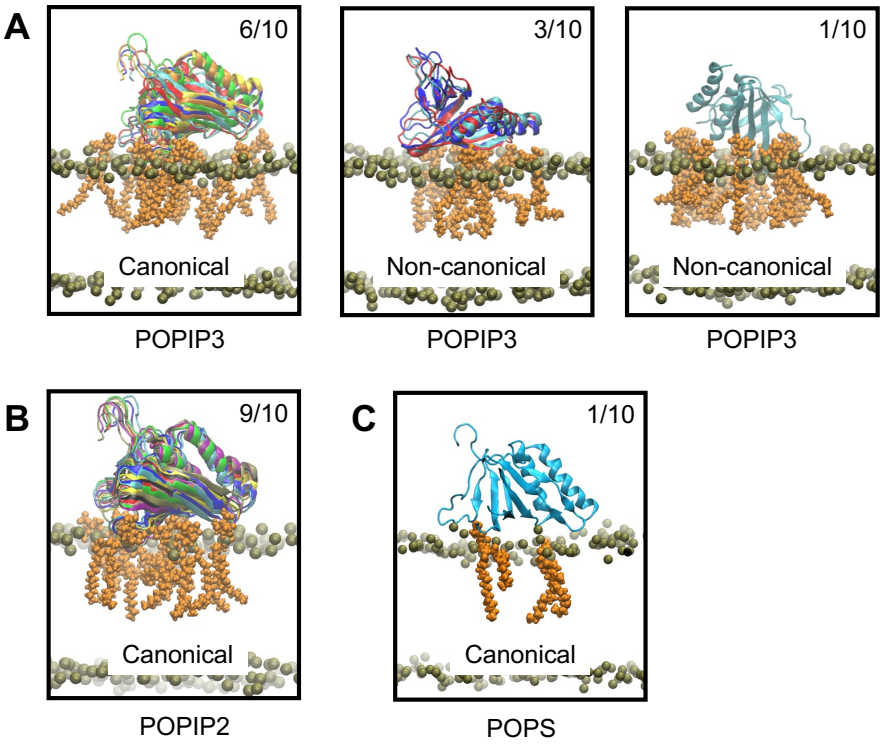


Figure 4.13 | Clustered K2-PH Binding Conformations Reveal Subgroups. Shown are the final CG binding poses of K2-PH, converted into AA and aligned along the membrane normal. For POPIP3 (**A**) 6/10 repeats bound in the canonical manner (left), 4/10 in the non-canonical manner whereby 3 of the latter had very similar conformation (middle) and 1 of the latter unique conformation (right). For POPIP2 (**B**) 9/10 repeats bound in the canonical manner, whereby 1/10 showed no binding. For the membrane without POPIPs (**C**) there was only one binding event out of 10 repeats. This binding event was in the canonical manner. The POPIP lipids within 5 Å of the bound K2-PH are shown in orange. For the POPIP-free membrane the POPS lipids within 5 Å of the bound K2-PH are shown in orange.

To investigate the binding processes of canonical binding further, the profiles of the protein-membrane distance over time were compared with the profiles of the protein orientation over time for all canonical binding repeats. For the calculation of the protein orientation, a previously applied approach was used.[46], [68] Hereby, the orientation of the PH domain relative to the membrane bound canonical binding conformation was obtained by the *zz* component of the rotation matrix, R_{zz}. Thus, R_{zz} = 1 means that the protein orientation along the membrane normal is identical to the reference structure and R_{zz} = -1 that the protein is rotated by 180°. As reference structure was the final pose of a repeat chosen which showed canonical K2-PH binding to the POPC:POPS:POPIP3 (7:2:1, mol:mol:mol) membrane (repeat 9, see also Appendix Figure 4.29). Interestingly, these results revealed that K2-PH

binds in the presence of POPIP3 in almost all repeats directly in the canonical orientation (Figure 4.14, **A**). This is indicated by an R_{zz} value of around 1 at the time of membrane binding and the fact, that R_{zz} stays around 1 after membrane binding. Solely one out of the six canonical repeats showed lower and varying R_{zz} values during and after membrane binding, suggesting a tumbling of the protein on the membrane surface before reaching the final canonical binding conformation (Figure 4.14, **A**, blue). In case of no POPIPs being present in the membrane, in the single repeat showing protein binding the K2-PH domain bound again directly with its canonical binding conformation (Figure 4.14, **C**). In contrast, in the presence of POPIP2 in 4 out of 9 canonical binding repeats the protein domain bound initially in a non-canonical mode and reached the productive binding conformation after a time period of tumbling on the membrane surface (Figure 4.14, **B**). This is again indicated by varying R_{zz} values below 1 during and after membrane binding. Therefore, the additionally calculated protein-membrane distance *versus* protein orientation density maps of K2-PH showed in the presence of POPIP3, as well as in absence of POPIPs one dominant binding mode at R_{zz} = 1, which is identical to the canonical/productive binding conformation of K2-PH (Figure 4.14, right column). However, in the presence of POPIP2 within the membrane, the binding landscape displayed a further binding mode at $R_{zz} \approx$ -0.3, additional to the canonical binding mode at R_{zz} = 1.

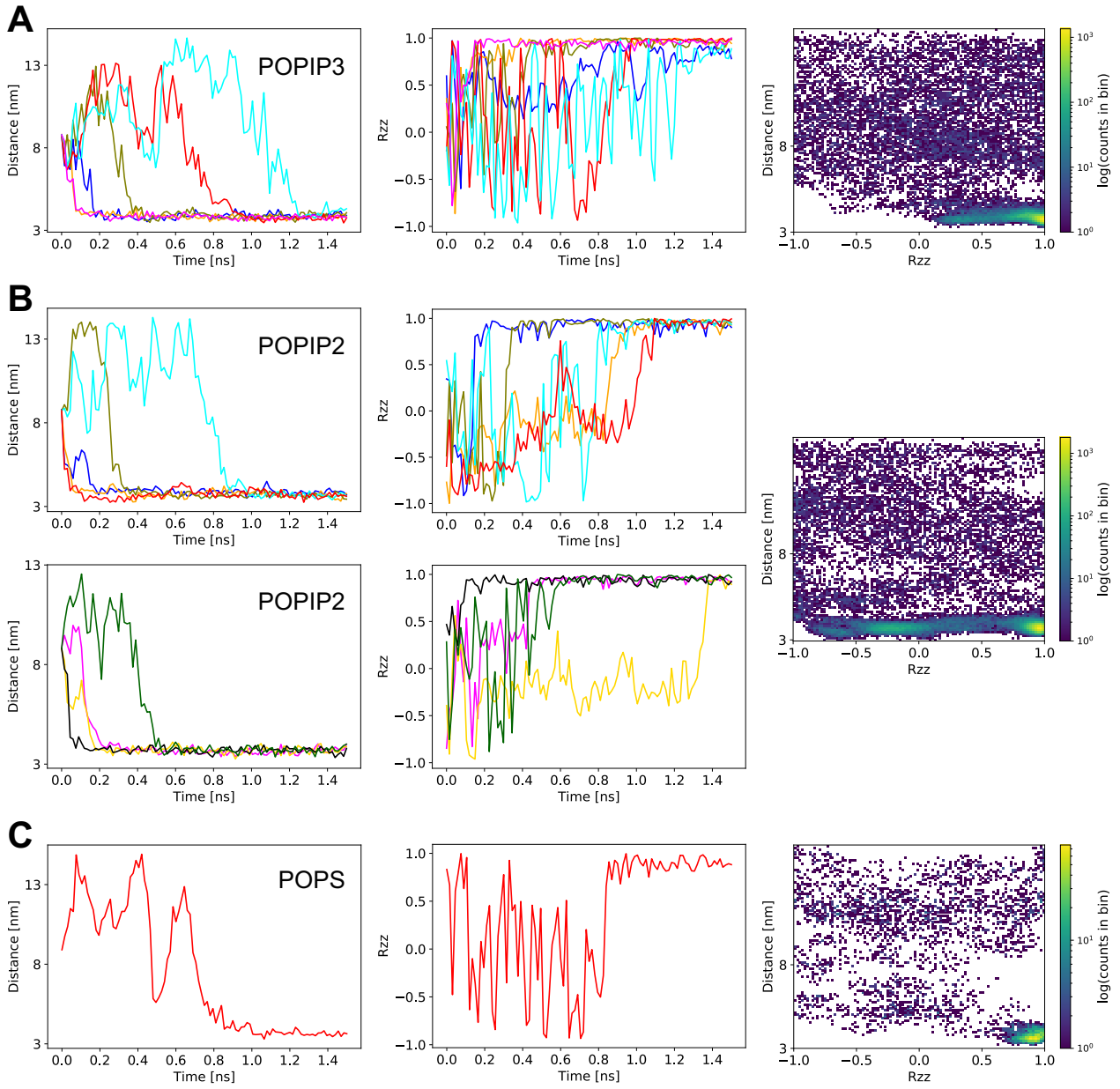


Figure 4.14 | K2-PH Membrane Binding Process. For all CG repeats which showed canonical membrane binding of K2-PH after 1.5 µs, the center of mass distance between protein and membrane (left), as well as the protein orientation (middle) are shown over time. Hereby, the membrane contained either POPIP3 (**A**), POPIP2 (**B**) or no POPIPs (**C**). The protein orientation is given by the *zz* component of the rotation matrix (R_{zz}) relative to the previously defined canonical binding conformation of K2-PH. For clarity, for the POPIP2 membrane system in panel **B**, the number of repeats were split across two plots. In **A-C** each color represents one repeat, with the color scheme between distance and orientation plot being identical within each panel/membrane system. In the right column, the density maps of the protein orientation *versus* the protein-membrane distance of the K2-PH domain for the different membrane systems are shown. Each density map represents the relative frequency, averaged across time and repeats of the protein orientation at a certain protein-membrane distance (on a logarithmic color scale from purple = low to yellow = high, see color bars).

In case of the TIAM2-PH domain, in 7/10 repeats TIAM2-PH bound to the POPIP2 containing membrane and in only 4/10 repeats to the POPIP3 containing membrane within the 1.5 µs of the CG simulations. Surprisingly, TIAM2-PH bound also in 5/10 repeats to the control membrane, which contained no POPIPs (Figure 4.15).

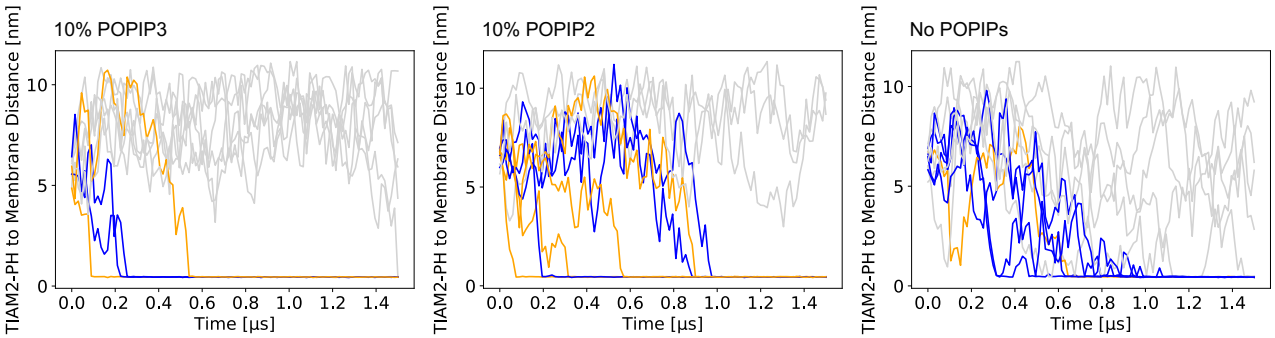


Figure 4.15 | Canonical Membrane Binding of CG TIAM2-PH Depends on Presence and Type of PIPs. Minimum distance between the TIAM2-PH and the membrane, composing of POPC:POPS:POPIP3 (7:2:1, mol:mol:mol, left), POPC:POPS:POPIP2 (7:2:1, mol:mol:mol, middle) and POPC:POPS (8:2, mol:mol, right), for each of the 10 repeats over the 1.5 µs CG simulation time period. The colors represent the different binding modes: orange (binding with non-canonical conformation), blue (binding with canonical conformation) and grey (no binding).

Within the 1.5 µs of the CG simulations in 2/10 repeats the TIAM2-PH domain bound in the canonical conformation to the POPIP3 containing membrane, in 3/10 to the POPIP2 containing membrane and in 4/10 to the POPIP-free membrane (Figure 4.16). The canonical binding conformation was defined as being similar to the model of membrane bound TIAM2-PH predicted in a previous study.[72] This model was obtained by a structural comparison between TIAM2-PH and its closest related PH domain, the β-spectrin PH domain, which revealed that a similar POPIP binding is likely. According to the POPIP3 binding site of the β-spectrin PH domain the POPIP binding residues correspond to the following TIAM2-PH residues: K514, R531, K532, W533, H579 and K581 (residue numbers correspond to mouse TIAM2). Figure 4.18 shows one of the POPIP2 canonical binding events, with the POPIP binding residues highlighted in yellow. In this binding event, three POPIP2 lipids were in contact with these POPIP binding residues (meaning within 5 Å, shown in orange).

In conclusion, TIAM2-PH seems to favour POPIP2 as anionic lipid binding partner over POPIP3 or POPS. However, there was more canonical binding in the presence of POPS and surprisingly high

amount of non-canonical binding in the presence of POPIP2, suggesting the potential of another productive binding mode of TIAM2-PH solely obtained in the presence of POPIP2.

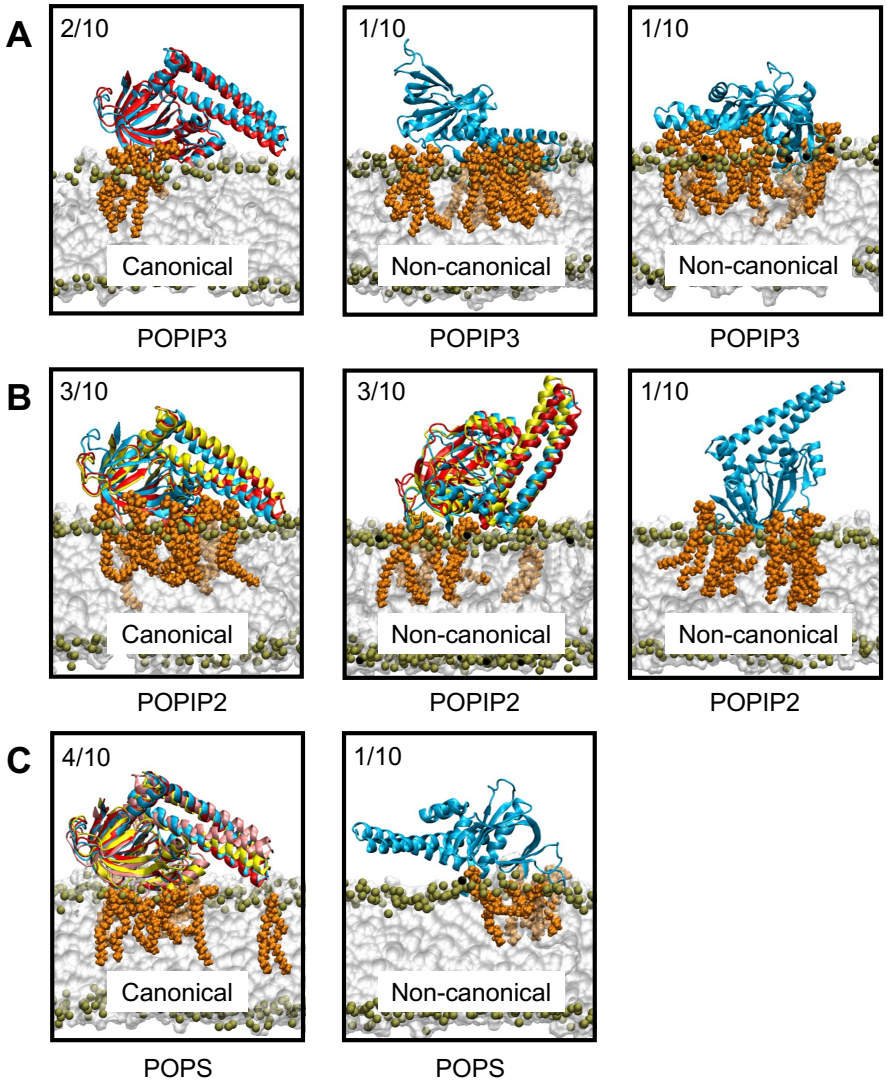


Figure 4.16 | Clustered TIAM2-PH Binding Conformations Reveal Subgroups. Shown are the final CG binding poses of TIAM2-PH, converted into AA and aligned along the membrane normal. For POPIP3 (**A**) 2/10 repeats bound in the canonical manner (left) and 2/10 in a non-canonical manner (middle, right). For POPIP2 (**B**) 3/10 repeats bound in the canonical manner (left) and 4/10 in a non-canonical manner whereby 3 of the latter had very similar conformation (middle). Interestingly, for the membrane without POPIPs (**C**) 4/10 repeats bound in the canonical manner (left) and 1/10 in a non-canonical manner (right).The POPIP lipids within 5 Å of the bound TIAM2-PH are shown in orange. For the POPIP-free membrane the POPS lipids within 5 Å of the bound TIAM2-PH are shown in orange.

Undertaking the same analysis process as previously done for the K2-PH, the protein orientation and protein-membrane distance profiles revealed that TIAM2-PH binds in the presence of either, POPIP2

or POPIP3, with its canonical membrane binding conformation (Figure 4.17, **A,B**). Thus, at the time of membrane binding the R_{zz} value is around 1, indicating that the TIAM2-PH conformation is almost identical to the reference structure. The reference structure was chosen to be the final frame of one of the repeats which showed canonical binding to the POPC:POPS:POPIP3 (7:2:1) membrane (repeat 7, see also Appendix Figure 4.33). In agreement with this observation, the density maps of the protein distance *versus* orientation showed only one binding mode at R_{zz} = 1 (Figure 4.17, **A,B**, right column). In contrast, without POPIPs present in the membrane, the flexibility in the orientation of TIAM2-PH is significantly higher after the initial membrane contact (Figure 4.17, **C**). The protein binds in two out of four discovered repeats not in its canonical binding conformation and undergoes a tumbling period before reaching the canonical binding conformation and constant R_{zz} value of around 1.

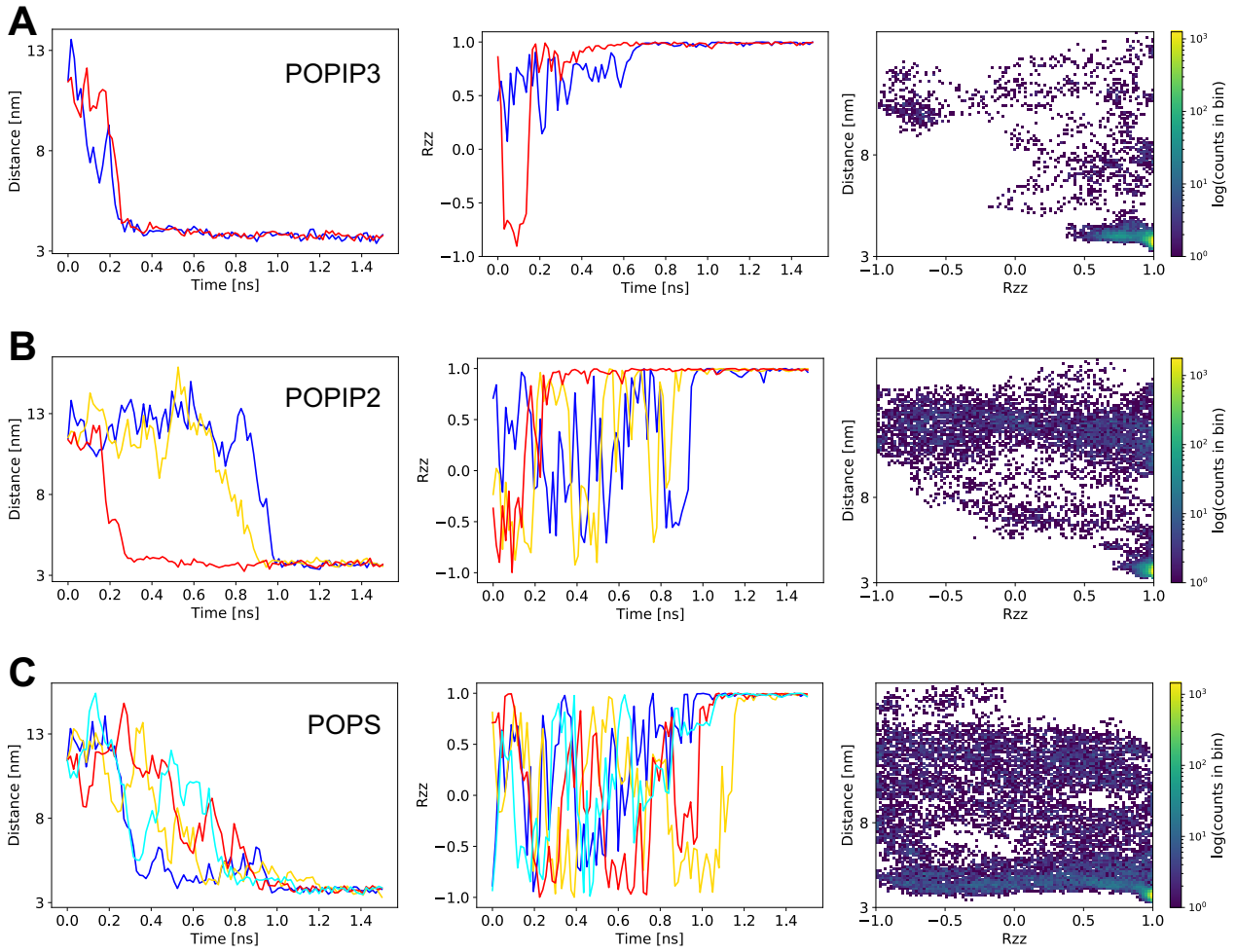


Figure 4.17 | TIAM2-PH Membrane Binding Process. For all CG repeats which showed canonical membrane binding of TIAM2-PH after 1.5 µs, the center of mass distance between protein and membrane (left), as well as the protein orientation (middle) are shown over time. Hereby, the membrane contained either POPIP3 (**A**), POPIP2 (**B**) or no POPIPs (**C**). The protein orientation is given by the *zz* component of the rotation matrix (R_{zz}) relative to the previously defined canonical binding conformation of TIAM2-PH. In **A-C** each color represents one repeat, with the color scheme between distance and orientation plot being identical within each panel/membrane system. In the right column, the density maps of the protein orientation *versus* the protein-membrane distance of the TIAM2-PH domain for the different membrane systems are shown. Each density map represents the relative frequency, averaged across time and repeats of the protein orientation at a certain protein-membrane distance (on a logarithmic color scale from purple = low to yellow = high, see color bars).

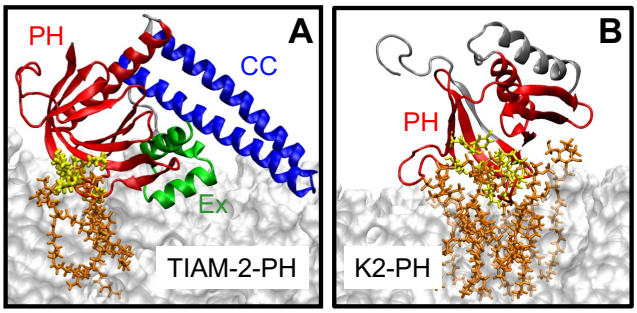


Figure 4.18 | Canonical Binding Conformations. One of the canonical final CG binding poses in which TIAM2-PH interacts with a POPC:POPS:POPIP2 (7:2:1, mol:mol: mol) membrane, converted into AA is shown in **A**. The side view of TIAM2-PH presents its three subdomains: the N-terminal PH subdomain (red), the CC region (blue) and the Ex domain (green). The connecting loops are shown in grey. A previous study suggested a POPIP binding side, highlighted with the stick model in yellow (K514, R531, K532, W533, H579 and K581).[72] Three POPIP2 lipids, which were in contact with this binding site, are shown in orange. In **B** one of the canonical final CG binding poses in which K2-PH interacts with a POPC:POPS:POPIP3 (7:2:1, mol:mol:mol) membrane, converted into AA is shown. The PH-domain (residue 380-476) is shown in red, while the additional loops are shown in grey. The previously suggested POPIP binding site is highlighted with the stick model in yellow (K383, K385, K386, K390, K393, K408, H419, Y395).[86] Six POPIP3 lipids, which were in contact with this binding side, are shown in orange.

Interestingly, the exclusion of the C-terminal Ex-domain (residue 707-741) from the TIAM2-PH construct, called TIAM2-PH-mEx, significantly increased the amount of binding events between TIAM2-PH-mEx and the POPIP3 containing membrane (Figure 4.19). Here, in 9/10 repeats the TIAM2-PH-mEx domain bound to the POPC:POPS:POPIP3 (7:2:1, mol:mol:mol) membrane within the 1.5 µs of the CG simulations. In contrast, the number of binding events for TIAM2-PH-mEx with the POPIP2 containing membrane, as well as with the POPIP-free membrane were with 6/10 repeats almost identical to the amount of binding events observed for TIAM2-PH including the Ex-domain (7/10 for POPIP2 and 5/10 for POPIP-free, Figure 4.15). However, in only one repeat out of the nine repeats showing binding events with the POPIP3 containing membrane the canonical binding conformation was observed (Figure 4.20, **A**). The number of canonical binding events to the POPIP-free membrane decreased from 4/10 in presence of the Ex domain (Figure 4.16, **C**) to 2/10 in absence of the Ex domain (Figure 4.20, **C**). For POPIP2 the number of canonical binding events seemed to be unaffected by the absence of the Ex domain and was with 3/10 repeats identical (Figure 4.16, 4.20, **B**). Taking these results together, the absence of the Ex domain seems to influence the TIAM2

binding to POPIP-free and POPIP3 containing membranes, much less though the binding to POPIP2 containing membranes. Therefore, the question results if the Ex domain might lead to some selectivity of TIAM2 favouring POPIP2 over POPIP3 by preventing binding to POPIP3.

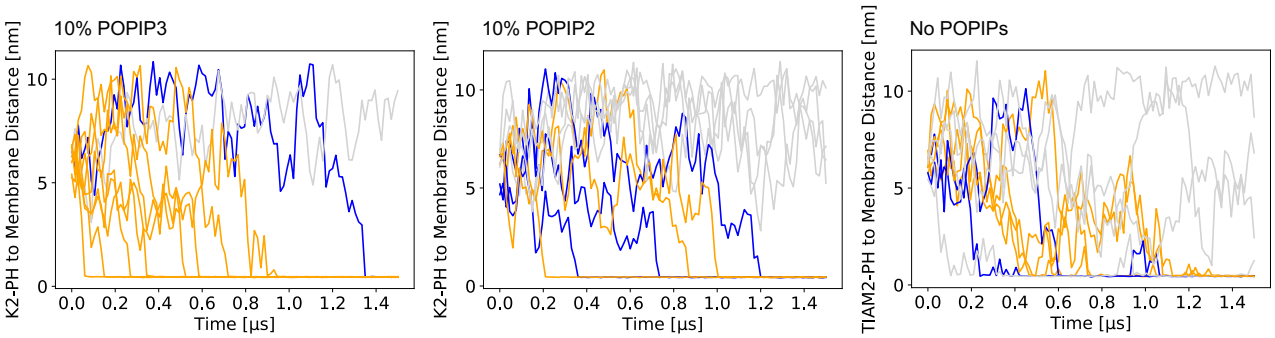


Figure 4.19 | The Ex-domain Influences Membrane Binding of CG TIAM2-PH. Minimum distance between the TIAM2-PH-mEx (no Ex-domain present) and the membrane, composed of POPC:POPS:POPIP3 (7:2:1, mol:mol:mol, left), POPC:POPS:POPIP2 (7:2:1, mol:mol:mol, middle) and POPC:POPS (8:2, mol:mol, right), for each of the 10 repeats over the 1.5 µs CG simulation time period. The colors represent the different binding modes: orange (binding with non-canonical conformation), blue (binding with canonical conformation) and grey (no binding).

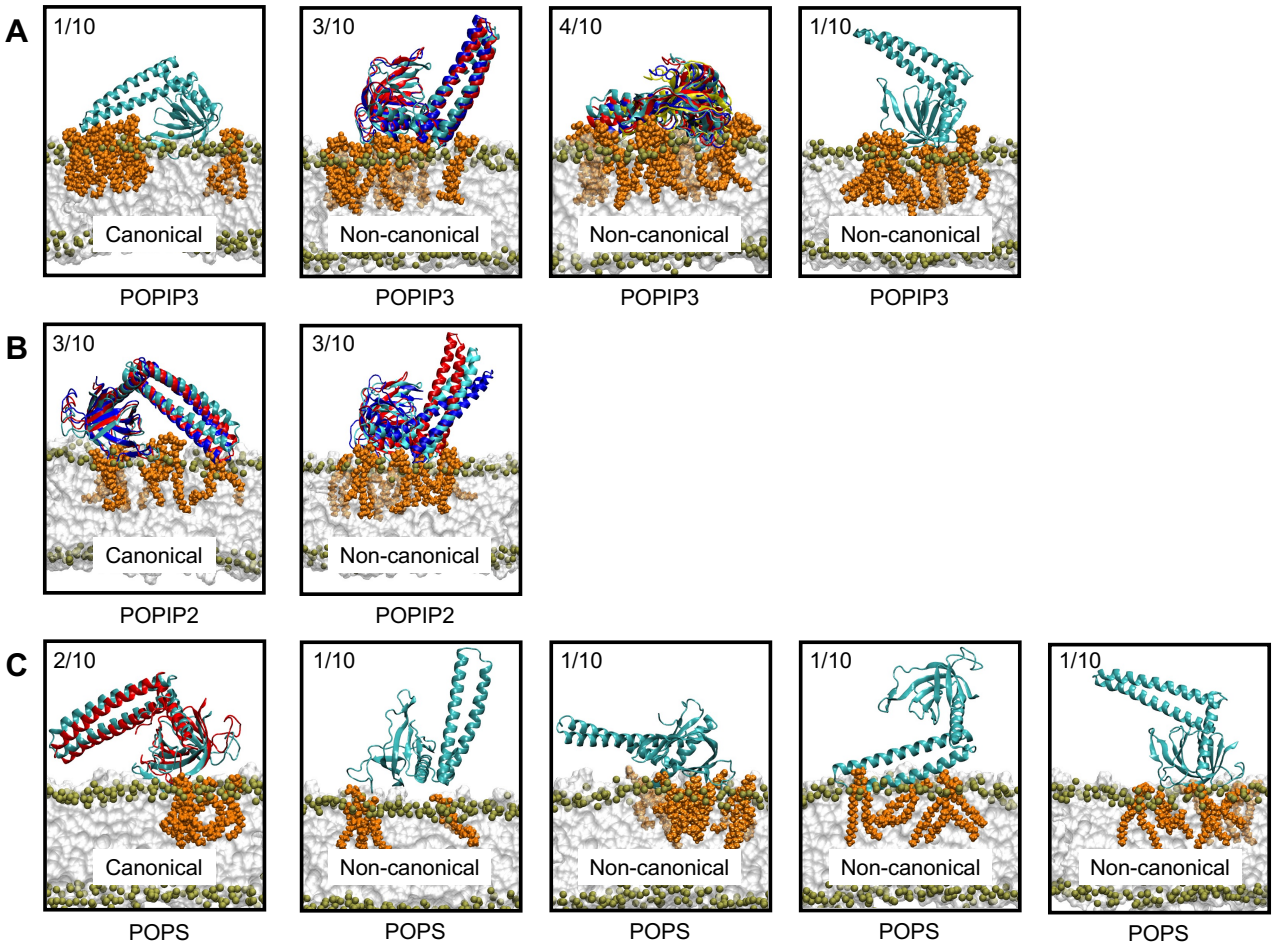


Figure 4.20 | Clustered TIAM2-PH-mEx CG Binding Conformations in AA Representation. Shown are the final CG binding poses of TIAM2-PH-mEx, converted into AA and aligned along the membrane normal. For POPIP3 (**A**) 1/10 repeat bound in the canonical manner (left) and 8/10 in a non-canonical manner. The non-canonical binding events were clustered into three different conformations. For POPIP2 (**B**) 3/10 repeats bound in the canonical manner (left) and 3/10 in a non-canonical manner whereby all of the latter had very similar conformation (middle left). Interestingly, for the membrane without POPIPs (**C**) 2/10 repeats bound in the canonical manner (left) and 4/10 in a non-canonical manner. All the non-canonical binding events showed no structural similarity. The POPIP lipids within 5 Å of the bound TIAM2-PH-mEx are shown in orange. For the POPIP-free membrane the POPS lipids within 5 Å of the bound TIAM2-PH-mEx are shown in orange.

Equilibrated CG Lipid Binding Sites Used to Define AA Starting Structures

To study the protein-lipid interactions in greater detail, we calculated the POPIP binding sites of the canonical and non-canonical binding events of K2-PH and TIAM2-PH, using the program PyLipID.[310] PylipID identifies protein-lipid binding sites based on residence time in MD simulations. The last half of the CG simulations (from 0.75 to 1.5 µs) were used for the PyLiID calculations. PyLipID initially identified eight POPIP3 binding sites (BSs) for the canonical binding of K2-PH to

the POPC:POPS:POPIP3 (7:2:1, mol:mol:mol) membrane. A further screening of these BSs dismissed BSs with an occupancy lower than the percentage of the POPIP3 molecules within the membrane, as well as BSs showing a larger absolute value than 1 μs^{-1} for the difference between the k_{off} from the BS curve fit and the bootstrapped k_{off} (Δk_{off}). This analysis resulted in three well equilibrated, validated POPIP3 BSs. The same procedure revealed three POPIP3 BSs for the non-canonical binding of K2-PH to the POPC:POPS:POPIP3 (7:2:1, mol:mol:mol) membrane and five POPIP2 BSs for the canonical binding of K2-PH to the POPC:POPS:POPIP2 (7:2:1, mol:mol:mol) membrane. The amino acids of K2-PH forming the different BSs are shown in Figure 4.21. Most amino acids, which are involved in POPIP3 interactions are also involved in POPIP2 interactions for the canonical binding of K2-PH (Figure 4.21, **A**, **C**), including the Lysine rich area forming the previously predicted PIP binding site (marked with asterisk).[86] Furthermore, there are several amino acids involved in POPIP2-, but not in POPIP3-interactions, resulting in five compared to three BSs for POPIP2 and POPIP3, respectively. However, the occupancy of these two additional POPIP2-BSs is with 12 and 57% low, suggesting lower affinity and significance of these PIP BSs in the interaction with K2-PH (for PyLipID key parameters see Appendix, Figure 4.28). As expected, the non-canonical binding conformation of K2-PH showed no interaction with the previously predicted PIP binding site.[86] Also, two out of three non-canonical PIP BSs had very different location in the protein compared to the canonical PIP BSs. To gain a structural insight of where the BSs are located within the K2-PH, the BSs are visualized in Figure 4.21.

The same calculation process was done for the TIAM2-PH simulations, revealing three, four and two POPIP-binding sites for the POPIP3 canonical, POPIP2 canonical and the POPIP2 non-canonical binding conformation of TIAM2-PH, respectively. For the POPIP-free POPC:POPS membrane (8:2, mol:mol) two POPS binding sites were identified for TIAM2-PH bound in the canonical conformation. See Figure 4.22 for the amino acids, which are involved in canonical TIAM2-PH membrane binding (for PyLipID key parameters see Appendix, Figure 4.32). Interestingly, the same amino acids of TIAM2-PH, which form POPS BSs are also forming POPI3 and POPIP2 BSs, suggesting low selectivity of these TIAM2-PH lipid binding sites. These less selective BSs includes the previously predicted PIP BS of TIAM2 (marked with asterisk).[72] However, there are two and one additional BS of POPIP2

and POPIP3, respectively, compared to the POPS BSs of TIAM2-PH. These additional BSs are located in between the other two non-selective BSs (Figure 4.22). This implies that the amino acids forming these more selective BSs are responsible for PIP selectivity and affinity of TIAM2.

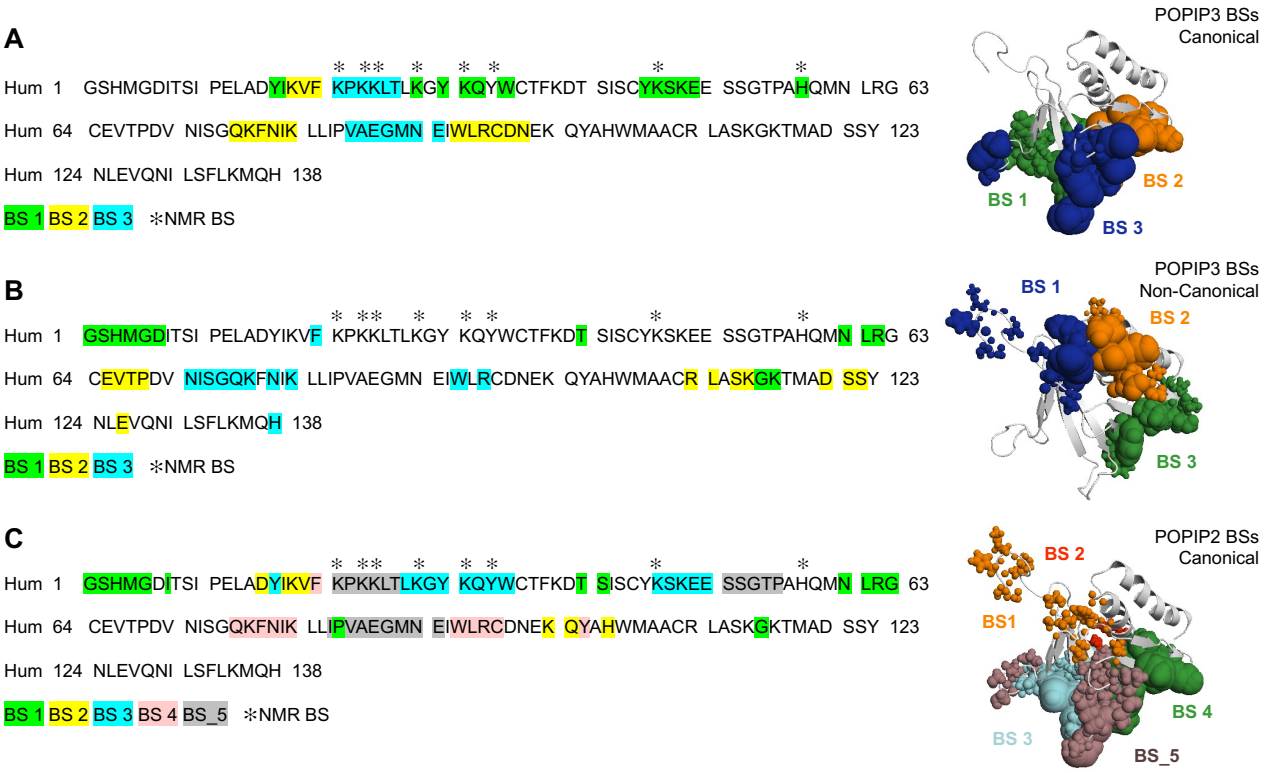


Figure 4.21 | Sequence of POPIP3 and POPIP2 BSs of K2-PH. Shown is the sequence of K2-PH with the residues building the different POPIP BSs highlighted in respective colours. **A** shows the POPIP3 BSs of K2-PH when K2-PH was canonical bound to the POPC:POPS:POPIP3 (7:2:1, mol:mol:mol) membrane. **B** shows the POPIP3 BSs of K2-PH when K2-PH was non-canonical bound to the POPC:POPS:POPIP3 (7:2:1, mol:mol:mol) membrane. **C** shows the POPIP2 BS of K2-PH when K2-PH was canonical bound to the POPC:POPS:POPIP2 (7:2:1, mol:mol:mol) membrane. The residues marked with an asterisk correspond to the previously suggested POPIP BS. [86]

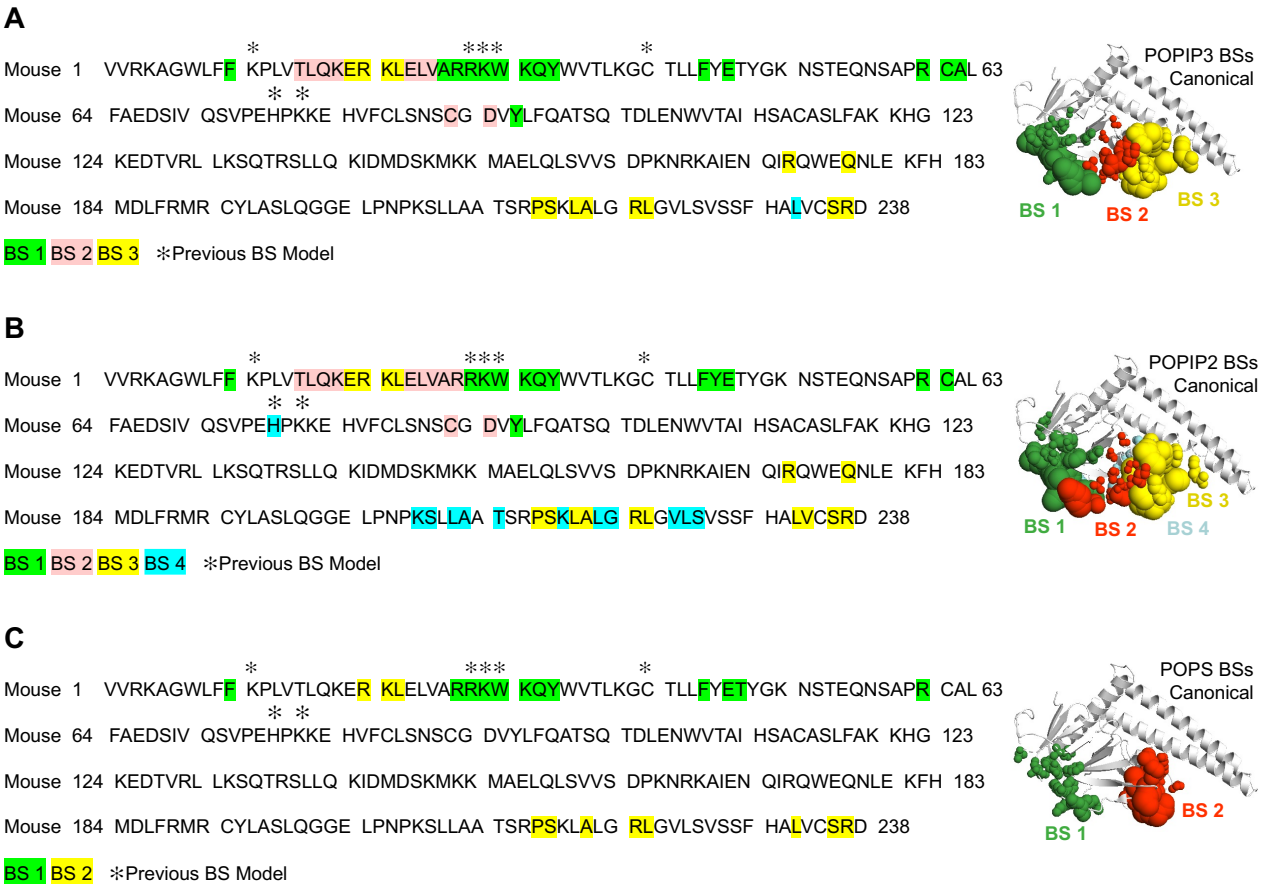


Figure 4.22 | Sequence of POPIP and POPS BSs of TIAM2-PH. Shown is the sequence of TIAM2-PH with the residues building the different POPIP BSs highlighted in respective colours. **A** shows the POPIP3 BSs of TIAM2-PH when TIAM2-PH was canonical bound to the POPC:POPS:POPIP3 (7:2:1, mol:mol:mol) membrane. **B** shows the POPIP2 BSs of TIAM2-PH when TIAM2-PH was canonical bound to the POPC:POPS:POPIP2 (7:2:1, mol:mol:mol) membrane. **C** shows the POPS BS of TIAM2-PH when TIAM2-PH was canonical bound to the POPC:POPS (8:2, mol:mol) membrane. The residues marked with an asterisk correspond to the previously suggested POPIP BS.[72]

Calculating the minimal distance between POPIP lipids and the identified POPIP BSs of K2-PH and TIAM2-PH over the simulation time showed in which repeats the POPIP lipids were equilibrated well around the protein by sitting in the respective BS. Details of the outcome of this analysis are shown at the end of this Chapter, in the Appendix, Figure 4.29, 4.30, 4.31, 4.33, 4.34, 4.35. The final poses of one of these well equilibrated CG repeats for non-canonical and canonical K2-PH and TIAM2-PH binding was converted into an all atomistic (AA) representation for further analysis, with particular interest in the stability of the different binding poses. Hereby, as a recent study suggested an influence of the 4′ phosphate protonation state on the binding affinity between K2-PH and POPIPs,[87]

different protonation states of POPIP3, as well as POPIP2 were generated when converting the K2-PH structure from CG to AA (see Appendix, Figure 4.25 for PIP structures).

AA Binding Poses for Direct Comparison with NR Results

The Cα RMSD calculations of the K2-PH and TIAM2-PH proteins over the time of the AA simulations showed that the protein structures were fairly stable after 300 ns of simulation time (Appendix, Figure 4.36). Therefore, we calculated the density profiles of the proteins bound to the membrane for the final 150 ns of the AA simulations. In case of TIAM2-PH the protein stayed bound to the membrane throughout the simulation, even for the POPIP-free membrane (Appendix, Figure 4.37, **B**). The thickness of the TIAM2-PH domain showed with 30-31 Å for the canonical binding conformation to all the membranes, containing POPIP3, POPIP2 or no POPIP, good agreement with the experimental NR thickness of 29 $\pm$ 4 Å (Figure 4.23, Table 4.2). However, also the observed non-canonical binding conformation of TIAM2-PH showed with a thickness of 28 Å good agreement with the experimental NR thickness. Furthermore, the similarity of the membrane penetration of canonical and non-canonical binding conformation made further assumptions concerning the dominant binding conformation observed in the NR experiments invalid. On the other hand, the K2-PH density profiles indicated for all system setups, including different protonation states of POPIP3 and POPIP2, for both canonical and non-canonical binding conformation with 23-29 Å a significantly smaller protein layer thickness than the NR experiments suggested with 68 $\pm$ 4 Å (Figure 4.23, Table 4.2). To investigate whether protein multimer formation on top of the membrane causes this significant increase in protein layer thickness on top of the membrane, we simulated multiple K2-PH proteins binding to the same POPC:POPS:POPIP3 (7:2:1 mol:mol:mol) membrane (see Methods 4.4.5). Indeed, we observed trimerization of K2-PH throughout a 1.5 µs CG simulation of nine K2-PH proteins, all starting 9 nm above the membrane, separated by 14 nm along x and y (Figure 4.24). After an initial dimerization in solution, a K2-PH dimer bound to a membrane bound K2-PH, forming a stable trimer across the final 400 ns of the CG simulation. With a thickness of around 62 Å the trimer of K2-PH showed much better agreement with the NR experiments.

These findings showed how well NR experiments and MD simulations can complement each other. While for TIAM2-PH the MD simulations confirmed our experimental findings concerning protein layer thickness on top of the membrane, for K2-PH the NR experiments provided the necessary indication to investigate potential protein multimer formation on the membrane via simulations. The latter confirmed K2-PH trimerization on top of the membrane and was in good agreement with our experimental results.

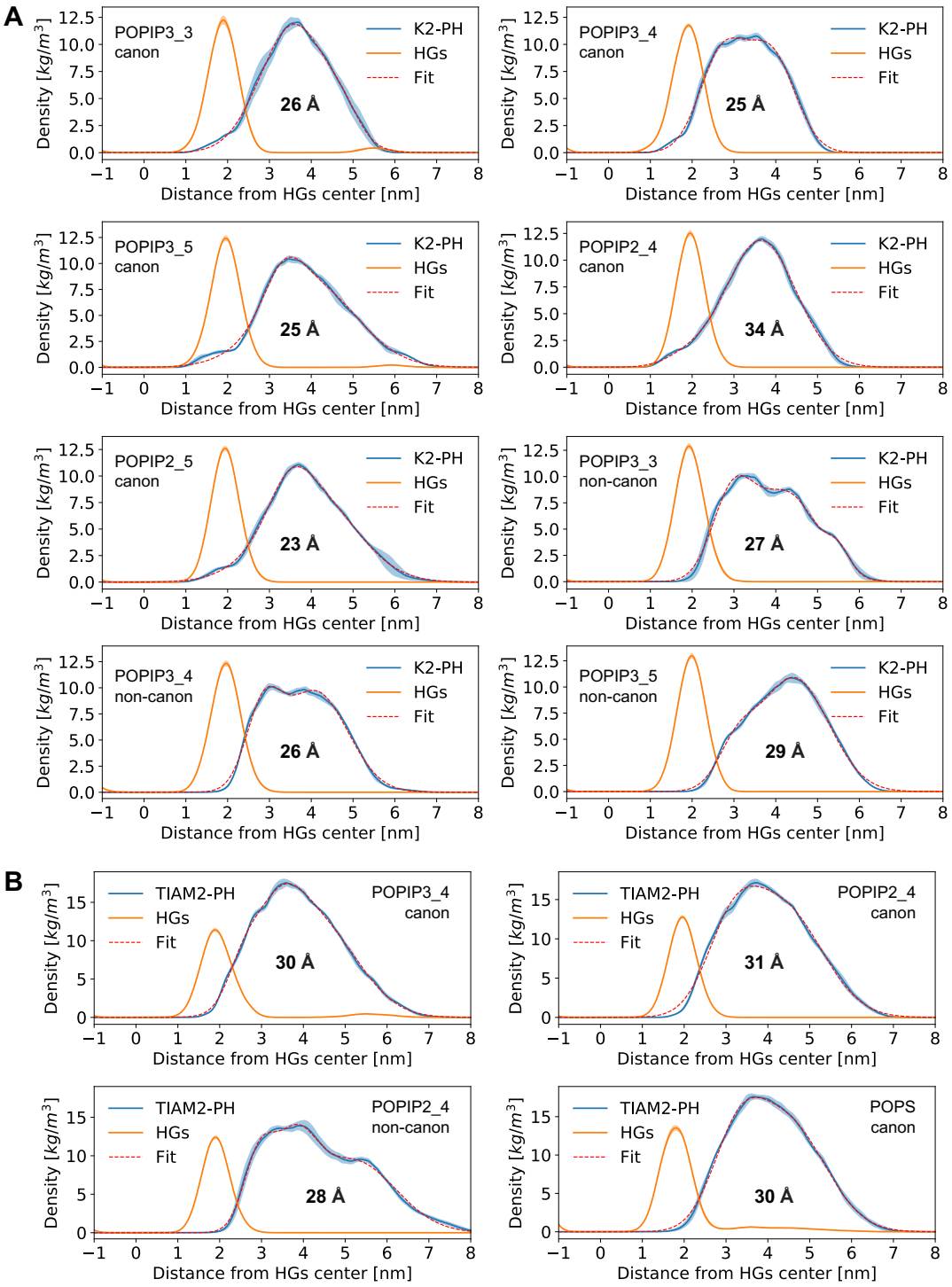


Figure 4.23 | AA Simulations Reveal Thickness and Membrane Penetration of Membrane-bound K2-PH and TIAM2-PH. Shown are the averaged density profiles over the last 150 ns of the AA simulations of K2-PH (**A**) and TIAM2-PH (**B**). The density distribution of the lipid head groups (HGs, orange), of the protein (blue) and the fit of the protein density profile using 2-3 Gaussian distributions (red, dashed) are shown. The legends show which POPIP was present in the POPC:POPS:POPIP (7:2:1 mol:mol:mol) membrane; the last number defines the position of the protonated phosphate group in the inositol ring (see Appendix, Figure 4.25 for PIP structures). "Canon" and "non-canon" stand for canonical and non-canonical binding conformation, respectively. The thickness of the protein layer defined as FWHM of the fitted Gaussian distributions is given for each plot. In order to visualize the density profiles of the proteins, the density of the HGs was divided by 2.

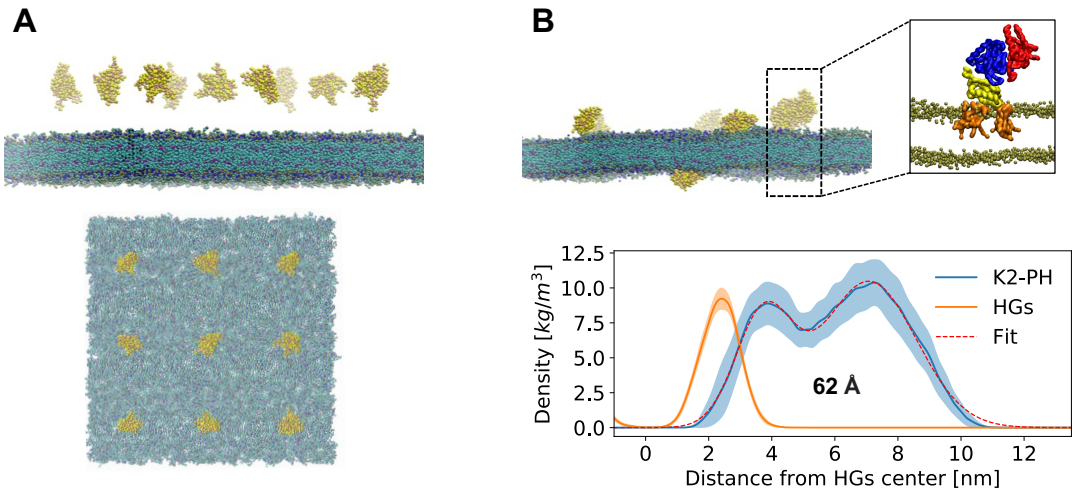


Figure 4.24 | CG Simulation of Multiple K2-PH Showed Protein Trimerzation. The initial setup of the CG simulation including nine K2-PH proteins placed in a grid, 9 nm above a POPC:POPS:POPIP3 (7:2:1 mol:mol:mol) membrane and with a distance of 14 nm along x and y between them is shown in **A**. A final snapshot of the 1.5 µs CG simulation including a zoom in of a K2-PH trimer structure formed over the course of the simulation is shown in **B**. Additionally, the density profiles calculated via the final 300 ns of the simulation is shown for the lipid head groups (HGs, orange) and the K2-PH trimer (blue). For the latter a fit built with two Gaussian distributions is shown in red, dashed. The FWHM of the fit, representing the thickness of the protein layer, was 62 Å.

Interestingly, the different protonation states of the POPIPs seemed to influence the binding conformation of the AA K2-PH (Appendix, Figure 4.37). For better comparison we calculated RMSDs using the canonical binding conformation of K2-PH bound to a membrane containing 10% POPIP3, protonated at position 4' of the inositol ring (POPIP3_4) as a reference structure (Appendix, Figure 4.37, cyan). Both canonical binding conformations of K2-PH bound to a membrane containing 10% of POPIP3, protonated at position 3' (POPIP3_3) or to a membrane containing 10% POPIP2, protonated at position 4' of the inositol ring (POPIP2_4) showed with an RMSD of 0.7 nm great similarity to the reference structure. On the other side, in the presence of 10% of POPIP3, protonated at position 5' (POPIP3_5) or 10% POPIP2, protonated at position 5' of the inositol ring (POPIP2_5), the canonical binding conformation of K2-PH seemed to differ considerably more from the reference structure (RMSD of 0.9 nm and 1.2 nm, respectively). Furthermore, only in the presence of POPIP3, protonated at position 4' of the inositol ring (POPIP3_4) the initially non-canonically bound K2-PH was able to

switch into the canonical binding conformation within the first few ns of the production run. In contrast, in presence of POIP3_5 and POPIP3_3 the K2-PH maintained its non-canonical binding conformation.

These findings suggested that the difference between the canonical PIP3- and PIP2-binding conformation of K2-PH is increased in the protonated 4' state compared to the unprotonated 4' state of the PIPs. Furthermore, the protonation of the phosphate group at position 4' might facilitate the canonical binding conformation of the membrane bound K2-PH.

4.3 Discussion

Our previous findings in *Chapter 3* showed that the novel free floating model membrane (FFM) system provides better membrane mimicking characteristics compared to other planar model membranes in which the membrane is either deposited directly onto a supporting substrate [107] or linked to the substrate surface by a hydrophilic polymer layer [234] or substrate attached polymeric membrane tethers.[127] Therefore, we were curious to see if we can use the FFM system for studying the membrane bound conformation of peripheral membrane proteins (PMPs).

One concern about the usage of the FFM system for studying PMPs was the sensitivity of the reflectivity data obtained with the FFM system concerning the changes the binding of a PMP causes. Compared to simpler planar model membrane systems, the FFM system contains more reflecting interfaces contributing to the reflectometry data. Multiple interfaces in the system lead to multiple interference of the reflected neutron waves and reflectivity profiles with more Kiessig fringes. This makes the data less sensitive to changes caused by the addition of a protein layer in the sample system and therefore the fitting procedure for capturing the parameters of the protein layer more challenging. Our results showed that by changing the substrate layer composition from silicon/silicon dioxide/Permally/gold to silicon/silicon dioxide/chromium/gold significantly increases the sensitivity of the reflectivity data concerning the binding of PMPs to the floating membrane (Figure 4.7). The change of the permalloy to a chromium layer effectively decreases the substrate from a four interface to a three interface substrate due to the similarity of the silicon dioxide and chromium scattering length density. Calculated model fits of this FFM system, decreased by one reflecting interface, showed

to be sensitive to the binding of even small peripheral membrane proteins of a thickness of around 30 Å (Figure 4.7). The neutron reflectometry (NR) measurements investigating the binding of the well established pleckstrin homology (PH) domain of the general receptor for phosphoinositides 1 (Grp1) protein confirmed this prediction and made our initial concern about the sensitivity of the FFM system invalid. So, we gained information about the thickness of the Grp1-PH protein bound to the membrane, which was with 30 ± 8 Å in good agreement with the dimensions of the crystal structure of Grp1-PH.[52] Furthermore, with our advanced model fits, which treat the lipid head group and lipid tail layer of the external membrane leaflet as mixed layers containing protein, water and lipid, we were able to gain information about the protein coverage outside and inside the membrane (Figure 4.8).

A further finding of importance was the effect Ca^{2+} seems to have on the membrane binding affinity of PH domains. NR, as well as attenuated total reflection (ATR) Fourier transform infrared (FTIR) spectroscopy (ATR-FTIR) revealed that for all three PH domains investigated in this study the binding got significantly decreased by the presence of Ca^{2+} in the sample system. The PH domains studied were the PH domain of the Grp1 protein (Grp1-PH), the kindlin-2 protein (K2-PH), as well as of the TIAM2 protein (TIAM2-PH). All three proteins are known to bind membranes containing the highly negatively charged phosphatidylinositol lipids (PIPs). Hereby, they show different selectivity and affinity concerning the various variations of PIP3 and PIP2.[63], [72], [86] Their membrane localization is crucial for the proteins to fulfil their function as co-activator of talin mediated integrin activation and EGFR stabilizer [305], [306], as activator of Rac1 GTPase [311], [312] and as a nucleotide exchange factor for the small GTP proteins of the ARF family [64] in case of K2, TIAM2 and Grp1, respectively. Interestingly, a key pathophysiological occurrence of insulin resistance, obesity and type 2 diabetes is an increased intracellular Ca^{2+} concentration in muscle and liver.[313]–[315] It has been previously shown that these elevated Ca^{2+} levels lead to tight binding between Ca^{2+} and PIPs, which prevents membrane recruitment of PH domains.[316] Our findings confirm this hypothesis and suggest that the range of associated diseases related to abnormal subcellular localization of PH domains due to elevated Ca^{2+} concentration might be even broader than suggested so far as many different PH domains in various proteins like K2 and TIAM2 with important signalling and activation functions might be influenced.

The comparison between our NR results with all atomistic (AA) molecular dynamics (MD) simulations showed good agreement concerning the thickness of the TIAM2-PH protein layer when bound to a PIP containing membrane (29 $\pm$ 4 Å in NR *versus* 30 $\pm$ 2 in MD, see Figures 4.23 and 4.11, **B**). However, the MD simulation results indicated similar protein thickness of the canonical and non-canonical membrane binding conformations of TIAM2-PH. Furthermore, the penetration of the protein was also similar between canonical and non-canonical binding conformations and reached no further than the lipid head group area (Figure 4.23, **B**). Therefore, we could make no further assumptions about the dominant TIAM2-PH membrane binding conformation observed in the NR experiment on the basis of the MD results. Additionally, the protein penetration observed in the MD results suggested that treating the lipid tail layer of the outer membrane leaflet as a mixed layer containing protein among lipids and water might not be suitable. Solely the lipid head group of the outer membrane leaflet should be treated as such a mixed layer. In the future we will use the MD results also in terms of defining the layers the protein might occupy in the membrane, which therefore have to be handled as mixed layers in the model fit.

While the TIAM2-PH protein was solely investigated with the supported lipid bilayer system so far, we used the more advanced FFM system to study the binding conformations of K2-PH interacting with floating membranes varying in PIP3 content. While our model fits were unable to capture a protein layer on top of the PIP3-free and 5 mol% PIP3 containing membrane, a K2-PH protein layer with a thickness of 68 $\pm$ 4 Å was predicted on top of the 10 mol% PIP3 containing floating membrane (Figure 4.6). In contrast, our AA MD simulations provided canonical and non-canonical binding conformations of K2-PH on top of various PIP containing membranes, which suggested a protein thickness within a range of 29 $\pm$ 4 Å (Figure 4.23, **A**). Interestingly, performed coarse grained (CG) MD simulations of multiple K2-PH proteins revealed trimerization of single K2-PH proteins upon binding to the membrane (Figure 4.24). The thickness of the K2-PH trimer on top of the membrane was with 62 Å much closer to our experimental result, implying K2-PH multimer formation on the membrane surface. It has been previously suggested that K2 activates integrin by facilitating the clusering of talin-activated integrin [92] and recently dimerization of K2, observed *in crystallo*, proposed as a mechanistic model

of how K2 promotes integrin clustering.[93] Although the K2-PH domain is missing in the previously published crystal structure, the K2-PH domain is likely positioned within the dimer-interface and might contributing to the formation of K2 dimers.[93] Our results support the model of K2 multimer formation being a possible facilitator of integrin clustering. However, it has been reported that the Martini 2 force field used for the multi K2-PH CG simulation might exaggerate protein-protein interactions, leading to unrealistic protein clusters.[210] In addition, the multimer formation of PMPs along the membrane normal as observed with K2-PH, rather than on the membrane surface to form protein clusters within the membrane, is quite unusual. Therefore, further simulations using either all atomistic resolutions or the newly parameterized Martini 3 force field, which introduced new beads and rebalanced all non-bonded interaction terms,[206] will be needed for additional validation of the observed K2-PH trimers. Furthermore, repeating the NR experiments using a substrate containing chromium instead of permalloy would increase the fitting quality of the NR data. These results are needed to confirm our initial NR results suggesting a K2-PH thickness of $\sim$68 Å after membrane binding, as well as to provide further insights in K2-PH orientation upon membrane binding and K2-PH membrane penetration.

Our multiscale MD simulations of the membrane binding processes of K2-PH and TIAM2-PH provided also some insights concerning PIP selectivity and binding conformation. K2-PH bound in 10 out of 10 (10/10) CG repeats and in 9/10 CG repeats to membranes containing PIP3 and PIP2, respectively. However, surprisingly, K2-PH bound only in 6/10 CG repeats with canonical conformation in the presence of PIP3 compared to 9/10 CG repeats in the presence of PIP2 (Figure 4.13) This was unexpected as there is previous evidence showing that PIP3 is a stronger binding partner of K2 compared to PIP2.[86] However, our computational results suggest that the stronger binding of POPIP3 compared to POPIP2 observed experimentally might be a result of canonical and non-canonical binding site interactions of the K2-PH domain. Thus, while POPIP3 shows stronger K2-PH affinity, POPIP2 leads more frequently to productive K2-PH binding. Although our simulations also showed that the process of reaching the canonical binding conformation takes sometimes longer and undergoes different non-canonical binding conformations in case of POPIP2, the number of canonical binding poses after 1.5 µs simulations was significantly higher compared to POPIP3, with 9 and 6 repeats,

respectively (Figure 4.14). Additionally, our AA simulations of membrane bound K2-PH showed that not only the number of phosphate groups on the inositol ring of the PIPs seems to influence the binding conformation of K2-PH, but also the protonation state of the single PIP phosphate groups. It has been previously shown that K2-PH binds in a PIP-protonation-state-dependent manner with PIPs deprotonated at 4' of the inositol ring showing the greatest differences in protein-PIP-contacts between POPIP2 and POPIP3.[87] In our results the RMSD of the K2-PH binding conformation to POPIP2 *versus* POPIP3 was also larger when PIP2/PIP3 were deprotonated at 4' compared to the protonated 4' state (0.9 nm *versus* 0.7 nm; Appendix, Figure 4.37). Furthermore, solely the K2-PH protein bound to POPIP3s protonated at 4' was able to switch from the non-canonical to the canonical binding conformation during the first few ns of the AA simulation. With POPIP3s deprotonated at 4' the K2-PH retained the non-canonical binding conformation. These results confirm the significance of the PIP protonation state for the binding conformation of K2 and suggest that the protonation at 4' might stabilize the canonical binding conformation. Free binding calculations of the K2-PH bound to differently protonated PIPs, as well as alchemical free energy perturbation calculations with differently protonated PIPs as starting and end state will be necessary for quantifying our findings.

In the case of TIAM2-PH, CG MD simulations with and without the C-terminal Ex-domain included in the protein showed that the presence of the membrane facing Ex-domain seems to decrease the binding to POPIP3, leading to higher selectivity towards POPIP2. Thus, although both lipids, POPIP2 and POPIP3, bound TIMA2-PH in its canonical binding conformation, showing almost no flexibility in protein orientation after membrane binding, POPIP2 displayed more frequent binding compared to POPIP3. Nevertheless, so far there was no selectivity between POPIP3 and POPIP2 observed for TIAM2.[57], [72] Again, further investigations by calculating free binding energies of TIAM2-PH bound to different PIP-containing membranes are needed to validate these hypotheses.

In conclusion we successfully demonstrated the usability of the FFM system to study PMPs, as well as the great addition MD simulations provide by complementing the data with all-atom resolution. However, our insights in the binding conformations were limited due to the small size and quite

spherical shape of the proteins used. Therefore, we suggest to use bigger proteins of more characteristic shape in order to get more information form the experimental NR data.

4.4 Methods

4.4.1 Materials

POPC (1-palmitoyl-2-oleoyl-*sn*-glycero-3-phosphocholine), POPS (1-palmitoyl-2-oleoyl-*sn*-glycero-3-phospho-L-serine), DOPIP3 (1,2-dioleoyl-*sn*-glycero-3-phospho-(10-myo-inositol-3',4',5'-trisphosphate), DOPIP2 (1,2-dioleoyl-*sn*-glycero-3-phospho-(1'-myo-inositol-4',5'-bisphosphate)) and SAPIP3 (1-stearoyl-2-arachidonoyl-*sn*-glycero-3-phospho-(1'-myo-inositol-3',4',5'-trisphosphate)) were obtained from Avanti polar lipids (Alabaster, AL, USA) and used without further purification. See Figure 4.25 for structural overview of used PIPs. OEG-SAM (HS-C_{11}-EG_3-OCH_2-COOH) was obtained from ProChimia surfaces (Gdansk, Poland). The Chemical structure of the OEG-SAM molecule is given in Figure 2.21. D_2O (Deuterium oxide) and HEPES sodium salt (*N*-(2-Hydroxyethyl)piperazine-*N*'-(2-ethanesulfonic acid) sodium salt) were sourced from Sigma-Aldrich (Gillingham, UK). $CaCl_2$ (Calcium chloride), NaCl (sodium chloride) and EDTA (Ethylenediaminetetraacetic) were sourced from Fisher Scientific (Loughborough, UK). Silicon substrates were obtained from Crystran (Poole, UK) as a bespoke request. The respective buffer solutions were prepared and pH/D adjusted at room temperature.

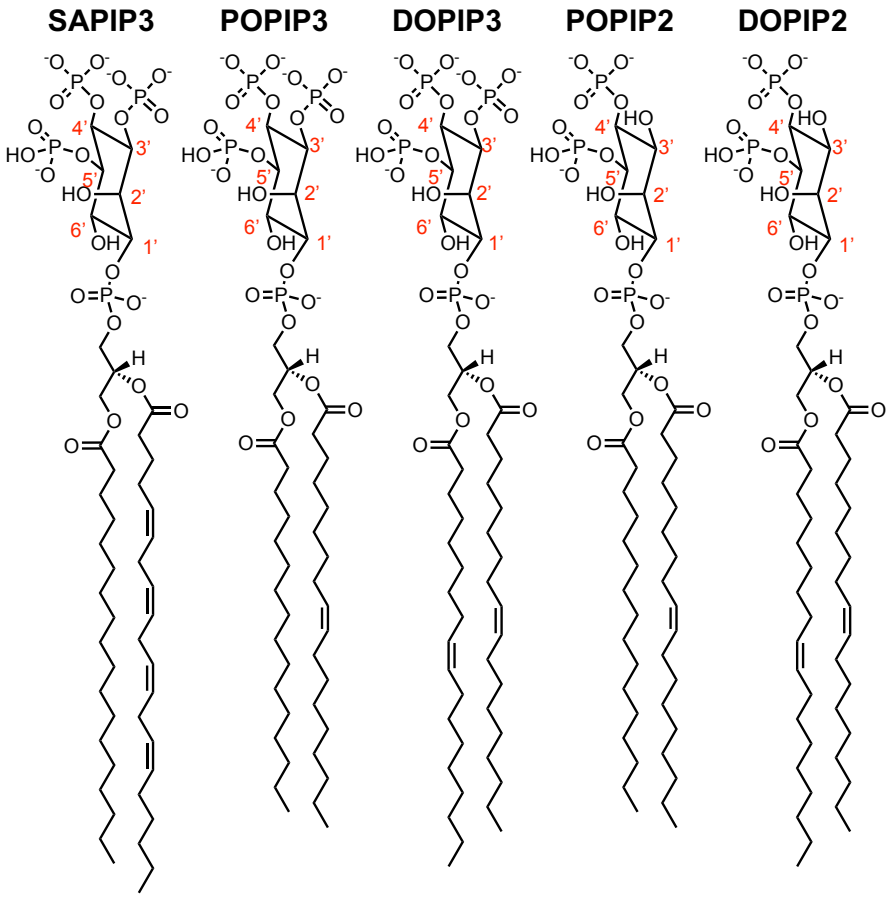


Figure 4.25 | Structures of Used Phosphatidylinositols (PIPs). In NR experiments DOPIP3 (1,2-dioleoyl-*sn*-glycero-3-phospho-(10-myo-inositol-3',4',5'-trisphosphate), DOPIP2 (1,2-dioleoyl-*sn*-glycero-3-phospho-(1'-myo-inositol-4',5'-bisphosphate)) and SAPIP3 (1-stearoyl-2-arachidonoyl-*sn*-glycero-3-phospho-(1'-myo-inositol-3',4',5'-trisphosphate)) were used; in MD simulations POPIP2 (1-palmitoyl-2-oleoyl-*sn*-glycero-3-phospho-(1'-myo-inositol-4',5'-bisphosphate)) and POPIP3 (1-palmitoyl-2-oleoyl-*sn*-glycero-3-phospho-(1'-myo-inositol-3',4',5'-trisphosphate)). All PIPs are visualized as protonated at 5'. In our MD studies we varied the position of the protonated phosphate group in the inositol ring. Structures were produced with ChemDraw.

4.4.2 Protein Constructs

For the experiments all proteins were provided by Dr. Susan Black. The experimental K2 construct included residues 367-511 of Uniprot Q8CIB5. This wild type mouse construct contained the K2-PH (residues 380-476) and differed from the human sequence by only two amino acids at position 410 and 421. For the MD simulations the NMR structure of the human K2-PH (PDB entry 2LKO) was used, which matched the human K2 sequence from residue 367 to 500 (for multi sequence alignment see Figure 4.26). The sequence used in the simulations has four additional N-terminal

residues compared to the experimentally used structure due to an N-terminal thrombin protease cut site (GSHM).[317] However, these additional residues didn't match the human sequence. Furthermore, the experimentally used construct had eleven additional C-terminal residues compared to the structure used in the simulations. These additional residues matched the human sequence (Figure 4.26).

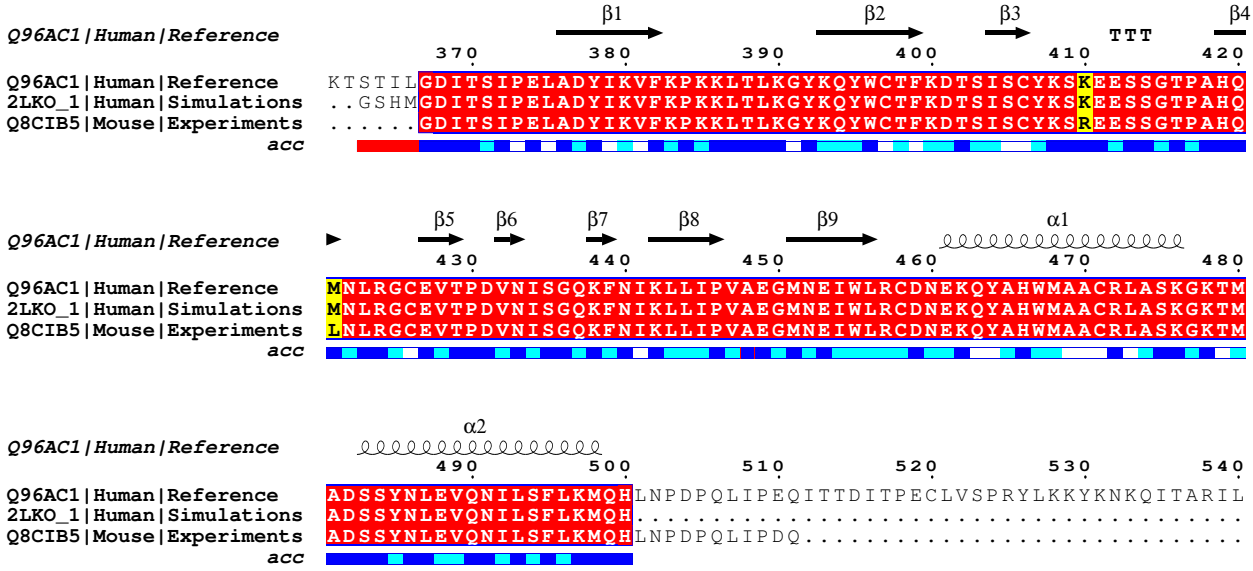


Figure 4.26 | Multi Sequence Alignment of K2-PH. The alignment was made using the Clustal Omega web server[318] and displayed by ESpript 3 software.[319] The human structure obtained from the PDB entry 2LKO, used in simulations (middle row) and the mouse structure obtained from the UniProt entry Q8CIB5, used in experiments (bottom row) were aligned to the human K2 sequence (top row). The residues highlighted in red are identical. While residues highlighted in yellow are not identical, they still show similarity in chemical properties like polarity and charge. Secondary structures are represented at the top for the K2-PH domain, while the surface accessibility is shown at the bottom (blue: surface accessible residues, cyan: partially accessible residues, white: buried residues, red: no accessibility was predicted). The data for the secondary structure was retrieved from the PDB structure 2LKO.

The experimental TIAM2 construct included residues 500-757 of mouse TIAM2 (PDB entry 3A8P), equivalent to residue 502-759 of human TIAM2 (Uniprot Q8IVF5). This mouse construct contained the TIAM2-PH (504-625), -CC (630-700) and -Ex (707-741) domain. For the MD simulations the whole resolved crystal structure obtained from the PDB entry 3A8P (residues 504-741) was used in order to match the experimental structure as closely as possible (for multiple sequence alignment see Figure 4.27). The residues of a flexible loop regions not resolved in the crystal structure (residue 554-559) were modelled using Swiss-Model.[320] While there are fourteen mismatches between

human and mouse sequence, nine of these mismatches show similarity in chemical properties like polarity and charge (residues highlighted in yellow in Figure 4.27). Thus, only at five positions the residues show very low similarity between human and mouse sequence (residues with white background within the construct in Figure 4.27).

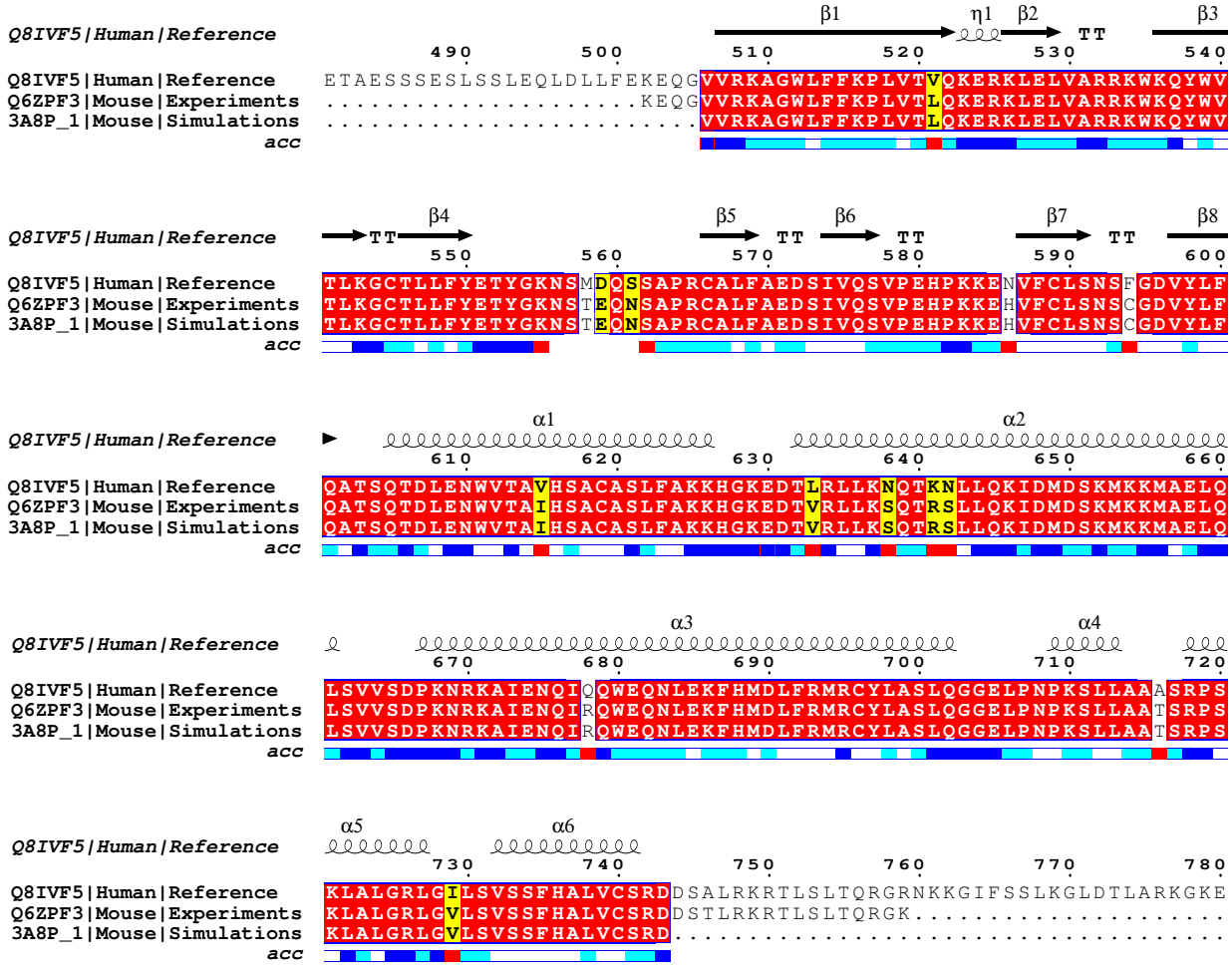


Figure 4.27 | Multi Sequence Alignment of TIAM2-PH. The alignment was made using the Clustal Omega web server[318] and displayed by ESpript 3 software.[319] The mouse sequence used in simulations and experiments (middle and bottom row) were aligned to the human TIAM2 sequence (top row). The residues highlighted in red are identical. While residues highlighted in yellow are not identical, they still show similarity in chemical properties like polarity and charge. Non-identical residues within the construct, which have no chemical similarity, have a white background. Secondary structures are represented at the top, while the surface accessibility is shown at the bottom (blue: surface accessible residues, cyan: partially accessible residues, white: buried residues, red: no accessibility was predicted). The data for the secondary structure was retrieved from the PDB structure 3A8P.

4.4.3 ATR-FTIR Experiments

The spectra were collected using a Thermo-Nicolet iSS50 instrument, including a cryo-cooled mercury cadmium telluride detector, in combination with an ATR flow through top-plate assembly (Sepcac). The water cooling loop of the latter was connected to a temperature-controlled water bath (set to 25 °C) and the inlet of the flow cell was connected to a syringe pump. To minimize the absorbance of water vapour, a dry-air purge operated at a flow rate of 40 L/min. The resolution of all spectra was 4 cm^{-1} and 128 interferograms were collected for each spectrum. Fourier self-deconvolution was performed by the data acquisition software OMNIC 9 (ThermoFisher Scientific) with a constant bandwidth applied across all spectra.

To set up the experiment, single-crystal silicon ATR substrates were cleaned for 10 min by UV-ozone cleaning followed by washing with ultra-pure water, drying and a second UV-ozone cleaning procedure. The inside of the flow cell, as well as in-/outlet were cleaned by rinsing with ethanol and ultra-pure water. The silicon substrate was mounted dry in the flow cell, which was then filled with salt buffer solution (20 mM HEPES, 150 mM NaCl, with or without 2 mM $CaCl_2$, pD 7.1 in D_2O; **Buffer A**). A spectrum for background correction was collected. The production of small unilammelar vesicles (SUVs) was performed as for the neutron reflectometry experiments and described in section 2.4.2. 3 mL of the 0.2 mg/mL SUV salt buffer solution were injected into the flow cell via the syringe pump at a flow rate of 0.1 mg/mL, at the target temperature of the following measurements (25 °C). The injected SUVs were incubated for around 15 min to allow for accumulation of the vesicles on the substrate surface. Then the flow cell was flushed with 10 mL of D_2O at a flow rate of 1 mL/min for rupturing the vesicles due to osmotic shock, resulting in membrane formation. The deposited membrane was washed with 10 mL buffer solution **A** at a flow rate of 1 mL/min.

The respective protein (TIAM2-PH, Grp1-PH or K2-PH) was thawed on ice and once thawed centrifuged at 15,000 g for 15 min. The supernatant was dialyzed into the deuterated salt buffer solution **A** using 3.5 kDa dialysis tubes. The dialyzed protein was diluted to 10 µM with deuterated salt buffer solution **A**. 6 mL of this protein solution was slowly injected into the flow cell using the syringe pump

at a flow rate of 0.15 mg/mL. Once the protein injection started, spectra were continuously collected every 80 s throughout 90 min. From each spectrum the initially collected background spectrum was subtracted. Baseline correction and plotting was performed using SpectroChemPy.[321]

4.4.4 Neutron Reflectometry Experiments

Sample Preparation

For the Grp1-PH supported lipid bilayer experiments the Langmuir-Blodgett-Langmuir-Schaefer deposition was used to deposit a POPC:POPS:POPIP2 (6:3:1, mol:mol:mol), as well as a POPC:POPS:SAPIP3 (6:3:1, mol:mol:mol) membrane.[164], [133] Piranha acid cleaned silicon crystals ($50 \times 80 \times 15$ mM^3) were cleaned by UV-ozone cleaning followed by washing with ultra-pure water, drying and a second UV-ozone cleaning procedure. For each membrane one of the cleaned silicon substrates were submerged into a clean solution subphase contained within a Langmuir-Trough with a custom dipping arm and auto-levelling device (Brown-Waite engineering, Coventry, UK). A lipid monolayer of the desired lipid composition of the membrane was deposited from a 1 mg/mL solution in chloroform:methanol (9:1, mol:mol) onto the air/liquid interface. Three compression and relaxation cycles of the interfacial monolayer (with a maximum pressure of 38 mN/m) were undertaken before the monolayer was compressed to 36 mN/m. The submerged silicon crystal was lifted through the monolayer at a speed of 2 mM/min whilst the monolayer surface pressure was held constant. Once this Langmuir-Blodgett deposition was completed, the trough was cleaned and the solution subphase was replaced. A second lipid monolayer of the same kind as the first was deposited and again pressure cycled between 0 and 38 mN/m before being held at 36 mN/m. The substrate was placed on the troughs dipping arm and the polished face of the silicon crystal was adjusted using a purpose built levelling device to make the crystal face parallel to the water surface. The lipid monolayer was then held at a surface pressure of 36 mN/m and the lipid monolayer coated silicon crystal was dipped through the air/liquid interface at a constant speed of 2 mM/min. Once this Langmuir-Schaefer was completed, the submerged, bilayer coated silicon crystal was lowered into a solid/liquid flow cell used for the NR experiments. The Grp1-PH supported lipid bilayer experiments were conducted in collaboration with Dr. Luke Clifton and Tao Ni.

For the TIAM2-PH supported lipid bilayer experiment the deposition of the POPC:POPS:POPIP2 (7:2:1, mol:mol:mol) membrane onto a cleaned silicon crystals was performed using small unilammelar vesicles (SUVs) and our heating/incubation procedure described previously for the free floating bilayer system (see Methods 2.4.2, FFM fabrication).

For the free floating bilayer experiments with Grp1-PH and K2-PH, the same substrates and methods as previously described were used for the generation of the floating membranes (see Methods 2.4.2). In case of the Grp1-PH experiment the only difference was that the substrate contained a chromium layer instead of the otherwise used permalloy layer.

NR Measurements

Specular neutron reflectometry (NR) measurements were carried out using different white beam reflectometers at the ISIS Spallation Neutron Source, Rutherford Appleton Laboratory (Oxfordshire, UK). Used reflectometer, neutron wavelengths and glancing angles at which the reflected intensity was measured are summarized in Table 4.3. Reflectivity was measured as a function of the momentum transfer Q_z, with $Q_z = (4\pi sin\theta) \,/\, \lambda$ where λ is wavelength and θ is the incident angle. Data were obtained at a nominal resolution $(dQ \,/\, Q)$ of 3.5%. The total illuminated sample length was $\sim$60 mm on an $\sim$80 mm substrate.

Experiment	Reflectometer	neutron wavelength [Å]	glancing angles [°]
Grp1-PH supported	SURF [261]	0.5-7.0	0.35, 0.65, 1.5
TIAM2-PH supported	INTER [322]	1.0-18.0	0.7, 2.3
K2-PH free floating	SURF [261]	0.5-7.0	0.35, 0.65, 1.5
Grp1-PH free floating	OFFSPEC [323]	1.0-14.0	0.7, 2.0

Table 4.3: Instrumental Details of NR Measurements.

Purpose built liquid flow cells for the analysis of the silicon-liquid interface were placed on a variable angle sample stage in the NR instrument and the inlet to the liquid cell was connected to a

liquid chromatography pump (L7100 HPLC pump, Merck, Hitachi) which allowed for easy change of the solution isotopic contrast within the solid-liquid sample cell (of 3 mL cell volume). For each solution isotopic contrast change, a total of 15 mL of buffer solution (for measuring buffer specifications see Table 4.4) was pumped through the cell (equivalent to 5 cell volumes) at a speed of 1.5 mL/min.

For the supported lipid bilayer systems, reflectivity data were obtained for the substrate in the presence of the bilayer at the bulk interface and then in the presence of the bilayer and the protein. Both data sets included three solution isotopic contrasts (H_2O, D_2O, SMW). For the free floating bilayer system, reflectivity data were obtained for (i) the substrate alone, (ii) the substrate in the presence of the bilayer at the bulk interface and then (iii) in the presence of the bilayer and the protein. The data sets of the substrate alone included two solution isotopic contrasts (H_2O, D_2O). The data sets with the bilayer present included two (H_2O, D_2O) and four (H_2O, D_2O, AuMW, PrMW) isotopic contrasts for the Grp1-PH and K2-PH experiment, respectively. Further experimental details are summarized in Table 4.4.

The respective protein (TIAM2-PH, Grp1-PH or K2-PH) was thawed on ice and once thawed centrifuged at 15,000 g for 15 min. For the protein solution in H_2O contrast, the supernatant was diluted to target protein concentration with H_2O measuring buffer (see Table 4.4). For the protein solution in D_2O contrast, the supernatant was dialyzed into the deuterated measuring buffer using 3.5 kDa dialysis tubes. The dialyzed protein was diluted to target protein concentration with deuterated measuring buffer. 10 mL of the protein solution at desired contrast was slowly injected into the flow cell using the syringe pump at a flow rate of 0.15 mg/mL.

Experiment	Deposition Buffer	Measuring Buffer	Temperature [°]	Protein Concentration [µM]
Grp1-PH supported	10 mM HEPES, 150 mM NaCl; pD 7.1	10 mM HEPES, 150 mM NaCl; pD 7.1	20	3.3 (0.05 mg/mL)
TIAM2-PH supported	20 mM HEPES, 150 mM NaCl, pD 7.1	20 mM HEPES, 150 mM NaCl, pD 7.1	25	5.7 (0.15 mg/mL)
K2-PH free floating	20 mM HEPES, 150 mM NaCl, 2 mM $CaCl_2$ pD 6.8	20 mM HEPES, 150 mM NaCl, 2 mM $CaCl_2$ pD 6.8	25	4.5 (0.05 mg/mL)
Grp1-PH free floating	20 mM HEPES, 150 mM NaCl, 2 mM $CaCl_2$; pD 6.8	20 mM HEPES, 150 mM NaCl; pD 6.8	25	3.3 (0.05 mg/mL)

Table 4.4: Experimental Details of NR Measurements.

NR Data Analysis

Neutron reflectometry data were analysed using the Python library refnx (v.0.1.16.).[159], [265] Refnx enables to define custom models of interfacial structures, from which parameters feed into the Abelès reflectivity model.[154], [266]

For the **slab model fits** of the supported lipid bilayer systems the model consisted of three slab objects, describing the two layers of the substrate (Si, SiO_2) and the protein layer on top of the membrane. Each slab was characterized by its SLD, thickness and roughness, with the Névot–Croce approach used to describe the roughness.[267] To estimate the water fraction in the SiO_2-surface, an additional flexible parameter was defined for the slab of the SiO_2-layer, modelling the intercalated volume fraction of solvent. The slab objects had a calculated SLD, which was fixed except for the slab of SiO_2. To define the membrane in the model, two LipidLeaflet objects were used. Each LipidLeaflet was made of two slices (head/tail region), one head layer at the interface with the SiO_2-layer, facing

towards the surface, the other at the interface with the bulk water. The head and tail components had a fixed SLD and volume parameter, summarized in Table 2.7 These parameters provided head and tail layers with a given thickness, whereby its roughness and intercalated volume fraction of solvent depended on the modelled area per molecule. To ensure that the number of head and tail components were equal, the area per molecule was set to be the same for the head and tail layers.

For the **mixed layer model fits** of the supported and the free floating bilayer systems, the model consisted of a slab for each layer in the system. Thus, the supported bilayer system was described by seven slab objects, describing the two layers of the substrate (Si, SiO_2), the two lipid head group layers, the two lipid tail layers and the protein layer. The model for the free floating bilayer system contained eleven slab objects, describing the four layers of the substrate (Si, SiO_2, permalloy, gold), the OEG-SAM, the water interlayer between OEG-SAM and membrane, the two lipid head group layers, the two lipid tail layers and the protein layer. Each slab was characterized by its SLD, thickness and roughness, with the Névot–Croce approach used to describe the roughness.[267] Additionally, the substrate layer adjacent to the bulk water (SiO_2 and OEG-SAM for the supported and free floating bilayer system, respectively) had an additional flexible parameter modelling the intercalated volume fraction of solvent. The SLD of the Si, gold and OEG-SAM slab object was fixed. The SLDs of the SiO_2, permalloy and the solvent were flexible parameters. The membrane and protein layers were described as mixed layers. Thus, their SLDs were defined by the fractions of the different molecules included in the layer.

The fraction of solvent in the membrane across all four membrane layers was modelled in form of a membrane coverage, a flexible parameter describing the volume fraction of lipids within the membrane layers. The layers of the outer membrane leaflet, facing towards the bulk solution, were defined as a mixture of lipids, water (both fractions described via the membrane coverage), as well as of protein. The fraction of the protein within the membrane (the internal membrane coverage of the protein) was a flexible parameter and linked to the external membrane coverage. The external membrane coverage was a flexible parameter describing the protein fraction within the mixed protein/water layer adjacent to the membrane. The internal membrane coverage was set to be equal or smaller than the external membrane coverage of the protein.

Further membrane parameters included the roughness of the lipid tail and head group layers, which were set to be equal. Additionally, the area per molecule was a flexible parameter, set to be the same for the head and tail layers to ensure that the number of head and tail components were equal (for some data sets the area per molecule was defined separately for each leaflet, for some to be identical across both leaflets - see Tables 4.2, 4.1). The area per molecule defined also the thickness of the lipid layers, which was described by the volume of the lipid part (head or tail) divided by the area per molecule. Furthermore, lipid head group bound water molecules were fitted for each membrane.

The fitting parameters across the different isotopic contrasts of each data set were set to be equal. Though there is some evidence that D_2O-based buffers can influence protein-protein interactions and phase behaviour [324], it was assumed that structures were effectively the same across the different contrasts. Only the SLD of the solvent, the scale factor and the background were allowed to vary for each isotopic contrast independently. Hereby, the SLD of each solvent isotopic contrast was set to be equal across all data sets of the respective sample system. The instrument resolution, as well as the parameters of the substrate (Si, SiO_2 or Si, SiO_2, permalloy, gold, OEG-SAM) were set to be equal across all solvent isotopic contrasts and all data sets of the respective sample system.

The best fit to the data was obtained by applying the differential evolution method, provided to refnx by the scipy library.[268] Then, the probability distribution function for each parameter was estimated via the MCMC sampling method available to refnx from the emcee library.[269] Hereby, 200 walkers were used over 8000 iterations of equilibration and 100,000 iterations of sampling. The sampled MCMC chain was thinned by 10,000 steps, equivalent to the iteration number at which the autocorrelation function of the parameters reached zero.

4.4.5 MD Simulations

CG Single Protein Simulations

CG simulations were run using GROMACS 2019.1.[275] The coarse-grained (CG) lipid bilayers were generated using the CHARMM-GUI membrane builder with the Martini 2.2 force field.[325], [326]

The lipid composition was 7:2:1 POPC:POPS:POPIP2, 7:2:1 POPC:POPS:POPIP3 (mol:mol:mol) and 8:2 POPC:POPS (mol:mol). The protein structures were transformed into a CG model using the martinize script.[326] The initial protein structures were rotated through a random angle, then centered above the membrane with a center of mass distance between membrane and protein of 9 nm and 11 nm for the K2-PH and TIAM2-PH, respectively. An elastic network was applied to the protein, with default settings and secondary structure was given as input using the DSSP algorithm.[327] The initial systems were solvated with martini water including 200 mM sodium cations. The cation concentration was calculated as [salt] = $N_c \times$ [water]/N_w, where N_c is the number of cations, [salt] the desired salt concentration, N_w the number of water molecules and [water] = 55.5 M.[228] Finally, the number of chloride ions necessary for neutralization was added. The initial box size of all systems was 9x9x30 nm^3. The systems were minimized with a steepest descend algorithm followed by 3 ns simulation in the isothermal-isobaric (NPT) ensemble with a time step of 3 fs and with v-rescale temperature coupling at 323 K.[276] Semi-isotropic Berendsen pressure coupling was used for the NPT ensemble coupling at 1 bar with a time constant of 4 ps and compressibility of 4.5 $\times$ 10^{-5} bar^{-1}.[203] Van der Waals and Coulomb cut-offs were both 1.1 nm. The simulations were constrained using the LINCS algorithm.[328] After equilibration, simulations were run for 1.5 µs with a time step of 3 fs. Here, a Parinello-Rahman pressure coupling with a time constant of 12 ps and a compressibility of 3 $\times$ 10^{-4} bar^{-1} was used.[277] All other settings were the same as for the equilibration. All CG simulations were repeated 25 times.

CG Multiple Protein Simulation

The solvent accessible surface area (SASA) of the K2-PH protein was determined using *gmx sasa*. A spherical shape of the protein was assumed. Thus, the protein surface was set to be equal to $4\pi r^2$ and the area the protein occupies on the membrane πr^2. The area all proteins cover on the membrane (the external membrane coverage) was set to be 10%. Therefore, for nine K2-PH proteins, each with a SASA of 80 nm^2, this approach led to a membrane area of 42.5 nm $\times$ 42.5 nm. A POPC:POPS:POPIP3 (7:2:1, mol:mol:mol) membrane was assembled using the CHARMM-GUI membrane builder with the Martini 2.2 force field.[325], [326] The final box size was 42.5 nm $\times$ 42.5 nm $\times$ 35 nm. The nine

proteins were placed 9 nm above the membrane, along a grid with x/y-positions at 7, 21 and 35 nm. The system was solvated with standard Martini water,[329] including 200 mM sodium cations. The cation concentration was calculated as [salt] = $N_c \times$ [water]/N_w, where N_c is the number of cations, [salt] the desired salt concentration, N_w the number of water molecules and [water] = 55.5 M.[228] Finally, the number of chloride ions necessary for neutralization was added. After a minimization with a steepest descend algorithm the system was equilibrated in the NPT ensemble for 200 ns and a time step of 2 fs. During the equilibration simulation, the protein backbones were position restrained by a force constant of 1000 kJ/mol in all directions. Finally, a 1.5 µs production run was generated with a time step of 2 fs and without position restraint on the proteins. All other settings during equilibration and production run were the same as for the CG single protein simulations (see previous section).

AA Simulations

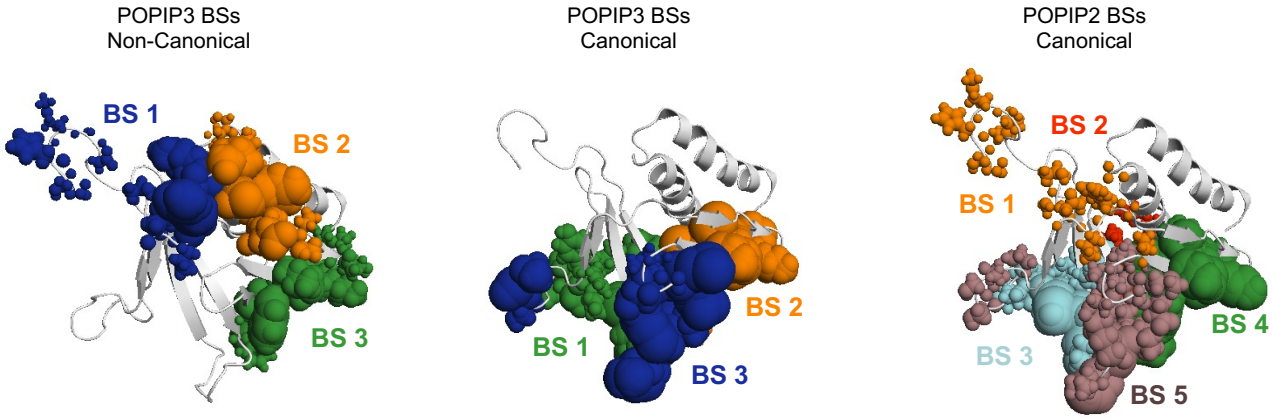
AA simulations were run using GROMACS 2019.1.[275] The coarse-grained (CG) binding poses were converted to all-atom (AA) resolution models using the Python tool *cg2at.py*.[211] Thereby for K2-PH three and two different AA structures were generated for CG structures containing POPIP3 and POPIP2 lipids, respectively. The POPIP3 and POPIP2 containing AA structures differed in the position of the protonated phosphate group in the inositol ring of the respective PIPs. So, depending on the AA starting structure all POIP3s contained a protonated phosphate group at position 3', 4' or 5' and all POPIP2s at position 4' or 5' in the inositol ring (see Figure 4.25 for PIP structures). For TIAM2-PH all POPIP3 and POPIP2 molecules contained the protonated phosphate group at position 4' of the inositol ring. After the transformation, the solvent and ions were excluded. Then, the structures were solvated with CHARMM36m TIP3P water,[205] including 200 mM sodium cations. The cation concentration was calculated as [salt] = $N_c \times$ [water]/N_w, where N_c is the number of cations, [salt] the desired salt concentration, N_w the number of water molecules and [water] = 55.5 M.[228] Finally, the number of chloride ions necessary for neutralization was added. The AA simulations were run with the CHARMM36m force field.[205] Cut-off distances for van der Waals and Coulomb forces were 1.2 nm. Long-range electrostatics were handled by the Particle Mesh Ewald algorithm.[280] The

system was first minimized with a steepest descend algorithm, then equilibrated in the NPT ensemble for 2.5 ns with a time step of 2 fs. A v-rescale thermostat was applied to keep the temperature at 323 K, with a time step of 0.1 ps.[276] A Berendsen semi-isotropic barostat was used to keep the pressure at 1 bar, with a time constant of 2 ps and compressibility of 4.5×10^{-5} bar^{-1}.[203] During the equilibration simulation all heavy atoms of the protein were position restrained by a force constant of 1000 kJ/mol in all directions. Finally, a 500 ns production run was generated with a time step of 2 fs and without position restraint on the protein. Here, a Parinello-Rahman pressure coupling was used.[277] All other setting were the same as for the equilibration.

Analysis of MD Simulations

The distance between the protein centre of mass and the membrane centre of mass (after centering of the protein in the box) was calculated with the GROMACS algorithm *gmx distance*. Lipid contacts were analysed using PyLipID.[310] The minimum distances were calculated with the *gmx mindist* tool. Root mean square deviations (RMSDs) were used to monitor the difference between the binding poses. The RMSD was calculated after alignment in the xy-plane (i.e. the approximate bilayer plane) and around the z-axis using an in-house script. RMSD was also used to monitor the structural change after converting the CG binding pose to AA structure and simulating it in the CHARMM-36m AA force field.[205] In that case, the frames were compared to the initial frame in the atomistic simulation and RMSDs were calculated for Cα atoms with GROMACS, using *gmx rms*. For the calculation of the density profiles the final 150 ns of each simulation were divided into 3×50 ns. For each time block the density profile was calculated with GROMACS, using *gmx density*. Then, the mean and the standard deviation of the three profiles were obtained. For the fits the curve_fit function of the scipy library was used.[268] The protein layer thickness was estimated as the FWHM (full width at half maximum) of the fitted Gaussian distributions. Structures were visualized using VMD.[278] Plots were generated in Python3, using Numpy [330] and Matplotlib [331].

4.5 Appendix



BS	Occupancy [%]	Residence Time [µs]	k_{off} [μs^{-1}] Curve Fit	Δk_{off}
POPIP3, Non-Cano, BS 1	97	0.14	7.0	-0.7
POPIP3, Non-Cano, BS 2	92	0.75	1.3	-1.0
POPIP3, Non-Cano, BS 3	89	0.18	5.4	0.7
POPIP3, Cano, BS 1	86	0.66	1.5	0.1
POPIP3, Cano, BS 2	87	0.47	2.1	0.3
POPIP3, Cano, BS 3	85	0.48	2.1	0.1
POPIP2, Cano, BS 1	12	0.06	17.7	-0.1
POPIP2, Cano, BS 2	57	0.17	5.8	0.3
POPIP2, Cano, BS 3	85	0.35	2.9	0.3
POPIP2, Cano, BS 4	97	0.35	2.9	0.7
POPIP2, Cano, BS 5	98	0.26	3.9	1.0

Figure 4.28 | Structure and Parameters of POPIP3 and POPIP2 BSs of K2-PH. Shown are the POPIP BSs of K2-PH predicted by PyLipID.[310] The amino acids involved in the respective BSs are shown as spheres, whereby the spheres scale corresponding to the residence time of each amino acid. The table presents all key parameters of each BS. Here, Δk_{off} corresponds to the difference between the k_{off} from the BS curve fit and the bootstrapped k_{off}.

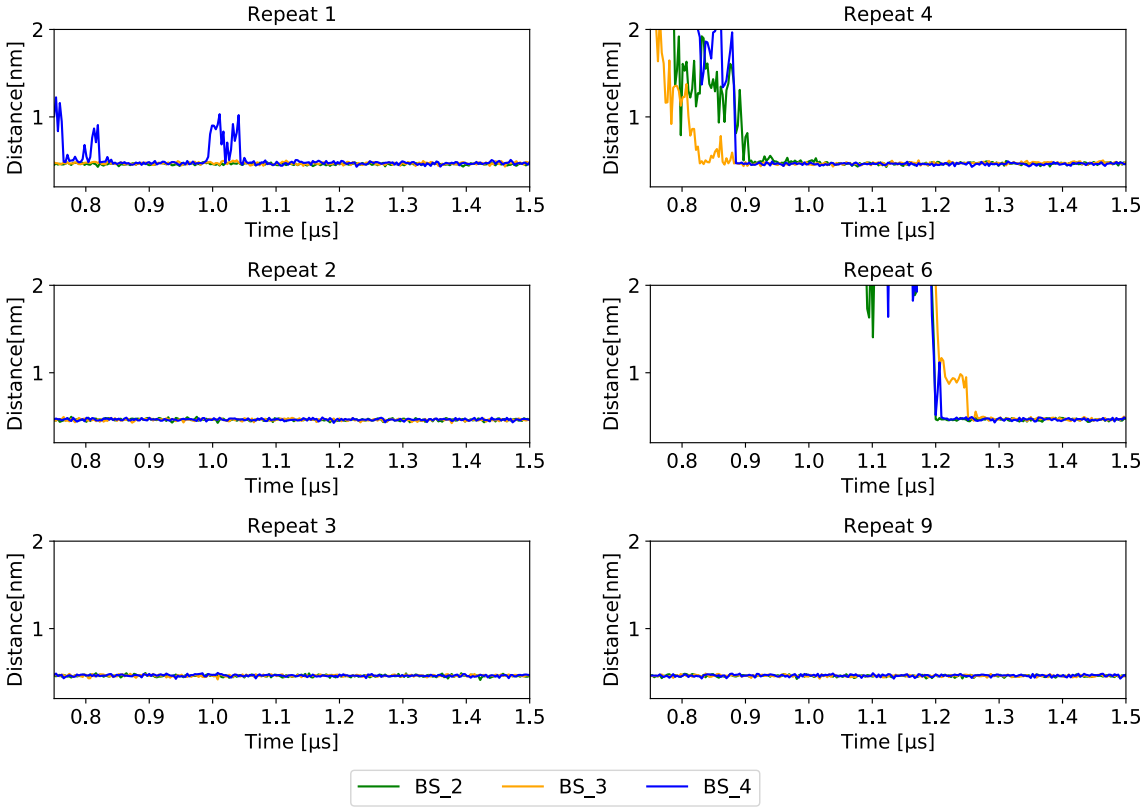


Figure 4.29 | Minimal Distance between POPIP3 and POPIP3 BSs of Canonical Bound K2-PH. Shown is the minimal distance between any POPIP3 lipid and the by PyLipID identified POPIP3 BSs of K2-PH over the second half of the CG simulations, which showed canonical binding of K2-PH to the POPC:POPS:POPIP3 (7:2:1, mol:mol:mol) membrane. The CG simulations, named as repeat 2, 3 and 9 showed well equilibrated POPIP3 around the identified POPIP3 BSs, called BS 2, 3 and 4. Therefore the final pose of repeat 9 was converted into an all atomistic (AA) representation for further studies.

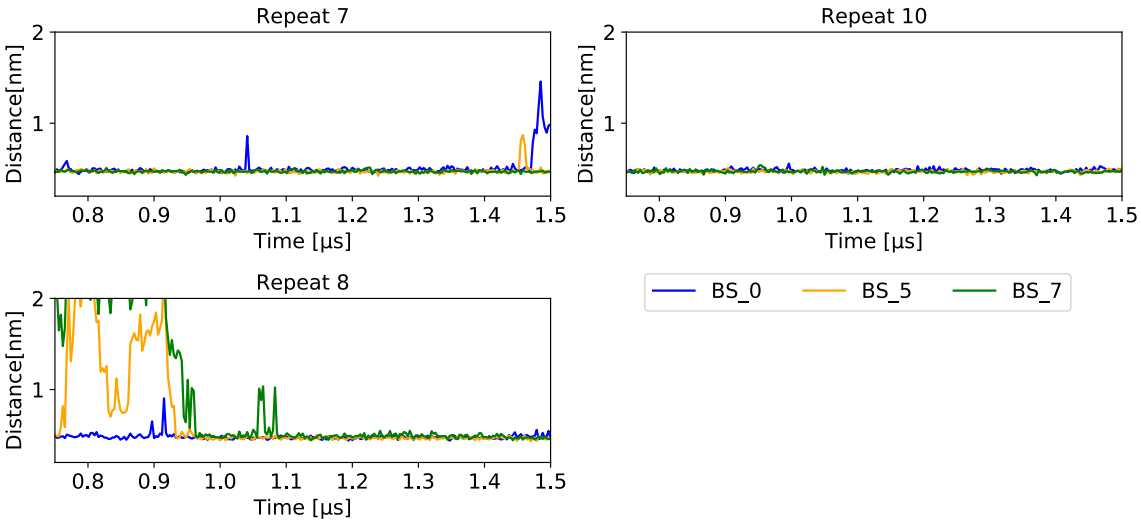


Figure 4.30 | Minimal Distance between POPIP3 and POPIP3 BSs of Non-Canonical Bound K2-PH. Shown is the minimal distance between any POPIP3 lipid and the by PyLipID identified POPIP3 BSs of K2-PH over the second half of the CG simulations, which showed non-canonical binding of K2-PH to the POPC:POPS:POPIP3 (7:2:1, mol:mol:mol) membrane. The CG simulations, named as repeat 8 and 10 showed well equilibrated POPIP3 around the identified POPIP3 BSs, called BS 0, 5 and 7. Therefore the final pose of repeat 10 was converted into an all atomistic (AA) representation for further studies.

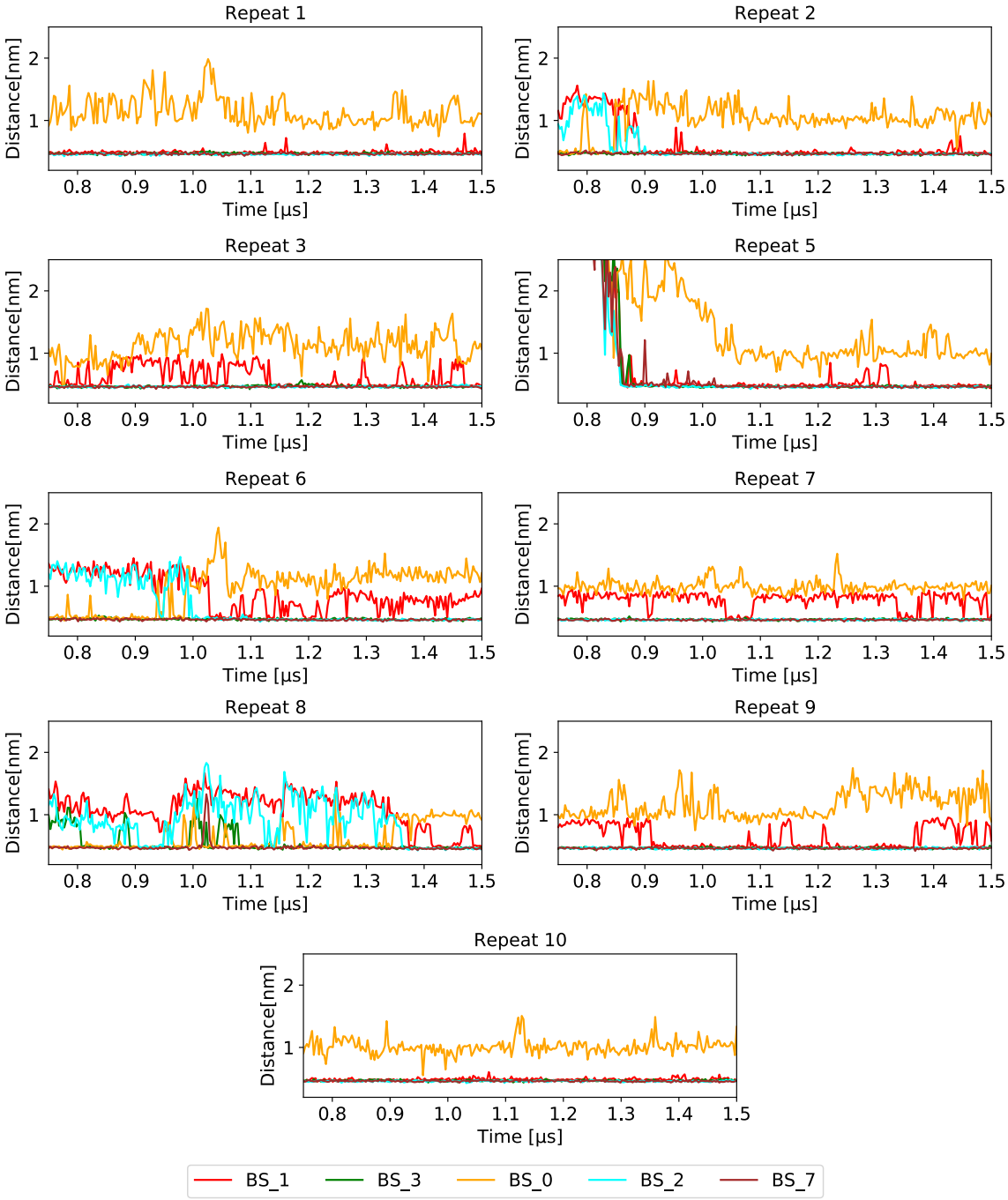
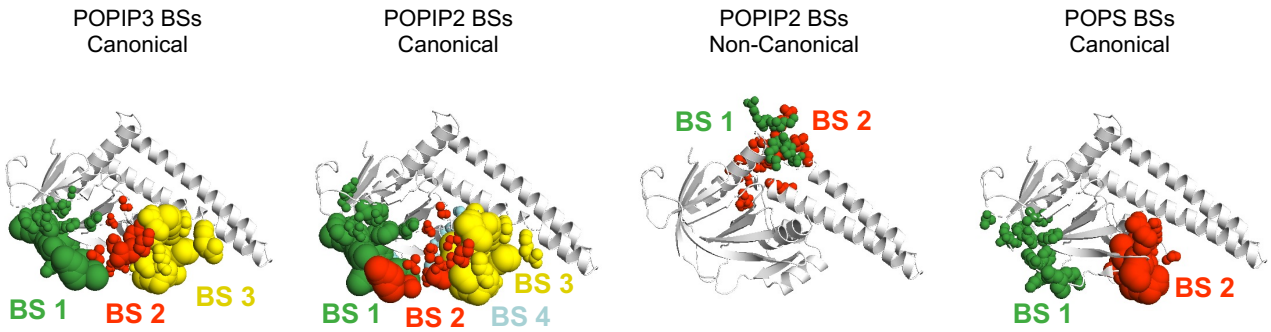


Figure 4.31 | Minimal Distance between POPIP2 and POPIP2 BSs of Canonical Bound K2-PH. Shown is the minimal distance between any POPIP2 lipid and the by PyLipID identified POPIP2 BSs of K2-PH over the second half of the CG simulations, which showed canonical binding of K2-PH to the POPC:POPS:POPIP2 (7:2:1, mol:mol:mol) membrane. The CG simulation, named as repeat 9 showed well equilibrated POPIP2 around the identified POPIP2 BSs, called BS 0, 1, 2, 3 and 7. Therefore the final pose of repeat 9 was converted into an all atomistic (AA) representation for further studies.



BS	Occupancy [%]	Residence Time [µs]	k_{off} [μs^{-1}] Curve Fit	Δk_{off}
POPIP3, Cano, BS 1	100	0.57	1.7	0.4
POPIP3, Cano, BS 2	80	0.16	6.4	0.1
POPIP3, Cano, BS 3	100	0.43	2.4	-0.4
POPIP2, Cano, BS 1	84	0.58	1.7	-0.8
POPIP2, Cano, BS 2	78	0.58	1.7	-0.6
POPIP2, Cano, BS 3	85	0.43	2.3	0.4
POPIP2, Cano, BS 4	81	0.21	4.8	-0.4
POPIP2, Non-Cano, BS 1	90	0.12	8.5	0.2
POPIP2, Non-Cano, BS 2	92	0.20	5.0	0.4
POPS, Cano, BS 1	60	0.02	42.7	-0.9
POPS, Cano, BS 2	53	0.13	7.8	0.7

Figure 4.32 | Structure and Parameters of POPIP3, POPIP2 and POPS BSs of TIAM2-PH. Shown are the POPIP and POPS BSs of TIAM2-PH predicted by PyLipID.[310] The amino acids involved in the respective BSs are shown as spheres, whereby the spheres scale corresponding to the residence time of each amino acid. The table presents all key parameters of each BS. Here, Δk_{off} corresponds to the difference between the k_{off} from the BS curve fit and the bootstrapped k_{off}.

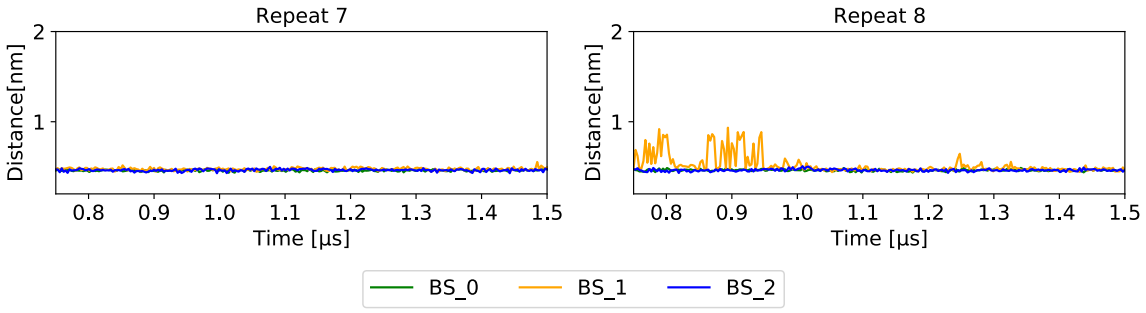


Figure 4.33 | Minimal Distance between POPIP3 and POPIP3 BSs of Canonical Bound TIAM2-PH. Shown is the minimal distance between any POPIP3 lipid and the by PyLipID identified POPIP3 BSs of TIAM2-PH over the second half of the CG simulations, which showed canonical binding of TIAM2-PH to the POPC:POPS:POPIP3 (7:2:1, mol:mol:mol) membrane. The CG simulations, named as repeat 7 and 8 showed well equilibrated POPIP3 around the identified POPIP3 BSs, called BS 0, 1 and 2. Therefore the final pose of repeat 7 was converted into an all atomistic (AA) representation for further studies.

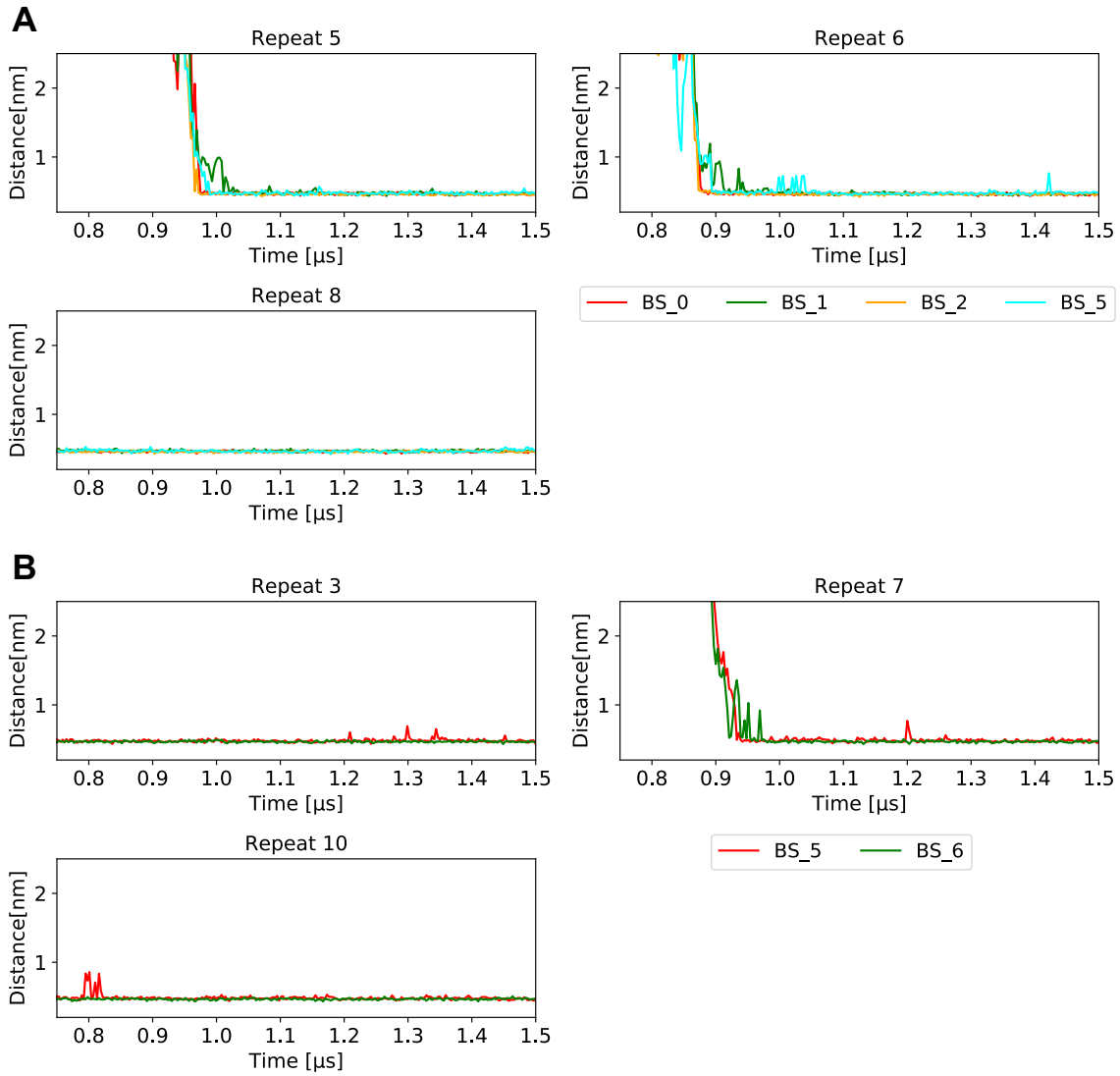


Figure 4.34 | Minimal Distance between POPIP2 and POPIP2 BSs of Canonical and Non-Canonical Bound TIAM2-PH. Shown is the minimal distance between any POPIP2 lipid and the by PyLipID identified POPIP2 BSs of TIAM2-PH over the second half of the CG simulations, which showed canonical (**A**) and non-canonical (**B**) binding of TIAM2-PH to the POPC:POPS:POPIP2 (7:2:1, mol:mol:mol) membrane. All CG simulations showed well equilibrated POPIP2 around the identified POPIP2 BSs, called BS 0, 1, 2, 5 for canonical and BS 5, 6 for non-canonical binding. Therefore the final pose of repeat 8 and repeat 3 was converted into an all atomistic (AA) representation for further studies of the canonical and non-canonical binding conformation, respectively.

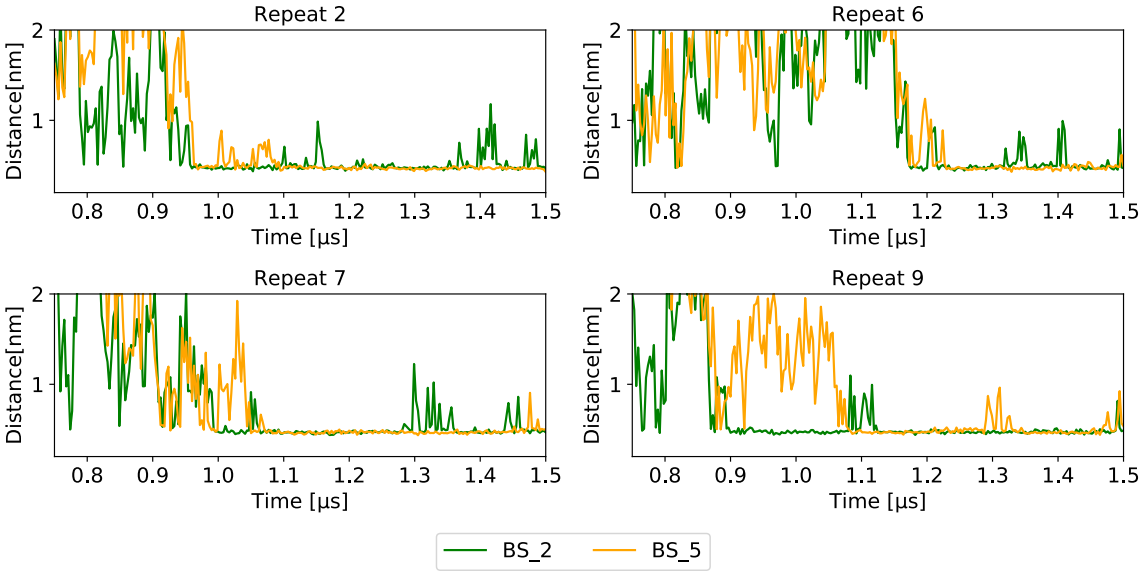


Figure 4.35 | Minimal Distance between POPS and POPS BSs of Canonical Bound TIAM2-PH. Shown is the minimal distance between any POPS lipid and the by PyLipID identified POPS BSs of TIAM2-PH over the second half of the CG simulations, which showed canonical binding of TIAM2-PH to the POPC:POPS (8:2, mol:mol) membrane. All CG repeats show similar equilibration of POPS around the POPS BSs. The final pose of repeat 2 was converted into an all atomistic (AA) representation for further studies.

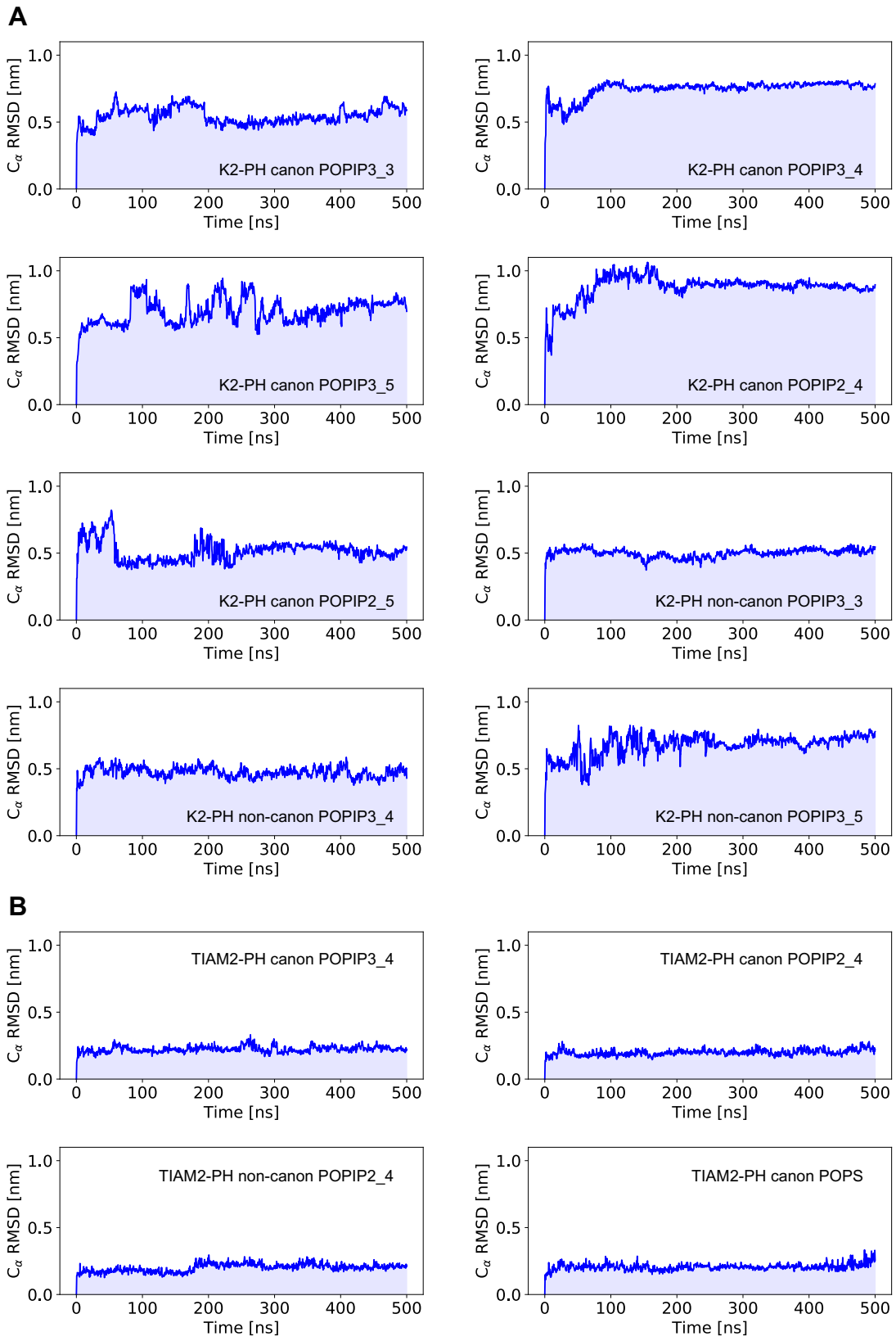


Figure 4.36 | Cα RMSDs for AA Simulations of K2-PH and TIAM2-PH. Shown are the Cα RMSDs over the time of the AA simulations of K2-PH (**A**) and TIAM2-PH (**B**). The legends show which POPIP was present in the POPC:POPS:POPIP (7:2:1, mol:mol:mol) membrane; the last number defines the position of the protonated phosphate group in the inositol ring. "Canon" and "non-canon" stand for canonical and non-canonical binding conformation, respectively.

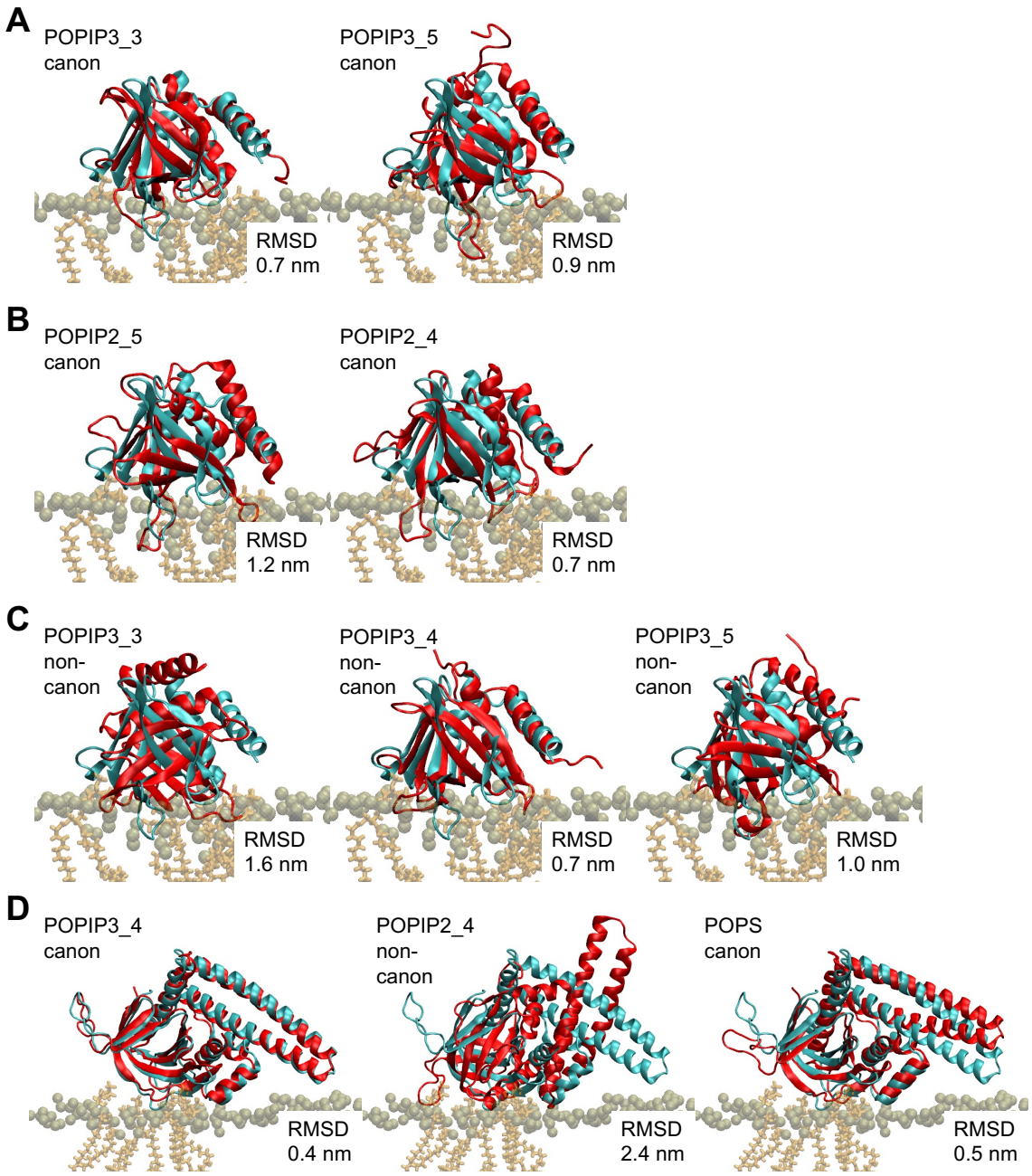


Figure 4.37 | Final Conformations of AA Simulations. Shown are the final frames of the 500 ns AA simulations of K2-PH (**A**-**C**) and TIAM2-PH (**D**). **A**-**C** For K2-PH the final canonical binding conformation of K2-PH bound to the POPC:POPS:POPIP3_4 (7:2:1, mol:mol:mol) membrane is shown in cyan in all plots. On top of that structure the final conformation of K2-PH bound to the membrane named by the legend is shown in red. **D** For TIAM2-PH the final canonical binding conformation of TIAM2-PH bound to the POPC:POPS:POPIP2_4 (7:2:1, mol:mol:mol) membrane is shown in cyan in all plots. On top of that structure the final conformation of TIAM2-PH bound to the membrane named by the legend is shown in red. The legends indicate which POPIP was present in the respective POPC:POPS:POPIP (7:2:1, mol:mol:mol) membrane. Hereby, the suffixed number corresponds the position of the protonated phosphate group in the inositol ring. The RMSD shown in each plot corresponds to the RMSD between the two structures shown in the respective plot. "Canon" and "non-canon" stand for canonical and non-canonical binding conformation, respectively, and refer to the initial name of the structure given by the final pose of the CG simulations.

5

Conclusion and Outlook

In this work we combined neutron reflectometry (NR) experiments with molecular dynamics (MD) simulations to investigate and apply a versatile planar model membrane system. The sample system of interest was an advanced planar model membrane system, the so called free floating model membrane (FFM) system. In comparison to previous planar model membrane systems, in the FFM system the membrane is separated from the adjacent substrate surface, which consists of a carboxylate terminated oligo (ethylene glycol) self assembling monolayer (OEG-SAM), by a water inter-layer, without any linkage to the substrate surface. The omitted contact of the membrane with the substrate surface leads to a better mimicking of natural membrane dynamics. Therefore, the goal of our studies was to use this advanced sample system to investigate interactions between peripheral membrane proteins and their target membranes. However, the acting forces between different sample components within the FFM system had not been fully understood. The understanding of these forces is essential in order to interpret experimental data correctly. Therefore, in *Chapter 2* and *Chapter 3* the effects of different buffer conditions on the membrane behaviour within the FFM system were examined using NR and MD. Furthermore, the effect of the adjacent substrate on membrane dynamics in dependency of the distance between the membrane and the surface was quantitatively investigated.

In *Chapter 2* NR experiments revealed that removing 2 mM Ca^{2+} ions, which were present in the buffer solution during the self assembling process of the FFM, leads to a substantial increase of more than 200 Å in the distance between the OEG-SAM surface and the FFM. Thus, in the absence of Ca^{2+} ions the FFM-to-SAM distance was around 200-600 Å, while in the presence of 2 mM Ca^{2+} ions around 12-15 Å. Interestingly, 200 mM Na^{+} ions in the buffer solution led to an intermediate

FFM-to-SAM distance of around 40-120 Å. To obtain a molecular understanding of the membrane behaviour observed in the NR experiments, multi-scale MD simulations were performed. Here, water and cation density profiles above the OEG-SAM and different phospholipid membranes used in the experiments, alongside cation binding energies to the OEG-SAM and the membranes were calculated. Our results suggested that both cations Ca^{2+} and Na^{+} preferably bind to the anionic OEG-SAM, thereby changing the surface charge and decreasing the repulsion force between anionic membrane and OEG-SAM. Hereby, Na^{+} showed a more diffuse binding compared to Ca^{2+}. Furthermore, Ca^{2+} indicated also some binding to the phospholipid FFMs while Na^{+} showed only in the presence of highly negatively charged FFM lipids diffuse membrane binding. Based on these findings, we suggested a bridging effect between OEG-SAM and FFM caused by the enhanced cation density in the water inter-layer, which is more pronounced for Ca^{2+} than for Na^{+} leading to the smaller FFM-to-SAM distance in the presence of Ca^{2+} compared to Na^{+}. A simulated multi-layer system including both layers, OEG-SAM and membrane, separated by a water layer, gave further validation of our predicted molecular model of the forces acting within the FFM system in absence and presence of cations. Finally, the experimental NR results were successfully reproduced by replicating the FFM system on a small gold sensor surface, which was then used for quartz crystal microbalance (QCM) measurements. Our QCM results demonstrate the potential of this advanced model membrane system to be readily utilized in biophysical membrane studies using benchtop analytical techniques like QCM.

In *Chapter 3* the effect of different OEG-SAM and membrane surface charges on the membrane behaviour was further investigated by applying different pH buffer conditions. Three pH conditions (pH 3, 7 and 10), each at a concentration of 2 mM $CaCl_2$ and 150 mM NaCl were probed. At pH 3, 7 and 10 the chemical groups of both membrane and OEG-SAM were fully, partly or not protonated, respectively. At pH 3 when membrane and OEG-SAM were neutral in charge, we observed very short distances between OEG-SAM and FFM of around 9-12 Å. Therefore, the absence of the repulsion force between OEG-SAM and FFM alone can cause short FFM-to-SAM distances, without an additional attractive bridging effect produced by cations being needed, as suggested in *Chapter 2*. MD simulations supported this finalized model by showing almost no binding of both cations Ca^{2+} and Na^{+}

to the phospholipid membranes at all three pH conditions, while showing strong affinity towards the OEG-SAM at middle and high pH of 7 and 10, respectively. Furthermore, our MD simulations provided interesting insights into the effects of pH changes on the OEG-SAM structure: With increasing pH the tilt angle of the OEG-SAM molecules decreased and water penetrated deeper into the OEG-SAM. These structural rearrangements led to less structured water on top of the OEG-SAM. The structured water on top of the OEG-SAM is a unique property of these SAMs used in many different applications, making our findings important to different areas in surface chemistry. Additionally, by simulating the multi-layer system with different distances between OEG-SAM and FFM, the actual effect of the adjacent OEG-SAM on membrane dynamics in terms of lipid diffusion and lipid conformation was examined. Based on our results, we suggested to increase the FFM-to-SAM distance above $\sim$ 25 Å in order to avoid surface effects like reduced lipid diffusion in the surface facing membrane leaflet.

In *Chapter 4* we applied the FFM sample system to investigate the membrane interaction of two peripheral membrane proteins, namely kindlin-2 (K2) and T-lymphoma invasion and metastasis 2 (TIAM2). K2 and TIAM2 are involved in integrin and Rac1 GTPase activation, respectively and contain both a pleckstrin homology (PH) domain, known to bind to membranes including phosphatidylinositol phospholipids (PIPs). While for TIAM2 the thickness of the membrane bound protein layer provided by NR experiments matched the thickness gained from MD simulations, for K2 the protein layer thickness was 2-3 times bigger in the NR experiments compared to the MD results. However, in each of these MD simulations there was jut one protein present in the system. In MD simulations containing multiple K2 proteins, trimerization of K2 was observed, with the trimers matching the protein thickness range obtained by the NR results and therefore suggesting K2 clustering upon membrane binding. Furthermore, our MD simulations confirmed the previously postulated relevance of the protonation state of the phosphate group at the position 4' in the inositol ring of PIPs for the conformation of membrane bound K2. Thus, our results suggested that PIP lipids protonated at the 4' position stabilize the canonical membrane binding conformation of K2. Also, the type of PIP lipids present in the membrane seemed to influence the binding conformation, with K2 showing increased canonical membrane binding

in the presence of PIP2 compared to PIP3. In case of TIAM2, the presence of the Ex-domain within the investigated TIAM2-protein complex led to higher selectivity towards PIP2 compared to PIP3.

Together, the combination of both NR and MD in this work provided a detailed understanding of the reversible, large scale membrane movements within the FFM system in dependency of both pH and cation concentration, as well as insights in the structural orientation and position of peripheral membrane proteins upon membrane binding. NR and MD have been used complementary before with the study of the tumor suppressor and signaling protein PTEN being one of the most detailed peripheral membrane protein studies which compared SLD profiles derived from experimental NR data with computed SLD profiles from time averaged MD trajectories.[308], [332] However, while so far only the final results derived from NR and MD had been compared, a closer linkage between the two techniques along the analysis process would be very powerful in terms of structural protein/membrane interaction studies. For instance, MD simulations can be used to predict how deep the protein penetrates the membrane and therefore, which layers of the membrane are best to be handled as mixed layers in the NR fitting model containing protein and lipids. Additionally, recently steered MD has been used to bias potentials in MD simulations towards experimental NR results.[333] This method was again applied to PTEN showing that equilibrium properties are reached faster and that resulting conformations are more frequently in close agreement with experimental NR SLD profiles than those from unbiased MD simulations. The combination of our novel FFM system in the NR experiments with steered MD analysis would provide an effective tool to study protein/membrane interactions. An extension to integral membrane proteins, as well as native membrane usage within the FFM system will expand the applications of the FFM system even further.

Bibliography

[1] H. I. Ingólfsson, M. N. Melo, F. J. Van Eerden, *et al.*, "Lipid organization of the plasma membrane", *Journal of the american chemical society*, vol. 136, no. 41, pp. 14 554–14 559, 2014.

[2] G. Van Meer, D. R. Voelker, and G. W. Feigenson, "Membrane lipids: Where they are and how they behave", *Nature reviews Molecular cell biology*, vol. 9, no. 2, pp. 112–124, 2008.

[3] J. E. Vance, "Phospholipid synthesis and transport in mammalian cells", *Traffic*, vol. 16, no. 1, pp. 1–18, 2015.

[4] S. Cockcroft, "Mammalian lipids: Structure, synthesis and function", *Essays in Biochemistry*, vol. 65, no. 5, pp. 813–845, 2021.

[5] A. Luchini and G. Vitiello, "Mimicking the mammalian plasma membrane: An overview of lipid membrane models for biophysical studies", *Biomimetics*, vol. 6, no. 1, p. 3, 2020.

[6] A. M. Cassim, P. Gouguet, J. Gronnier, *et al.*, "Plant lipids: Key players of plasma membrane organization and function", *Progress in Lipid Research*, vol. 73, pp. 1–27, 2019.

[7] T. Harayama and H. Riezman, "Understanding the diversity of membrane lipid composition", *Nature reviews Molecular cell biology*, vol. 19, no. 5, pp. 281–296, 2018.

[8] B. Fadeel and D. Xue, "The ins and outs of phospholipid asymmetry in the plasma membrane: Roles in health and disease", *Critical reviews in biochemistry and molecular biology*, vol. 44, no. 5, pp. 264–277, 2009.

[9] D. L. Daleke, "Regulation of phospholipid asymmetry in the erythrocyte membrane", *Current opinion in hematology*, vol. 15, no. 3, pp. 191–195, 2008.

[10] P. F. Devaux, "Static and dynamic lipid asymmetry in cell membranes", *Biochemistry*, vol. 30, no. 5, pp. 1163–1173, 1991.

[11] D. Lingwood and K. Simons, "Lipid rafts as a membrane-organizing principle", *science*, vol. 327, no. 5961, pp. 46–50, 2010.

[12] I. Levental, K. R. Levental, and F. A. Heberle, "Lipid rafts: Controversies resolved, mysteries remain", *Trends in cell biology*, vol. 30, no. 5, pp. 341–353, 2020.

[13] J. L. Robertson, "The lipid bilayer membrane and its protein constituents", *Journal of General Physiology*, vol. 150, no. 11, pp. 1472–1483, 2018.

[14] Z. Cournia, T. W. Allen, I. Andricioaei, *et al.*, "Membrane protein structure, function, and dynamics: A perspective from experiments and theory", *The Journal of membrane biology*, vol. 248, pp. 611–640, 2015.

[15] V. Monje-Galvan and J. B. Klauda, "Peripheral membrane proteins: Tying the knot between experiment and computation", *Biochimica et Biophysica Acta (BBA)-Biomembranes*, vol. 1858, no. 7, pp. 1584–1593, 2016.

[16] J. P. Overington, B. Al-Lazikani, and A. L. Hopkins, "How many drug targets are there?", *Nature reviews Drug discovery*, vol. 5, no. 12, pp. 993–996, 2006.

[17] K. Gupta, J. A. Donlan, J. T. Hopper, *et al.*, "The role of interfacial lipids in stabilizing membrane protein oligomers", *Nature*, vol. 541, no. 7637, pp. 421–424, 2017.

[18] J. L. Parker, R. A. Corey, P. J. Stansfeld, and S. Newstead, "Structural basis for substrate specificity and regulation of nucleotide sugar transporters in the lipid bilayer", *Nature communications*, vol. 10, no. 1, p. 4657, 2019.

[19] A. Rosenhouse-Dantsker, D. Mehta, and I. Levitan, "Regulation of ion channels by membrane lipids", *Compr Physiol*, vol. 2, no. 1, pp. 31–68, 2012.

[20] J. Fantini and F. J. Barrantes, "How cholesterol interacts with membrane proteins: an exploration of cholesterol-binding sites including CRAC, CARC, and tilted domains", *Frontiers in physiology*, vol. 4, p. 31, 2013.

[21] I. Levitan, D. K. Singh, and A. Rosenhouse-Dantsker, "Cholesterol binding to ion channels", *Frontiers in physiology*, vol. 5, p. 65, 2014.

[22] D. K. Singh, A. Rosenhouse-Dantsker, C. G. Nichols, D. Enkvetchakul, and I. Levitan, "Direct regulation of prokaryotic Kir channel by cholesterol", *Journal of Biological Chemistry*, vol. 284, no. 44, pp. 30 727–30 736, 2009.

[23] V. G. Romanenko, Y. Fang, F. Byfield, *et al.*, "Cholesterol sensitivity and lipid raft targeting of Kir2.1 channels", *Biophysical journal*, vol. 87, no. 6, pp. 3850–3861, 2004.

[24] N. Barbera, M. A. Ayee, B. S. Akpa, and I. Levitan, "Molecular dynamics simulations of Kir2.2 interactions with an ensemble of cholesterol molecules", *Biophysical journal*, vol. 115, no. 7, pp. 1264–1280, 2018.

[25] T. Balla, "Inositol-lipid binding motifs: Signal integrators through protein-lipid and protein-protein interactions", *Journal of cell science*, vol. 118, no. 10, pp. 2093–2104, 2005.

[26] C. A. Caffalette, R. A. Corey, M. S. Sansom, P. J. Stansfeld, and J. Zimmer, "A lipid gating mechanism for the channel-forming O antigen ABC transporter", *Nature communications*, vol. 10, no. 1, p. 824, 2019.

[27] S. R. Bushell, A. C. Pike, M. E. Falzone, *et al.*, "The structural basis of lipid scrambling and inactivation in the endoplasmic reticulum scramblase TMEM16K", *Nature communications*, vol. 10, no. 1, p. 3956, 2019.

[28] K. Renard and B. Byrne, "Insights into the role of membrane lipids in the structure, function and regulation of integral membrane proteins", *International Journal of Molecular Sciences*, vol. 22, no. 16, p. 9026, 2021.

[29] A. L. Duncan, W. Song, and M. S. Sansom, "Lipid-dependent regulation of ion channels and g protein–coupled receptors: Insights from structures and simulations", *Annual Review of Pharmacology and Toxicology*, vol. 60, pp. 31–50, 2020.

[30] V. Corradi, B. I. Sejdiu, H. Mesa-Galloso, *et al.*, "Emerging diversity in lipid–protein interactions", *Chemical reviews*, vol. 119, no. 9, pp. 5775–5848, 2019.

[31] P.-C. Wen, P. Mahinthichaichan, N. Trebesch, *et al.*, "Microscopic view of lipids and their diverse biological functions", *Current opinion in structural biology*, vol. 51, pp. 177–186, 2018.

[32] R. J. Clarke, K. R. Hossain, and K. Cao, "Physiological roles of transverse lipid asymmetry of animal membranes", *Biochimica et Biophysica Acta (BBA)-Biomembranes*, vol. 1862, no. 10, p. 183 382, 2020.

[33] T. Balla, "Phosphoinositides: Tiny lipids with giant impact on cell regulation", *Physiological reviews*, vol. 93, no. 3, pp. 1019–1137, 2013.

[34] G. R. Hammond and T. Balla, "Polyphosphoinositide binding domains: Key to inositol lipid biology", *Biochimica Et Biophysica Acta (BBA)-Molecular and Cell Biology of Lipids*, vol. 1851, no. 6, pp. 746–758, 2015.

[35] R. L. Schnaar, "Glycosphingolipids in cell surface recognition", *Glycobiology*, vol. 1, no. 5, pp. 477–485, 1991.

[36] M. Zuverink and J. T. Barbieri, "Protein toxins that utilize gangliosides as host receptors", *Progress in molecular biology and translational science*, vol. 156, pp. 325–354, 2018.

[37] K. I. Le Huray, H. Wang, F. Sobott, and A. C. Kalli, "Systematic simulation of the interactions of pleckstrin homology domains with membranes", *Science Advances*, vol. 8, no. 27, eabn6992, 2022.

[38] A. L. Duncan, R. A. Corey, and M. S. Sansom, "Defining how multiple lipid species interact with inward rectifier potassium (Kir2) channels", *Proceedings of the National Academy of Sciences*, vol. 117, no. 14, pp. 7803–7813, 2020.

[39] A. C. Kalli, G. Morgan, and M. S. Sansom, "Interactions of the auxilin-1 PTEN-like domain with model membranes result in nanoclustering of phosphatidyl inositol phosphates", *Biophysical journal*, vol. 105, no. 1, pp. 137–145, 2013.

[40] D. L. Parton, A. Tek, M. Baaden, and M. S. Sansom, "Formation of raft-like assemblies within clusters of influenza hemagglutinin observed by MD simulations", *PLoS Computational Biology*, vol. 9, no. 4, e1003034, 2013.

[41] W. Pezeshkian, H. Gao, S. Arumugam, *et al.*, "Mechanism of Shiga toxin clustering on membranes", *ACS nano*, vol. 11, no. 1, pp. 314–324, 2017.

[42] G. Di Paolo and P. De Camilli, "Phosphoinositides in cell regulation and membrane dynamics", *Nature*, vol. 443, no. 7112, pp. 651–657, 2006.

[43] T. G. Kutateladze, "Translation of the phosphoinositide code by PI effectors", *Nature chemical biology*, vol. 6, no. 7, pp. 507–513, 2010.

[44] K. Moravcevic, C. L. Oxley, and M. A. Lemmon, "Conditional peripheral membrane proteins: Facing up to limited specificity", *Structure*, vol. 20, no. 1, pp. 15–27, 2012.

[45] A. H. Larsen, L. H. John, M. S. Sansom, and R. A. Corey, "Specific interactions of peripheral membrane proteins with lipids: What can molecular simulations show us?", *Bioscience Reports*, vol. 42, no. 4, BSR20211406, 2022.

[46] A. H. Larsen and M. S. Sansom, "Binding of Ca2+-independent C2 domains to lipid membranes: A multi-scale molecular dynamics study", *Structure*, vol. 29, no. 10, pp. 1200–1213, 2021.

[47] J. P. DiNitto, T. C. Cronin, and D. G. Lambright, "Membrane recognition and targeting by lipid-binding domains", *Science's STKE*, vol. 2003, no. 213, re16–re16, 2003.

[48] N. Singh, A. Reyes-Ordoñez, M. A. Compagnone, *et al.*, "Redefining the specificity of phosphoinositide-binding by human PH domain-containing proteins", *Nature communications*, vol. 12, no. 1, pp. 1–13, 2021.

[49] M. Saraste and M. Hyvönen, "Pleckstrin homology domains: A fact file", *Current opinion in structural biology*, vol. 5, no. 3, pp. 403–408, 1995.

[50] M. Rebecchi and S. Scarlata, "Pleckstrin homology domains: A common fold with diverse functions", *Annual review of biophysics and biomolecular structure*, vol. 27, no. 1, pp. 503–528, 1998.

[51] K. Scheffzek and S. Welti, "Pleckstrin homology (PH) like domains–versatile modules in protein–protein interaction platforms", *FEBS letters*, vol. 586, no. 17, pp. 2662–2673, 2012.

[52] S. E. Lietzke, S. Bose, T. Cronin, *et al.*, "Structural basis of 3-phosphoinositide recognition by pleckstrin homology domains", *Molecular cell*, vol. 6, no. 2, pp. 385–394, 2000.

[53] N. Blomberg, E. Baraldi, M. Nilges, and M. Saraste, "The PH superfold: A structural scaffold for multiple functions", *Trends in biochemical sciences*, vol. 24, no. 11, pp. 441–445, 1999.

[54] W. Y. Jong, J. M. Mendrola, A. Audhya, *et al.*, "Genome-wide analysis of membrane targeting by S. cerevisiae pleckstrin homology domains", *Molecular cell*, vol. 13, no. 5, pp. 677–688, 2004.

[55] K. M. Ferguson, J. M. Kavran, V. G. Sankaran, *et al.*, "Structural basis for discrimination of 3-phosphoinositides by pleckstrin homology domains", *Molecular cell*, vol. 6, no. 2, pp. 373–384, 2000.

[56] S. J. Isakoff, T. Cardozo, J. Andreev, *et al.*, "Identification and analysis of PH domain-containing targets of phosphatidylinositol 3-kinase using a novel in vivo assay in yeast", *The EMBO journal*, vol. 17, no. 18, pp. 5374–5387, 1998.

[57] D. F. Ceccarelli, I. M. Blasutig, M. Goudreault, *et al.*, "Non-canonical interaction of phosphoinositides with pleckstrin homology domains of tiam1 and ArhGAP9", *Journal of Biological Chemistry*, vol. 282, no. 18, pp. 13 864–13 874, 2007.

[58] X. Jian, W.-K. Tang, P. Zhai, *et al.*, "Molecular basis for cooperative binding of anionic phospholipids to the PH domain of the Arf GAP ASAP1", *Structure*, vol. 23, no. 11, pp. 1977–1988, 2015.

[59] E. Yamamoto, J. Domański, F. B. Naughton, *et al.*, "Multiple lipid binding sites determine the affinity of PH domains for phosphoinositide-containing membranes", *Science advances*, vol. 6, no. 8, eaay5736, 2020.

[60] J. He, R. M. Haney, M. Vora, V. V. Verkhusha, R. V. Stahelin, and T. G. Kutateladze, "Molecular mechanism of membrane targeting by the GRP1 PH domain", *Journal of lipid research*, vol. 49, no. 8, pp. 1807–1815, 2008.

[61] K. Narayan and M. A. Lemmon, "Determining selectivity of phosphoinositide-binding domains", *Methods*, vol. 39, no. 2, pp. 122–133, 2006.

[62] D. Manna, A. Albanese, W. S. Park, and W. Cho, "Mechanistic basis of differential cellular responses of phosphatidylinositol 3, 4-bisphosphate-and phosphatidylinositol 3, 4, 5-trisphosphate-binding pleckstrin homology domains", *Journal of Biological Chemistry*, vol. 282, no. 44, pp. 32 093–32 105, 2007.

[63] F. B. Naughton, A. C. Kalli, and M. S. Sansom, "Association of peripheral membrane proteins with membranes: Free energy of binding of GRP1 PH domain with phosphatidylinositol phosphate-containing model bilayers", *The journal of physical chemistry letters*, vol. 7, no. 7, pp. 1219–1224, 2016.

[64] M. Clodi, P. Vollenweider, J. Klarlund, *et al.*, "Effects of general receptor for phosphoinositides 1 on insulin and insulin-like growth factor I-induced cytoskeletal rearrangement, glucose transporter-4 translocation, and deoxyribonucleic acid synthesis", *Endocrinology*, vol. 139, no. 12, pp. 4984–4990, 1998.

[65] B. D. Hopkins, M. D. Goncalves, and L. C. Cantley, "Insulin–PI3K signalling: An evolutionarily insulated metabolic driver of cancer", *Nature Reviews Endocrinology*, vol. 16, no. 5, pp. 276–283, 2020.

[66] C. N. Lumb, J. He, Y. Xue, *et al.*, "Biophysical and computational studies of membrane penetration by the grp1 pleckstrin homology domain", *Structure*, vol. 19, no. 9, pp. 1338–1346, 2011.

[67] C. N. Lumb and M. S. Sansom, "Finding a needle in a haystack: The role of electrostatics in target lipid recognition by PH domains", *PLoS computational biology*, vol. 8, no. 7, e1002617, 2012.

[68] E. Yamamoto, A. C. Kalli, K. Yasuoka, and M. S. Sansom, "Interactions of pleckstrin homology domains with membranes: Adding back the bilayer via high-throughput molecular dynamics", *Structure*, vol. 24, no. 8, pp. 1421–1431, 2016.

[69] C.-L. Lai, A. Srivastava, C. Pilling, A. R. Chase, J. J. Falke, and G. A. Voth, "Molecular mechanism of membrane binding of the GRP1 PH domain", *Journal of molecular biology*, vol. 425, no. 17, pp. 3073–3090, 2013.

[70] S. Pant and E. Tajkhorshid, "Microscopic characterization of GRP1 PH domain interaction with anionic membranes", *Journal of computational chemistry*, vol. 41, no. 6, pp. 489–499, 2020.

[71] H.-C. Chen, B. P. Ziemba, K. E. Landgraf, J. A. Corbin, and J. J. Falke, "Membrane docking geometry of GRP1 PH domain bound to a target lipid bilayer: An EPR site-directed spin-labeling and relaxation study", *PLoS One*, vol. 7, no. 3, e33640, 2012.

[72] S.-i. Terawaki, K. Kitano, T. Mori, *et al.*, "The PHCCEx domain of Tiam1/2 is a novel protein-and membrane-binding module", *The EMBO journal*, vol. 29, no. 1, pp. 236–250, 2010.

[73] M. Hoshino, M. Sone, M. Fukata, *et al.*, "Identification of the stef gene that encodes a novel guanine nucleotide exchange factor specific for rac1", *Journal of Biological Chemistry*, vol. 274, no. 25, pp. 17 837–17 844, 1999.

[74] L. C. Haeusler, L. Blumenstein, P. Stege, R. Dvorsky, and M. R. Ahmadian, "Comparative functional analysis of the rac GTPases", *FEBS letters*, vol. 555, no. 3, pp. 556–560, 2003.

[75] D. Frances, N. Sharma, R. Pofahl, *et al.*, "A role for rac1 activity in malignant progression of sebaceous skin tumors", *Oncogene*, vol. 34, no. 43, pp. 5505–5512, 2015.

[76] P. De, J. C. Aske, and N. Dey, "RAC1 takes the lead in solid tumors", *Cells*, vol. 8, no. 5, p. 382, 2019.

[77] A. Payapilly and A. Malliri, "Compartmentalisation of RAC1 signalling", *Current opinion in cell biology*, vol. 54, pp. 50–56, 2018.

[78] P. Penzes and M. E. Cahill, "Deconstructing signal transduction pathways that regulate the actin cytoskeleton in dendritic spines", *Cytoskeleton*, vol. 69, no. 7, pp. 426–441, 2012.

[79] S. Takemoto-Kimura, N. Ageta-Ishihara, M. Nonaka, *et al.*, "Regulation of dendritogenesis via a lipid-raft-associated ca2+/calmodulin-dependent protein kinase CLICK-iii/camkiγ", *Neuron*, vol. 54, no. 5, pp. 755–770, 2007.

[80] K. L. Rossman, C. J. Der, and J. Sondek, "GEF means go: Turning on RHO GTPases with guanine nucleotide-exchange factors", *Nature reviews Molecular cell biology*, vol. 6, no. 2, pp. 167–180, 2005.

[81] D. K. Worthylake, K. L. Rossman, and J. Sondek, "Crystal structure of rac1 in complex with the guanine nucleotide exchange region of tiam1", *Nature*, vol. 408, no. 6813, pp. 682–688, 2000.

[82] N. Matsuo, M. Hoshino, M. Yoshizawa, and Y.-i. Nabeshima, "Characterization of STEF, a guanine nucleotide exchange factor for Rac1, required for neurite growth", *Journal of Biological Chemistry*, vol. 277, no. 4, pp. 2860–2868, 2002.

[83] T. Nishimura, T. Yamaguchi, K. Kato, *et al.*, "PAR-6–PAR-3 mediates Cdc42-induced Rac activation through the rac GEFs STEF/Tiam1", *Nature cell biology*, vol. 7, no. 3, pp. 270–277, 2005.

[84] J. Maltas, H. Reed, A. Porter, and A. Malliri, "Mechanisms and consequences of dysregulation of the Tiam family of Rac activators in disease", *Biochemical Society Transactions*, vol. 48, no. 6, pp. 2703–2719, 2020.

[85] W. Bu, Z. Levitskaya, Z. Y. Loh, *et al.*, "Structural basis of human full-length kindlin-3 homotrimer in an auto-inhibited state", *PLoS Biology*, vol. 18, no. 7, e3000755, 2020.

[86] J. Liu, K. Fukuda, Z. Xu, *et al.*, "Structural basis of phosphoinositide binding to kindlin-2 protein pleckstrin homology domain in regulating integrin activation", *Journal of Biological Chemistry*, vol. 286, no. 50, pp. 43 334–43 342, 2011.

[87] R. D. Palmere, D. A. Case, and A. J. Nieuwkoop, "Simulations of kindlin-2 PIP binding domains reveal protonation-dependent membrane binding modes", *Biophysical Journal*, 2021.

[88] D. S. Harburger, M. Bouaouina, and D. A. Calderwood, "Kindlin-1 and-2 directly bind the c-terminal region of β integrin cytoplasmic tails and exert integrin-specific activation effects", *Journal of biological chemistry*, vol. 284, no. 17, pp. 11 485–11 497, 2009.

[89] X. Shi, Y.-Q. Ma, Y. Tu, *et al.*, "The mig-2/integrin interaction strengthens cell-matrix adhesion and modulates cell motility", *Journal of Biological Chemistry*, vol. 282, no. 28, pp. 20 455–20 466, 2007.

[90] Z. Haydari, H. Shams, Z. Jahed, and M. R. Mofrad, "Kindlin assists talin to promote integrin activation", *Biophysical journal*, vol. 118, no. 8, pp. 1977–1991, 2020.

[91] I. Delon and N. H. Brown, "Integrins and the actin cytoskeleton", *Current opinion in cell biology*, vol. 19, no. 1, pp. 43–50, 2007.

[92] F. Ye, B. G. Petrich, P. Anekal, *et al.*, "The mechanism of kindlin-mediated activation of integrin αiibβ3", *Current Biology*, vol. 23, no. 22, pp. 2288–2295, 2013.

[93] H. Li, Y. Deng, K. Sun, *et al.*, "Structural basis of kindlin-mediated integrin recognition and activation", *Proceedings of the National Academy of Sciences*, vol. 114, no. 35, pp. 9349–9354, 2017.

[94] Y.-H. M. Chan and S. G. Boxer, "Model membrane systems and their applications", *Current opinion in chemical biology*, vol. 11, no. 6, pp. 581–587, 2007.

[95] L. A. Clifton, R. A. Campbell, F. Sebastiani, *et al.*, "Design and use of model membranes to study biomolecular interactions using complementary surface-sensitive techniques", *Advances in colloid and interface science*, vol. 277, p. 102 118, 2020.

[96] N.-J. Cho, C. W. Frank, B. Kasemo, and F. Höök, "Quartz crystal microbalance with dissipation monitoring of supported lipid bilayers on various substrates", *Nature protocols*, vol. 5, no. 6, pp. 1096–1106, 2010.

[97] T. K. Lind and M. Cárdenas, "Understanding the formation of supported lipid bilayers via vesicle fusion—A case that exemplifies the need for the complementary method approach", *Biointerphases*, vol. 11, no. 2, p. 020 801, 2016.

[98] A. Åkesson, T. Lind, N. Ehrlich, D. Stamou, H. Wacklin, and M. Cárdenas, "Composition and structure of mixed phospholipid supported bilayers formed by POPC and DPPC", *Soft Matter*, vol. 8, no. 20, pp. 5658–5665, 2012.

[99] A. Luchini, A. N. Nzulumike, T. K. Lind, *et al.*, "Towards biomimics of cell membranes: Structural effect of phosphatidylinositol triphosphate (PIP3) on a lipid bilayer", *Colloids and Surfaces B: Biointerfaces*, vol. 173, pp. 202–209, 2019.

[100] T. K. Lind, H. Wacklin, J. Schiller, *et al.*, "Formation and characterization of supported lipid bilayers composed of hydrogenated and deuterated escherichia coli lipids", *PloS one*, vol. 10, no. 12, e0144671, 2015.

[101] P. Plunkett, B. A. Camley, K. L. Weirich, J. Israelachvili, and P. J. Atzberger, "Simulation of edge facilitated adsorption and critical concentration induced rupture of vesicles at a surface", *Soft Matter*, vol. 9, no. 35, pp. 8420–8427, 2013.

[102] T. K. Lind, M. W. Skoda, and M. Cárdenas, "Formation and characterization of supported lipid bilayers composed of phosphatidylethanolamine and phosphatidylglycerol by vesicle fusion, a simple but relevant model for bacterial membranes", *ACS omega*, vol. 4, no. 6, pp. 10 687–10 694, 2019.

[103] J. Kurniawan, J. F. Ventrici de Souza, A. T. Dang, G.-y. Liu, and T. L. Kuhl, "Preparation and characterization of solid-supported lipid bilayers formed by Langmuir–Blodgett deposition: A tutorial", *Langmuir*, vol. 34, no. 51, pp. 15 622–15 639, 2018.

[104] L. A. Clifton, M. W. Skoda, E. L. Daulton, *et al.*, "Asymmetric phospholipid: Lipopolysaccharide bilayers; a Gram-negative bacterial outer membrane mimic", *Journal of the royal society interface*, vol. 10, no. 89, p. 20 130 810, 2013.

[105] O. B. Florek, L. A. Clifton, M. Wilde, T. Arnold, R. J. Green, and R. A. Frazier, "Lipid composition in fungal membrane models: Effect of lipid fluidity", *Acta Crystallographica Section D: Structural Biology*, vol. 74, no. 12, pp. 1233–1244, 2018.

[106] M. Przybylo, J. Sỳkora, J. Humpolickova, A. Benda, A. Zan, and M. Hof, "Lipid diffusion in giant unilamellar vesicles is more than 2 times faster than in supported phospholipid bilayers under identical conditions", *Langmuir*, vol. 22, no. 22, pp. 9096–9099, 2006.

[107] A. Alessandrini and P. Facci, "Phase transitions in supported lipid bilayers studied by AFM", *Soft matter*, vol. 10, no. 37, pp. 7145–7164, 2014.

[108] M. Tanaka and E. Sackmann, "Polymer-supported membranes as models of the cell surface", *Nature*, vol. 437, no. 7059, pp. 656–663, 2005.

[109] I. P. McCabe and M. B. Forstner, "Polymer supported lipid bilayers", 2013.

[110] M. Tanaka, F. F. Rossetti, and S. Kaufmann, "Native supported membranes: Creation of two-dimensional cell membranes on polymer supports", *Biointerphases*, vol. 3, no. 2, FA12–FA16, 2008.

[111] J. Andersson and I. Köper, "Tethered and polymer supported bilayer lipid membranes: Structure and function", *Membranes*, vol. 6, no. 2, p. 30, 2016.

[112] E. Sackmann and M. Tanaka, "Supported membranes on soft polymer cushions: Fabrication, characterization and applications", *Trends in biotechnology*, vol. 18, no. 2, pp. 58–64, 2000.

[113] T. Wang, D. Li, X. Lu, *et al.*, "Single lipid bilayers constructed on polymer cushion studied by sum frequency generation vibrational spectroscopy", *The Journal of Physical Chemistry C*, vol. 115, no. 15, pp. 7613–7620, 2011.

[114] N. Kohli, S. Vaidya, R. Y. Ofoli, R. M. Worden, and I. Lee, "Arrays of lipid bilayers and liposomes on patterned polyelectrolyte templates", *Journal of colloid and interface science*, vol. 301, no. 2, pp. 461–469, 2006.

[115] M. Kühner, R. Tampe, and E. Sackmann, "Lipid mono-and bilayer supported on polymer films: Composite polymer-lipid films on solid substrates", *Biophysical Journal*, vol. 67, no. 1, pp. 217–226, 1994.

[116] X. Lu, A. L. Ottova, and H. T. Tien, "Biophysical aspects of agar-gel supported bilayer lipid nembranes: A new method for forming and studying planar bilayer lipid membranes", *Bioelectrochemistry and Bioenergetics*, vol. 39, no. 2, pp. 285–289, 1996.

[117] A. J. Diaz, F. Albertorio, S. Daniel, and P. S. Cremer, "Double cushions preserve transmembrane protein mobility in supported bilayer systems", *Langmuir*, vol. 24, no. 13, pp. 6820–6826, 2008.

[118] E. B. Watkins, R. J. El-khouri, C. E. Miller, *et al.*, "Structure and thermodynamics of lipid bilayers on polyethylene glycol cushions: Fact and fiction of PEG cushioned membranes", *Langmuir*, vol. 27, no. 22, pp. 13 618–13 628, 2011.

[119] R. Naumann, S. M. Schiller, F. Giess, *et al.*, "Tethered lipid bilayers on ultraflat gold surfaces", *Langmuir*, vol. 19, no. 13, pp. 5435–5443, 2003.

[120] G. Valincius, D. J. McGillivray, W. Febo-Ayala, D. J. Vanderah, J. J. Kasianowicz, and M. Lösche, "Enzyme activity to augment the characterization of tethered bilayer membranes", *The Journal of Physical Chemistry B*, vol. 110, no. 21, pp. 10 213–10 216, 2006.

[121] V. Jagalski, R. D. Barker, M. B. Thygesen, *et al.*, "Grafted biomembranes containing membrane proteins–the case of the leucine transporter", *Soft Matter*, vol. 11, no. 39, pp. 7707–7711, 2015.

[122] R. Budvytyte, M. Mickevicius, D. J. Vanderah, F. Heinrich, and G. Valincius, "Modification of tethered bilayers by phospholipid exchange with vesicles", *Langmuir*, vol. 29, no. 13, pp. 4320–4327, 2013.

[123] M. Maccarini, E. B. Watkins, B. Stidder, J.-P. Alcaraz, B. A. Cornell, and D. K. Martin, "Nanostructural determination of a lipid bilayer tethered to a gold substrate", *The European Physical Journal E*, vol. 39, pp. 1–8, 2016.

[124] F. Heinrich, T. Ng, D. J. Vanderah, *et al.*, "A new lipid anchor for sparsely tethered bilayer lipid membranes", *Langmuir*, vol. 25, no. 7, pp. 4219–4229, 2009.

[125] B. Raguse, V. Braach-Maksvytis, B. A. Cornell, *et al.*, "Tethered lipid bilayer membranes: Formation and ionic reservoir characterization", *Langmuir*, vol. 14, no. 3, pp. 648–659, 1998.

[126] S. Park, S. Y. Avsar, B. Cornell, *et al.*, "Probing the influence of tether density on tethered bilayer lipid membrane (tBLM)-peptide interactions", *Applied Materials Today*, vol. 18, p. 100 527, 2020.

[127] D. J. McGillivray, G. Valincius, D. J. Vanderah, *et al.*, "Molecular-scale structural and functional characterization of sparsely tethered bilayer lipid membranes", *Biointerphases*, vol. 2, no. 1, pp. 21–33, 2007.

[128] B. A. Cornell, V. Braach-Maksvytis, L. King, *et al.*, "A biosensor that uses ion-channel switches", *Nature*, vol. 387, no. 6633, pp. 580–583, 1997.

[129] T. Baumgart, M. Kreiter, H. Lauer, *et al.*, "Fusion of small unilamellar vesicles onto laterally mixed self-assembled monolayers of thiolipopeptides", *Journal of colloid and interface science*, vol. 258, no. 2, pp. 298–309, 2003.

[130] S. Shenoy, R. Moldovan, J. Fitzpatrick, D. J. Vanderah, M. Deserno, and M. Lösche, "In-plane homogeneity and lipid dynamics in tethered bilayer lipid membranes (tBLMs)", *Soft matter*, vol. 6, no. 6, pp. 1263–1274, 2010.

[131] A. V. Hughes, S. A. Holt, E. Daulton, *et al.*, "High coverage fluid-phase floating lipid bilayers supported by ω-thiolipid self-assembled monolayers", *Journal of The Royal Society Interface*, vol. 11, no. 98, p. 20 140 447, 2014.

[132] G. Fragneto, T. Charitat, and J. Daillant, "Floating lipid bilayers: Models for physics and biology", *European Biophysics Journal*, vol. 41, no. 10, pp. 863–874, 2012.

[133] L. A. Clifton, N. Paracini, A. V. Hughes, *et al.*, "Self-assembled fluid phase floating membranes with tunable water interlayers", *Langmuir*, vol. 35, no. 42, pp. 13 735–13 744, 2019.

[134] H. I. Petrache, T. Zemb, L. Belloni, and V. A. Parsegian, "Salt screening and specific ion adsorption determine neutral-lipid membrane interactions", *Proceedings of the National Academy of Sciences*, vol. 103, no. 21, pp. 7982–7987, 2006.

[135] W. Helfrich, "Elastic properties of lipid bilayers: Theory and possible experiments", *Zeitschrift für Naturforschung c*, vol. 28, no. 11-12, pp. 693–703, 1973.

[136] K. R. Mecke, T. Charitat, and F. Graner, "Fluctuating lipid bilayer in an arbitrary potential: Theory and experimental determination of bending rigidity", *Langmuir*, vol. 19, no. 6, pp. 2080–2087, 2003.

[137] A. V. Hughes, J. R. Howse, A. Dabkowska, R. A. Jones, M. J. Lawrence, and S. J. Roser, "Floating lipid bilayers deposited on chemically grafted phosphatidylcholine surfaces", *Langmuir*, vol. 24, no. 5, pp. 1989–1999, 2008.

[138] G. Pabst, A. Hodzic, J. Štrancar, S. Danner, M. Rappolt, and P. Laggner, "Rigidification of neutral lipid bilayers in the presence of salts", *Biophysical journal*, vol. 93, no. 8, pp. 2688–2696, 2007.

[139] E.-K. Sinner and W. Knoll, "Functional tethered membranes", *Current opinion in chemical biology*, vol. 5, no. 6, pp. 705–711, 2001.

[140] D. A. Costello, C.-Y. Hsia, J. K. Millet, T. Porri, and S. Daniel, "Membrane fusion-competent virus-like proteoliposomes and proteinaceous supported bilayers made directly from cell plasma membranes", *Langmuir*, vol. 29, no. 21, pp. 6409–6419, 2013.

[141] D. A. Costello, J. K. Millet, C.-Y. Hsia, G. R. Whittaker, and S. Daniel, "Single particle assay of coronavirus membrane fusion with proteinaceous receptor-embedded supported bilayers", *Biomaterials*, vol. 34, no. 32, pp. 7895–7904, 2013.

[142] M. J. Richards, C.-Y. Hsia, R. R. Singh, *et al.*, "Membrane protein mobility and orientation preserved in supported bilayers created directly from cell plasma membrane blebs", *Langmuir*, vol. 32, no. 12, pp. 2963–2974, 2016.

[143] L. A. Clifton, S. C. Hall, N. Mahmoudi, T. J. Knowles, F. Heinrich, and J. H. Lakey, "Structural investigations of protein–lipid complexes using neutron scattering", *Lipid-Protein Interactions*, pp. 201–251, 2019.

[144] *ISIS Neutron and Muon Source*. [Online]. Available: https://www.isis.stfc.ac.uk/Pages/home.aspx, accessed: 08.04.2023.

[145] D. Findlay, J. Thomason, S. Fletcher, R. de Laune, and E. Cooper, "A practical guide to the ISIS neutron and muon source", 2021, Last accessed 23 March 2023. [Online]. Available: https://www.isis.stfc.ac.uk/Pages/News21_PracticalGuide.aspx.

[146] T. Charlton, R. Coleman, R. M. Dalgliesh, *et al.*, "Advances in neutron reflectometry at ISIS", *Neutron News*, vol. 22, no. 2, pp. 15–18, 2011.

[147] D. S. Sivia, *Elementary scattering theory: for X-ray and neutron users*. Oxford University Press, 2011.

[148] L. De Broglie, "Recherches sur la théorie des quanta", Ph.D. dissertation, Migration-université en cours d'affectation, 1924.

[149] J. R. Copley and T. J. Udovic, "Neutron time-of-flight spectroscopy", *Journal of research of the National Institute of Standards and Technology*, vol. 98, no. 1, p. 71, 1993.

[150] J. H. Lakey, "Neutrons for biologists: A beginner's guide, or why you should consider using neutrons", *Journal of the Royal Society Interface*, vol. 6, no. suppl_5, S567–S573, 2009.

[151] C. Neylon, "Small angle neutron and X-ray scattering in structural biology: Recent examples from the literature", *European Biophysics Journal*, vol. 37, pp. 531–541, 2008.

[152] A. P. Le Brun, L. A. Clifton, S. A. Holt, P. J. Holden, and J. H. Lakey, "Deuterium labeling strategies for creating contrast in structure–function studies of model bacterial outer membranes using neutron reflectometry", in *Methods in Enzymology*, vol. 566, Elsevier, 2016, pp. 231–252.

[153] O. Dunne, M. Weidenhaupt, P. Callow, *et al.*, "Matchout deuterium labelling of proteins for small-angle neutron scattering studies using prokaryotic and eukaryotic expression systems and high cell-density cultures", *European Biophysics Journal*, vol. 46, pp. 425–432, 2017.

[154] L. G. Parratt, "Surface studies of solids by total reflection of X-rays", *Physical review*, vol. 95, no. 2, p. 359, 1954.

[155] F. Abelès, "La théorie générale des couches minces", *Journal de Physique et le Radium*, vol. 11, no. 7, pp. 307–309, 1950.

[156] M. Born and E. Wolf, *Principles of optics: electromagnetic theory of propagation, interference and diffraction of light*. Elsevier, 2013.

[157] A. R. Mazzer, L. A. Clifton, T. Perevozchikova, P. D. Butler, C. J. Roberts, and D. G. Bracewell, "Neutron reflectivity measurement of protein A–antibody complex at the solid-liquid interface", *Journal of Chromatography A*, vol. 1499, pp. 118–131, 2017.

[158] J. Als-Nielsen and D. McMorrow, *Elements of modern X-ray physics*. John Wiley & Sons, 2011.

[159] A. R. Nelson and S. W. Prescott, "Refnx: Neutron and X-ray reflectometry analysis in Python", *Journal of applied crystallography*, vol. 52, no. 1, pp. 193–200, 2019.

[160] A. Nelson, "Co-refinement of multiple-contrast neutron/X-ray reflectivity data using motofit", *Journal of applied crystallography*, vol. 39, no. 2, pp. 273–276, 2006.

[161] *Rascal*. [Online]. Available: `https://sourceforge.net/projects/rscl`, accessed: 29.03.2023.

[162] Y. Gerelli, "Aurore: New software for neutron reflectivity data analysis", *Journal of Applied Crystallography*, vol. 49, no. 1, pp. 330–339, 2016.

[163] F. Heinrich and M. Lösche, "Zooming in on disordered systems: Neutron reflection studies of proteins associated with fluid membranes", *Biochimica et Biophysica Acta (BBA)-Biomembranes*, vol. 1838, no. 9, pp. 2341–2349, 2014.

[164] L. A. Clifton, S. A. Holt, A. V. Hughes, *et al.*, "An accurate in vitro model of the e. coli envelope", *Angewandte Chemie International Edition*, vol. 54, no. 41, pp. 11 952–11 955, 2015.

[165] H. P. Vacklin, F. Tiberg, G. Fragneto, and R. Thomas, "Phospholipase A2 hydrolysis of supported phospholipid bilayers: A neutron reflectivity and ellipsometry study", *Biochemistry*, vol. 44, no. 8, pp. 2811–2821, 2005.

[166] L. A. Clifton, M. W. Skoda, A. P. Le Brun, *et al.*, "Effect of divalent cation removal on the structure of gram-negative bacterial outer membrane models", *Langmuir*, vol. 31, no. 1, pp. 404–412, 2015.

[167] Y. Gerelli, L. Porcar, and G. Fragneto, "Lipid rearrangement in DSPC/DMPC bilayers: A neutron reflectometry study", *Langmuir*, vol. 28, no. 45, pp. 15 922–15 928, 2012.

[168] D. P. Hoogerheide, S. Y. Noskov, D. Jacobs, *et al.*, "Structural features and lipid binding domain of tubulin on biomimetic mitochondrial membranes", *Proceedings of the National Academy of Sciences*, vol. 114, no. 18, E3622–E3631, 2017.

[169] A. U. Mushtaq, J. Ådén, L. A. Clifton, *et al.*, "Neutron reflectometry and NMR spectroscopy of full-length Bcl-2 protein reveal its membrane localization and conformation", *Communications Biology*, vol. 4, no. 1, p. 507, 2021.

[170] L. A. Clifton, H. P. Wacklin-Knecht, J. Aden, A. U. Mushtaq, T. Sparrman, and G. Grobner, "Bax forms a membrane surface protein-lipid complex as it initiates apoptosis", *bioRxiv*, pp. 2022–11, 2022.

[171] N. Paracini, L. A. Clifton, and J. H. Lakey, "Studying the surfaces of bacteria using neutron scattering: Finding new openings for antibiotics", *Biochemical Society Transactions*, vol. 48, no. 5, pp. 2139–2149, 2020.

[172] S. Katzir, *The beginnings of piezoelectricity: a study in mundane physics*. Springer, 2006, vol. 246.

[173] M. Rodahl, F. Höök, A. Krozer, P. Brzezinski, and B. Kasemo, "Quartz crystal microbalance setup for frequency and Q-factor measurements in gaseous and liquid environments", *Review of Scientific Instruments*, vol. 66, no. 7, pp. 3924–3930, 1995.

[174] C. Tonda-Turo, I. Carmagnola, and G. Ciardelli, "Quartz crystal microbalance with dissipation monitoring: A powerful method to predict the in vivo behavior of bioengineered surfaces", *Frontiers in bioengineering and biotechnology*, vol. 6, p. 158, 2018.

[175] G. Sauerbrey, "Verwendung von Schwingquarzen zur Wägung dünner Schichten und zur Mikrowägung", *Zeitschrift für physik*, vol. 155, no. 2, pp. 206–222, 1959.

[176] S. B. Nielsen and D. E. Otzen, "Quartz crystal microbalances as tools for probing protein–membrane interactions", in *Lipid-Protein Interactions*, Springer, 2019, pp. 31–52.

[177] M. V. Voinova, M. Rodahl, M. Jonson, and B. Kasemo, "Viscoelastic acoustic response of layered polymer films at fluid-solid interfaces: Continuum mechanics approach", *Physica Scripta*, vol. 59, no. 5, p. 391, 1999.

[178] N.-J. Cho, K. K. Kanazawa, J. S. Glenn, and C. W. Frank, "Employing two different quartz crystal microbalance models to study changes in viscoelastic behavior upon transformation of lipid vesicles to a bilayer on a gold surface", *Analytical chemistry*, vol. 79, no. 18, pp. 7027–7035, 2007.

[179] S. X. Liu and J.-T. Kim, "Application of kevin—voigt model in quantifying whey protein adsorption on polyethersulfone using QCM-D", *JALA: Journal of the Association for Laboratory Automation*, vol. 14, no. 4, pp. 213–220, 2009.

[180] I. Carton, A. R. Brisson, and R. P. Richter, "Label-free detection of clustering of membrane-bound proteins", *Analytical chemistry*, vol. 82, no. 22, pp. 9275–9281, 2010.

[181] A. Tsortos, G. Papadakis, and E. Gizeli, "The intrinsic viscosity of linear DNA", *Biopolymers*, vol. 95, no. 12, pp. 824–832, 2011.

[182] D. Milioni, A. Tsortos, M. Velez, and E. Gizeli, "Extracting the shape and size of biomolecules attached to a surface as suspended discrete nanoparticles", *Analytical chemistry*, vol. 89, no. 7, pp. 4198–4203, 2017.

[183] P. Mateos-Gil, A. Tsortos, M. Vélez, and E. Gizeli, "Monitoring structural changes in intrinsically disordered proteins using QCM-D: Application to the bacterial cell division protein ZipA", *Chemical Communications*, vol. 52, no. 39, pp. 6541–6544, 2016.

[184] P. Atkins and J. De Paula, *Elements of physical chemistry*. Oxford University Press, USA, 2013.

[185] S. E. Glassford, B. Byrne, and S. G. Kazarian, "Recent applications of ATR FTIR spectroscopy and imaging to proteins", *Biochimica et Biophysica Acta (BBA)-Proteins and Proteomics*, vol. 1834, no. 12, pp. 2849–2858, 2013.

[186] S. G. Kazarian and K. A. Chan, "Micro-and macro-attenuated total reflection fourier transform infrared spectroscopic imaging: Plenary lecture at the 5th international conference on advanced vibrational spectroscopy, 2009, melbourne, australia", *Applied spectroscopy*, vol. 64, no. 5, 135A–152A, 2010.

[187] F. M. Mirabella Jr, "Strength of interaction and penetration of infrared radiation for polymer films in internal reflection spectroscopy", *Journal of Polymer Science: Polymer Physics Edition*, vol. 21, no. 11, pp. 2403–2417, 1983.

[188] K. K. Chittur, "FTIR/ATR for protein adsorption to biomaterial surfaces", *Biomaterials*, vol. 19, no. 4-5, pp. 357–369, 1998.

[189] S. A. Tatulian, "Attenuated total reflection fourier transform infrared spectroscopy: A method of choice for studying membrane proteins and lipids", *Biochemistry*, vol. 42, no. 41, pp. 11 898–11 907, 2003.

[190] N. Paracini, L. A. Clifton, M. W. Skoda, and J. H. Lakey, "Liquid crystalline bacterial outer membranes are critical for antibiotic susceptibility", *Proceedings of the National Academy of Sciences*, vol. 115, no. 32, E7587–E7594, 2018.

[191] Y. Shai, "ATR-FTIR studies in pore forming and membrane induced fusion peptides", *Biochimica et Biophysica Acta (BBA)-Biomembranes*, vol. 1828, no. 10, pp. 2306–2313, 2013.

[192] M. D. Lad, F. Birembaut, L. A. Clifton, R. A. Frazier, J. R. Webster, and R. J. Green, "Antimicrobial peptide-lipid binding interactions and binding selectivity", *Biophysical Journal*, vol. 92, no. 10, pp. 3575–3586, 2007.

[193] S. A. Tatulian, "Toward understanding interfacial activation of secretory phospholipase A2 (PLA2): Membrane surface properties and membrane-induced structural changes in the enzyme contribute synergistically to pla2 activation", *Biophysical Journal*, vol. 80, no. 2, pp. 789–800, 2001.

[194] S. A. Tatulian, "Structural effects of covalent inhibition of phospholipase A2 suggest allosteric coupling between membrane binding and catalytic sites", *Biophysical Journal*, vol. 84, no. 3, pp. 1773–1783, 2003.

[195] S. A. Tatulian, "Structural characterization of membrane proteins and peptides by FTIR and ATR-FTIR spectroscopy", *Lipid-protein interactions: methods and protocols*, pp. 177–218, 2013.

[196] S. Frey and L. K. Tamm, "Orientation of melittin in phospholipid bilayers. a polarized attenuated total reflection infrared study", *Biophysical journal*, vol. 60, no. 4, pp. 922–930, 1991.

[197] B. H. Stuart, *Biological applications of infrared spectroscopy*. John Wiley & Sons, 1997.

[198] P.-c. Chen, R. Shevchuk, F. M. Strnad, *et al.*, "Combined small-angle X-ray and neutron scattering restraints in molecular dynamics simulations", *Journal of chemical theory and computation*, vol. 15, no. 8, pp. 4687–4698, 2019.

[199] A. R. Leach and A. R. Leach, *Molecular modelling: principles and applications*. Pearson education, 2001.

[200] M. Born and W. Heisenberg, "Zur quantentheorie der molekeln", *Original Scientific Papers Wissenschaftliche Originalarbeiten*, pp. 216–246, 1985.

[201] L. Verlet, "Computer" experiments" on classical fluids. i. Thermodynamical properties of Lennard-Jones molecules", *Physical review*, vol. 159, no. 1, p. 98, 1967.

[202] J.-P. Hansen and I. R. McDonald, *Theory of simple liquids: with applications to soft matter*. Academic press, 2013.

[203] H. J. Berendsen, J. v. Postma, W. F. Van Gunsteren, A. DiNola, and J. R. Haak, "Molecular dynamics with coupling to an external bath", *The Journal of chemical physics*, vol. 81, no. 8, pp. 3684–3690, 1984.

[204] M. Bonomi and C. Camilloni, *Biomolecular Simulations*. Springer, 2019, vol. 2022.

[205] J. Huang, S. Rauscher, G. Nawrocki, *et al.*, "CHARMM36m: An improved force field for folded and intrinsically disordered proteins", *Nature methods*, vol. 14, no. 1, pp. 71–73, 2017.

[206] P. C. Souza, R. Alessandri, J. Barnoud, *et al.*, "Martini 3: A general purpose force field for coarse-grained molecular dynamics", *Nature methods*, vol. 18, no. 4, pp. 382–388, 2021.

[207] S. J. Marrink, H. J. Risselada, S. Yefimov, D. P. Tieleman, and A. H. De Vries, "The MARTINI force field: Coarse grained model for biomolecular simulations", *The journal of physical chemistry B*, vol. 111, no. 27, pp. 7812–7824, 2007.

[208] L. Monticelli, S. K. Kandasamy, X. Periole, R. G. Larson, D. P. Tieleman, and S.-J. Marrink, "The MARTINI coarse-grained force field: Extension to proteins", *Journal of chemical theory and computation*, vol. 4, no. 5, pp. 819–834, 2008.

[209] R. Alessandri, P. C. Souza, S. Thallmair, M. N. Melo, A. H. De Vries, and S. J. Marrink, "Pitfalls of the Martini model", *Journal of chemical theory and computation*, vol. 15, no. 10, pp. 5448–5460, 2019.

[210] M. Javanainen, H. Martinez-Seara, and I. Vattulainen, "Excessive aggregation of membrane proteins in the Martini model", *PloS one*, vol. 12, no. 11, e0187936, 2017.

[211] O. N. Vickery and P. J. Stansfeld, "CG2AT2: An enhanced fragment-based approach for serial multi-scale molecular dynamics simulations", *Journal of chemical theory and computation*, vol. 17, no. 10, pp. 6472–6482, 2021.

[212] T. A. Wassenaar, K. Pluhackova, R. A. Böckmann, S. J. Marrink, and D. P. Tieleman, "Going backward: A flexible geometric approach to reverse transformation from coarse grained to atomistic models", *Journal of chemical theory and computation*, vol. 10, no. 2, pp. 676–690, 2014.

[213] A. C. Kalli, I. Devaney, and M. S. Sansom, "Interactions of phosphatase and tensin homologue (PTEN) proteins with phosphatidylinositol phosphates: Insights from molecular dynamics simulations of pten and voltage sensitive phosphatase", *Biochemistry*, vol. 53, no. 11, pp. 1724–1732, 2014.

[214] C. I. Lynch, S. Rao, and M. S. Sansom, "Water in nanopores and biological channels: A molecular simulation perspective", *Chemical reviews*, vol. 120, no. 18, pp. 10 298–10 335, 2020.

[215] W. L. Jorgensen, J. Chandrasekhar, J. D. Madura, R. W. Impey, and M. L. Klein, "Comparison of simple potential functions for simulating liquid water", *The Journal of chemical physics*, vol. 79, no. 2, pp. 926–935, 1983.

[216] W. L. Jorgensen and J. D. Madura, "Temperature and size dependence for Monte Carlo simulations of TIP4P water", *Molecular Physics*, vol. 56, no. 6, pp. 1381–1392, 1985.

[217] W. R. Scott, P. H. Hünenberger, I. G. Tironi, *et al.*, "The GROMOS biomolecular simulation program package", *The Journal of Physical Chemistry A*, vol. 103, no. 19, pp. 3596–3607, 1999.

[218] P. K. Weiner and P. A. Kollman, "AMBER: Assisted model building with energy refinement. A general program for modeling molecules and their interactions", *Journal of Computational Chemistry*, vol. 2, no. 3, pp. 287–303, 1981.

[219] W. L. Jorgensen and J. Tirado-Rives, "The OPLS [optimized potentials for liquid simulations] potential functions for proteins, energy minimizations for crystals of cyclic peptides and crambin", *Journal of the American Chemical Society*, vol. 110, no. 6, pp. 1657–1666, 1988.

[220] A. D. MacKerell Jr, D. Bashford, M. Bellott, *et al.*, "All-atom empirical potential for molecular modeling and dynamics studies of proteins", *The journal of physical chemistry B*, vol. 102, no. 18, pp. 3586–3616, 1998.

[221] J. F. Ouyang and R. P. Bettens, "Modelling water: A lifetime enigma", *Chimia*, vol. 69, no. 3, pp. 104–104, 2015.

[222] C. M. Baker, V. M. Anisimov, and A. D. MacKerell Jr, "Development of CHARMM polarizable force field for nucleic acid bases based on the classical Drude oscillator model", *The journal of physical chemistry B*, vol. 115, no. 3, pp. 580–596, 2011.

[223] H. Li, J. Chowdhary, L. Huang, X. He, A. D. MacKerell Jr, and B. Roux, "Drude polarizable force field for molecular dynamics simulations of saturated and unsaturated zwitterionic lipids", *Journal of chemical theory and computation*, vol. 13, no. 9, pp. 4535–4552, 2017.

[224] C. Zhang, C. Lu, Z. Jing, *et al.*, "AMOEBA polarizable atomic multipole force field for nucleic acids", *Journal of chemical theory and computation*, vol. 14, no. 4, pp. 2084–2108, 2018.

[225] J. W. Ponder, C. Wu, P. Ren, *et al.*, "Current status of the AMOEBA polarizable force field", *The journal of physical chemistry B*, vol. 114, no. 8, pp. 2549–2564, 2010.

[226] J. Melcr, H. Martinez-Seara, R. Nencini, J. Kolafa, P. Jungwirth, and O. S. Ollila, "Accurate binding of sodium and calcium to a POPC bilayer by effective inclusion of electronic polarization", *The Journal of Physical Chemistry B*, vol. 122, no. 16, pp. 4546–4557, 2018.

[227] I. Leontyev and A. Stuchebrukhov, "Accounting for electronic polarization in non-polarizable force fields", *Physical Chemistry Chemical Physics*, vol. 13, no. 7, pp. 2613–2626, 2011.

[228] J. Melcr, T. M. Ferreira, P. Jungwirth, and O. S. Ollila, "Improved cation binding to lipid bilayers with negatively charged POPS by effective inclusion of electronic polarization", *Journal of chemical theory and computation*, vol. 16, no. 1, pp. 738–748, 2019.

[229] M. Kohagen, P. E. Mason, and P. Jungwirth, "Accounting for electronic polarization effects in aqueous sodium chloride via molecular dynamics aided by neutron scattering", *The Journal of Physical Chemistry B*, vol. 120, no. 8, pp. 1454–1460, 2016.

[230] M. Kohagen, P. E. Mason, and P. Jungwirth, "Accurate description of calcium solvation in concentrated aqueous solutions", *The journal of physical chemistry B*, vol. 118, no. 28, pp. 7902–7909, 2014.

[231] E. Pluhařová, H. E. Fischer, P. E. Mason, and P. Jungwirth, "Hydration of the chloride ion in concentrated aqueous solutions using neutron scattering and molecular dynamics", *Molecular Physics*, vol. 112, no. 9-10, pp. 1230–1240, 2014.

[232] T. Martinek, E. Duboué-Dijon, Š. Timr, *et al.*, "Calcium ions in aqueous solutions: Accurate force field description aided by ab initio molecular dynamics and neutron scattering", *The Journal of chemical physics*, vol. 148, no. 22, p. 222 813, 2018.

[233] R. P. Richter, R. Bérat, and A. R. Brisson, "Formation of solid-supported lipid bilayers: An integrated view", *Langmuir*, vol. 22, no. 8, pp. 3497–3505, 2006.

[234] H. L. Smith, M. S. Jablin, A. Vidyasagar, *et al.*, "Model lipid membranes on a tunable polymer cushion", *Physical review letters*, vol. 102, no. 22, p. 228 102, 2009.

[235] G. Fragneto, T. Charitat, F. Graner, K. Mecke, L. Perino-Gallice, and E. Bellet-Amalric, "A fluid floating bilayer", *EPL (Europhysics Letters)*, vol. 53, no. 1, p. 100, 2001.

[236] J. Daillant, E. Bellet-Amalric, A. Braslau, *et al.*, "Structure and fluctuations of a single floating lipid bilayer", *Proceedings of the National Academy of Sciences*, vol. 102, no. 33, pp. 11 639–11 644, 2005.

[237] A. Melcrová, S. Pokorna, S. Pullanchery, *et al.*, "The complex nature of calcium cation interactions with phospholipid bilayers", *Scientific reports*, vol. 6, no. 1, pp. 1–12, 2016.

[238] P. Jurkiewicz, L. Cwiklik, A. Vojtıšková, P. Jungwirth, and M. Hof, "Structure, dynamics, and hydration of POPC/POPS bilayers suspended in NaCl, KCl, and CsCl solutions", *Biochimica et Biophysica Acta (BBA)-Biomembranes*, vol. 1818, no. 3, pp. 609–616, 2012.

[239] Y. He, Y. Chang, J. C. Hower, J. Zheng, S. Chen, and S. Jiang, "Origin of repulsive force and structure/dynamics of interfacial water in OEG–protein interactions: A molecular simulation study", *Physical Chemistry Chemical Physics*, vol. 10, no. 36, pp. 5539–5544, 2008.

[240] S. Herrwerth, W. Eck, S. Reinhardt, and M. Grunze, "Factors that determine the protein resistance of oligoether self-assembled monolayers- internal hydrophilicity, terminal hydrophilicity, and lateral packing density", *Journal of the American Chemical Society*, vol. 125, no. 31, pp. 9359–9366, 2003.

[241] T. Ekblad, G. Bergström, T. Ederth, *et al.*, "Poly (ethylene glycol)-containing hydrogel surfaces for antifouling applications in marine and freshwater environments", *Biomacromolecules*, vol. 9, no. 10, pp. 2775–2783, 2008.

[242] J. H. Lakey, N. Paracini, and L. A. Clifton, "Exploiting neutron scattering contrast variation in biological membrane studies", *Biophysics Reviews*, vol. 3, no. 2, p. 021 307, 2022.

[243] L. Boudière, M. Michaud, D. Petroutsos, *et al.*, "Glycerolipids in photosynthesis: Composition, synthesis and trafficking", *Biochimica et Biophysica Acta (BBA)-Bioenergetics*, vol. 1837, no. 4, pp. 470–480, 2014.

[244] M. L. Valentine, A. E. Cardenas, R. Elber, and C. R. Baiz, "Physiological calcium concentrations slow dynamics at the lipid-water interface", *Biophysical journal*, vol. 115, no. 8, pp. 1541–1551, 2018.

[245] M. Bloomfield, *Roughness Concepts*, 2006. [Online]. Available: `https://homepages.rpi.edu/~bloomm2/roughness.pdf`, accessed: 10.06.2023.

[246] G. Fragneto, T. Charitat, E. Bellet-Amalric, R. Cubitt, and F. Graner, "Swelling of phospholipid floating bilayers: The effect of chain length", *Langmuir*, vol. 19, no. 19, pp. 7695–7702, 2003.

[247] C. Keller, K. Glasmästar, V. Zhdanov, and B. Kasemo, "Formation of supported membranes from vesicles", *Physical Review Letters*, vol. 84, no. 23, p. 5443, 2000.

[248] *Martini3 beta*. [Online]. Available: `http://cgmartini.nl/index.php/martini3beta`, accessed: 21.07.2020.

[249] K. P. Fears, S. E. Creager, and R. A. Latour, "Determination of the surface pK of carboxylic-and amine-terminated alkanethiols using surface plasmon resonance spectroscopy", *Langmuir*, vol. 24, no. 3, pp. 837–843, 2008.

[250] M. D. Porter, T. B. Bright, D. L. Allara, and C. E. Chidsey, "Spontaneously organized molecular assemblies. 4. structural characterization of N-alkyl thiol monolayers on gold by optical ellipsometry, infrared spectroscopy, and electrochemistry", *Journal of the American Chemical Society*, vol. 109, no. 12, pp. 3559–3568, 1987.

[251] A. Ulman, "Formation and structure of self-assembled monolayers", *Chemical reviews*, vol. 96, no. 4, pp. 1533–1554, 1996.

[252] L. Strong and G. M. Whitesides, "Structures of self-assembled monolayer films of organosulfur compounds adsorbed on gold single crystals: Electron diffraction studies", *Langmuir*, vol. 4, no. 3, pp. 546–558, 1988.

[253] E. Schulze and M. Stein, "Simulation of mixed self-assembled monolayers on gold: Effect of terminal alkyl anchor chain and monolayer composition", *The Journal of Physical Chemistry B*, vol. 122, no. 31, pp. 7699–7710, 2018.

[254] J. Huang and A. D. MacKerell Jr, "CHARMM36 all-atom additive protein force field: Validation based on comparison to NMR data", *Journal of computational chemistry*, vol. 34, no. 25, pp. 2135–2145, 2013.

[255] A. Nikitin and G. Del Frate, "Development of nonbonded models for metal cations using the electronic continuum correction", *Journal of Computational Chemistry*, vol. 40, no. 28, pp. 2464–2472, 2019.

[256] A. J. Pertsin and M. Grunze, "Computer simulation of water near the surface of oligo (ethylene glycol)-terminated alkanethiol self-assembled monolayers", *Langmuir*, vol. 16, no. 23, pp. 8829–8841, 2000.

[257] J. Zheng, L. Li, S. Chen, and S. Jiang, "Molecular simulation study of water interactions with oligo (ethylene glycol)-terminated alkanethiol self-assembled monolayers", *Langmuir*, vol. 20, no. 20, pp. 8931–8938, 2004.

[258] T. Paul and J. Saha, "Effect of head group orientation on phospholipid assembly", *Physical Review E*, vol. 95, no. 6, p. 062 703, 2017.

[259] J. N. Sachs, H. Nanda, H. I. Petrache, and T. B. Woolf, "Changes in phosphatidylcholine headgroup tilt and water order induced by monovalent salts: Molecular dynamics simulations", *Biophysical journal*, vol. 86, no. 6, pp. 3772–3782, 2004.

[260] P. T. Vernier, M. J. Ziegler, and R. Dimova, "Calcium binding and head group dipole angle in phosphatidylserine- phosphatidylcholine bilayers", *Langmuir*, vol. 25, no. 2, pp. 1020–1027, 2009.

[261] J. Penfold, R. Richardson, A. Zarbakhsh, *et al.*, "Recent advances in the study of chemical surfaces and interfaces by specular neutron reflection", *Journal of the Chemical Society, Faraday Transactions*, vol. 93, no. 22, pp. 3899–3917, 1997.

[262] J. Penfold, R. Ward, and W. Williams, "A time-of-flight neutron reflectometer for surface and interfacial studies", *Journal of Physics E: Scientific Instruments*, vol. 20, no. 11, p. 1411, 1987.

[263] L. A. Clifton, F. Ciesielski, M. W. Skoda, N. Paracini, S. A. Holt, and J. H. Lakey, "The effect of lipopolysaccharide core oligosaccharide size on the electrostatic binding of antimicrobial proteins to models of the gram negative bacterial outer membrane", *Langmuir*, vol. 32, no. 14, pp. 3485–3494, 2016.

[264] B. W. Treece, P. A. Kienzle, D. P. Hoogerheide, C. F. Majkrzak, M. Lösche, and F. Heinrich, "Optimization of reflectometry experiments using information theory", *Journal of applied crystallography*, vol. 52, no. 1, pp. 47–59, 2019.

[265] A. Nelson, S. Prescott, kwertyops, A. McCluskey, and igresh, *Refnx/refnx: Rel: V0.1.16*, version v0.1.16, Jul. 2020. DOI: 10.5281/zenodo.3960984. [Online]. Available: https://doi.org/10.5281/zenodo.3960984.

[266] F. Abeles, "Sur la propagation des ondes électromagnétiques dans les milieux sratifiés", in *Annales de physique*, EDP Sciences, vol. 12, 1948, pp. 504–520.

[267] 1. Nevot and P. Croce, "Caractérisation des surfaces par réflexion rasante de rayons X. application à l'étude du polissage de quelques verres silicates", *Revue de Physique appliquée*, vol. 15, no. 3, pp. 761–779, 1980.

[268] P. Virtanen, R. Gommers, T. E. Oliphant, *et al.*, "SciPy 1.0: Fundamental algorithms for scientific computing in Python", *Nature methods*, vol. 17, no. 3, pp. 261–272, 2020.

[269] D. Foreman-Mackey, W. M. Farr, M. Sinha, *et al.*, "Emcee v3: A Python ensemble sampling toolkit for affine-invariant MCMC", *arXiv preprint arXiv:1911.07688*, 2019.

[270] H. I. Petrache, S. Tristram-Nagle, K. Gawrisch, D. Harries, V. A. Parsegian, and J. F. Nagle, "Structure and fluctuations of charged phosphatidylserine bilayers in the absence of salt", *Biophysical journal*, vol. 86, no. 3, pp. 1574–1586, 2004.

[271] *Molinspiration, calculation of molecular properties and bioactivity score*. [Online]. Available: https://www.molinspiration.com/cgi-bin/properties, accessed: 30.07.2020.

[272] S.-W. Chiu, E. Jakobsson, S. Subramaniam, and H. L. Scott, "Combined Monte Carlo and molecular dynamics simulation of fully hydrated dioleyl and palmitoyl-oleyl phosphatidylcholine lipid bilayers", *Biophysical Journal*, vol. 77, no. 5, pp. 2462–2469, 1999.

[273] A. M. Smondyrev and M. L. Berkowitz, "Molecular dynamics simulation of the structure of dimyristoylphosphatidylcholine bilayers with cholesterol, ergosterol, and lanosterol", *Biophysical journal*, vol. 80, no. 4, pp. 1649–1658, 2001.

[274] L. Li, S. Chen, J. Zheng, B. D. Ratner, and S. Jiang, "Protein adsorption on oligo (ethylene glycol)-terminated alkanethiolate self-assembled monolayers: The molecular basis for nonfouling behavior", *The Journal of Physical Chemistry B*, vol. 109, no. 7, pp. 2934–2941, 2005.

[275] D. Van Der Spoel, E. Lindahl, B. Hess, G. Groenhof, A. E. Mark, and H. J. Berendsen, "GROMACS: Fast, flexible, and free", *Journal of computational chemistry*, vol. 26, no. 16, pp. 1701–1718, 2005.

[276] G. Bussi, D. Donadio, and M. Parrinello, "Canonical sampling through velocity rescaling", *The Journal of chemical physics*, vol. 126, no. 1, p. 014 101, 2007.

[277] M. Parrinello and A. Rahman, "Polymorphic transitions in single crystals: A new molecular dynamics method", *Journal of Applied physics*, vol. 52, no. 12, pp. 7182–7190, 1981.

[278] W. Humphrey, A. Dalke, and K. Schulten, "VMD: Visual molecular dynamics", *Journal of molecular graphics*, vol. 14, no. 1, pp. 33–38, 1996.

[279] H. J. Berendsen, D. van der Spoel, and R. van Drunen, "GROMACS: A message-passing parallel molecular dynamics implementation", *Computer physics communications*, vol. 91, no. 1-3, pp. 43–56, 1995.

[280] T. Darden, D. York, and L. Pedersen, "Particle mesh ewald: An *N* log (N) method for Ewald sums in large systems", *The Journal of chemical physics*, vol. 98, no. 12, pp. 10 089–10 092, 1993.

[281] S. Lee, A. Tran, M. Allsopp, J. B. Lim, J. Hénin, and J. B. Klauda, "CHARMM36 united atom chain model for lipids and surfactants", *The journal of physical chemistry B*, vol. 118, no. 2, pp. 547–556, 2014.

[282] S. Kim, J. Lee, S. Jo, C. L. Brooks III, H. S. Lee, and W. Im, *CHARMM-GUI ligand reader and modeler for CHARMM force field generation of small molecules*, 2017.

[283] T. A. Wassenaar, H. I. Ingólfsson, R. A. Bockmann, D. P. Tieleman, and S. J. Marrink, "Computational lipidomics with insane: A versatile tool for generating custom membranes for molecular simulations", *Journal of chemical theory and computation*, vol. 11, no. 5, pp. 2144–2155, 2015.

[284] J. Hautman, J. P. Bareman, W. Mar, and M. L. Klein, "Molecular dynamics investigations of self-assembled monolayers", *Journal of the Chemical Society, Faraday Transactions*, vol. 87, no. 13, pp. 2031–2037, 1991.

[285] H. Lee, A. H. de Vries, S.-J. Marrink, and R. W. Pastor, "A coarse-grained model for polyethylene oxide and polyethylene glycol: Conformation and hydrodynamics", *The journal of physical chemistry B*, vol. 113, no. 40, pp. 13 186–13 194, 2009.

[286] E. Evans and E. Sackmann, "Translational and rotational drag coefficients for a disk moving in a liquid membrane associated with a rigid substrate", *Journal of Fluid Mechanics*, vol. 194, pp. 553–561, 1988. DOI: 10.1017/S0022112088003106.

[287] L. H. John, G. M. Preston, M. S. Sansom, and L. A. Clifton, "Large scale model lipid membrane movement induced by a cation switch", *Journal of colloid and interface science*, vol. 596, pp. 297–311, 2021.

[288] J. Israelachvili and H. Wennerström, "Role of hydration and water structure in biological and colloidal interactions", *Nature*, vol. 379, no. 6562, pp. 219–225, 1996.

[289] N. T. Flynn, T. N. T. Tran, M. J. Cima, and R. Langer, "Long-term stability of self-assembled monolayers in biological media", *Langmuir*, vol. 19, no. 26, pp. 10 909–10 915, 2003.

[290] R. S. Shawgo, A. C. R. Grayson, Y. Li, and M. J. Cima, "BioMEMS for drug delivery", *Current Opinion in Solid State and Materials Science*, vol. 6, no. 4, pp. 329–334, 2002.

[291] S. Herrwerth, T. Rosendahl, C. Feng, *et al.*, "Covalent coupling of antibodies to self-assembled monolayers of carboxy-functionalized poly (ethylene glycol): Protein resistance and specific binding of biomolecules", *Langmuir*, vol. 19, no. 5, pp. 1880–1887, 2003.

[292] F. Schreiber, "Self-assembled monolayers: From 'simple'model systems to biofunctionalized interfaces", *Journal of Physics: Condensed Matter*, vol. 16, no. 28, R881, 2004.

[293] S. Block, "Brownian motion at lipid membranes: A comparison of hydrodynamic models describing and experiments quantifying diffusion within lipid bilayers", *Biomolecules*, vol. 8, no. 2, p. 30, 2018.

[294] Y. Xue, X. Li, H. Li, and W. Zhang, "Quantifying thiol–gold interactions towards the efficient strength control", *Nature communications*, vol. 5, no. 1, pp. 1–9, 2014.

[295] D. De Jong and A. Heuer, "The influence of solid scaffolds on flat and curved lipid membranes", *AIP Advances*, vol. 7, no. 7, p. 075 007, 2017.

[296] K. Weiß and J. Enderlein, "Lipid diffusion within black lipid membranes measured with dual-focus fluorescence correlation spectroscopy", *ChemPhysChem*, vol. 13, no. 4, pp. 990–1000, 2012.

[297] W. Cho and R. V. Stahelin, "Membrane-protein interactions in cell signaling and membrane trafficking", *Annu. Rev. Biophys. Biomol. Struct.*, vol. 34, pp. 119–151, 2005.

[298] J. H. Hurley, "Membrane binding domains", *Biochimica et Biophysica Acta (BBA)-Molecular and Cell Biology of Lipids*, vol. 1761, no. 8, pp. 805–811, 2006.

[299] T.-T. Huang, E. J. Lampert, C. Coots, and J.-M. Lee, "Targeting the PI3K pathway and DNA damage response as a therapeutic strategy in ovarian cancer", *Cancer treatment reviews*, vol. 86, p. 102 021, 2020.

[300] L. C. Cantley, "The phosphoinositide 3-kinase pathway", *Science*, vol. 296, no. 5573, pp. 1655–1657, 2002.

[301] S. Matsuoka and M. Ueda, "Mutual inhibition between PTEN and PIP3 generates bistability for polarity in motile cells", *Nature communications*, vol. 9, no. 1, pp. 1–15, 2018.

[302] L. A. Clifton, C. Neylon, and J. H. Lakey, "Examining protein–lipid complexes using neutron scattering", in *Lipid-Protein Interactions*, Springer, 2013, pp. 119–150.

[303] J. Mistry, S. Chuguransky, L. Williams, *et al.*, "Pfam: The protein families database in 2021", *Nucleic acids research*, vol. 49, no. D1, pp. D412–D419, 2021.

[304] R. V. Stahelin, J. L. Scott, and C. T. Frick, "Cellular and molecular interactions of phosphoinositides and peripheral proteins", *Chemistry and physics of lipids*, vol. 182, pp. 3–18, 2014.

[305] B. Guo, J. Gao, J. Zhan, and H. Zhang, "Kindlin-2 interacts with and stabilizes EGFR and is required for EGF-induced breast cancer cell migration", *Cancer letters*, vol. 361, no. 2, pp. 271–281, 2015.

[306] H. D. Perera, Y.-Q. Ma, J. Yang, J. Hirbawi, E. F. Plow, and J. Qin, "Membrane binding of the N-terminal ubiquitin-like domain of kindlin-2 is crucial for its regulation of integrin activation", *Structure*, vol. 19, no. 11, pp. 1664–1671, 2011.

[307] O. Soubias, S. Pant, F. Heinrich, *et al.*, "Membrane surface recognition by the ASAP1 PH domain and consequences for interactions with the small GTPase Arf1", *Science advances*, vol. 6, no. 40, eabd1882, 2020.

[308] S. Shenoy, P. Shekhar, F. Heinrich, *et al.*, "Membrane association of the PTEN tumor suppressor: Molecular details of the protein-membrane complex from SPR binding studies and neutron reflection", *PloS one*, vol. 7, no. 4, e32591, 2012.

[309] T. Ni, A. C. Kalli, F. B. Naughton, *et al.*, "Structure and lipid-binding properties of the kindlin-3 pleckstrin homology domain", *Biochemical Journal*, vol. 474, no. 4, pp. 539–556, 2017.

[310] W. Song, R. A. Corey, T. B. Ansell, *et al.*, "PyLipID: A python package for analysis of protein–lipid interactions from molecular dynamics simulations", *Journal of Chemical Theory and Computation*, 2022.

[311] Z.-Y. Zhao, C.-G. Han, J.-T. Liu, C.-L. Wang, Y. Wang, and L.-Y. Cheng, "TIAM2 enhances non-small cell lung cancer cell invasion and motility", *Asian Pacific Journal of Cancer Prevention*, vol. 14, no. 11, pp. 6305–6309, 2013.

[312] T. R. Shepherd, R. L. Hard, A. M. Murray, D. Pei, and E. J. Fuentes, "Distinct ligand specificity of the tiam1 and tiam2 PDZ domains", *Biochemistry*, vol. 50, no. 8, pp. 1296–1308, 2011.

[313] H.-W. Park and J. H. Lee, "Calcium channel blockers as potential therapeutics for obesity-associated autophagy defects and fatty liver pathologies", *Autophagy*, vol. 10, no. 12, pp. 2385–2386, 2014.

[314] K. S. Gwiazda, T.-L. B. Yang, Y. Lin, and J. D. Johnson, "Effects of palmitate on er and cytosolic ca2+ homeostasis in β-cells", *American Journal of Physiology-Endocrinology and Metabolism*, vol. 296, no. 4, E690–E701, 2009.

[315] R. L. Byyny, M. L. Verde, S. Lloyd, W. Mitchell, and B. Draznin, "Cytosolic calcium and insulin resistance in elderly patients with essential hypertension", *American journal of hypertension*, vol. 5, no. 7, pp. 459–464, 1992.

[316] J. K. Kang, O.-H. Kim, J. Hur, *et al.*, "Increased intracellular ca2+ concentrations prevent membrane localization of ph domains through the formation of ca2+-phosphoinositides", *Proceedings of the National Academy of Sciences*, vol. 114, no. 45, pp. 11 926–11 931, 2017.

[317] O. Guven, M. Gul, E. Ayan, *et al.*, "Case study of high-throughput drug screening and remote data collection for SARS-CoV-2 Main Protease by using serial femtosecond X-ray crystallography", *Crystals*, vol. 11, no. 12, p. 1579, 2021.

[318] C. Notredame, D. G. Higgins, and J. Heringa, "T-Coffee: A novel method for fast and accurate multiple sequence alignment", *Journal of molecular biology*, vol. 302, no. 1, pp. 205–217, 2000.

[319] P. Gouet, E. Courcelle, D. I. Stuart, and F. M© toz, "ESPript: Analysis of multiple sequence alignments in PostScript.", *Bioinformatics (Oxford, England)*, vol. 15, no. 4, pp. 305–308, 1999.

[320] A. Waterhouse, M. Bertoni, S. Bienert, *et al.*, "SWISS-MODEL: Homology modelling of protein structures and complexes", *Nucleic acids research*, vol. 46, no. W1, W296–W303, 2018.

[321] A. Travert and C. Fernandez, *Spectrochempy, a framework for processing, analyzing and modeling spectroscopic data for chemistry with python*, version 0.5.1.dev1, Jan. 2023. DOI: 10.5281/zenodo.3823841. [Online]. Available: https://www.spectrochempy.fr.

[322] J. Webster, S. Holt, and R. Dalgliesh, "INTER the chemical interfaces reflectometer on target station 2 at ISIS", *Physica B: Condensed Matter*, vol. 385, pp. 1164–1166, 2006.

[323] R. Dalgliesh, S. Langridge, J. Plomp, V. De Haan, and A. Van Well, "Offspec, the ISIS spin-echo reflectometer", *Physica B: Condensed Matter*, vol. 406, no. 12, pp. 2346–2349, 2011.

[324] S. Bucciarelli, N. Mahmoudi, L. Casal-Dujat, M. Jéhannin, C. Jud, and A. Stradner, "Extended law of corresponding states applied to solvent isotope effect on a globular protein", *The journal of physical chemistry letters*, vol. 7, no. 9, pp. 1610–1615, 2016.

[325] E. L. Wu, X. Cheng, S. Jo, *et al.*, *CHARMM-GUI membrane builder toward realistic biological membrane simulations*, 2014.

[326] D. H. de Jong, G. Singh, W. D. Bennett, *et al.*, "Improved parameters for the martini coarse-grained protein force field", *Journal of chemical theory and computation*, vol. 9, no. 1, pp. 687–697, 2013.

[327] W. Kabsch and C. Sander, "Dictionary of protein secondary structure: Pattern recognition of hydrogen-bonded and geometrical features", *Biopolymers: Original Research on Biomolecules*, vol. 22, no. 12, pp. 2577–2637, 1983.

[328] B. Hess, H. Bekker, H. J. Berendsen, and J. G. Fraaije, "LINCS: A linear constraint solver for molecular simulations", *Journal of computational chemistry*, vol. 18, no. 12, pp. 1463–1472, 1997.

[329] S. O. Yesylevskyy, L. V. Schäfer, D. Sengupta, and S. J. Marrink, "Polarizable water model for the coarse-grained MARTINI force field", *PLoS computational biology*, vol. 6, no. 6, e1000810, 2010.

[330] C. R. Harris, K. J. Millman, S. J. Van Der Walt, *et al.*, "Array programming with NumPy", *Nature*, vol. 585, no. 7825, pp. 357–362, 2020.

[331] J. D. Hunter, "Matplotlib: A 2D graphics environment", *Computing in science & engineering*, vol. 9, no. 03, pp. 90–95, 2007.

[332] L. H. John, F. B. Naughton, M. S. Sansom, and A. H. Larsen, "The Role of C2 Domains in Two Different Phosphatases: PTEN and SHIP2", *Membranes*, vol. 13, no. 4, p. 408, 2023.

[333] B. W. Treece, F. Heinrich, A. Ramanathan, and M. Losche, "Steering molecular dynamics simulations of membrane-associated proteins with neutron reflection results", *Journal of Chemical Theory and Computation*, vol. 16, no. 5, pp. 3408–3419, 2020.